ACTIVE CONTROL OF ACOUSTIC RADIATION DUE TO DISCONTINUITIES ON THIN BEAMS

by

Kenneth D. Frampton

Thesis submitted to the Faculty of the
Virginia Polytechnic Institute and State University
in partial fulfillment of the requirements for the degree of
MASTER OF SCIENCE
in
Mechanical Engineering

APPROVED:

Dr. Chris R. Fuller, Chairman

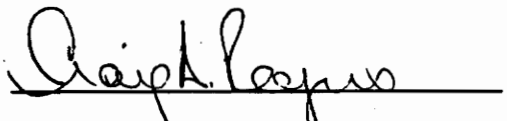

Dr. Craig A. Rogers

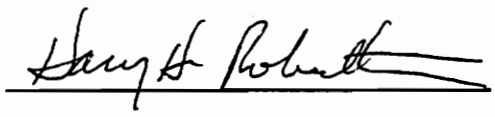

Dr. Harry H. Robertshaw

April, 1991

Blacksburg, Virginia

ACTIVE CONTROL OF ACOUSTIC RADIATION DUE TO DISCONTINUITIES ON INFINITE BEAMS

by

Kenneth D. Frampton

Committee Chairman: Chris R. Fuller Mechanical Engineering

(ABSTRACT)

Two experiments were conducted to study the active control of acoustic radiation due to discontinuities on thin beams. One experiment investigated the radiation from a clamped end condition and the other investigated the radiation from a blocking mass. The beams were excited by subsonic flexural traveling waves which "scattered" (or produced reflected and transmitted traveling and near-field waves) when they encountered the discontinuity. This "scattering" produced supersonic wavenumber components in the beam vibrational response which were responsible for the acoustic radiation. The main purpose of these experiments was to control the acoustic radiation from discontinuities on beams by actively changing the characteristics of the "scattered" waves with control actuators.

In each experiment the system was disturbed by a harmonic, subsonic input from a point force shaker. Control actuator(s) (in the form of shakers and piezoelectric actuators) were attached to the beam near the discontinuity. Error microphone(s) were positioned in the acoustic field which supplied an error signal to the digital controller. The digital controller employed was the filtered-x version of the adaptive LMS algorithm programmed on a dedicated signal processing board in a personal computer.

An array of accelerometers was attached to the beam which were used to decompose the complex amplitudes of an assumed displacement equation. By applying a spatial Fourier transform to the displacement equation the wavenumber components present in the beam displacement were calculated. This aided in the investigation of the mechanism by which control of the acoustic field was affected.

Results from these experiments showed that large attenuations at the error microphones were possible (as much as $50dB$) along with global attenuation of the acoustic field. The mechanism by which the control of the acoustic far-field was achieved was demonstrated as a decrease in the supersonic wavenumber components in the beam vibrational response.

Acknowledgements

First of all I would like to thank my parents, Don and Patsy Frampton, for providing me with every opportunity in life, particularly my education. Their support throughout my education has been invaluable and I sincerely appreciate their sacrifices.

I would also like to thank my advisor Chris Fuller for providing me with the opportunity to study under him and for his patience with me throughout my graduate studies. Working with him has certainly prepared me for a successful career. Thanks also to Craig Rogers and Harry Robertshaw for their contributions as members of my advisory committee.

I also owe a great deal to Rob Clark for his assistance in so many things. Experimental expertise, analytical insight, leisurely golf and a compatible sense of humor are only a small part of his contribution to this thesis and the time spent preparing it. Thanks to Cathy Guigou for her analytical contributions to this thesis. Her support provided much guidance in the experiments behind it.

Finally, and most importantly, I would like to thank my new bride Lynlee Burton. I can only hope that our future together will be as rewarding as our past.

Contents

List of Figures

List of Tables

Nomenclature

A,B,C,D,E,F,G	= coefficients of the assumed displacement
E	= Youngs modulus
F_{in}	= input force magnitude
F_j^c	= magnitude of the j^{th} control force
F_o	= discontinuity reaction force
I	= area moment of inertia
i	= $\sqrt{-1}$
J_b	= blocking mass moment of inertia
k	= wavenumber
k_b	= structural wavenumber
k_o	= acoustic medium wavenumber
l	= piezoelectric actuator length
M_j^c	= magnitude of the j^{th} control moment
M_o	= discontinuity reaction moment
m_b	= mass of the blocking mass
P_{mn}	= filtered-x transfer function
R, θ, ϕ	= cylindrical coordinates
U	= vector of unknown complex amplitudes

W	= optimal weighting coefficients
$\tilde{w}$	= spatial Fourier transform of the beam displacment
X	= FIR filter input
X	= linear regression matrix
Y	= FIR filter output
Y	= vector of accelerometer data points
x, y, z	= cartesian coordinates
α_{in}	= input force location
α_j^c	= location of the j^{th} control actuator
$\delta(\cdots)$	= Dirac delta function
ϵ	= LMS error signal
γ_x, γ_y	= spatial fourier transform parameters
ρ	= mass per unit length
ω	= excitation angular frequency

Chapter 1

Introduction

Many structures in use today incorporate beams as integral components. Structural elements such as aircraft and maritime vessel infrastructures, building frames and heavy machinery mounts can all include various forms of beams in their designs. As these structures are excited by machinery, noise, and other environmental effects, subsonic vibrational waves propagate through the system. When these subsonic vibrational waves, traveling along structural components (such as beams), encounter a discontinuity (such as a joint between two structural members) sound is often produced in this area. This emission of sound from the area of structural discontinuities is caused by the scattering of traveling waves into reflected near-field and reflected traveling waves (as well as transmitted waves) which in turn produces supersonic wavenumber components in the vibrational response. These supersonic wavenumber components are the cause of the acoustic radiation. For this reason, control of structural vibrations (and control of subsonic wave scattering) for the purpose of reducing the sound emanating from such structural discontinuities is of great interest.

In the past, passive approaches have been taken to controlling structural vibrations and the resulting acoustic radiation. These passive control approaches are limited in their range of effective frequency and generally have poor performance at low frequencies. More recently developed active control approaches have many advantages over passive techniques. For example active control systems can adapt to changing system characteristics, they perform well at low frequencies, and their overall attenuation of sound and vibration levels is much better.

1.1 Previous Work

1.1.1 Active Noise and Vibration Control

Active noise and vibration control systems are a relatively recent development. A typical active control system, such as the one presented by Widrow, et al. [1], requires three basic components as listed below:

1. **Error sensors:** these provide the "nervous system" of an active control system by producing an electrical signal proportional to the signal to be controlled (such as vibrational response or sound pressure levels).

2. **Control system:** this supplies the "intelligence" of the system which calculates the control signal to be applied based on the error signal. It is generally in the form of a digital signal processing system.

3. **Control actuator:** these supply the "muscle" to forcibly control the error signal.

The "nervous system", or error sensor, can be any transducer which converts the signal to be controlled into an electrical signal. Gonidou [2] used an accelerometer attached to a beam to sense power flow of bending waves. A microphone in the acoustic field was used by Fuller et al. [3] to sense sound transmitted through a plate. Microphones were also used by Clark and Fuller [4] to sense acoustic radiation from plates. A more recently developed sensor, incorporating piezoelectric patches, was used by Fuller, Gibbs and Silcox [5] to simultaneously sense bending and extensional waves in beams. Piezoelectric films, recently utilized as sensors, were used by Clark and Fuller [6] to sense spatially filtered modes on a simply supported plate. Any of these error sensors, and many more transducer types, can be used in an active control system. In the experiments presented in this thesis, microphones were used as error sensors.

Second, an active control system must have some sort of "intelligence" which does the "thinking" for the control system. In many of the previously conducted active control experiments this was in the form of a digital signal processing (DSP) board hosted by a personal computer. The DSP board sampled the signal from the error sensor and, based on this error signal, calculated a control signal to send to the control actuator. The method used by Gonidou [2], Fuller et al. [3] and Clark and Fuller [4, 6] for calculating the control signal (and the method used in these experiments) was the filtered-x version of the adaptive least mean square (LMS) algorithm. This algorithm used a steepest gradient descent method which minimized the least square of the error signal by converging on the set of optimal weighting coefficients for the adaptive filter. Elliot, Stothers and Nelson [7] describe this algorithm in detail and it is also discussed in Sec. 3.2 of this thesis.

The final component of a typical active control system is the control actuator. The purpose of the control actuator is to forcibly change the structures vibrational characteristics such that error signal is minimized. Gonidou [2] used point force shakers as actuators to control power flow in beams. Fuller et al. [3] used point force shakers to control sound transmission through plates. Clark and Fuller [4, 6] used piezoelectric actuators to control acoustic radiation from plates. Fuller, Gibbs, and Silcox [5] used piezoelectric actuators to simultaneously control flexural and extensional waves in beams. Both of the previously mentioned actuator types were used in the experiments presented in this thesis.

B. R. Mace [8] did some further studies on active control of flexural vibrations. It was shown how several point sensors and actuators distributed along a waveguide (either a beam or a duct) could be combined with either of two types of control systems to attenuate the flexural waves. One of the control systems employed displacement and rotation measurements along with a point force and a point moment control actuator. The second control system used two displacement measurements and two point force controllers. For each case the optimal active controller was derived and some results from each configuration were shown. Mace concluded that, this simple two input, two output control system could easily be expanded to accommodate a much larger system.

A further study on the active control of flexural wave reflections in beams was performed by Scheuren [9]. A control system was developed which would cancel the reflections from broad band flexural waves by means of two measurement accelerometers and one point force actuator. It was shown that reflected wave attenuations of $25dB$ to $30dB$ were possible with this system depending on the quality of the

approximate transfer functions employed in the controller.

Another study on active control was performed by Miller, Hall and von Flotow [10]. The optimal control of power flow at structural junctions was investigated. A physical measurement feedback system was used to mimic the feedforward of incoming waves. The characteristics of this control system were derived by minimizing a cost function which incorporated the steady state power flow and minimum control effort. These authors were able to demonstrate several advantages to a wave control approach as opposed to a modal control approach. These advantages included taking advantage of the finite speed with which waves propagate through a system, employing a much smaller controller (in terms of calculations required), and the fact that wave control models are much more accurate than modal control models.

Active control principles have been used to control disturbances besides vibrations and acoustics such as electrical noise control in communications equipment, and signal processing. However, among the extensive application of active control systems to structural acoustic radiation, very little work has been published on active control of acoustic radiation from beams.

1.1.2 Acoustics of Infinite Beams

Although little experimentation has previously been done on acoustic radiation from beams, much analytical work has been done. Fahy [11] describes the radiation from several planar radiators, including beams and plates, with various boundary conditions. The mechanisms by which structural vibrations produce acoustic radiation are also discussed. It was shown that, through reflection and transmission of travel-

ing waves from discontinuities in structures, and by the the semi-infinite nature of traveling waves (since they may exist only in the region of $0 < x < \infty$), supersonic wavenumber components are produced which cause acoustic waves to propagate away from the structure.

Junger and Feit [12] also discuss acoustic radiation from beams. Like Fahy, Junger and Feit discuss the presence of reflected and transmitted waves associated with structural discontinuities and the production of supersonic wavenumber components which cause acoustic radiation.

Keltie [13] gives an excellent description of acoustic radiation due to wave scattering from discontinuities on beams excited by subsonic flexural waves. The displacement equation is presented for a beam with a general discontinuity (including incident, reflected, and transmitted traveling and near-field waves). The equation for power radiating from the beam is developed which requires the derivation of the spatial Fourier transform. From the spatial Fourier transform of the displacement, it was shown that the presence of supersonic wavenumber components created by near-field waves (both reflected and transmitted) was the dominant contributor to the radiated sound power. This paper is the basis for much of the analysis presented in this thesis.

Keltie also discusses acoustic radiation from beams subjected to point force excitation [14]. In this paper he addresses the effects of damping on the radiated sound power and the relative contributions to the acoustic field from traveling and near-field waves. The conclusion was drawn that, for subsonic flexural waves, the sound power radiated by the propagating and near-field waves was equivalent. However, for frequencies approaching the critical frequency, the propagating waves dominated

the sound power radiation.

Mace performed an analysis of wave reflections and transmissions in beams [15]. Although this does not directly involve acoustics of beams, the waves present in the structural response is very important as shown in [13]. The traveling and near-field waves present in a beams response were examined. Then, expressions were derived for the waves present with various types of discontinuities including point discontinuities, end conditions, point forces and cross sectional changes. Several results are presented for various sizes of discontinuities and the resulting, relative magnitudes of the reflected and transmitted waves.

Extensive analytical work has been done by Guigou [16] but has not been published to date. Her work focused on active control of acoustic radiation from discontinuities on beams. The structural response due to excitation by subsonic flexural waves and the resulting acoustic radiation caused by scattering of structural waves were investigated. Some of the results from Guigou's work are presented in this thesis and are compared with the corresponding experiments.

1.2 Scope of Work

Two experiments were conducted with the intention of demonstrating the feasibility of active control of acoustic radiation due to subsonic wave scattering by discontinuities on thin beams. The beams were excited by subsonic flexural waves. When these waves encountered a discontinuity, reflected traveling and near-field waves were produced (as well as transmitted waves). This scattering created supersonic wavenumber components as did the semi-infinite nature of the traveling waves. Since

the traveling waves were defined only over the region of $0 < x < \infty$ or $-\infty < x < 0$ they contributed supersonic wavenumber components to the wavenumber spectrum along with the corresponding spectral peaks. This manufacturing of supersonic wavenumber components caused acoustic radiation to propagate away from the discontinuity region. It was the intention of these experiments to actively affect these scattered flexural waves in such a manner as to minimize the acoustic radiation at particular points in the acoustic field. In addition, the changes in the beam vibrational response under control were investigated in order to better understand the mechanism by which the active control was achieved.

To demonstrate this concept two experimental rigs were constructed. The first was a beam with a clamped discontinuity at one end. The other end of the beam was placed in an anechoic termination which made the beam appear infinite to traveling waves by preventing their reflections. The second experiment implemented a beam with a blocking mass discontinuity attached to it. Both ends of this beam were placed in anechoic terminations while a metal blocking mass was attached to the middle of the beam.

A harmonic signal was used to drive an input shaker fastened to each beam which acted as the system disturbance. Subsonic flexural waves produced by the input shaker traveled along the beam and encountered the discontinuity. This resulted in reflected near-field and traveling waves (as well as transmitted traveling and near-field waves in the experiments on the beam and blocking mass) as well as traveling waves defined in a semi-infinite space. The scattering and semi-infinite nature of the incident waves produced supersonic wavenumber components which caused acoustic radiation to propagate from the region of the discontinuity.

A semicircular array of microphones was used to sample the acoustic field associated with the system disturbance and the discontinuity. This microphone array was positioned in the acoustic "near-field" (due to space limitations in the anechoic chamber) for the operating frequencies of these experiments. This reference to the "near-field" is used loosely. It does not imply that the microphone array is very close to the beam, rather, it means that the microphone array is not in the far-field. This implication of acoustic "near-field" meaning not in the acoustic far-field is used throughout this thesis.

In addition, an array of accelerometers was used to measure the acceleration of the beam at several points. From these accelerometer data points the complex amplitudes for an assumed displacement equation were calculated using a least squares regression method. By using the method of least squares to decompose the coefficients for the displacement equation, the effects of any error in the accelerometer data was minimized.

Once the acoustic field and vibrational response data was obtained for a particular experimental situation (either the clamped beam or the beam with a blocking mass) the controller was activated. By sending an error signal from the error microphone(s) to the controller (a filtered–x LMS algorithm) an optimal control signal was calculated and sent to the control actuator(s) attached to the beam near the discontinuity. When the error signal was minimized a set of data was again taken from the microphone array and the accelerometer array. By comparing the two sets of microphone data (before and after control) the effectiveness of the control on the acoustic field was established.

To describe the mechanism by which the control was achieved the vibrational char-

acteristics of the beam were studied. By taking the spatial Fourier transform of the statistically decomposed displacement equation the wavenumber components present in the beam vibrational response before and after control were revealed. It has previously been shown in [11, 12] that only structural wavenumber components in the supersonic region (where the structural wavenumber is less than the wavenumber in the acoustic medium $|k| < k_o$) are responsible for acoustic radiation. This concept is discussed further in Sec. 1.3.4.

Results for several experiments with the clamped beam and the beam with a blocking mass are presented here. These results include comparisons for experimental cases at various frequencies, error microphone locations, number of error microphones, actuator locations, number of actuators and for different actuator types. It was shown that active control of "near-field" acoustic radiation from discontinuities on beams was possible. Cases showing as much as $40dB$ of acoustic attenuation at the error microphone have been documented. It has also been shown that along with large attenuations at the error microphone, the acoustic field was globally attenuated and that, while controlling the acoustic "near-field", the far-field acoustic radiation was attenuated in the clamped beam experiments. However, this attenuation of the far-field while controlling the near-field did not occur for the beam with a blocking mass. In addition, the mechanism by which the control of the far-field acoustic radiation was affected was demonstrated as a decrease in the supersonic wave number components in the beam vibration under control.

1.3 Theoretical Background

In this section a general development of baffled, infinite, thin beam vibration and acoustic radiation theory is given. The general differential equations of motion for point force actuation and piezoelectric actuation are presented along with the corresponding solutions of the differential equation. Each of these solutions were derived by Guigou [16] and they are presented in this thesis without the intermediary steps. Finally, the equations describing the acoustic radiation from infinite beams with discontinuities are presented. This theory was used to calculate values to compare with the experimental results presented in this thesis.

1.3.1 Differential Equation of Motion for Thin Beams

To derive the differential equation of motion for a beam with a discontinuity and subjected to a distributed loading, $p(x,t)$,the free body diagram of a beam element was considered (as shown in Fig. 1.1). Where T is the shear force and M_f is the bending moment about the y axis.

It is shown in [17] that:

$$M_f = EI\frac{\partial^2 z}{\partial x^2} \tag{1.1}$$

where E is Youngs modulus and I is the area moment of inertia. By summing moments on the beam element (and neglecting rotary effects) we find that:

$$T = -\frac{\partial M_f}{\partial x} \tag{1.2}$$

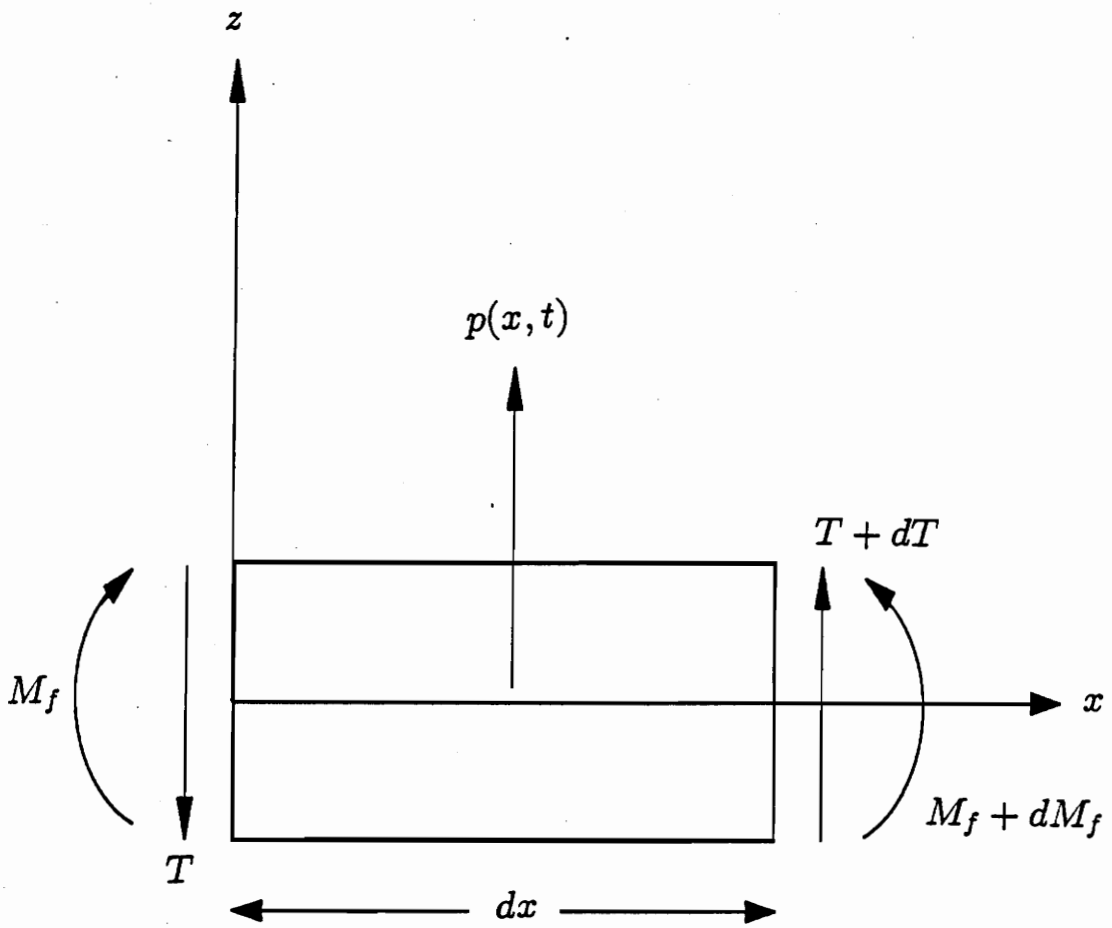

Figure 1.1: Free body diagram of a beam element.

And, by summing forces on the beam element, we find that:

$$\partial T + p\partial x = \rho \partial x \frac{\partial^2 z}{\partial t^2} \tag{1.3}$$

Combining Eqs. 1.2 and 1.3 and substituting from Eq. 1.1 we get:

$$EI\frac{\partial^4 z}{\partial x^4} + \rho\frac{\partial^2 z}{\partial t^2} = p \tag{1.4}$$

Assuming a harmonic time dependence of the form $e^{-i\omega t}$, were ω is the frequency of excitation, Eq. 1.4 reduces to:

$$EI\frac{\partial^4 z}{\partial x^4} - \rho\omega^2 z = p \tag{1.5}$$

1.3.2 Point Force Excitation of Beams with Discontinuities

The differential equation describing the point forced vibration of a beam with point control forces is given below.

$$\begin{aligned} EI\frac{d^4 z(x)}{dx^4} - \rho\omega^2 z(x) &= F_{in}\delta(x-\alpha_{in}) \\ &\quad + \sum_{j=1}^{n} F_j^c \delta(x-\alpha_j^c) + F_o\delta(x) + M_o\delta'(x) \end{aligned} \tag{1.6}$$

Where $z(x)$ is the transverse displacement of the beam as a function of x the co-ordinate along the beam. F_{in} is the magnitude of the input (or disturbance) force (which was a point force in all experiments), $\delta(\cdots)$ is the Dirac delta function of the argument and α_{in} is the location of the input force. F_j^c is the magnitude of the jth control force and α_j^c is the location of the jth control force. Equation 1.6 is the same as Eq. 1.5 with the input, control and discontinuity reaction forces and moments substituted for the distributed load.

The unknown terms F_o and M_o are introduced to model the reaction force and moment of the discontinuity (clamped or blocking mass). Figure 1.2 shows the equivalent force and moment associated with a clamped end condition. F_o and M_o can be calculated from the following boundary conditions for a clamped discontinuity.

$$z(0) = 0 \tag{1.7}$$

$$\frac{\partial z}{\partial x} = 0 \tag{1.8}$$

These boundary conditions are equivalent to saying that the displacement and slope of the beam at the clamp are zero.

By solving Eq. 1.6 and then using the above boundary conditions to solve for the unknown coefficients F_o and M_o the displacement equation for the semi-infinite/clamped beam with point force control (for $x > 0$) is:

$$\begin{aligned} z(x) = & \frac{iF_{in}}{4EIk_b^3}\left[e^{-ik_b(x-\alpha_{in})} + ie^{ik_b(x+\alpha_{in})} - (1+i)e^{ik_b\alpha_{in}-k_bx}\right] \\ & + \sum_{j=1}^{n} \frac{iF_j^c}{4EIk_b^3}\left[e^{ik_b|x-\alpha_j^c|} + ie^{-k_b|x-\alpha_j^c|}\right. \\ & \left. + (ie^{ik_b\alpha_j^c} - (1+i)e^{-k_b\alpha_j^c})e^{ik_bx} + (e^{-k_b\alpha_j^c} - (1+i)e^{ik_b\alpha_j^c})e^{-k_bx}\right] \end{aligned} \tag{1.9}$$

where k_b, the structural wavenumber, is defined as:

$$k_b = \sqrt[4]{\frac{\rho A\omega^2}{EI}} \tag{1.10}$$

and A is the cross sectional area of the beam.

For the case of an infinite beam with a blocking mass and point force controllers the differential equation of motion is the same as in Eq. 1.6. However, the associated

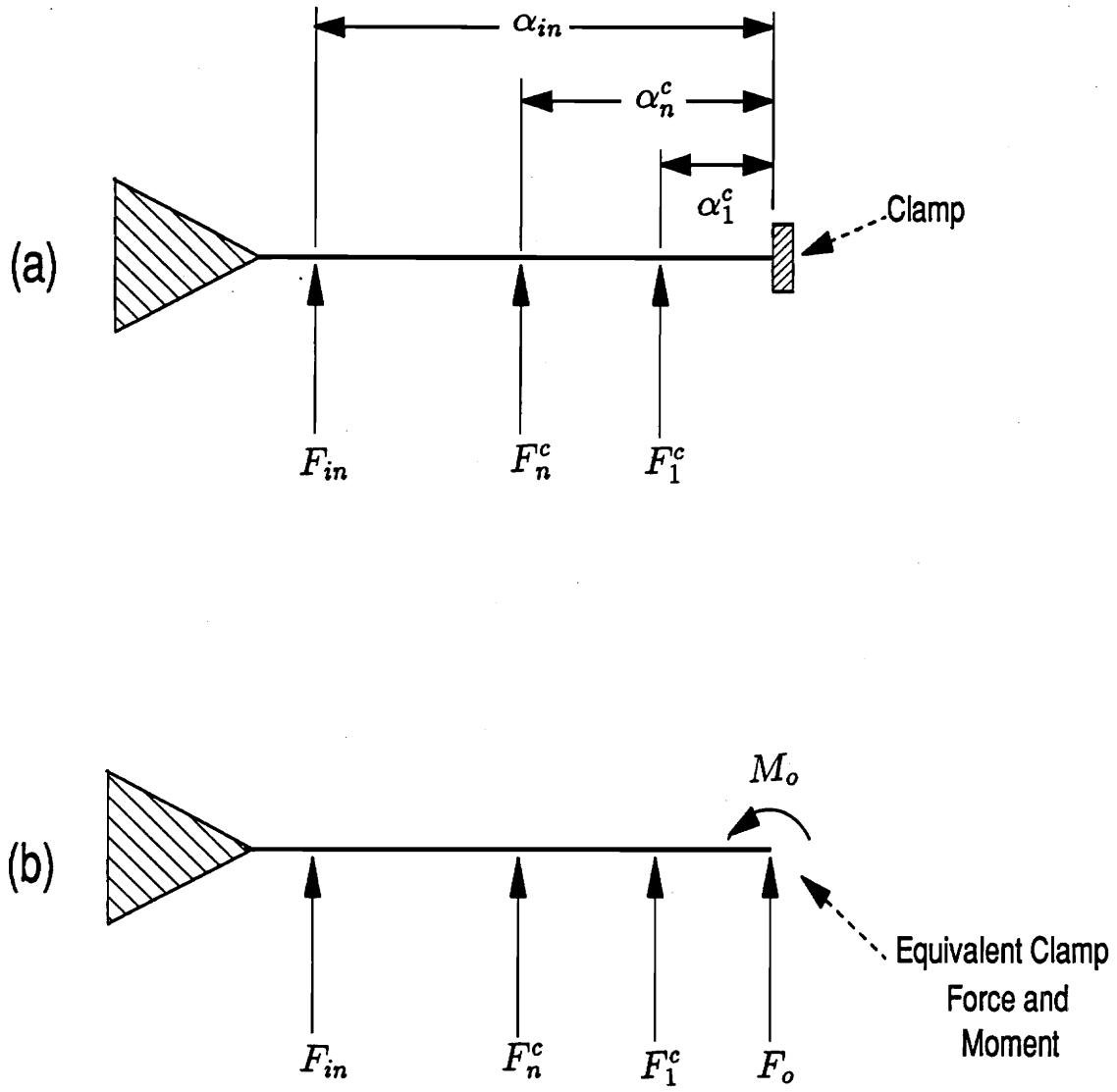

Figure 1.2: (a) Semi-infinite/clamped beam and the input and control forces. (b) Equivalent semi-infinite beam with reaction force and moment due to the clamped end condition.

boundary conditions for the blocking mass are as follows:

$$F_o = -m_b \ddot{z}(0,t) = \omega^2 m_b z(0) \tag{1.11}$$

$$M_o = -J_b \ddot{\theta}(0,t) = \omega^2 J_b \left.\frac{\partial z}{\partial x}\right|_{x=0} \tag{1.12}$$

where m_b is the mass of the blocking mass, and J_b is the mass moment of inertia of the blocking mass. These equations are the same as saying that the equivalent force (F_o) of the blocking mass equals the product of its mass and acceleration and that the equivalent moment (M_o) is the product of the blocking mass moment of inertia and its rotational acceleration.

Figure 1.3 shows the equivalent force and moment associated with a blocking mass discontinuity. By using the boundary conditions for the blocking mass discontinuity and solving for the unknown equivalent force and moment (F_o and M_o) the equation for an infinite beam with a blocking mass and point force control is:

$$\begin{aligned} z(x) \;=\; & \frac{iF_{in}}{4EIk_b^3}\left[e^{ik_b(x-\alpha_{in})} + \frac{i\omega^2 m_b e^{-ik_b\alpha_{in}}}{4EIk_b^3 + m_b\omega^2(1-i)}(e^{ik_b|x|} + ie^{-k_b|x|}) \right. \\ & \left. -\frac{i\mathbf{sgn}[x]J_b\omega^2}{4EIk_b + J_b\omega^2(1-i)}e^{-ik_b\alpha_{in}}(e^{ik_b|x|} - e^{-k_b|x|})\right] \\ & +\sum_{j=1}^{n}\frac{iF_i^c}{4EIk_b^3}\left[e^{ik_b|x-\alpha_j^c|} + ie^{-k_b|x-\alpha_j^c|} + \right. \\ & \frac{i\omega^2 m_b(e^{ik_b|\alpha_j^c|} + ie^{-k_b|\alpha_j^c|})}{4EIk_b^3 + m_b\omega^2(1-i)}(e^{ik_b|x|} + ie^{-k_b|x|}) \\ & \left. +\frac{i\mathbf{sgn}[x]\mathbf{sgn}[\alpha_j^c]J_b\omega^2}{4EIk_b + J_b\omega^2(1-i)}(e^{ik_b|\alpha_j^c|} - e^{-k_b|\alpha_j^c|})(e^{ik_b|x|} - e^{-k_b|x|})\right] \end{aligned} \tag{1.13}$$

where $\mathbf{sgn}[\cdots]$ is the sign ($\pm$) of the argument and the other variables are as defined previously.

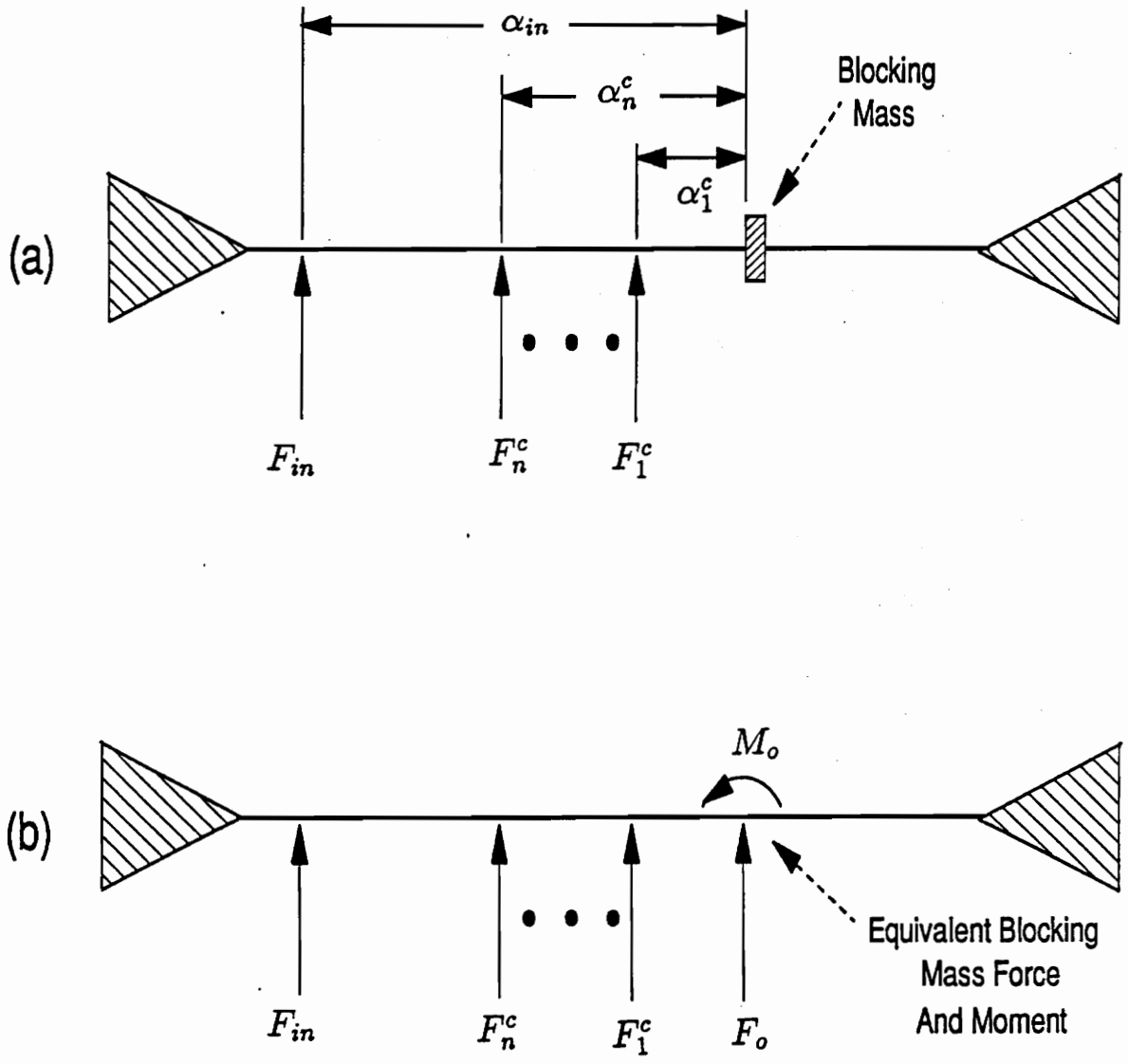

Figure 1.3: (a) Infinite beam with a blocking mass and the input and control forces. (b) Equivalent infinite beam with reaction force and moment due to the blocking mass discontinuity.

1.3.3 Piezoelectric Excitation of Infinite Beams

Piezoelectric actuators consist of thin patches of PZT ceramic. This material has the unique property of producing a strain when a polarization voltage is applied across the crystalline lattice. The PZT ceramic is produced in thin sheets which can be cut into any desired shape. When the PZT (or piezoelectric) patch is bonded to the surface of a structure, it is able to induce a strain in the structure. By soldering an electrical lead to each surface of the piezoelectric patch an AC voltage could be applied to the patch. Exciting the piezoelectric patch in this way caused a sinusoidal excitation to be transmitted to the structure. A fundamental description of piezoelectric actuators can be found in [18].

Piezoelectric excitation of various structures has been widely studied. The best treatment of the topic of beam excitation is presented by Gibbs and Fuller [23] and by Crawley and Anderson in [19]. Crawley and Anderson demonstrated that a pair of piezoelectric actuators, bonded exactly opposite each other on a beam, and driven 180° out of phase effectively produce two line moments at each edge of the piezoelectric pair. This concept is further demonstrated by Gibbs and Fuller. They demonstrated the various excitation effects when the phase between two opposite patches is varied. When the two patches were driven in phase a purely extensional wave was produced in the beam. When they were driven out of phase, a purely flexural wave was produce in the beam.

Since these experiments dealt with bending waves in infinite beams, the piezoelectric actuators were employed as two equal sized patches located exactly opposite from each other on the beam and excited 180° out of phase from each other. This

arrangement of actuators produced pure bending waves in the beams.

The differential equation of motion describing a beam with a general discontinuity, excited by a point force and controlled by line moments is:

$$EI\frac{d^4z(x)}{dx^4} - \rho\omega^2 z(x) = F_{in}\delta(x-\alpha_{in}) + \sum_{j=1}^{n} M_j^c[\delta'(x-\alpha_j^c) - \delta'(x-(\alpha_j^c+l))] + F_o\delta(x) + M_o\delta'(x) \quad (1.14)$$

(1.15)

where M_j^c is the magnitude of the line moment imparted by the piezoelectric actuator with one end located at $x = \alpha_j^c$ with a length of l. Equation 1.14 is the same as Eq. 1.6 except that the control is affected by line moments instead of point forces. Figure 1.4 shows a portion of a beam with piezoelectric actuators and the equivalent line moments associated with them. The concept of piezoelectric actuators and their effects on beam response are discussed further in Ch. 2.

Solving Eq. 1.14 and then substituting Eq. 1.7 into the solution of Eq. 1.14 to solve for the unknown, effective force (F_o) and moment (M_o) of the clamped end condition the displacement equation for a semi-infinite/clamped beam with piezoelectric control actuators is:

$$\begin{aligned} z(x) = {} & \frac{iF_{in}}{4EIk_b^3}\left[e^{-ik_b(x-\alpha_{in})} + ie^{ik_b(x+\alpha_{in})} - (1+i)e^{ik_b\alpha_{in}-k_bx}\right] \\ & + \sum_{j=1}^{n}\frac{M_j^c}{4EIk_b^2}\left[\mathsf{sgn}[x-(\alpha_j^c+l)](e^{ik_b|x-(\alpha_j^c+l)|} - e^{-k_b|x-(\alpha_j^c+l)|}\right) \\ & -\mathsf{sgn}[x-\alpha_j^c](e^{ik_b|x-\alpha_j^c|} - e^{k_b|x-\alpha_j^c|}) \\ & +(-ie^{ik_b(\alpha_j^c+l)} - (1-i)e^{-k_b(\alpha_j^c+l)} + ie^{ik_b\alpha_j^c} + (1-i)e^{k_b\alpha_j^c})e^{ik_bx} \end{aligned} \quad (1.16)$$

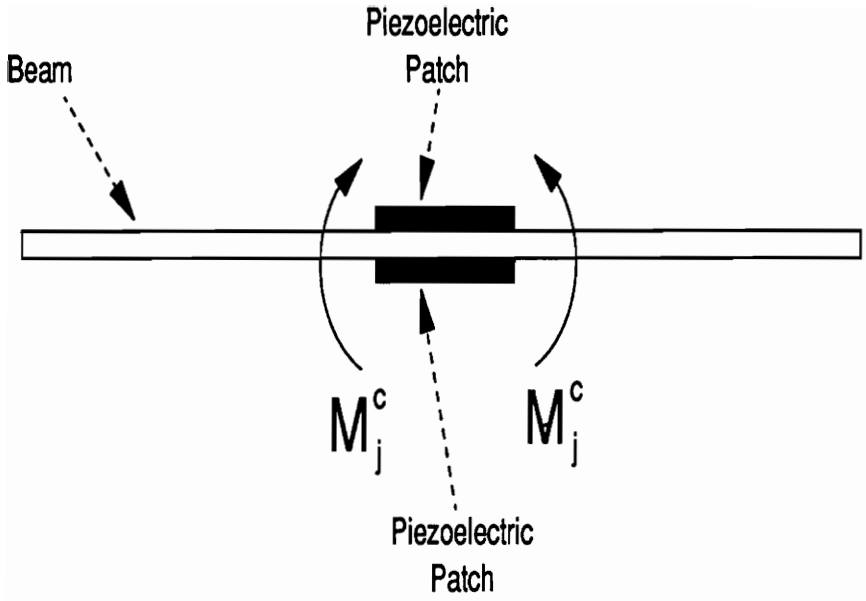

Figure 1.4: Line moments associated with piezoelectric actuators.

$$+((1+i)e^{ik_b(\alpha_j^c+l)} - ie^{-k_b(\alpha_j^c+l)} - (1+i)e^{ik_b\alpha_j^c} + ie^{k_b\alpha_j^c})e^{-k_bx}\Big]$$

For the case of an infinite beam with a blocking mass Eq. 1.14 is solved and Eq. 1.11 is used to solve for the unknown coefficients (F_o and M_o as depicted in Fig. 1.3). The resulting equation for an infinite beam with a blocking mass and piezoelectric actuator control is:

$$\begin{aligned} z(x) \;=\; & \frac{iF_{in}}{4EIk_b^3}\left[e^{ik_b(x-\alpha_{in})} + \frac{i\omega^2 m_b e^{-ik_b\alpha_{in}}}{4EIk_b^3 + m_b\omega^2(1-i)}(e^{ik_b|x|} + ie^{-k_b|x|}) \right. \\ & \left. -\frac{i\,\mathsf{sgn}[x]J_b\omega^2}{4EIk_b + J_b\omega^2(1-i)}e^{-ik_b\alpha_{in}}(e^{ik_b|x|} - e^{-k_b|x|})\right] \\ & +\sum_{j=1}^{n}\frac{M_i^c}{4EIk_b^2}\Big\{\mathsf{sgn}[x-(\alpha_j^c+l)](e^{ik_b|x-\alpha_j^c|} - e^{-k_b|x-(\alpha_j^c+l)|}) \\ & -\mathsf{sgn}[x-\alpha_j^c](e^{ik_b|x-\alpha_j^c|} - e^{-k_b|x-\alpha_j^c|}) \\ & -\frac{i\omega^2 m_b}{4EIk_b^3 + m_b\omega^2(1-i)}\Big[\mathsf{sgn}[\alpha_j^c+l](e^{ik_b|\alpha_j^c+l|} - e^{-k_b|\alpha_j^c+l|}) \\ & -\mathsf{sgn}[\alpha_j^c](e^{ik_b|\alpha_j^c|} - e^{-k_b|\alpha_j^c|})\Big]\,(e^{ik_b|x|} + ie^{-k_b|x|}) \\ & -\frac{i\,\mathsf{sgn}[x]J_b\omega^2}{4EIk_b + J_b\omega^2(1+i)}(ie^{ik_b|\alpha_j^c+l|} + e^{-k_b|\alpha_j^c+l|} - ie^{ik_b|\alpha_j^c|} + e^{-k_b|\alpha_j^c|}) \\ & (e^{ik_b|x|} - e^{-k_b|x|})\Big\} \end{aligned} \tag{1.17}$$

1.3.4 Acoustic Radiation from Beams

Acoustic radiation from baffled beams can be placed under the more general class of acoustic radiation from planar sources (including pistons, plates and beams). Junger and Feit [12] discuss this general class of radiators in detail. Beginning with the surface vibrations of a planar radiator the equation for the far-field sound pressure level was derived and is given here as:

$$p(R,\theta,\phi) = \frac{\rho_o e^{ik_oR}}{2\pi R}\tilde{\tilde{w}}(k_o\sin\theta\cos\phi, k_o\sin\theta\sin\phi) \tag{1.18}$$

where $p(R, \theta, \phi)$ is the far-field pressure at a point located by the angles θ and ϕ and the radius R (see Fig. 1.5 for these coordinates), ρ_o is the density of the acoustic medium, and k_o is the wavenumber in the acoustic medium. $\tilde{\ddot{w}}$ is the spatial fourier transform of the acceleration distribution on the planar radiator defined by

$$\tilde{\ddot{w}}(\gamma_x, \gamma_y) = \int_S \ddot{w}(x, y) e^{-i(\gamma_x x + \gamma_y y)} dS \tag{1.19}$$

where $\gamma_x = k \sin\theta \cos\phi$ and $\gamma_y = k \sin\theta \sin\phi$ are the spatial transform parameters.

Since the displacement of the beam is a constant in the y direction (assuming no variation in the lateral beam vibration) Eq. 1.19 may be reduced to:

$$\tilde{\ddot{w}}(\gamma_x) = \int_S \ddot{w}(x) e^{-i(\gamma_x x)} dS \tag{1.20}$$

which reduces the equation of the far-field pressure (Eq. 1.18) to:

$$p(R, \theta, \phi) = \frac{\rho_o e^{ik_o R}}{2\pi R} \tilde{\ddot{w}}(k_o \sin\theta \cos\phi) \tag{1.21}$$

Note that in Eq. 1.21 the far-field pressure is dependent on those wavenumber components less than the wavenumber in the acoustic medium (since the argument of the spatial fourier transform, $\tilde{\ddot{w}}$, is $k_o \sin\theta \cos\phi \leq |k_o|$).

To further describe the dependence of acoustic radiation on the structural wavenumber relative to the wavenumber in the acoustic medium, consider one of the fundamental boundary conditions for the coupling of structural vibration and acoustic radiation. This condition states that the particle velocity in the acoustic medium must be equal to the surface velocity of the vibrating structure at the interface of the acoustic medium and the structure. This boundary condition was expressed by

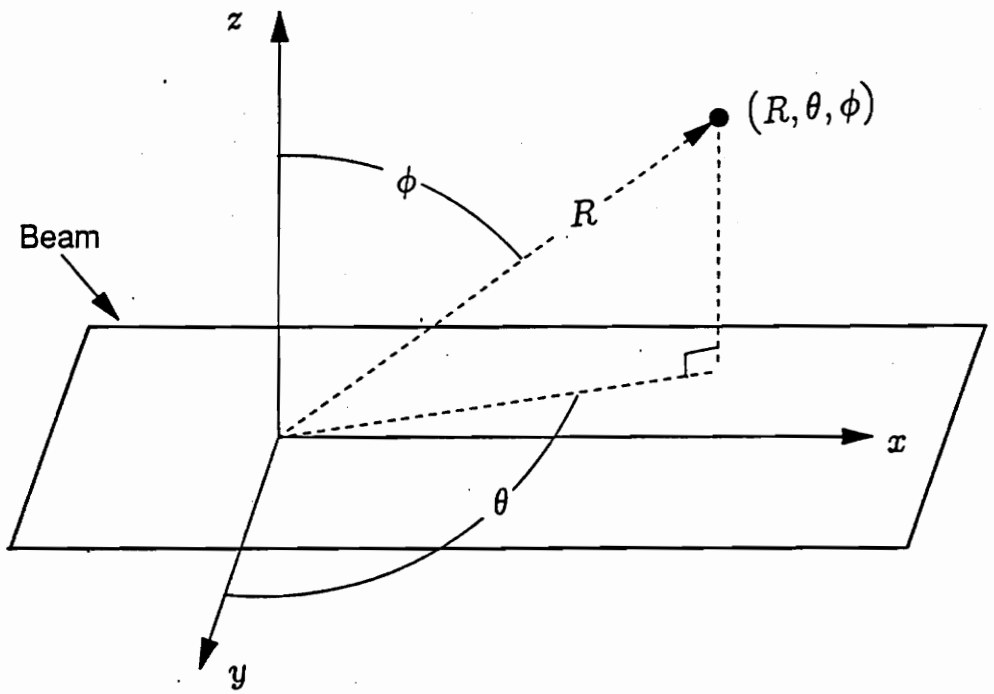

Figure 1.5: Coordinates used in Eq. 1.16 for the acoustic radiation from a planar radiator.

Junger and Feit [12] as:

$$\frac{\partial p(x,y,z)}{\partial z} = -\rho_o \ddot{w}(x,y) \tag{1.22}$$

A result of this boundary condition is that the trace wavelength of the acoustic medium must equal the structural wavelength. In other words, the component of the acoustic wavelength along the plane of the vibrating surface must be equal to the structural wavelength. This further implies that the trace wavenumber of the in the acoustic medium must equal the structural wavenumber (since $k = 2\pi/\lambda$). This can be expressed mathematically using the Pythagorean theorem as:

$$k_z = \sqrt{k_o^2 - k_b^2} \tag{1.23}$$

where k_z is the component of the ambient wavenumber in the z direction, k_o is the total ambient wavenumber, and k_b is the structural wavenumber (recall that the component of the ambient wavenumber in the x direction must equal the structural wavelength, $k_b = k_x$).

Note in Eq. 1.23 that k_z is real only if $|k_b| < k_o$. This is the condition under which acoustic energy propagates away from the structure (in the z direction). If, on the other hand, $|k_b| > k_o$ then k_z will be imaginary and no acoustic energy will propagate away from the structure. This is how the concept of supersonic wavenumbers is defined. Structural wavenumbers which fall in the region $|k_b| < k_o$ are called supersonic and are responsible for acoustic radiation which propagates away from the structure.

In the previous discussion the wavenumber in the y direction was ignored. However, the wavenumber in the y direction is significant to the acoustic radiation from a

structure. Since the lateral vibration of the beams in these experiments was assumed to be constant, the lateral wavenumber was zero and, therefore, was not considered in this discussion.

In light of the discussion of supersonic wavenumber components and Eq. 1.21 some conclusions may be drawn on controlling the acoustic radiation from beams with discontinuities. Since the far-field radiation depends on the supersonic wavenumber components, attenuation of these components will result in the attenuation of the far-field sound pressure levels.

Keltie [13] discusses the relative contributions to the wavenumber spectrum of various waves produced by simple structural discontinuities. He states that, for incident subsonic structural wavenumbers ($|k_b| < k_o$), the supersonic wavenumber region (and hence the acoustic power radiated) is dominated by the interaction between traveling waves and near-field waves. This means that the supersonic wavenumber region magnitude depends on the relative phasing between traveling and near-field wave wavenumber spectrum contributions. By changing the way these two wavenumber spectrum contributors interact, the magnitude of the supersonic wavenumber components can be attenuated, and hence the sound power radiated can be attenuated.

For example, if, through some control mechanism, the traveling wave and near-field wave contributions to the supersonic wavenumber region can be changed such that they interfere destructively with each other (or are out of phase) then the supersonic wavenumber region can be attenuated. This would have the result of attenuating the far-field sound pressure level.

A different approach to describing the physical mechanism for controlling the acoustic radiation due to wave scattering by discontinuities on beams can be inferred from the more general acoustic radiation equation derived from the Raleigh integral. This form of describing the acoustic radiation from a beam with a discontinuity applies to the entire acoustic field (not just the far-field). The equation was derived by Guigou [16] as follows:

$$p(R,\theta,\phi) = \frac{\rho}{2\pi}\int_S \frac{e^{ik_o[R^2+x^2+y^2-2R\sin\theta(x\cos\phi+y\sin\phi)]^{1/2}}}{[R^2+x^2+y^2-2R\sin\theta(x\cos\phi+y\sin\phi)]^{1/2}}\ddot{w}(x,y)dS \quad (1.24)$$

Since this integral has no closed form solution it is hard to draw conclusions about controlling the acoustic radiation while it was obvious in Eq. 1.21 that, to control the far-field sound pressure level, the supersonic wavenumber region had to be attenuated. However, in experiments performed on a beam with a blocking mass discontinuity (discussed in Ch. 4 of this thesis), while the sound pressure levels were attenuated in the acoustic "near-field" the supersonic region of the wavenumber spectrum increased. It is important to note that, in this thesis, when the acoustic "near-field" is referred to this does not imply that region of the acoustic field very close to the source. Rather, when the acoustic "near-field" is referred to, this means that portion of the acoustic field not in the far-field. This point is important because much of the discussion about the acoustic field in the Ch. 4 refers to this "grey" area between the acoustic far-field and that part of the acoustic field very close to the radiating source.

This type of behavior, where the acoustic "near-field" is attenuated while the supersonic wavenumber region increases, was, in addition to being evident in experimental studies, further supported by analytical studies performed by Guigou [16]. The in-

crease in the supersonic region of the wavenumber spectrum implies that, while the acoustic "near-field" is being attenuated, the far-field sound pressure levels increase.

In an attempt to qualitatively discuss the mechanism by which control of the acoustic "near-field" can occur while the far-field levels increase, a simple case of two point sources (separated by a distance of $2e = 0.1m$) was considered as shown in Fig. 1.6. The sound pressure levels were calculated for two points in the acoustic field at a frequency of 318Hz. One point was located in the far-field (at a radius of $R_f = 10.0m$) and the other point was located in the "near-field" (at $R_n = 0.1m$). The far-field acoustic levels were calculated with the following equation:

$$P_f = \rho_o \ddot{Q} \left[\frac{e^{ik(R_f - e/2)}}{R_f - e/2} + \frac{e^{ik(R_f + e/2)}}{R_f + e/2} e^{i\phi} \right] \tag{1.25}$$

where $\ddot{Q}$ is the source volume and ϕ is the phase angle difference between the two point sources. Equation 1.25 describes the pressure created by two point sources radiating with a relative phase between them of ϕ. The derivation of this equation can be found in [12].

Similarly, the acoustic levels in the "near-field" were calculated with the following equation:

$$P_n = \rho_o \ddot{Q} \left[\sqrt{\frac{a}{c}} e^{ikc} + \sqrt{\frac{b}{c}} e^{ikb} e^{i\phi} \right] \tag{1.26}$$

where

$$a = R_n^2 + e^2 + R_n e \tag{1.27}$$

$$b = R_n^2 + e^2 - R_n e \tag{1.28}$$

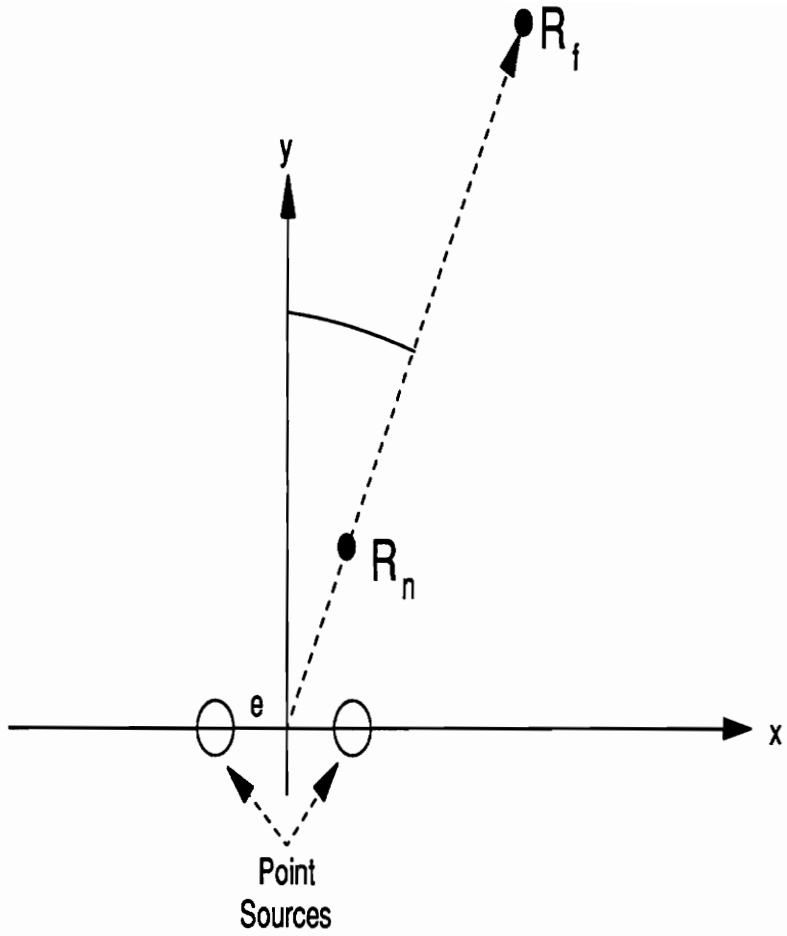

Figure 1.6: Diagram of two point sources and their coordinate system. $e = 0.05m$, $\theta = 30°$, $R_n = 0.1m$ and $R_f = 10.0m$.

and

$$c = [R_n^2 + e^2]^2 + [R_n e]^2 \tag{1.29}$$

(Note that Eq. 1.26 reduces to Eq. 1.25 when the far-field assumptions that ke^2/R_f and $(k/e)^2 << 1$ are made [12]).

The results of this analysis are shown in Fig. 1.7. First, consider one of the point sources to be the disturbance and the other point source to be a controller. The acoustic field in this case would correspond to the cases in Fig. 1.7 without control. Now, if the attenuation of the acoustic "near-field" is desired, a situation could arise where the "near-field" was attenuated and the far-field levels increase when the second or control source was turned on. This would correspond to the region in Fig. 1.7 of $3.9 < \phi < 4.2$.

It is obvious that the case of a beam with a discontinuity would be far more complex than this simple case of two point sources. This simple case, however, shows that attenuating the "near-field" does not necessarily mean that the far-field radiation will be attenuated. Also, if this kind of behavior can exist in this simple case, then it could occur in the more complex case of a beam with a discontinuity excited by subsonic waves. The situation of the acoustic radiation from a beam with a discontinuity as described in Eq. 1.24 is, in fact, a summation of an infinite number of point sources (since an integral is an infinite sum). If two point sources can display this type of behavior then it is likely that the case of a beam with a discontinuity described by the Raleigh integral can also behave this way.

One final point to address in the acoustics of an infinite beam is the possibility of acoustic radiation being emitted from the edges of the beam. Since the beams in

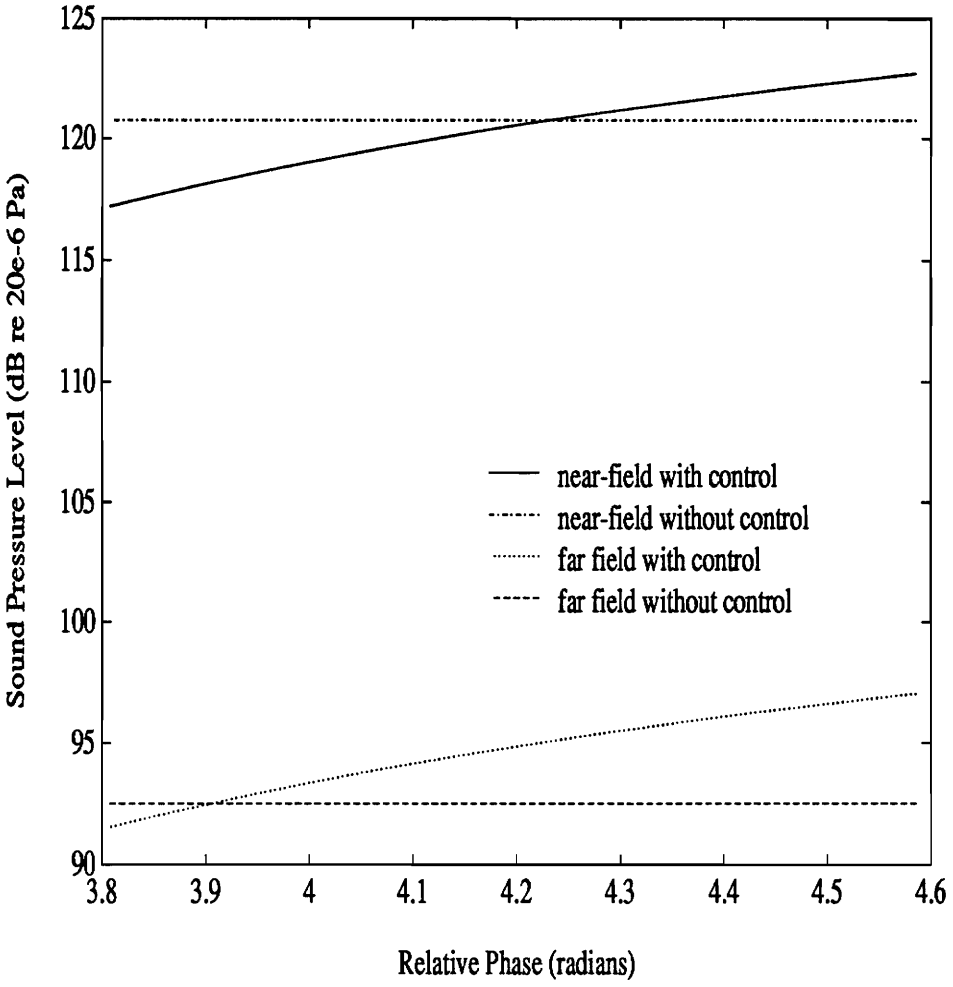

Figure 1.7: Acoustic levels in the "near-field" and far-field for two point sources with variable phase.

these experiments were of finite width, it was conceivable that the discontinuity associated with the lateral edges of the beams could produce acoustic radiation. This topic was indirectly addressed by Lyon in [24]. The acoustic radiation associated with the scattering of waves in a plate that were obliquely incident on a line discontinuity was investigated. It was shown that, far-field acoustic radiation would only occur if the trace wavelength along the discontinuity line was greater than the wavelength in the acoustic medium or if the wavenumber component along the line discontinuity was less than the wavenumber in the acoustic medium.

In these experiments the waves traveled parallel to the lateral edges of the beam. Hence, the trace wavenumber along the edges was equal to the structural wavenumber. Since the structural wavenumbers in these experiments were all less than the wavenumber in the acoustic medium (or were subsonic), the trace wavenumber along the edges was subsonic. Therefore, no far-field acoustic waves were radiated from the edges of the beams.

1.3.5 Flexural Waves and the Wavenumber Spectrum

It has previously been stated that acoustic radiation from structures is due to the presence of supersonic wavenumber components in the structural response [11, 12]. This section describes how these supersonic wavenumber components are produced by the various wave types present in the beam response.

First, consider an infinite beam with a traveling wave in the positive direction (see Fig. 1.8) which is described below without the time dependent portion.

$$z(x) = Ae^{ik_b x} \tag{1.30}$$

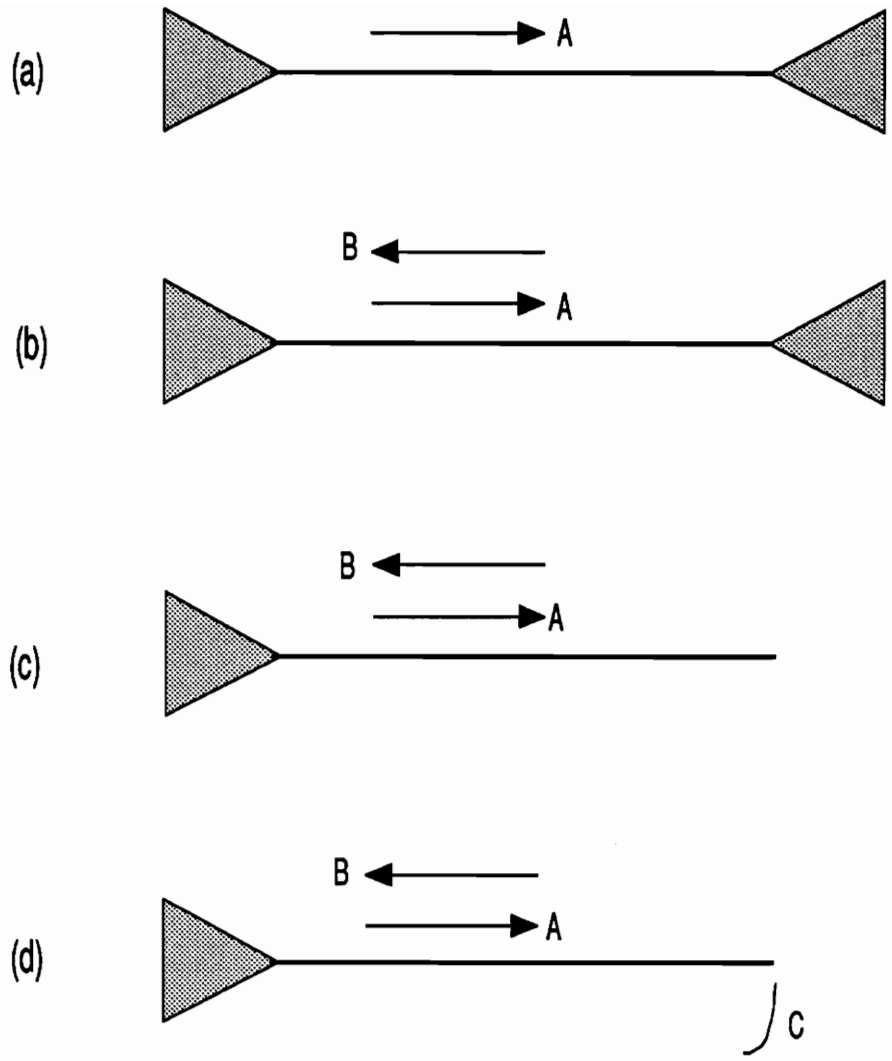

Figure 1.8: (*a*) infinite beam with a traveling wave in the positive direction. (*b*) infinite beam with a traveling wave in both directions. (*c*) a semi-infinite beam with traveling waves in both directions. (*d*) a semi-infinite beam with traveling waves in both directions and a near-field wave. A is the positive traveling wave amplitude, B is the negative traveling wave amplitude and C is the near-field amplitude.

In order to reveal those wavenumber components present in the beam response of Eq. 1.30 the spatial Fourier transform must be invoked as follows:

$$\tilde{Z}(k) = \frac{1}{\sqrt{2\pi}} \int_{-\infty}^{\infty} z(x) e^{ikx} dx \tag{1.31}$$

where ω is the excitation frequency.

Applying Eq. 1.31 to Eq. 1.30 the following result is obtained.

$$\tilde{Z}(k) = A\delta(k - k_b) \tag{1.32}$$

where $\delta(\cdots)$ is the Dirac delta function. This equation results in a spectral peak at the structural wavenumber, k_b, as shown in Fig. 1.9 which was constructed assuming that $A = 1.5$. Although the Dirac delta function is infinite where it is defined, its integral is one and is shown as having finite amplitude in Fig. 1.9. In addition, the Fourier transform shown in Fig. 1.9 was constructed using a digital Fourier transform (as were the other plots presented in this discussion) which caused leakage into nearby wavenumbers. Also notice the vertical lines in Fig. 1.9. These define the region of supersonic wavenumber components, $|k| < k_o$. This assumes a structural wavenumber, k_b, of $21m^{-1}$ and a wavenumber in the acoustic medium of $k_o = 5.75m^{-1}$ which corresponds to the experiments presented in this thesis performed at 320Hz for an aluminum beam $0.00318m$ thick.

Since the wavenumber spectrum is zero for all wavenumbers other than the structural wavenumber, and since the structural wavenumber is greater than the wavenumber in the acoustic medium, no acoustic radiation would be emitted to the far-field. This is to say that, an infinite beam, excited by a subsonic traveling wave, will produce no far-field acoustic radiation. This concept has been presented previously in [11, 12].

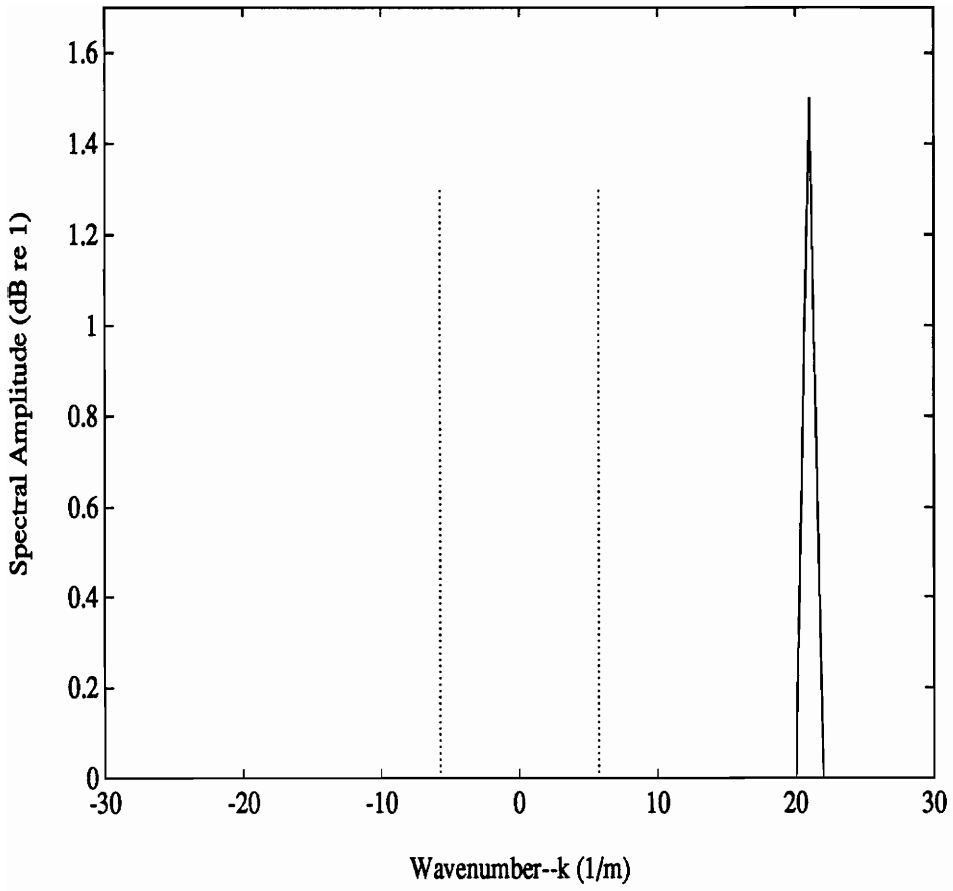

Figure 1.9: Wavenumber spectrum for an infinite beam with a traveling wave in the positive direction. $k_b = 21m^{-1}$ and $k_o = 5.75m^{-1}$.

Next consider an infinite beam excited by two traveling waves propagating in the opposite direction (see Fig. 1.8). The equation describing this situation is:

$$z(x) = Ae^{ik_b x} + Be^{-ik_b x} \tag{1.33}$$

and, applying Eq. 1.31 to Eq. 1.33 yields:

$$\tilde{Z}(k) = A\delta(k - k_b) + B\delta(k + k_b) \tag{1.34}$$

The results of Eq. 1.34 are shown in Fig. 1.10 which was constructed assuming that $A = B = 1.5$. Notice that this figure is the same as for the infinite beam with a traveling wave in one direction (Fig. 1.9) except that there are spectral peaks at both $\pm k_b$. The peak at $+k_b$ corresponds to the positive traveling wave A and the peak at $-k_b$ corresponds to the negative traveling wave B.

Notice, once again, that there are no supersonic components associated with the two traveling waves over an infinite beam. Therefore, no acoustic radiation would be emitted.

Now consider the case of a semi-finite beam (existing for $x > 0$ only) with two traveling waves (see Fig. 1.8). The equation defining the displacement for this situation is:

$$z(x) = Ae^{ik_b x} + Be^{-ik_b x},\ x \geq 0 \tag{1.35}$$

$$z(x) = 0,\ x < 0$$

In order to evaluate the integral of Eq. 1.31 over a semi-infinite space, the following

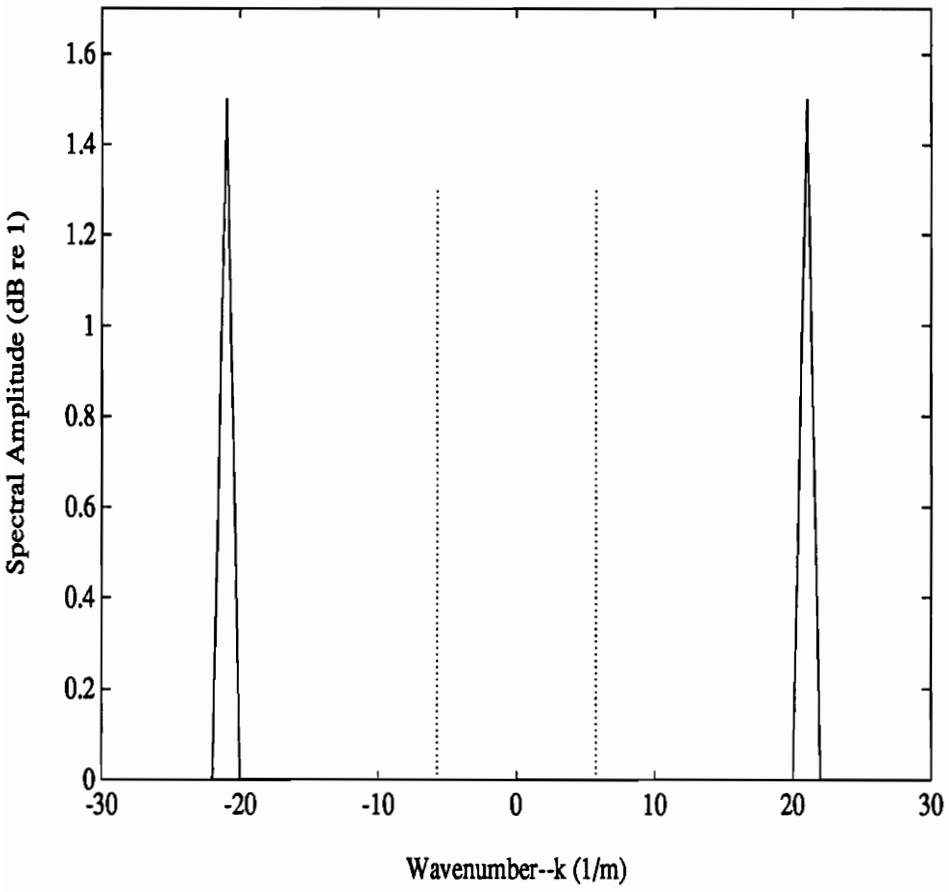

Figure 1.10: Wavenumber spectrum for an infinite beam with traveling waves in both directions. $k_b = 21m^{-1}$ and $k_o = 5.75m^{-1}$.

definition must be employed:

$$\int_0^\infty e^{iux} dx = \pi\delta(u) + \frac{i}{u} \tag{1.36}$$

Now, applying Eqs. 1.31 and 1.36 to Eq. 1.35 the following result is obtained:

$$z(k) = A\left[\delta(k - k_b) + \frac{i}{k - k_b}\right] + B\left[\delta(k + k_b) + \frac{i}{k + k_b}\right] \tag{1.37}$$

The results from Eq. 1.37 are shown in Fig. 1.11 assuming that $A = B = 1.5$. Notice that the spectral peaks associated with the positive and negative traveling waves are present. But, in addition, there is a "spreading" of all wavenumber components as well. This is a result of the semi-infinite "windowing" associated with the traveling waves being defined over the semi-infinite region of $x > 0$. In effect the transform of the "window" shape is convolved with the infinite beam transform of Eq. 1.34 giving response at all wavenumbers.

This "windowing" effect is one mechanism by which supersonic wavenumber components were produced in these experiments on beams with discontinuities. For the experiments on the semi-infinite clamped beam, the displacement field is defined only for the region of $x > 0$ where the clamped discontinuity is at $x = 0$. For the experiments on the infinite beam with a blocking mass the displacement field is split into two regions: one for $x > 0$ and the other for $x < 0$. In each of the regions of the infinite beam with a blocking mass the amplitudes of the traveling waves are different in magnitude and phase and thus contribute to the supersonic wavenumber region. If, in the case of the infinite beam with a blocking mass, the traveling waves on either side of the discontinuity were of the same magnitude and phase (and there were no near-fields or reflected waves involved), the supersonic contributions from

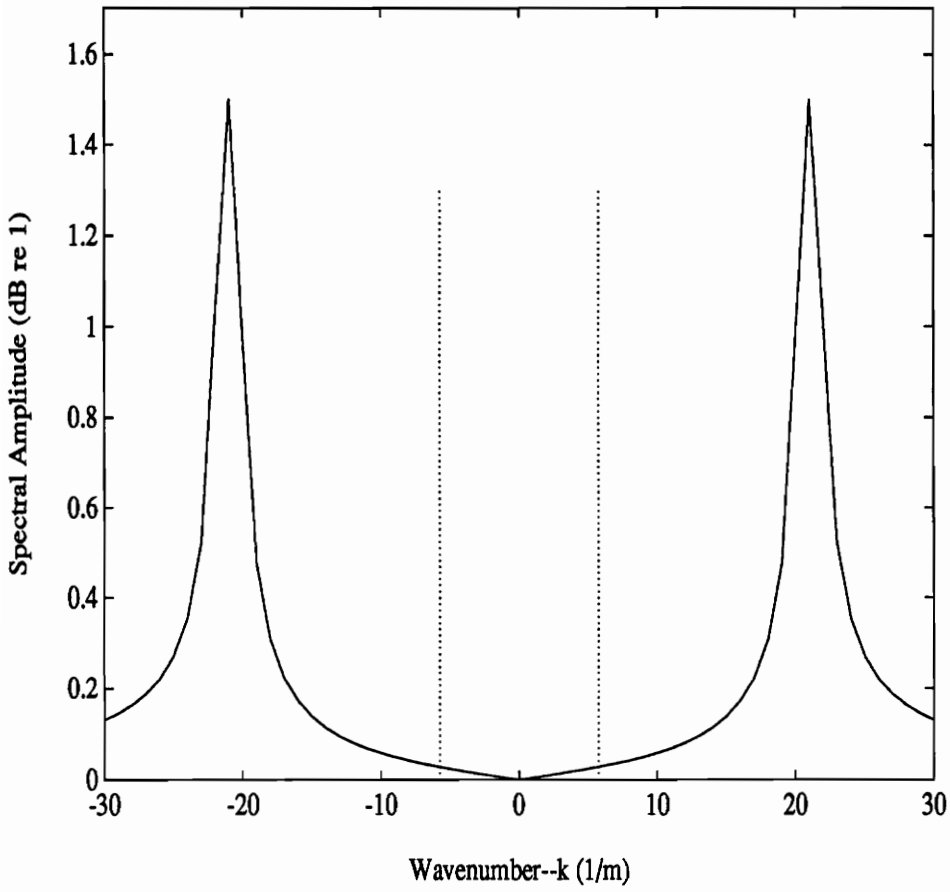

Figure 1.11: Wavenumber spectrum for a semi-infinite beam with traveling waves in both directions. $k_b = 21m^{-1}$ and $k_o = 5.75m^{-1}$.

each traveling wave would cancel out and the case shown in Fig. 1.9 would result.

Therefore, in each experiment, the displacement field is defined over a semi-infinite space and the "windowing" of these traveling waves produced supersonic wavenumber components which resulted in acoustic radiation from the structure.

Another source of supersonic wavenumber components is the flexural near-field. Consider a semi-infinite beam with only a flexural near-field governing its displacement (assuming no traveling waves are present). The governing equation for this situation is:

$$z(x) = Ce^{-k_b x},\ x \geq 0 \tag{1.38}$$

$$z(x) = 0,\ x < 0$$

Taking the spatial Fourier transform of Eq. 1.38 results in the following equation:

$$z(k) = C\frac{i}{k + ik_b} \tag{1.39}$$

The results of Eq. 1.39 are shown in Fig. 1.12 assuming that $C = 1.5$. Notice that the flexural near-field contributes significantly to the supersonic wavenumber region. This is the second mechanism by which supersonic wavenumber components were produced in these experiments.

Another way to describe the mechanism by which flexural near-fields contribute to acoustic radiation can be inferred from Eq. 1.23. Comparing the basic equation for a traveling wave (Eq. 1.30) and the basic equation describing a near-field wave (Eq. 1.38) it can be deduced that the wavenumber for a near-field wave is purely

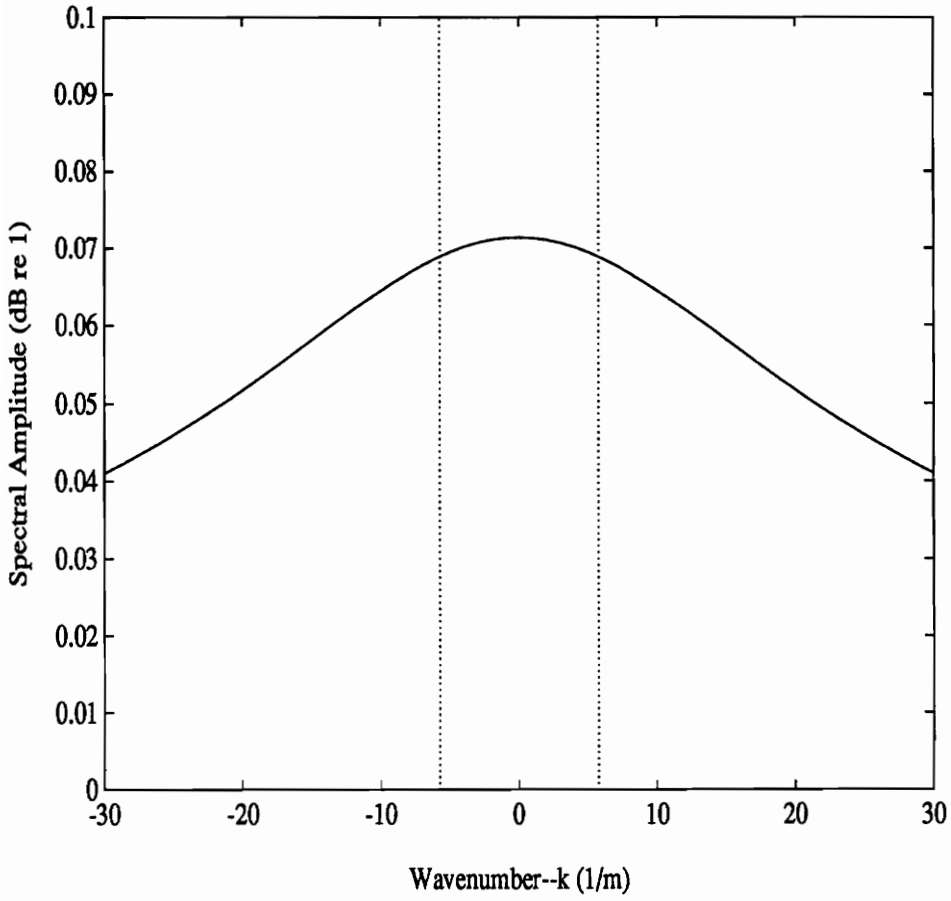

Figure 1.12: Wavenumber spectrum for a semi-infinite beam with a near-field wave. $k_b = 21m^{-1}$ and $k_o = 5.75m^{-1}$.

imaginary, since $i^2 = -1$. Substituting this fact ($k_b = ik_b$) into Eq. 1.23 we obtain:

$$k_z = \sqrt{k_o^2 - ik_b^2} \tag{1.40}$$

which reduces to

$$k_z = \sqrt{k_o^2 + k_b^2} \tag{1.41}$$

Thus, k_z associated with a structural, flexural near-field is always real and, therefore, by earlier conclusions, always results in acoustic energy being radiated to the far-field.

Finally, the wavenumber spectrum associated with a semi-infinite beam with traveling waves in both directions and a near-field wave is shown in Fig. 1.13. This figure was created by combining Eqs. 1.37 and 1.39 assuming that $A = B = C = 1.5$. Fig. 1.13 is typical of the wavenumber spectra obtained from experimental results which are presented in Ch. 4.

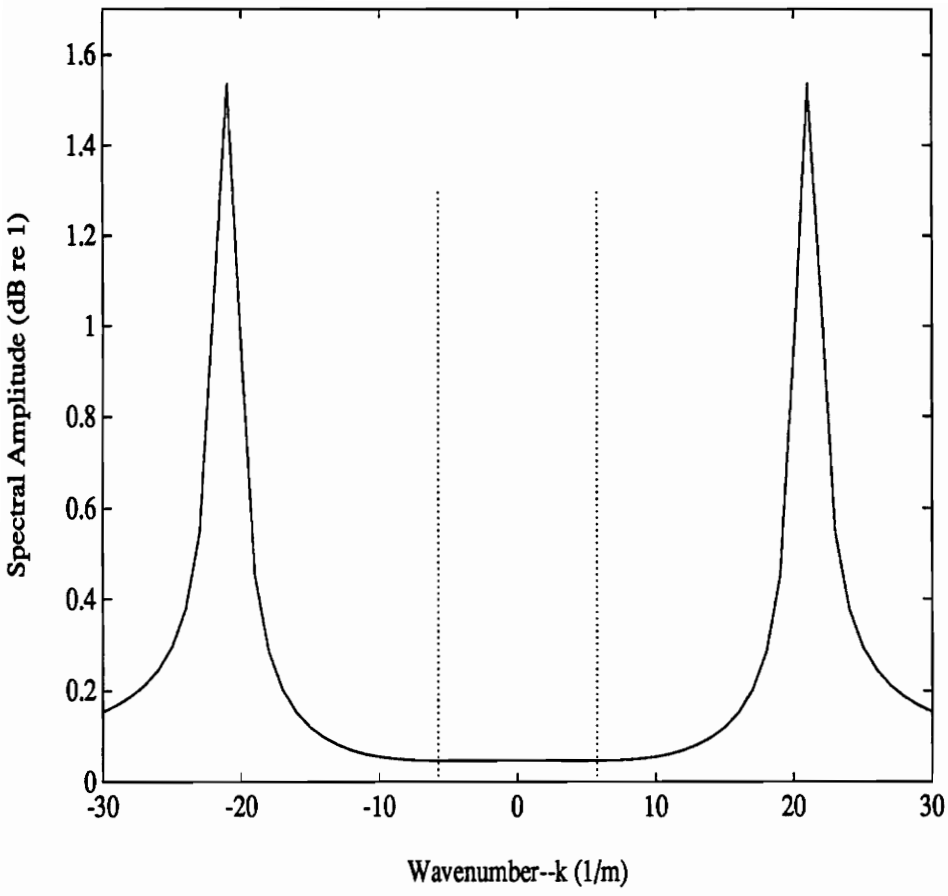

Figure 1.13: Wavenumber spectrum for a semi-infinite beam with traveling waves in both directions and a near-field wave. $k_b = 21m^{-1}$ and $k_o = 5.75m^{-1}$.

Chapter 2

Experimental Apparatus and Procedure

2.1 Experimental Apparatus

This section describes the apparatuses for both the semi-infinite/clamped beam and infinite beam with a blocking mass experiments. Although these beams are not actually semi-infinite and infinite respectively, an approximation was made by placing the ends of the beams in anechoic terminations which made the beams appear infinite at certain frequencies of excitation. The anechoic terminations are described in detail in Sec. 2.1.2.

Figure 2.1 is a schematic of the semi-infinite/clamped experiment while Fig. 2.2 shows the infinite beam with a blocking mass experiment. In addition, photographs of each experimental rig are shown in Fig. 2.3 and Fig. 2.4.

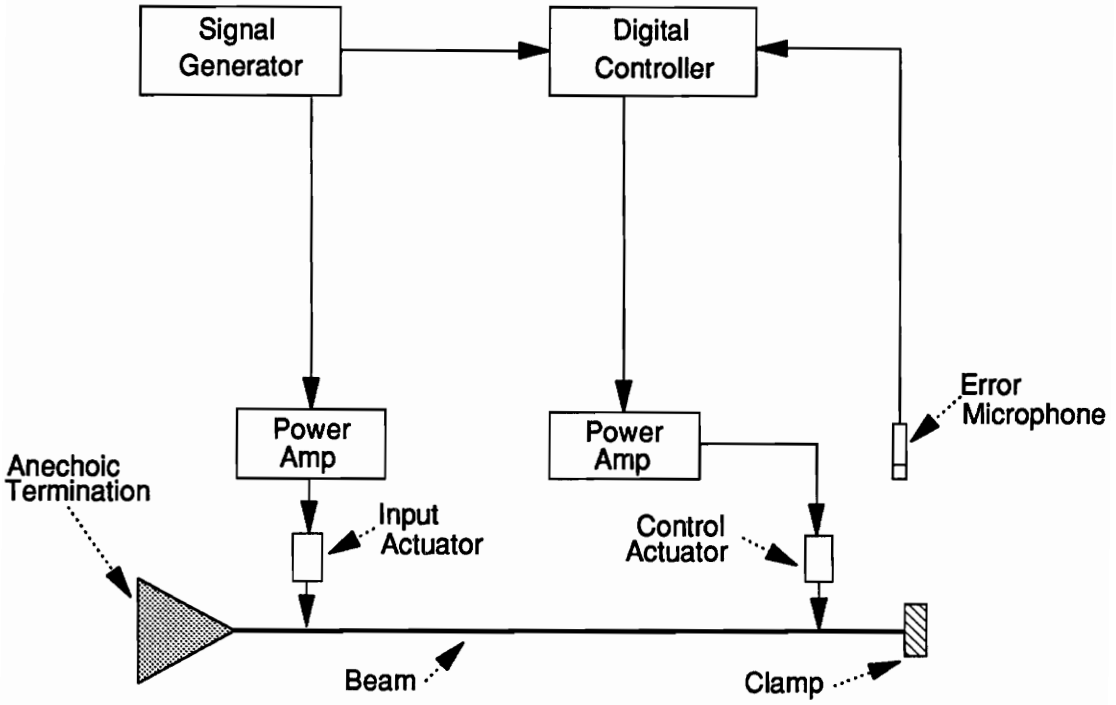

Figure 2.1: Schematic of Semi-infinite/Clamped Beam Experiment

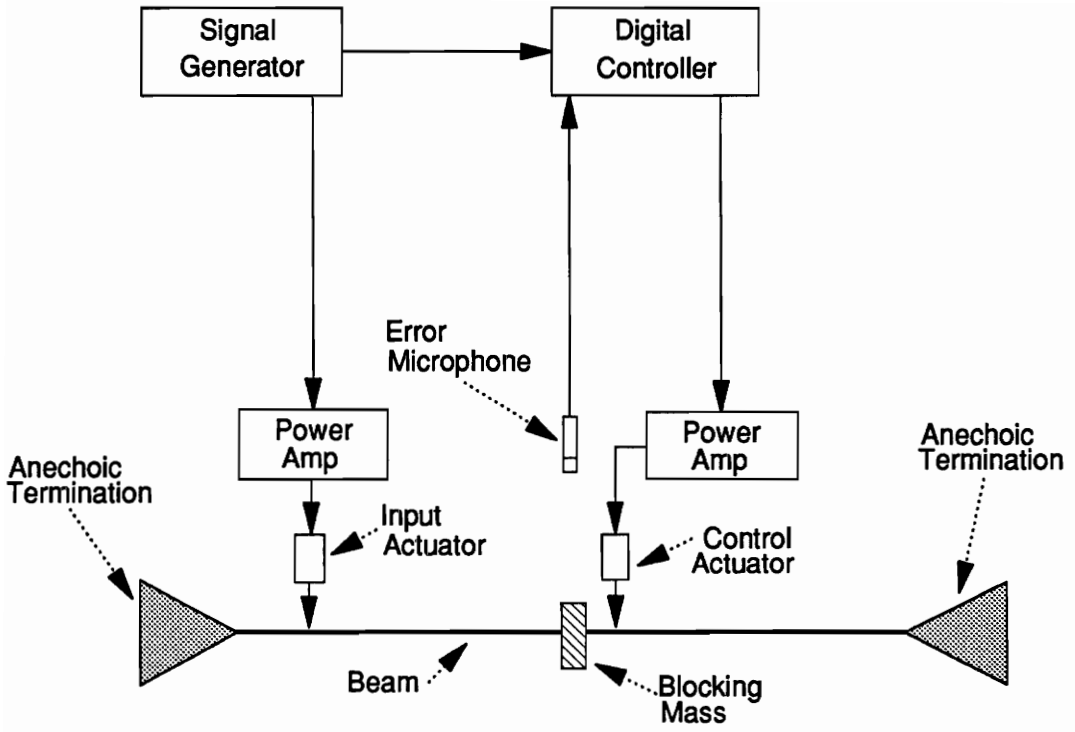

Figure 2.2: Schematic of Infinite Beam with a Blocking Mass Experiment

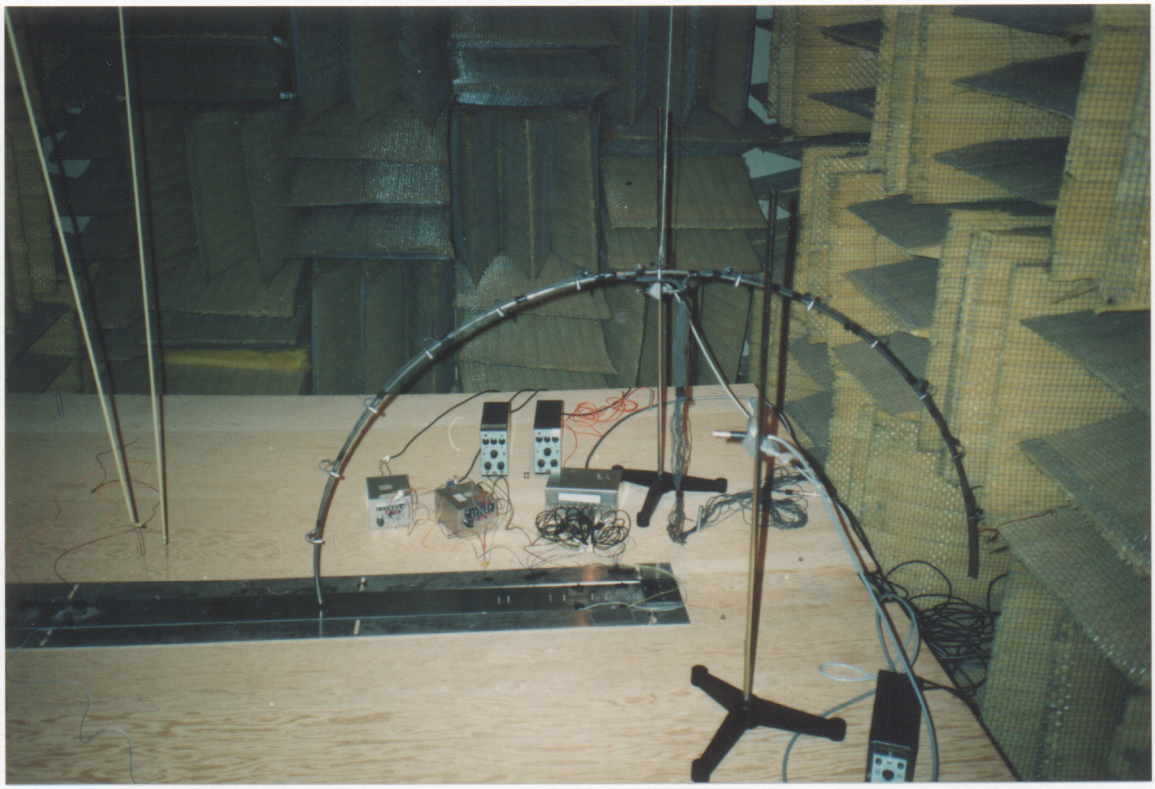

Figure 2.3: Photograph of Semi-infinite/Clamped Beam Experiment

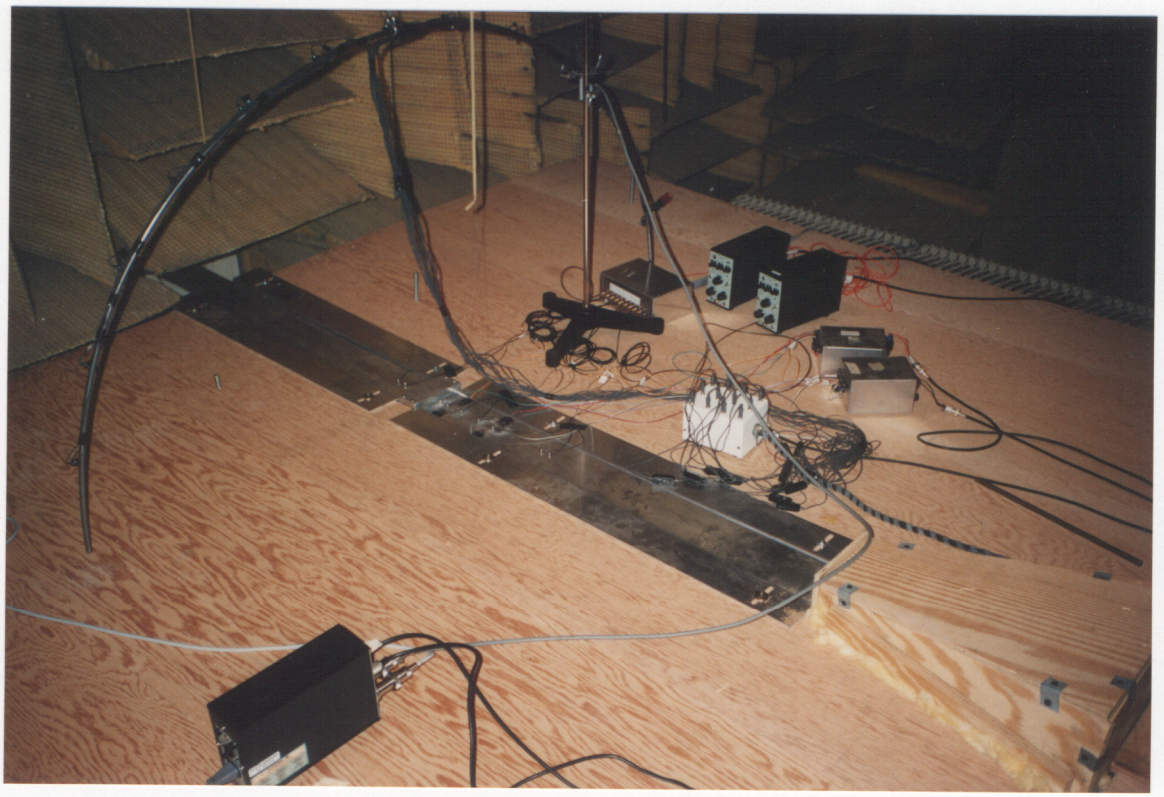

Figure 2.4: Photograph of Infinite Beam with Blocking Mass Experiment

2.1.1 Beams

The beams used in both experiments were made of 6061 aluminum and were $3.66m$ long, $0.102m$ wide and $0.00318m$ thick. The properties of the beams are summarized in Table 2.1.

The beams were arranged such that one end was outside of the anechoic chamber. This end of the beam was placed in an anechoic termination and passed through a slit in the wall of the anechoic chamber. The anechoic termination served to make the beam appear infinite to traveling waves incident upon it. This concept is further discussed later in Sec. 2.1.2.

Along with the anechoic termination, the input shaker was fastened to the beam outside of the anechoic chamber. Since the input shaker produced a significant amount of noise, it could have affected the outcome of the experiments. By attaching the input shaker to the beam outside of the anechoic chamber and passing the beam through a narrow ($1cm$) slit in the wall of the chamber and through an attenuation duct (a rectangular duct $25cm$ long made of plywood and lined with fiberglass insulation) the amount of noise produced by the input shaker that entered the anechoic chamber was minimized. This topic is discussed further along with the discussion of the input shaker in Sec. 2.1.7.

Figure 2.5 shows a photograph of the section of the beam outside the chamber, the attached input shaker, the slit in the chamber wall through which the beam passed and the anechoic termination.

For the purpose of studying the radiation from the beams in the half plane and for

Table 2.1: Beam Properties

Material	6061 Aluminum
Total length	3.66 m
Width	0.102 m
Thickness	0.00318 m
Modulus	$7.1 \times 10^{10} N/m^2$
Density	$2700 kg/m^3$
Speed of Sound	$5150 m/s$
Critical Freq.	4148 Hz

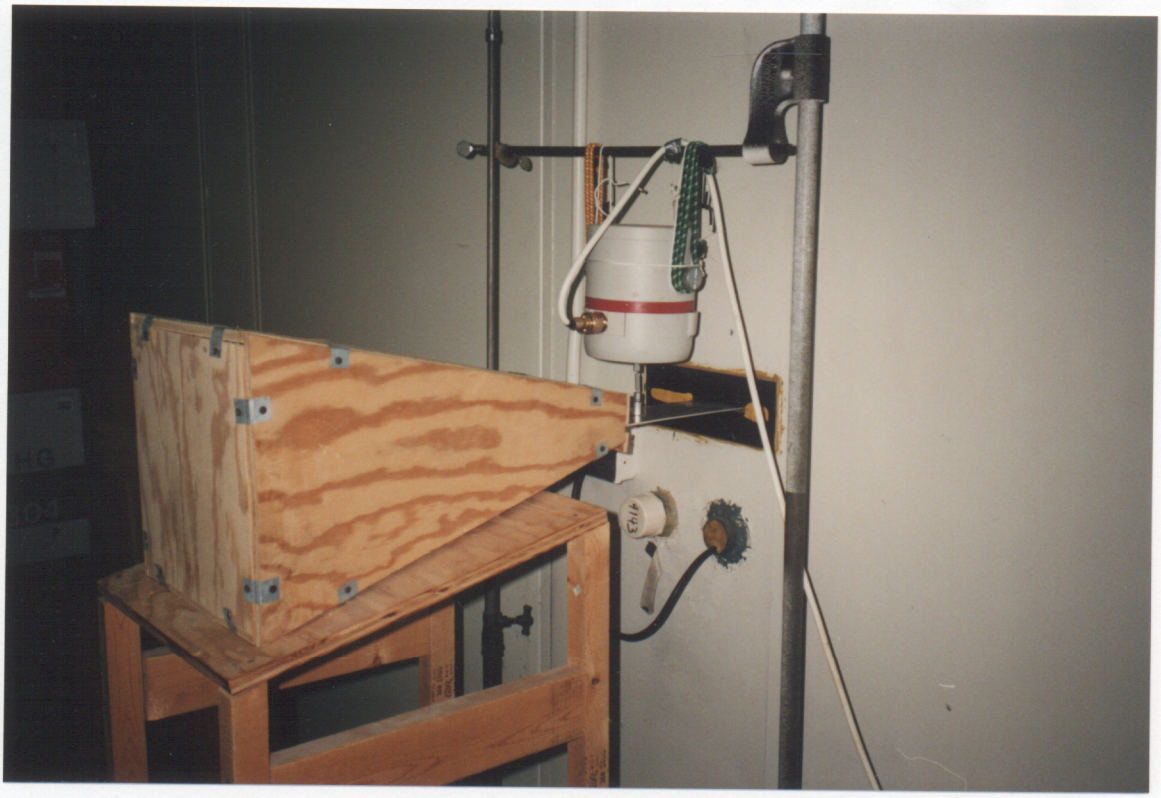

Figure 2.5: Photograph of the beam, anechoic termination, and input shaker outside of the anechoic chamber.

comparison with theoretical models, the beams were surrounded by a baffle in the horizontal (x, y) plane. Since the theoretical model assumes an infinite baffle, some difference between the infinitely baffled theory and the finitely baffled experiments was expected. In addition, the assumption was made in the theoretical model that none of the air near the surface of the beam was able to move back and forth (or "slump") across the baffle. Since it would be impossible to achieve a perfect seal between the edge of the baffle and the edge of the beam without interfering with the vibrational response of the beam, some "slumping" did occur in the experiments. These differences were manifested as a decreased acoustic radiation efficiency by the experimental beam as compared to the theoretical model caused by losses associated with the air near the surface of the beam "slumping" back and forth across the baffle, particularly along the small gap between the beam and baffle edges.

The baffle was made of plywood supported on adjustable legs on either side of the beam. The edges of the baffle which ran along the beam were edged with angle aluminum that had an L shaped cross section. These aluminum edgings provided a smooth surface which could be adjusted such that they were as close to the beam as possible without interfering with the vibrations of the beam. The baffles with the aluminium edges can be seen in Figs. 2.3 and 2.4.

2.1.2 Anechoic Termination

The anechoic terminations used in each experiment served the purpose of making the beam appear infinite to traveling waves at the end of the beam set into the terminations. This was accomplished by causing the travelling waves to "see" a gradual increase in impedance near the end of the beam. This gradual impedance

increase prevented wave reflections while the energy of the traveling waves was absorbed by the termination. The terminations consisted of a pyramid shaped wooden box full of sand. Additionally, damping material (such as foam and beryllium impregnated vinyl) was fastened to the beam along the part set into the termination. This produced a more gradual impedance transition between the beam and sand [2].

The clamped beam had one end of the beam set into an anechoic termination (which was located outside the anechoic chamber) while the other end (inside the chamber) was attached to the clamp discontinuity (discussed in detail later in Sec. 2.1.4). To produce the beam with a blocking mass, one end of the beam was placed in the anechoic termination outside the chamber while the other end of the beam was placed in a termination located inside the anechoic chamber.

To ensure that the anechoic terminations were affective, data had to be collected to calculate the power reflection ratio for the terminations. The power reflection ratio is the ratio of the reflected vibrational power to the incident vibrational power. For an infinite beam, the ideal power reflection ratio would be zero at all frequencies.

To calculate the power reflection ratio [Φ] the beam was excited with random noise by a shaker. Two accelerometers were positioned between the shaker and termination (and sufficiently far from each to avoid near-field effects). Then the autospectrum and cross–spectrum information from their signals were collected using a Bruel & Kjaer model 2032 signal analyzer. From this information the power reflection ratio was calculated as follows [2]:

$$\Phi = \frac{S_1 + S_2 - 2C_{12}\cos(k_b\Delta) + 2Q_{12}\sin(k_b\Delta)}{S_1 + S_2 - 2C_{12}\cos(k_b\Delta) - 2Q_{12}\sin(k_b\Delta)} \tag{2.1}$$

where S_1 and S_2 are the autospectra of the accelerometer signals, C_{12} is the real component of the cross–spectrum, Q_{12} is the imaginary component of the cross–spectrum, k_b is the structural wavenumber in the beam as calculated in Eq. 1.10, and Δ is the distance between the accelerometers.

Two Bruel & Kjaer type 4374 accelerometers were used and the data was taken by a Bruel & Kjaer model 2032 dual channel signal analyzer (which also provided the random noise signal via an on board signal generator). The beam was excited by a Ling Dynamic Systems model V203 shaker powered by a Proton A1150 power amplifier. The acquired data and Eq. 2.1 were used to calculate the power reflection ratio from 0Hz to 800Hz as shown in Fig. 2.6.

For the experiments employing the beam with a blocking mass a second anechoic termination was used. To test the effectiveness of termination #2 the same method that was used to test termination #1 was employed (as described above). Figure 2.7 shows the results of this test.

This type of anechoic termination is only effective above a particular frequency. As is shown in Fig. 2.6 termination #1 had a power reflection ratio less than 0.1 for frequencies above 180 Hz. Although the second termination did not show as good of a performance between 200Hz and 400Hz, a frequency for experimentation was selected in this range (320Hz) where termination #2 had a low reflection ratio of 0.11.

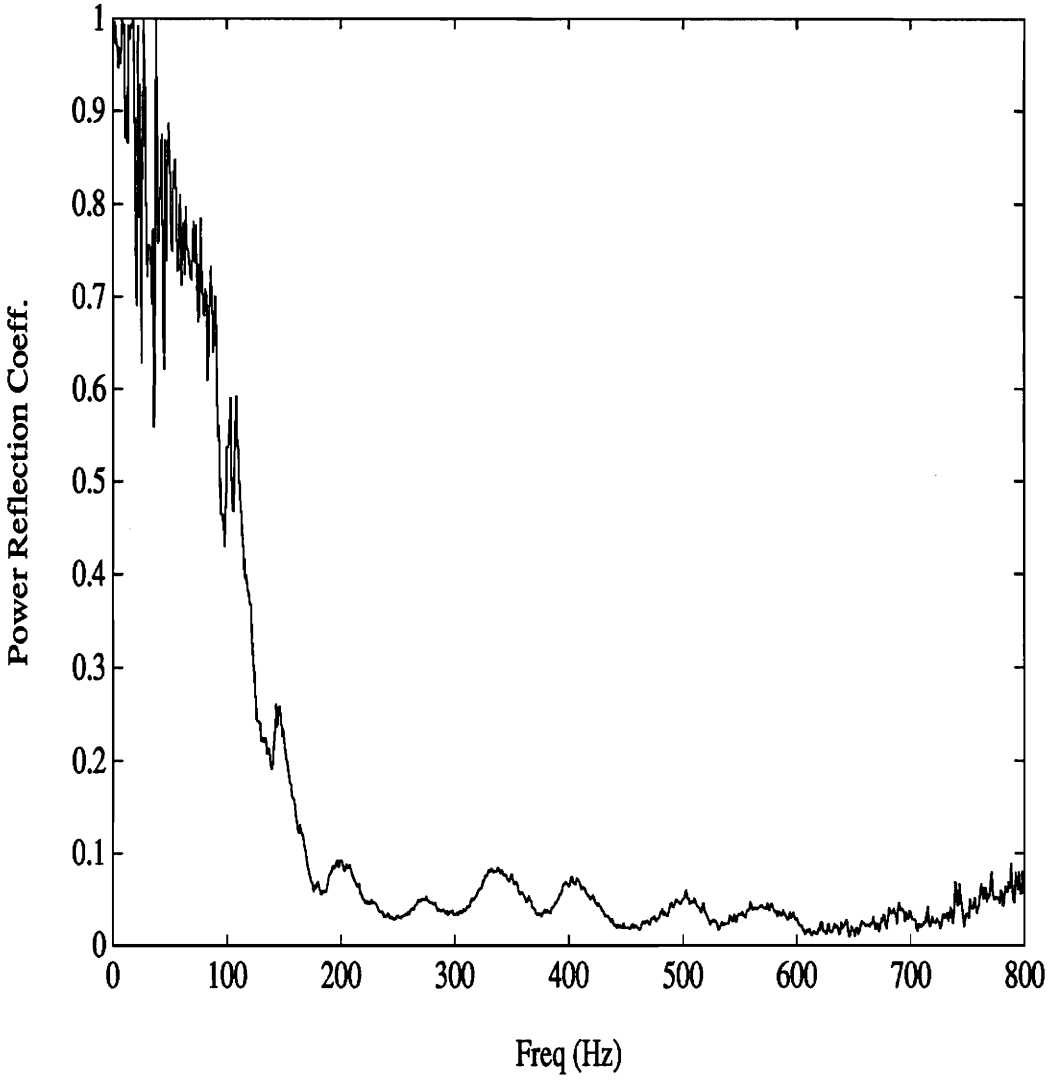

Figure 2.6: Power reflection ratio for anechoic termination #1.

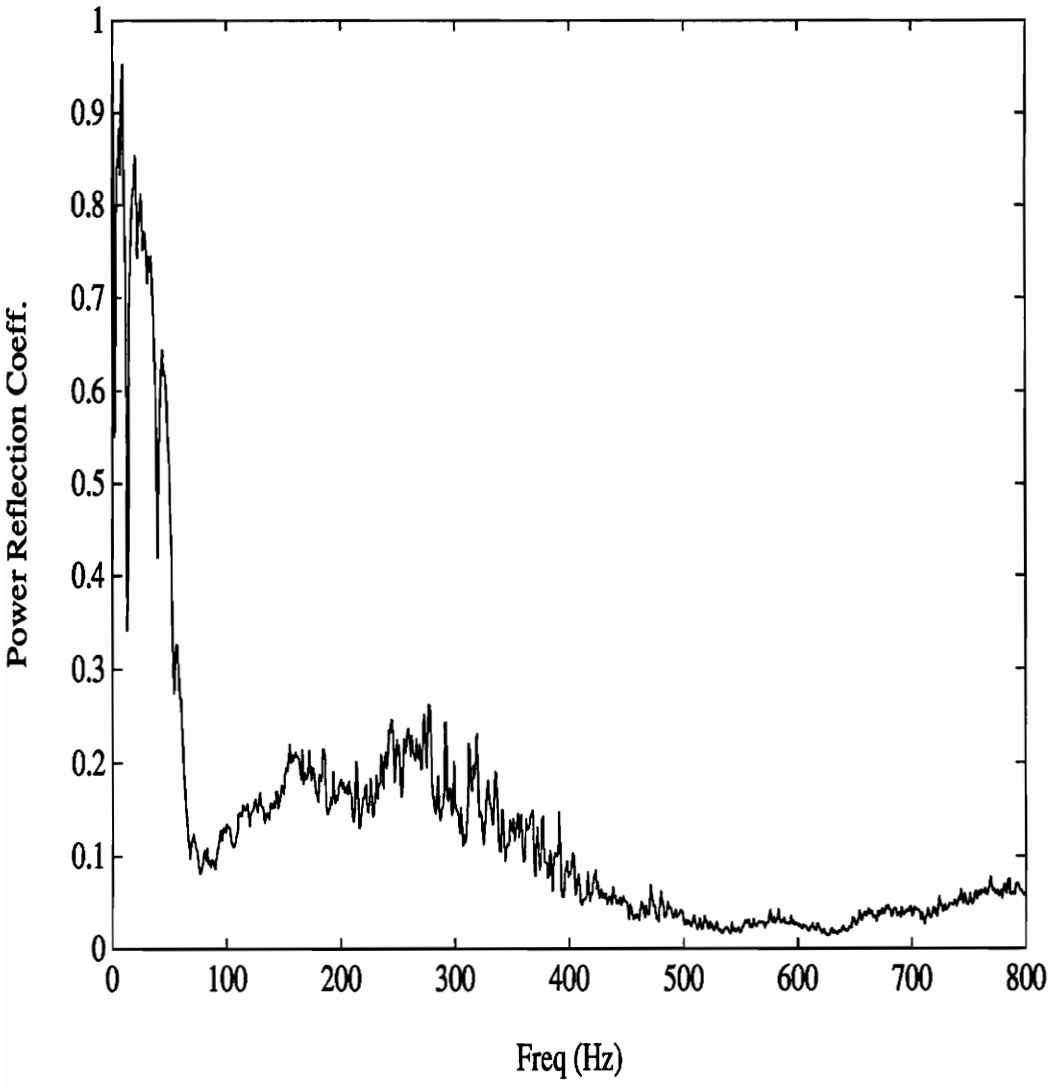

Figure 2.7: Power reflection ratio for the anechoic termination #2 used with the infinite beam with a blocking mass.

2.1.3 Supports

In both experiments, the beams were supported by elastic tubing. The tubing was fastened to the ceiling of the anechoic chamber. A small hook at the end of the tubing held a loop of fishing line which wrapped around the beam. The tubing was of sufficient length and stiffness such that their natural frequencies were far below the operating frequencies of the experiments.

A verification of the good behavior by these supports is evident in the studies done on the anechoic terminations. If these supports affected the vibrational response of the beams at the operating frequencies, then they would act like discontinuities on the beams. This would produce reflected waves which would in turn produce standing waves on the beam. Any standing waves present in the beam response would have been evident when the power reflection ratio for the anechoic terminations was calculated (Figs. 2.6 and 2.7). Since, in the regions of the operating frequencies, the power reflection ratios were small (and hence, any standing waves on the beam were small) it was determined that the supports had a negligible effect on the beam vibrational response in the frequency range used in these experiments.

2.1.4 Discontinuities

In the two experiments, two different discontinuities were used; a clamped end condition in one experiment and a blocking mass in the other. Schematics of the clamp and blocking mass are shown in Fig. 2.8 and Fig. 2.9 respectively.

The clamped discontinuity was constructed from a large ($10cm \times 7cm \times 20cm$) block of aluminium. By placing $2cm$ of the end of the beam between the clamping plate

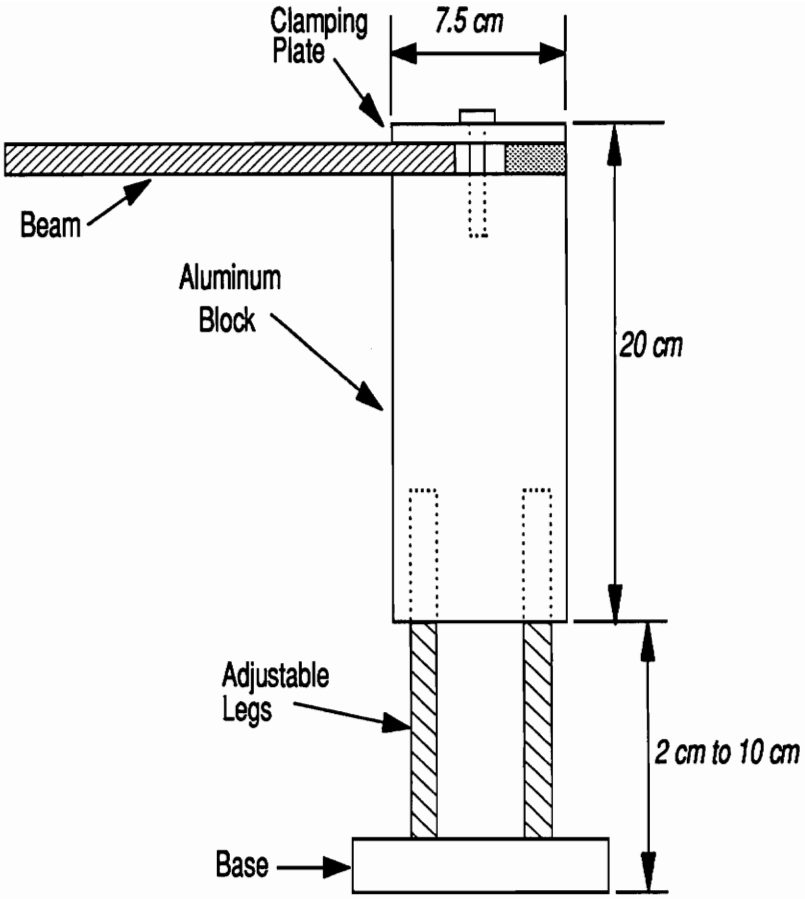

Figure 2.8: Clamped Discontinuity

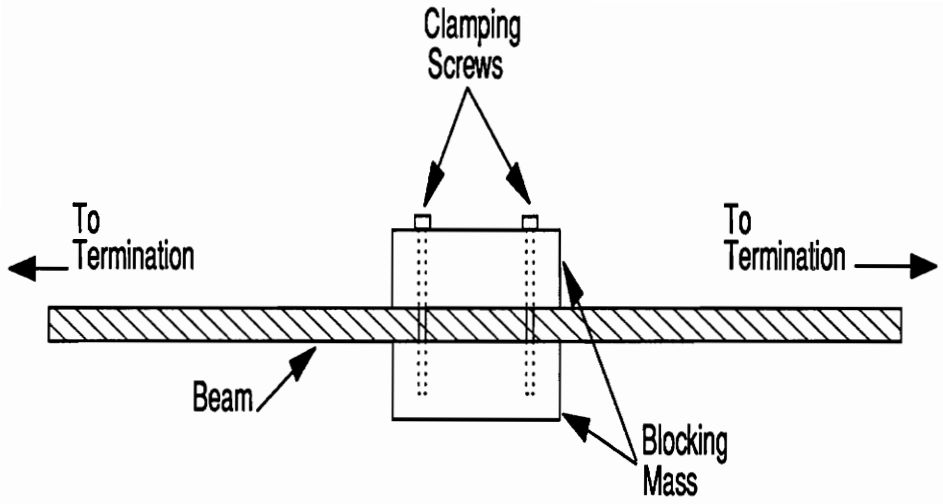

Figure 2.9: Blocking Mass Discontinuity

and the block and tightening three clamping screws (see Fog. 2.8), an approximate clamped end condition was achieved.

In order to determine the effectiveness of the clamped discontinuity a test was run to determine its power reflection ratio. This test was performed exactly like the test run to examine the anechoic terminations. For an ideal clamp the power reflection ratio would be unity for all frequencies. Fig. 2.10 shows the results of the test. For all frequencies above 280 Hz the power reflection coefficient is greater than 0.95. All experiments were performed above this frequency.

Although, according to the power reflection ration of the clamped end condition, the performance was very good, the clamped end condition was by no means perfect. The end of the beam was still able to displace in the transverse direction, but only a very small amount compared to the beam vibrational response. To compensate for this, the assumed displacement equation for the clamped beam experiments (discussed in Ch. 3) did not employ the boundary conditions associated with a clamped end condition (displacement and slope being zero). Instead, it was assumed that the clamped end condition was a general discontinuity (behaving like a very large blocking mass). This topic is discussed in more detail in Ch. 3.

For the infinite beam with blocking mass experiments two different blocking masses were used. The specifics of each blocking mass are shown in Table 2.2.

Each blocking mass consisted of two blocks of metal which were placed on either side of the beam and clamped together with screws. The main draw back associated with this configuration was that the theory assumed the blocking mass was of infinitesimal width. This caused some differences in the results from the experiments and the

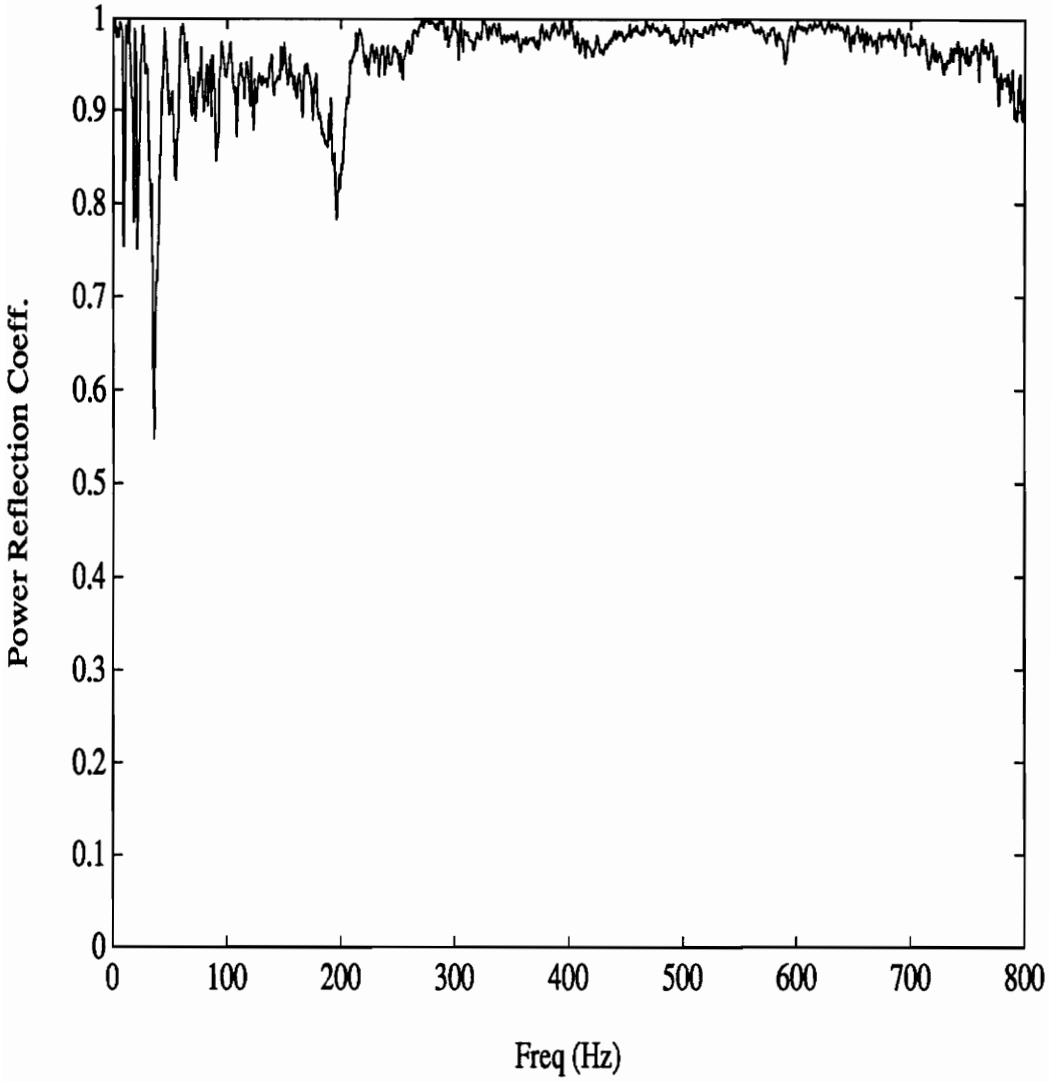

Figure 2.10: Clamped Discontinuity Power Reflection Ratio

Table 2.2: Blocking Mass Properties

Blocking Mass No. 1	
Material	aluminum
Density	2700 kg/m^3
Length	5.08 cm
Width	12.7 cm
Height	3.81 cm
Mass	675 g
Blocking Mass No. 2	
Material	steel
Density	7700 kg/m^3
Length	2.54 cm
Width	12.7 cm
Height	5.08 cm
Mass	1288 g

theoretical model. This topic is treated more thoroughly along with the presentation of the results of the beam with a blocking mass experiments in Ch. 4.

2.1.5 Microphones

The 13 acoustic sensors (microphones) used in both experiments were Radio Shack Tie Pin Microphones attached to a semicircular, steel array centered over the discontinuity and suspended from the anechoic chamber ceiling. The angular positions of each microphone in the array is shown in Table 2.3. In each case the array could be situated in either a perpendicular or axial position. While in the perpendicular position the semicircular array was perpendicular to the long axis of the beam as shown in Fig. 2.12 and, while in the axial position the microphone array was parallel to the long axis of the beam as shown in Fig. 2.11. In the case of the semi-infinite/clamped beam the array was at at radius of $0.86m$ and in the case of the infinite beam with a blocking mass the array was at a radius of $0.76m$. In each case, the array was made as large as the space in the anechoic chamber (which had dimensions of $5.6m \times 2.8m$ and $2.1m$ high) would allow such that the array could be rotated from the axial position to the perpendicular position. These two array positions (perpendicular and axial) of the microphone array allowed a global selection of acoustical data to be taken in each experiment.

It should be noted that these radii for the microphone arrays places the microphones in the acoustic near-field (or, more precisely, not in the far-field). An attempt was made to place a partial array (located at a radius of $1.8m$) in the far-field (the results are discussed in Ch. 4) but it was demonstrated that this $1.8m$ microphone array was still not in the far-field.

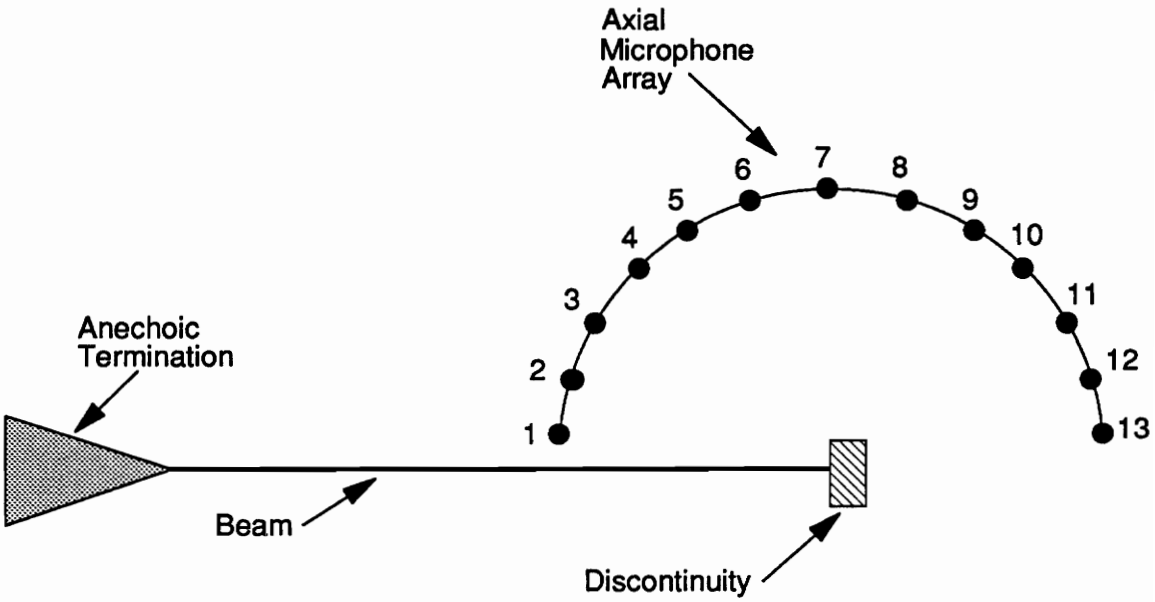

Figure 2.11: Axial Microphone Array

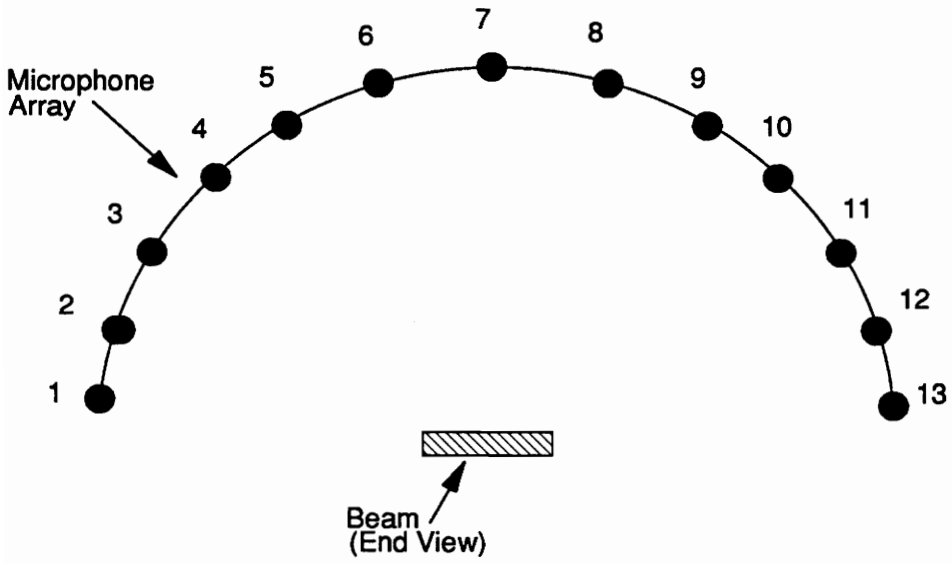

Figure 2.12: Perpendicular Microphone Array

Table 2.3: Microphone Positions in Semicircular Array

Microphone No.	Position (deg.)
1	12.9
2	25.7
3	38.6
4	51.4
5	64.3
6	77.1
7	90.0
8	102.9
9	115.7
10	128.6
11	141.4
12	154.3
13	167.1

At the highest frequency of operation (690Hz) the wavelength in the acoustic medium was $0.5m$ which corresponds to the shortest wavelength for the three operating frequencies (320Hz, 510Hz, 690Hz). When the radius of the $0.76m$ and $0.86m$ arrays is compared to the shortest wavelength it was noted that the clamped beam microphone array was only 1.7 wavelengths away from the discontinuity. In the case of the beam with a blocking mass the array was 1.5 wavelengths away. In order for the microphone array to be in the acoustic far-field it should be approximately 10 wavelengths or more away from the source. However, size limitations in the anechoic chamber prevented this large of an array.

Since the microphone array was moved during each experiment it was necessary to have stationary error microphones so that the entire acoustic field could be sampled while the digital controller was operating. For this reason two Bruel & Kjaer type 4166 condenser microphones were used with Bruel & Kjaer type 2619 preamplifiers which were driven by a Bruel & Kjaer type 2807 power supply. The Bruel & Kjaer microphones also had a superior signal to noise ratio which allowed improved attenuations by the controller.

2.1.6 Vibration Sensors

10 Bruel & Kjaer type 4374 accelerometers along with two Bruel & Kjaer type 2635 charge amplifiers were used to sense the beam vibrations in each experiment. One accelerometer was used as a reference and the other nine were run through a switching box. The reference accelerometer signal was run through one charge amplifier while the switching box output was run through the other. The switching box was operated remotely from outside of the anechoic chamber by way of relay switches.

When taking vibrational data the magnitude of the reference accelerometer was measured and then the transfer functions between the reference accelerometer and each of the other accelerometers were measured. A schematic of the switching box is shown in Fig. 2.13.

The accelerometers were positioned on the beams such that most were in the region affected by the flexural near-fields while the rest were in the flexural far-field. This ensured that enough information on the beam near-field response (due to discontinuities and control actuators) was available for the statistical decomposition of the beam equation of motion. The positions of the accelerometers are shown in Table 2.4 as per the coordinates shown in Figs. 2.16 and 2.17.

The data received from the accelerometers was used to statistically decompose the complex amplitudes of the assumed displacement equations (discussed in Ch. 3). From the displacement equation an analysis of the beam response allowed a detailed examination of the mechanism by which control of the acoustic field was achieved.

2.1.7 Shakers

The input shaker used in each experiment was a Ling Dynamic Systems, Ltd. 14.1 kg model V400 and was attached to the beams (with a stinger and super glue) outside the anechoic chamber. This location prevented any noise from the input shaker from influencing the acoustic field inside the chamber. To quantify the effect of the input shakers acoustic radiation on the experiments the shaker was driven at the experimental operating frequencies while disconnected from the beam. Microphone measurements were taken for all of the operating frequencies inside the chamber and

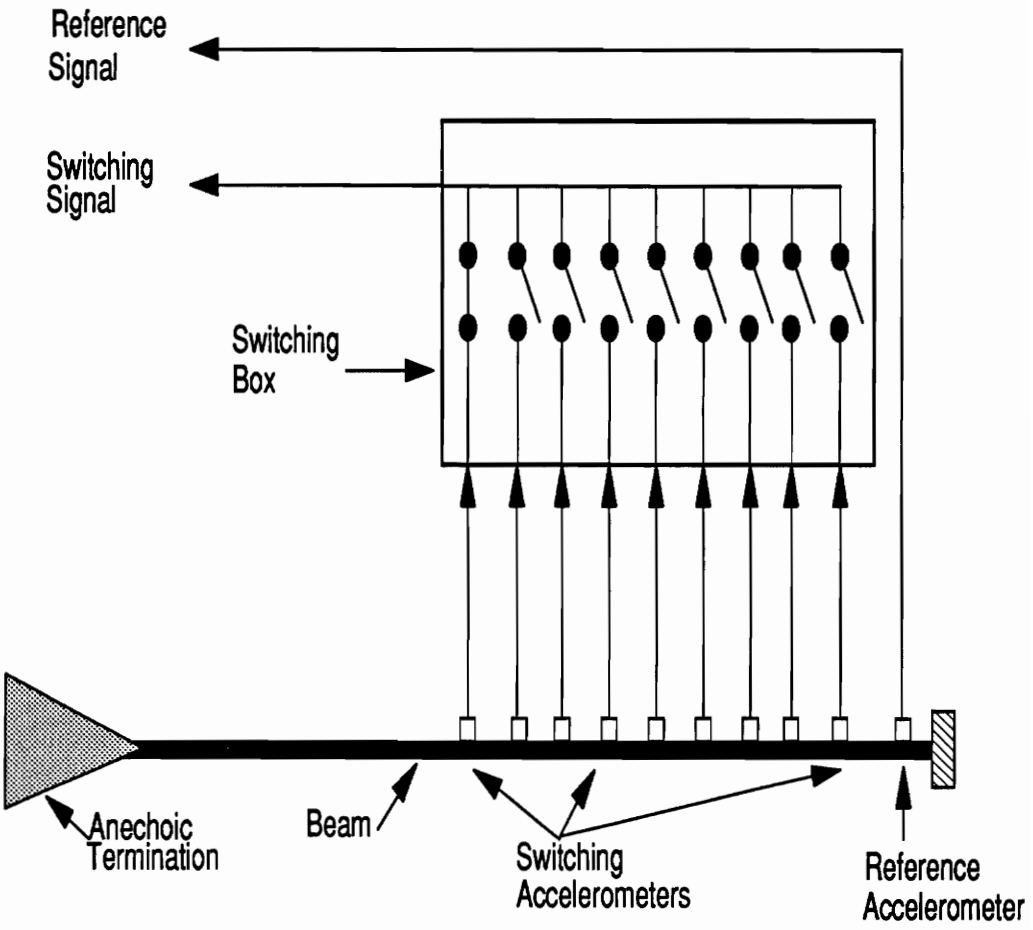

Figure 2.13: Accelerometer Switching Box Schematic

Table 2.4: Accelerometer Positions

Clamped Beam		Blocking Mass Beam	
Acc. No.	Position (m)	Acc. No.	Position (m)
1	0.005	1	0.035
2	0.01	2	0.075
3	0.02	3	0.095
4	0.03	4	-.035
5	0.08	5	-.055
6	0.11	6	-.095
7	0.17	7	-.145
8	0.20	8	-.185
9	0.29	9	-.315
ref	0.31	ref	-.335

all levels due to the disconnected input shaker were less than $10dB$ re $20\mu Pa$. Since operating levels for the experiments were on the order of $50 \rightarrow 60dB$ the effects of the input shaker were deemed negligible.

The control shakers used in each experiment were Ling Dynamic Systems, Ltd. 3.8 kg model V203 shakers. They were attached to the beam (with a stinger and super glue) near the discontinuity as shown in Figs. 2.14 and 2.15. The control shakers were positioned near the discontinuity because it was expected that the best control of the acoustic field would be achieved in this position. This was suggested by analytical studies by Guigou [16] on the optimal location of control actuators. It will be shown in Ch. 4 that the control actuators closest to the discontinuity show the best attenuation of the acoustic field.

In the case of the semi-infinite/clamped beam the control shakers were located at $x = 14.0cm$ and $x = 3.8cm$ while the control shakers were located at $x = \pm 3.2cm$ on the beam with a blocking mass. The shakers were attached to the beam from a position underneath the beam and baffle.

These control shakers also produce noise which was attenuated by wrapping them in a $15cm$ layer of fiberglass insulation. When driven at experimental frequencies and disconnected from the beam, these shakers produced sound levels of less than $7dB$ around the microphone arrays.

In the case of the infinite beam with a blocking mass one additional control shaker location was tried. This was for the shaker located at $x = 0$ or fastened directly to the blocking mass with a stinger and super glue. The results of these experiments are presented in Ch. 4.

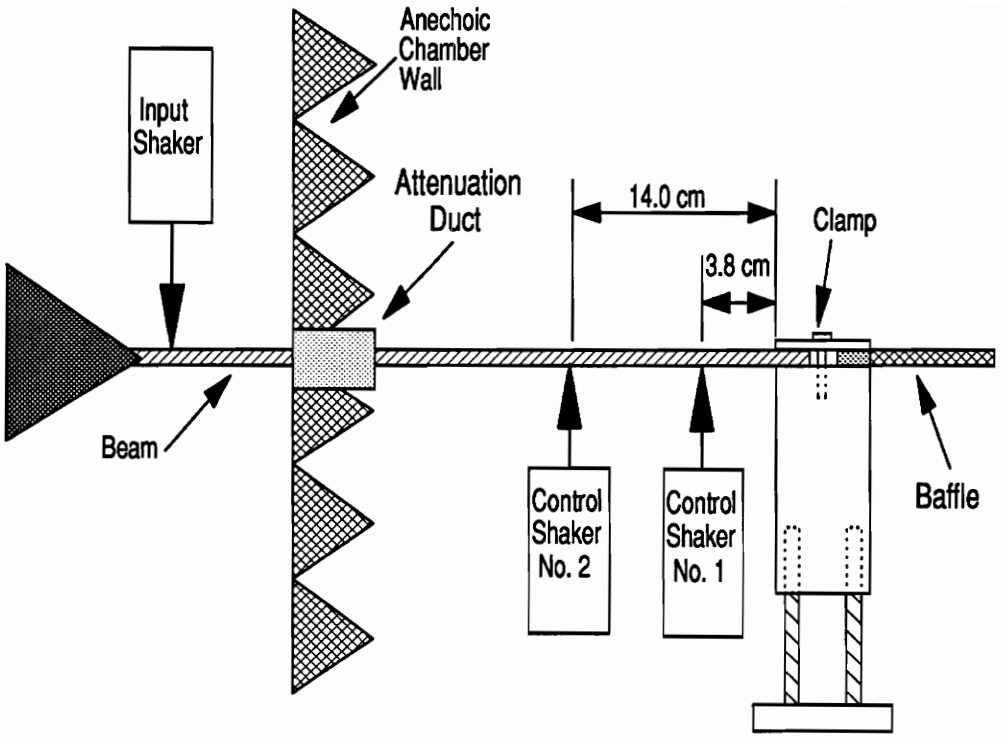

Figure 2.14: Control and Input Shaker Arrangement for Clamped Experiment

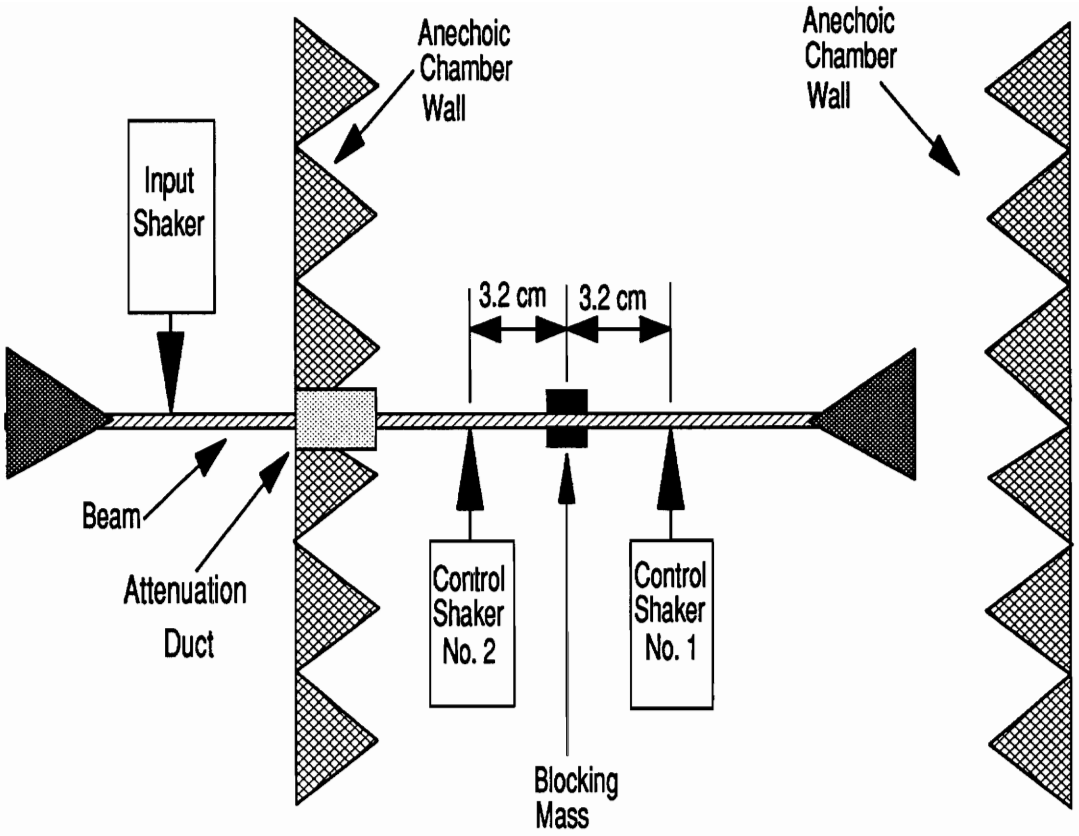

Figure 2.15: Control and Input Shaker Arrangement for Blocking Mass Experiment

The control shakers were driven by a two channel Proton A1150 power amplifier with 50 watts/channel. The input shaker was driven by a Harman/Kardon Citation 22 power amplifier with 200 watts/channel.

2.1.8 Piezoelectric Actuators

The piezoelectric actuators used in each experiment were supplied by Piezo Systems, Inc. They were bonded to the beam using cyanoacrylate strain gage glue in the positions shown in Fig. 2.16 and Fig. 2.17. Each patch had dimensions of $2.06cm \times 3.81cm \times .0191cm$. It is important to note that four individual piezoelectric patches were operating dependently as one actuator. Each actuator consisted of two pairs of piezoelectric patches while each pair consisted of two individual patches bonded directly opposite each other on the beam. In each pair, the two opposite patches were driven 180° out of phase from each other. At the same time, any two patches of the same actuator foursome on the same side of the beam were operating in phase.

The piezoelectric patches were operated in pairs bonded to the beam exactly opposite from each other and driven 180° out of phase in order to produce pure bending moments. (A pair acting in phase would create purely extensional excitations [23].) The reason for having two dependent pairs placed symmetrically about the center axis of the beam was that the center axis of the beam needed to be open for connection of the shakers and positioning of the accelerometer array.

The piezoelectric patches were driven by a Proton A1150 power amp through a 17:1 transformer. The transformer was employed because the piezoelectric patches require very high voltages and very low current.

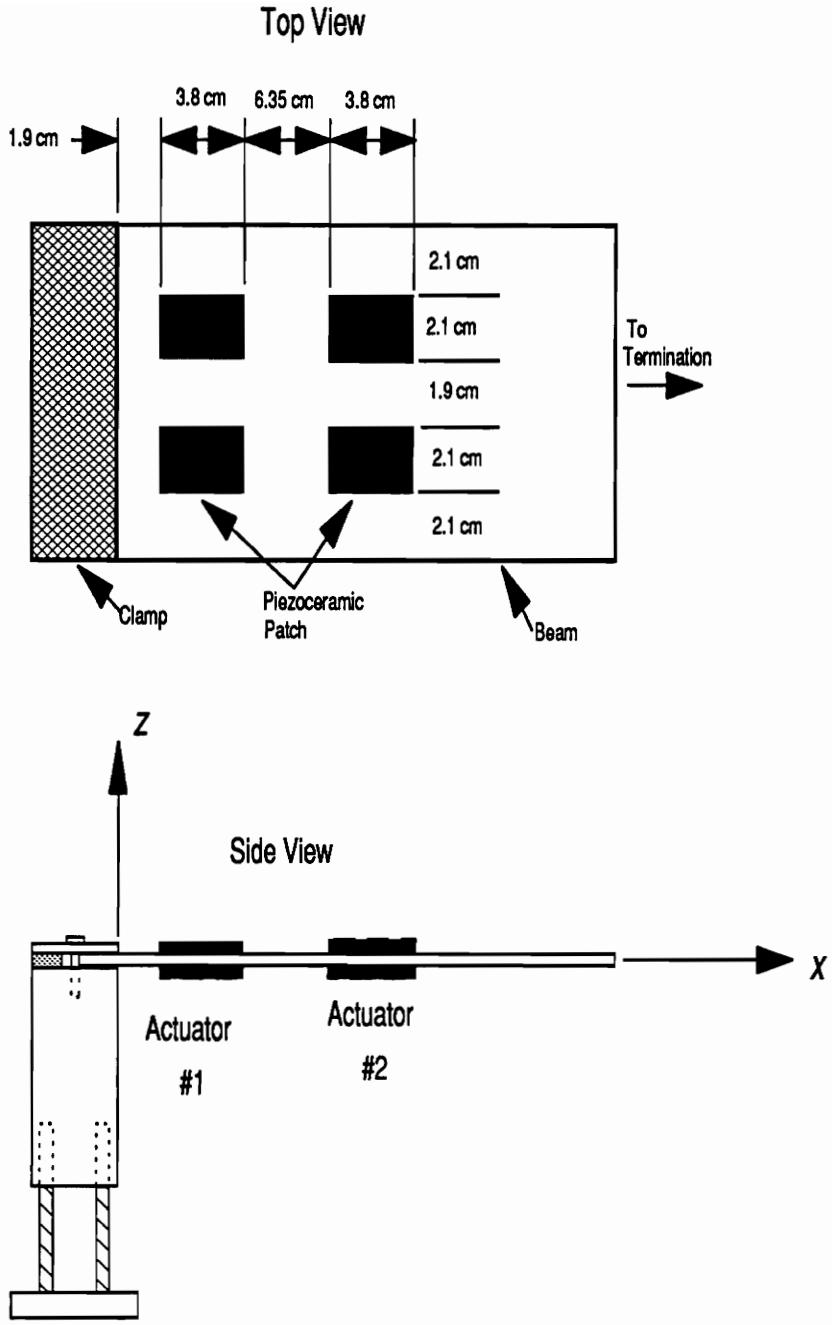

Figure 2.16: Piezoelectric patch locations: Semi-infinite/clamped beam

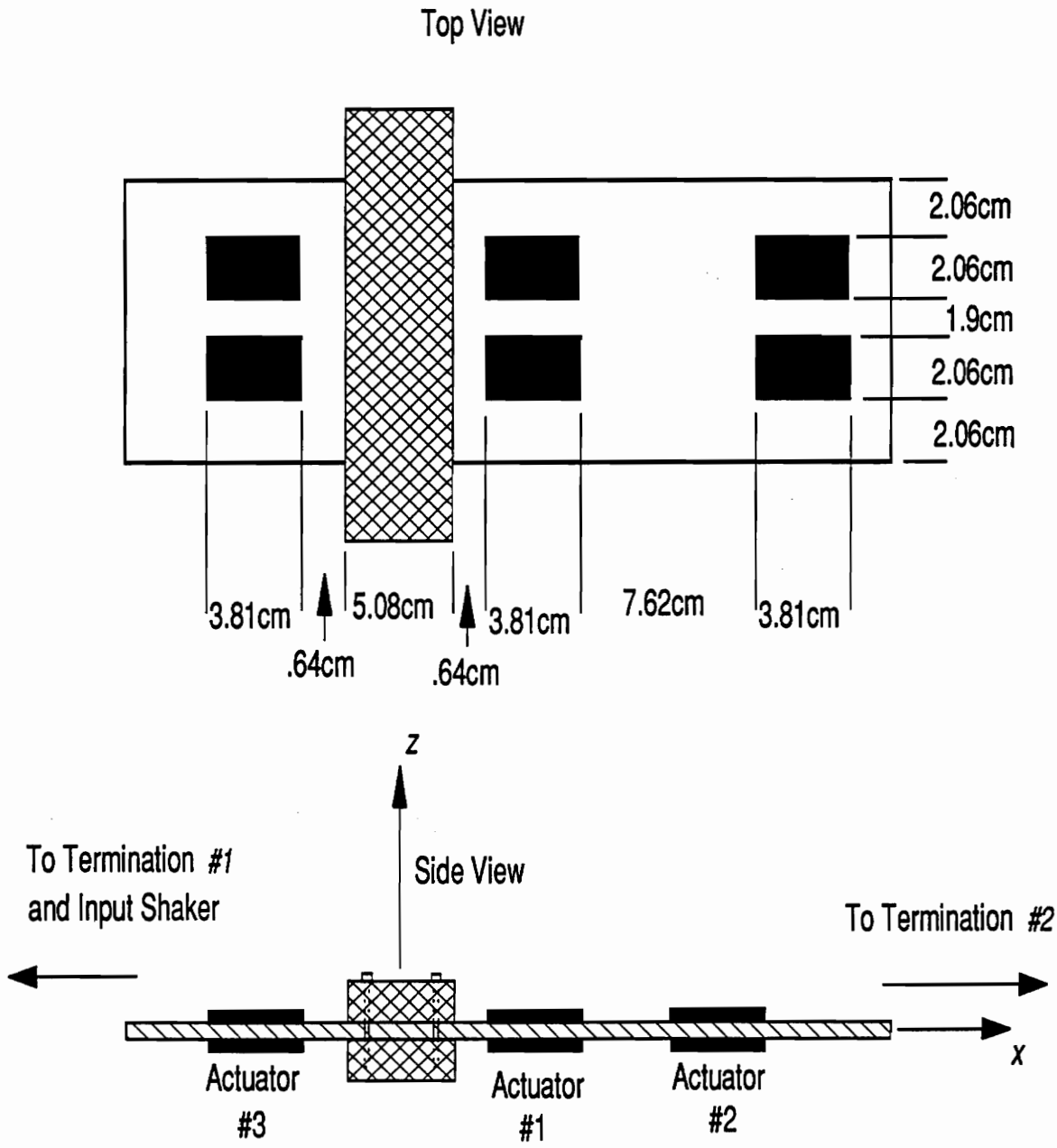

Figure 2.17: Piezoelectric patch locations: Infinite beam with blocking mass

2.1.9 Instrumentation

Several pieces of instrumentation were used for these experiments. They are listed below along with a brief description of their purpose.

- Wavetek model 275 Signal Generator – This produced the reference signal which was sent to the controller and to the power amplifier which drove the disturbance shaker.
- Ithaco model 455 Amplifiers – Used to amplify the error microphone signals.
- Ithaco model 4302 Dual High/Low Pass Filters – Used to band pass the error microphone signals to improve the performance of the digital controller by eliminating noise in the signal.
- Frequency Devices model 9002 Low Pass Filters – Used to filter the control signals to prevent alliasing in the control signal.
- JDR Instruments model 3500 Oscilloscope – Used to monitor the error and control signals in real time to prevent overloading the control actuators or the DSP board.
- Bruel & Kjaer model 2032 Dual Channel Signal Analyzer – Used to sample the microphone array signals and the accelerometer array signals.

2.2 The Least Mean Square (LMS) Adaptive Control Algorithm

The control system used in these experiments was the multiple channel LMS algorithm described by Elliot et al. [7]. Experimental use of this control algorithm for vibration control are discussed by Gonidou [2] while Clark and Fuller [4] have used the LMS algorithm for noise control.

This type of control system implements a variable coefficient FIR filter. The coefficients of the FIR filter are updated by the LMS algorithm which employs a steepest gradient descent method for minimizing the least square error. A more detailed discussion of this system follows.

2.2.1 The LMS Algorithm

The LMS algorithm is a gradient decent algorithm which adapts the coefficients of a variable coefficient finite impulse response (FIR) filter (shown in Fig. 2.18). These coefficients are continuously updated by the least mean square (LMS) algorithm such that they converge on the set of optimal weighting coefficients (W) to minimize the error signal.

In Fig. 2.18, for the input $X_{i,j}$, 'j' is the discrete time step index, n is the number of filter coefficients and Y_j is the filter output. For use as a controller, $X_{i,j}$ would be related to the reference signal while Y_j would be the output to the control actuator.

Applying the LMS algorithm to a FIR filter with variable coefficients (as depicted in Fig. 2.19 for a two input, two output system) permits the LMS algorithm to update

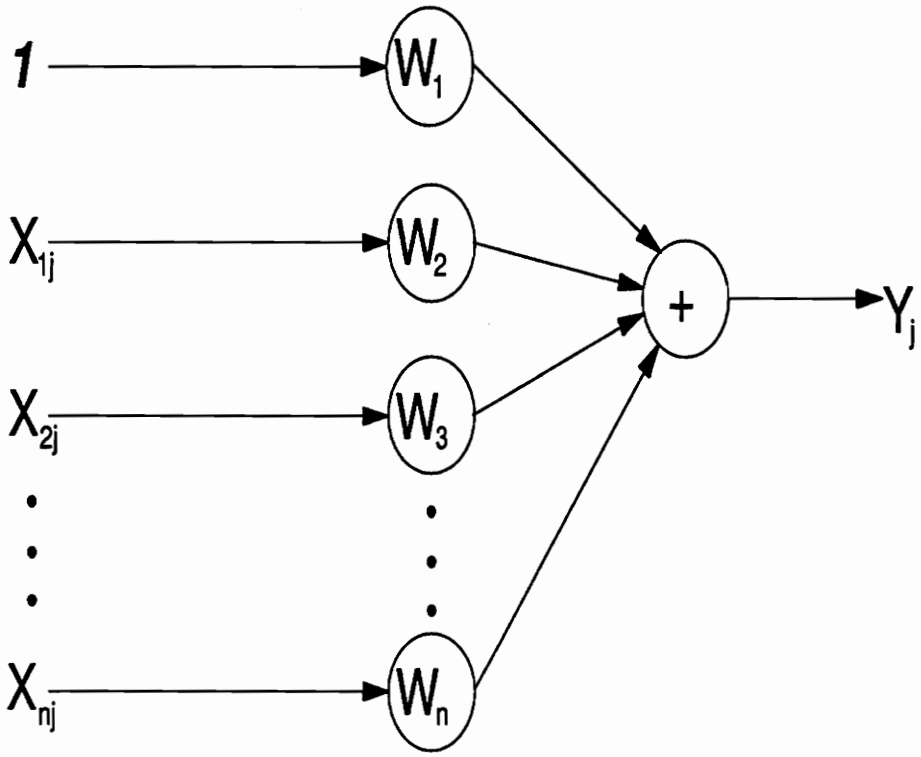

Figure 2.18: Finite Impulse Response Filter

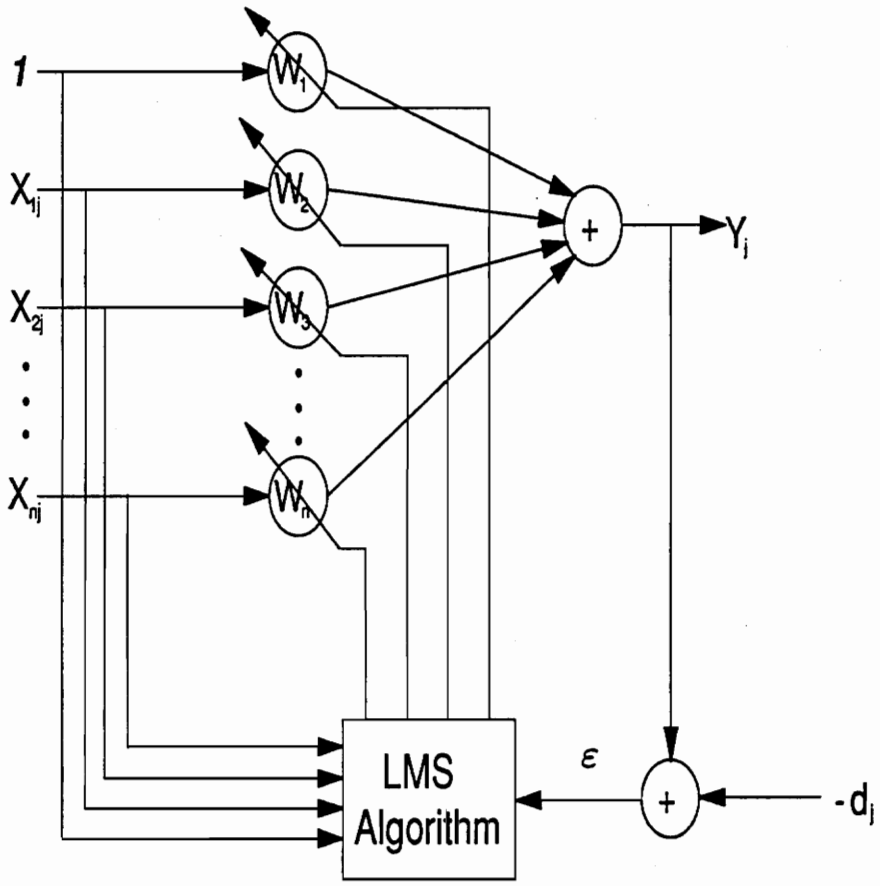

Figure 2.19: The LMS Adaptive Filter

the FIR coefficients and converge to their optimal values to minimize a gradient cost function.

For these experiments, the error signal $[\varepsilon_j]$ is supplied by microphones in the acoustic field of the radiating beam. The adaptive filter output $[Y_j]$ is the signal which drives the control shaker or piezoelectric actuator. In vector notation, the FIR filter output for a single input, single output system is:

$$Y_j = X_j^T W = W^T X_j \tag{2.2}$$

where

$$X_j = [X_{0j}, X_{1j}, \ldots, X_{nj}]^T \tag{2.3}$$

and

$$W = [W_0, W_1, \ldots, W_n]^T \tag{2.4}$$

From this the error is defined by:

$$\varepsilon_j = Y_j - d_j = X_j^T W - d_j = W^T X_j - d_j \tag{2.5}$$

The purpose of the LMS algorithm is to minimize the mean square of the error. This is given by:

$$E[\varepsilon_j^2] = E[d_j^2] - 2E[X_j^T d_j]W + W^T E[X_j X_j^T]W \tag{2.6}$$

where $E[\cdots]$ is the expected value of the argument.

If we let

$$P = E[X_j^T d_j] \tag{2.7}$$

and

$$R = E[X_j X_j^T] \tag{2.8}$$

and substitute these into Eq. 2.6 we get:

$$E[\varepsilon_j^2] = E[d_j^2] - 2PW + W^T RW \tag{2.9}$$

The minimum of Eq. 2.9 (which is a quadratic surface) can be found by employing a gradient method. The gradient of the mean square error function can be found by differentiating Eq. 2.9 with respect to the weighting coefficients $[W]$ as follows:

$$\nabla(E[\varepsilon_j^2]) = \left[\frac{\partial E[\varepsilon_j^2]}{\partial w_0}, \ldots, \frac{\partial E[\varepsilon_j^2]}{\partial w_n}\right]^T = -2P + 2RW \tag{2.10}$$

Setting this partial derivative equal to zero (corresponding to the minimum of Eq. 2.10) we can solve for the optimal weighting coefficients necessary to minimize the mean square error.

$$W = R^{-1}P \tag{2.11}$$

Although these are the optimal coefficients, the real time controller does not use Eq. 2.11 to calculate the coefficients. Instead, a steepest decent of the gradient method is used as follows:

$$W_{j+1} = W_j + \mu\nabla_j \tag{2.12}$$

The gradient, ∇_j, should come from the paraboloid formed by the quadratic of $E[\varepsilon_j^2]$ in Eq. 2.6. However, the LMS algorithm uses the instantaneous value of ε_j^2 instead

of the estimated value. This approximation of the expected value, $[E[\varepsilon_j^2]]$, converges to the optimal solution [20]. Thus, the approximation of the gradient is given by:

$$\hat{\nabla}_j = \left[\frac{\partial \varepsilon_j^2}{\partial w_0}, \ldots, \frac{\partial \varepsilon_j^2}{\partial w_n}\right]^T = -2\varepsilon_j X_j \tag{2.13}$$

In these equations, μ is called the convergence parameter. It controls how fast the adaptive filter can converge on the optimal weighting coefficients. It also controls the stability of the convergence. This algorithm can be easily extended to a multiple input, multiple output system as discussed by Elliott et al. [7].

2.2.2 The Filtered-X LMS Algorithm

The filtered-x LMS algorithm (as shown in Fig. 2.20 with dual channel capabilities) is different from the LMS algorithm in that it takes into account the transfer function between the control actuator and the error sensor. Since it takes a finite amount of time for the control signal to propagate from the LMS algorithm, through the D/A converter, to the control actuator, through the acoustic medium to the error microphone, back through the A/D converter , and to the LMS algorithm, the signal will be altered by some constant phase and magnitude. If this phase and magnitude shift is not corrected in the control loop, the system could become unstable. In Fig. 2.20 P_{mn} is the transfer function between actuator n and error sensor m. This serves to pre filter the reference signal to correct for any relative phase error between the reference signal and the error signal which might cause instabilities.

To calculate the pre-filter values (P_{mn}) a secondary adaptive filter was employed. First, the reference signal was used to directly drive the control actuator(s) with

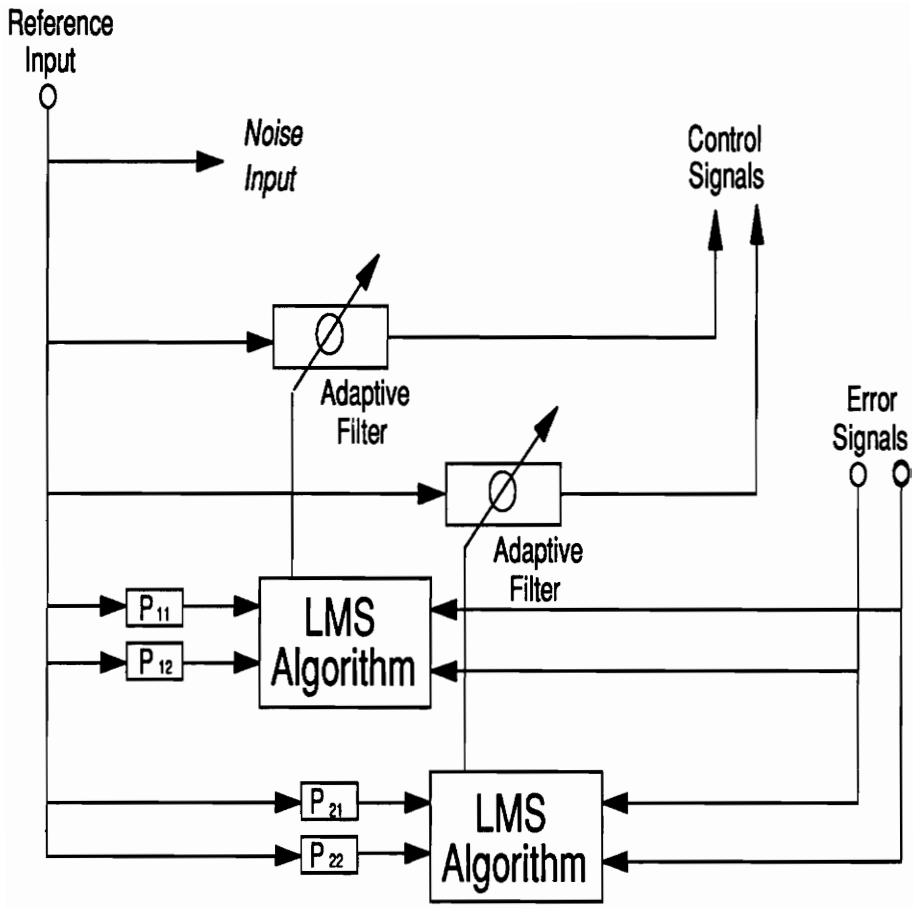

Figure 2.20: The Filtered-x LMS Adaptive Filter

no disturbance input to the system. The reference input was then filtered by the secondary adaptive filter and subtracted from the error microphone signal. This difference was used as the error signal sent to the secondary LMS algorithm. When the secondary adaptive filter had converged to its optimal value (when the difference between the filtered reference signal an the error microphone signal was zero), its transfer function was an approximation of the transfer function from control actuator to error microphone. This approximate transfer function was then used as the fixed pre-filter value, $[\hat{P}_{nm}]$, which accounted for the magnitude and phase shift from control actuator to error microphone.

2.2.3 Implementation of the Filtered-X LMS Algorithm

The algorithm was implemented from a TMS320C25 digital signal processing board manufactured by Spectrum Signal Processing, Inc. and hosted by a Swan 286 computer. It was capable of 2 channels of control (two error inputs, two control outputs and a reference input).

The implementation of the controller board consisted of two programs. One program written in Microsoft C ran on the host computer. This program set the sampling rate and set the convergence parameter $[\mu]$. The second program was written in assembly language and was resident on the controller board and ran independent of the host computer. This assembly language program performed the calculations involved in the LMS algorithm.

The version of the filtered-x LMS algorithm used in these experiments employed a FIR filter with two variable coefficients. It can be shown that a sinusoidal signal can

be modified in phase and magnitude by a FIR filter with two coefficients. Although this limits the controller to narrow band disturbances, it also decreases the number of calculations the DSP board must perform. This increases the speed at which the controller can operate. The highest input frequency at which the controller used in these experiments could converge was approximately $1k$Hz.

The first step to initialize the controller was to set the sampling rate. Here a multiple of the operating frequency was used for improved performance [1, 7]. If the sample frequency selected was too slow, the Nyquist criterion may be violated. On the other hand, if the sampling frequency was too fast, consecutive data points may be close enough that digital round off error became significant and caused phase errors to develop. For these reasons a sampling rate of eight times the operating frequency was selected.

The next step to initialize the controller was to set the convergence parameter [μ]. If too low of a convergence parameter is selected then the performance of the controller is slow and not as good as it could be. Too high of a convergence parameter and the system will be unstable.

The process of selecting an appropriate convergence parameter was iterative. The initial value was selected and then the controller was run and its performance evaluated. The convergence parameter was then adjusted and the controller was applied again. After a few attempts, the optimal convergence parameter was found.

The final step to initialize the controller was to measure the filtered-x transfer functions. This was accomplished by a sub-program within the driving program. With the input disturbance turned off the reference signal was used to drive the control

actuator. The secondary LMS algorithm (as described in Sec. 2.2.2) then converged on the transfer function(s) between the control actuator(s) and the error microphone signal(s) which was used as the estimates for the fixed, pre-filter value(s) ($\hat{P}_{mn}$).

With the estimates of the pre-filter values, the convergence parameter and sample rate set the controller was ready to operate.

2.3 Experimental Procedure

The experimental procedure had four basic steps, each of which is described below.

1. **Initialize the controller.** This step was done as described in the previous section. Once the levels of the input signal were set, the sample rate and convergence parameter were determined and then the filtered-x transfer functions were measured. Then the controller was turned on to ensure that it was operating properly. At this point special care was taken to ensure that the error signals did not exceed the input maximum of the DSP board. The control signals sent to the control actuators were closely monitored to be sure that the actuators were not overloaded.

2. **Collect microphone and accelerometer data before control.** With the controller deactivated, autospectrum data was collected from the perpendicular and axial microphone signals. Then the reference accelerometer signal autospectrum was measured followed by the transfer functions between the reference and all of the switching box accelerometers. This data provided a basis from which to quantify the effect of control on the acoustic field and

beam vibration. All of the signal processing in this step was performed on a Bruel & Kjaer model 2032 dual channel spectrum analyzer.

3. **Control implementation.** Next the controller was started and converged towards the optimal weighting coefficients for the minimization of the error signal.

4. **Collect microphone and accelerometer data after control.** Once again autospectrum data was collected from the perpendicular and axial microphone signals. Accelerometer data was also collected as in step 2. This data served to quantify the acoustic control performance and the change in the beams vibrational characteristics while under control. This data was also collected using the Bruel & Kjaer signal analyzer.

Numerous experiments were performed on both the semi-infinite/clamped beam and the infinite beam with a blocking mass. Several variables were examined in the experiments as listed below:

- **Frequency:** Three subsonic frequencies were used. These were 320 Hz, 510 Hz and 690 Hz. These frequencies were selected for several reasons:

  1. To avoid 60 Hz noise and its harmonics.
  2. To exploit good performance frequencies for the anechoic terminations.
  3. To exploit good performance frequencies for the control algorithm.

- **Error Microphone Locations:** The error microphone locations used in single actuator experiments were close to 45° axial, 45° perpendicular, and

90°. This allowed for the comparison of error microphone location at several points throughout the acoustic field. For experiments employing two control actuators two error microphones were required. These were located close to 45° and 135° perpendicular and 45° and 135° axially. The actual locations of these microphones was measured at 51.4°, 128.6° and 90° on the microphone array.

- **Actuator Type:** Two types of actuators were used; the point force shaker and the line moment piezoelectric actuator.

- **Actuator Location:** For the semi-infinite/clamped beam two actuator locations were used. These were $3.81cm$ and $13.97cm$ (measured from the edge of the clamp). In the case of the infinite beam the actuators were located at $-5.715cm$, $-17.145cm$ and $2.54cm$ (measured from the center of the blocking mass, positive was toward the input shaker). The shakers were attached at these points while the piezoelectric patches were centered about these points (as shown in Figs 2.14, 2.15, 2.16 and 2.17). These locations allowed a comparison to be made between control actuators located near the discontinuity with those farther away.

- **Blocking Mass Size:** In the case of the infinite beam with a blocking mass, two different blocking masses were used (see Table 2.2). One was $1288g$ while the other was $675g$. This allowed comparisons to be made between two blocking masses of different size.

Results from some of these experiments are presented in Ch. 4. While the results from all of the experiments are not presented, enough are discussed to allow an

examination of the effects of the previously listed variables. The results presented are also representative of the behavior seen in all of the experiments.

Chapter 3

Beam Displacement Decomposition and the Spatial Fourier Transform

In order to explain the mechanism by which active control of the acoustic field was accomplished, the changes in the beam vibration characteristics had to be investigated. From the beam vibration equations a spatial Fourier transform was employed to show how changes in the beam vibration affected acoustic control. This chapter discusses the decomposition of the complex wave amplitudes in the beam displacement equations and the associated spatial Fourier transforms applied to these equations.

3.1 Beam Displacement Decomposition

In order to study the changes in beam vibration characteristics with and without control, the complex coefficients of the displacement equation for the beam had to be determined. This was accomplished by taking acceleration data from an array of

accelerometers (as described in Ch. 2). This acceleration data was used to decompose the unknown, complex amplitudes in an assumed displacement equation by means of a least mean square regression method. This section presents the assumed displacement equations and unknown, complex wave amplitude decomposition for both the semi-infinite/clamped beam and the infinite beam with a blocking mass.

3.1.1 Semi-infinite/Clamped Beam

Assumed Equation of Motion

For the case of the semi-infinite/clamped beam five basic wave types were assumed to be present in the beam displacement as follows:

- **Incident traveling wave**: This wave was generated by the input shaker. It had the form of a traveling bending wave.
- **Reflected near-field wave**: This wave was created by the clamped discontinuity. It took the form of a reflected, decaying, exponential near-field.
- **Reflected traveling wave**: This wave was reflected by the clamped discontinuity in the form of a traveling bending wave.
- **Controller near-field wave**: This was a decaying near-field wave created by the control force (or moment) which was symmetric about the application point of the control force (or moment).
- **Controller traveling wave**: This wave was created by the control force (or moment) and was also symmetric about the application point of the control force (or moment). It took the form of a traveling bending wave.

Figure 3.1 shows these waves and their sources schematically.

Combining these waves into an expression, the assumed equation of motion for a semi-infinite/clamped beam with point force control is:

$$z(x) = Ae^{ik_b x} + Be^{-k_b|x-\alpha|} + Ce^{ik_b|x-\alpha|} + De^{-k_b x} + Ee^{-ik_b x} \tag{3.1}$$

Where $z(x)$ is the beam displacement at x, the coordinate along the beam, i is equal to the square root of negative one ($\sqrt{-1}$), k_b is the structural wave number, α is the location of application of the control force and the unknown, complex amplitudes are as follows:

$A \cong$ incident traveling wave

$B \cong$ controller decaying near-field wave

$C \cong$ controller traveling wave

$D \cong$ reflected decaying near-field wave

$E \cong$ reflected traveling wave

Similarly, the assumed equation of motion for a semi-infinite/clamped beam with piezoelectric actuator control is:

$$\begin{aligned} z(x) \;=\; & Ae^{ik_b x} + B\left[e^{-k_b|x-\alpha|} - e^{-k_b|x-(\alpha+l)|}\right] + C\left[e^{ik_b|x-\alpha|} - e^{ik_b|x-(\alpha+l)|}\right] \\ & + De^{-k_b x} + Ee^{-ik_b x} \end{aligned} \tag{3.2}$$

$$\tag{3.3}$$

where α is the location of one end of the piezoelectric actuator whose length is l.

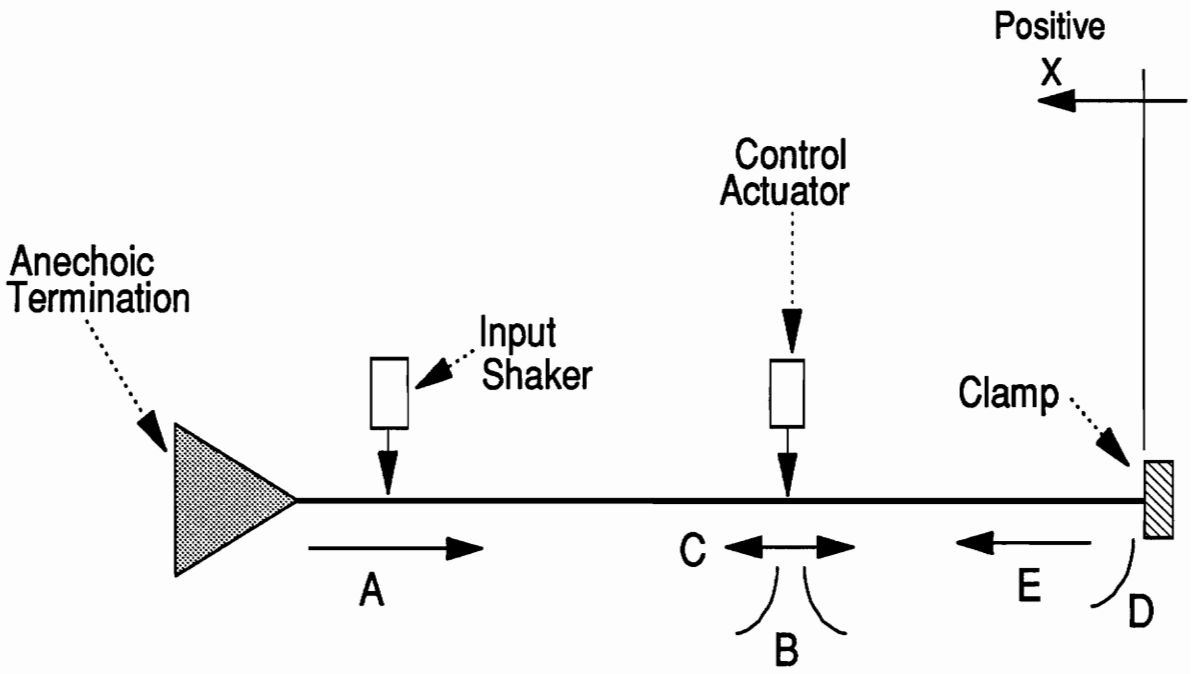

Figure 3.1: Assumed waves present in the semi-infinite/clamped beam. A=incident traveling wave, B=controller decaying near-field wave, C=controller traveling wave, D=reflected near-field wave, E=reflected traveling wave.

Note that in Eq. 3.2 the assumed to be moments exerted at each end of the piezoelectric patch are of equal magnitude but opposite sign. This is because a pair of piezoelectric patches, operating opposite each other and 180° out of phase produce two line moments, at either end of the patch pair, that are of equal magnitude and in the opposite direction. This is proven by Crawley et al. in [19].

Note that the near field component of the input shaker is not considered. This is because the accelerometer array was far enough away from the input shaker for the near-field wave to be negligible. This assumption was also made in the infinite beam with a blocking mass experiments.

Equations 3.1 and 3.2 represent the assumed displacement equation for the semi-infinite/clamped beam with one point force and one piezoelectric control actuator respectively. If two controllers were used (shaker or piezoelectric) a second set of controller waves (both near-field and traveling) were added to the displacement equation at the appropriate point of application.

When decomposing the complex amplitudes in the beam displacement equation before control, only the three waves (incident, reflected travelling, and reflected near-field) not produced by the control actuators were considered. This is equivalent to saying that, when the control actuators were not in use they produced no near-field or traveling waves and, therefore, were not considered.

Least Square Curve Fit

In order to find the unknown, complex amplitudes for the displacement equation a set of dependent equations had to be solved. Since ten accelerometers were used and

there were only three, five or seven complex amplitudes (depending on the number of control actuators) to calculate, the system of equations was over-determined. Therefore a least mean square regression method was used to decompose these complex amplitudes. By using a least square regression method the error in the complex amplitudes, due to accelerometer measurement error, was minimized.

With ten data points, ten equations (of the form in Eq. 3.1) could be written (one for each data point). The method of least mean squares was applied to this set of ten equations to calculate the complex amplitudes. This method, as described by Draper and Smith [21], is derived below, in matrix form, for the semi-infinite/clamped beam with one point force controller .

Let

$$Y = \begin{bmatrix} z_1(x_1) \\ \vdots \\ z_n(x_n) \end{bmatrix}, \tag{3.4}$$

$$X = \begin{bmatrix} X_1^a & X_1^b & X_1^c & X_1^d & X_1^e \\ \vdots & \vdots & \vdots & \vdots & \vdots \\ X_n^a & X_n^b & X_n^c & X_n^d & X_n^e \end{bmatrix} \tag{3.5}$$

where

$$\begin{aligned} X_i^a &= e^{ik_b x_i} \\ X_i^b &= e^{-k_b|x_i-\alpha|} \\ X_i^c &= e^{ik_b|x_i-\alpha|} \\ X_i^d &= e^{-k_b x_i} \\ X_i^e &= e^{-ik_b x_i} \end{aligned} \tag{3.6}$$

and

$$U = \begin{bmatrix} A \\ B \\ C \\ D \\ E \end{bmatrix}. \tag{3.7}$$

In the above equations z_i is the displacement measured at x_i and n is the number of data points.

From these definitions we can write the set of n linear equations in matrix form as:

$$XU = Y \tag{3.8}$$

Pre-multiplying each side by X^T we get the least square equation as:

$$X^T XU = X^T Y \tag{3.9}$$

Solving for the unknown coefficients we get:

$$U = (X^T X)^{-1} X^T Y \tag{3.10}$$

Equation 3.10 was derived assuming one point force controller. These equations can easily be expanded to accommodate more control forces or moments.

A computer program using Eq. 3.10 was written to solve for the unknown, complex amplitudes. This program is listed in App. B and the results of the program are presented in Ch. 4.

3.1.2 Infinite Beam with Blocking Mass

Assumed Equation of Motion

For the case of the infinite beam with a blocking mass seven basic wave types were assumed to be present in the beam displacement as follows:

- **Incident traveling wave:** This wave was generated by the input shaker. It had the form of a traveling bending wave.
- **Reflected near-field wave:** This wave was created by the blocking mass discontinuity. It took the form of a reflected, decaying, exponential near-field.
- **Reflected traveling wave:** This wave was reflected by the blocking mass discontinuity in the form of a traveling bending wave.
- **Transmitted near-field wave:** This wave was transmitted through the blocking mass in the form of a decaying exponential, near-field wave.
- **Transmitted traveling wave:** This wave was transmitted through the blocking mass. It took the form of a traveling bending wave.
- **Controller near-field wave:** This was a decaying near-field wave created by the control force (or moment) which was symmetric about the application point of the control force (or moment).
- **Controller traveling wave:** This wave was created by the control force (or moment) and was also symmetric about the application point of the control force (or moment). It took the form of a traveling bending wave.

Figure 3.2 shows these waves and their sources schematically.

Combining these waves into an expression the following equations are obtained.

For $x > 0$:

$$z(x) = Ae^{ik_b x} + Be^{-k_b x} + Ce^{-ik_b x} \tag{3.11}$$

and for $x < 0$:

$$z(x) = De^{k_b x} + Ee^{ik_b x} + Fe^{-k_b|x-\alpha|} + Ge^{ik_b|x-\alpha|} \tag{3.12}$$

The unknown, imaginary coefficients are as follows:

$A \cong$ incident traveling wave

$B \cong$ reflected decaying near field wave

$C \cong$ reflected traveling wave

$D \cong$ transmitted decaying near field wave

$E \cong$ transmitted traveling wave

$F \cong$ controller decaying near field wave

$G \cong$ controller traveling wave

Equations 3.11 and 3.12 describe the displacement of the infinite beam with a blocking mass and a point force control actuator located at $\alpha < 0$. If more control actuators are used, terms can be added to the equations to accommodate them as

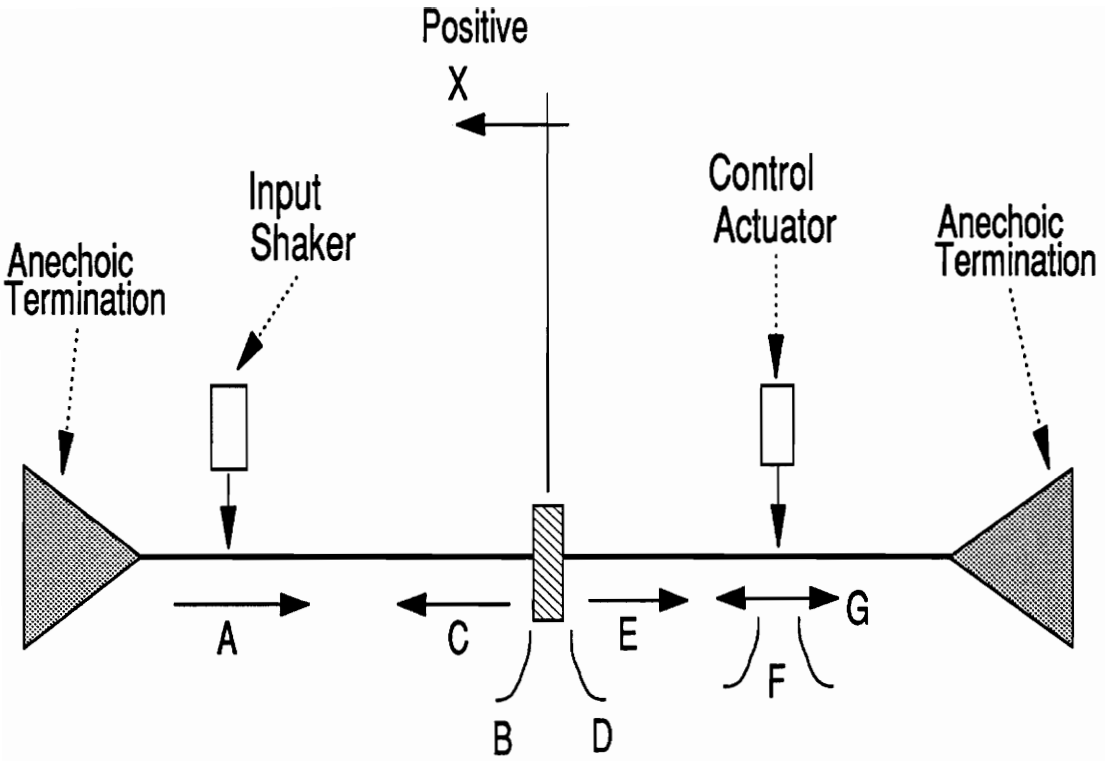

Figure 3.2: Assumed waves present in the infinite beam with a blocking mass. A=incident traveling wave, B=reflected decaying near-field wave, C=reflected traveling wave, D=transmitted near-field wave, E=transmitted traveling wave, F=controller decaying, near-field wave, G=controller traveling wave.

described previously. Also, if the control actuator is located such that $\alpha > 0$ the terms for the controller waves can be added to the equation defined for $x > 0$.

For the infinite beam with a blocking mass and one piezoelectric actuator located in the region $\alpha > 0$ the assumed equation of motion is:

For $x > 0$:

$$\begin{aligned} z(x) &= Ae^{ik_b x} + Be^{-k_b x} + Ce^{-ik_b x} + F\left[e^{-k_b|x-\alpha|} - e^{-k_b|x-(\alpha+l)|}\right] \\ &\quad + G\left[e^{ik_b|x-\alpha|} - e^{ik_b|x-(\alpha+l)|}\right] \end{aligned} \tag{3.13}$$

$$\tag{3.14}$$

and for $x < 0$:

$$z(x) = De^{k_b x} + Ee^{ik_b x} \tag{3.15}$$

Least Square Curve Fit

With ten data points, ten equations (of the form in Eqs. 3.11 & 3.15) could be written. The method of least mean squares was applied to this set of ten equations to calculate the unknown, complex amplitudes. By using the least mean square method the error in the complex amplitudes was minimized.

Similar to the semi-infinite/clamped beam case, the least square method is defined below in matrix form for the infinite beam with a blocking mass and one point force controller.

If we let

$$Y^+ = \begin{bmatrix} z_1^+(x_1^+) \\ \vdots \\ z_n^+(x_n^+) \end{bmatrix}, \tag{3.16}$$

$$X^+ = \begin{bmatrix} X_1^a & X_1^b & X_1^c \\ \vdots & \vdots & \vdots \\ X_n^a & X_n^b & X_n^c \end{bmatrix} \tag{3.17}$$

where

$$\begin{aligned} X_i^a &= e^{ik_b x_i} \\ X_i^b &= e^{-k_b x_i} \\ X_i^c &= e^{-ik_b x_i} \end{aligned} \tag{3.18}$$

and

$$U^+ = \begin{bmatrix} A \\ B \\ C \end{bmatrix}. \tag{3.19}$$

In the above equations z_i is the displacement measured at x_i and n is the number of data points located in the region of $x > 0$. In addition, the superscript $(+)$ corresponds to the function defined for $x > 0$.

From these definitions we can write the set of n linear equations in matrix form as:

$$X^+U^+ = Y^+ \tag{3.20}$$

Pre-multiplying each side by $(X^+)^T$ we get the least square equation as:

$$(X^+)^T X^+ U^+ = (X^+)^T Y^+ \tag{3.21}$$

Solving for the unknown coefficients we get:

$$U^+ = [(X^+)^T X^+]^{-1}(X^+)^T Y^+ \tag{3.22}$$

Similarly, for the region of $x < 0$ (denoted by th superscript $(-)$), the equations can be defined as:

$$Y^- = \begin{bmatrix} z_1^-(x_1^-) \\ \vdots \\ z_m^-(x_m^-) \end{bmatrix}, \tag{3.23}$$

$$X^- = \begin{bmatrix} X_1^d & X_1^e & X_1^f & X_1^g \\ \vdots & \vdots & \vdots & \vdots \\ X_m^d & X_m^e & X_m^f & X_m^g \end{bmatrix} \tag{3.24}$$

where

$$\begin{aligned} X_i^d &= e^{k_b x_i} \\ X_i^e &= e^{ik_b x_i} \\ X_i^f &= e^{-k_b|x_i-\alpha|} \\ X_i^g &= e^{ik_b|x_i-\alpha|} \end{aligned} \tag{3.25}$$

and

$$U^- = \begin{bmatrix} D \\ E \\ F \\ G \end{bmatrix}. \tag{3.26}$$

In the above equations z_i is the displacement measured at x_i and m is the number of data points located at $x < 0$.

From these definitions we can write the set of m linear equations in matrix form as:

$$X^- U^- = Y^- \tag{3.27}$$

Pre-multiplying each side by $(X^-)^T$ we get the least square equation as:

$$(X^-)^T X^- U^- = (X^-)^T Y^- \tag{3.28}$$

Solving for the unknown coefficients we get:

$$U^- = [(X^-)^T X^-]^{-1} (X^-)^T Y^- \tag{3.29}$$

Since the regions of $x > 0$ and $x < 0$ are defined independently, the computation of their respective coefficients is performed independently. A computer program was written to perform these calculations and is listed in App. B. The results of these computations is presented in Ch. 4.

3.2 Spatial Fourier Transform (Wavenumber Domain) of Beam Velocity Response

The mechanism by which the active control of the acoustic far-field is manifested can best be described in terms of the wavenumber domain. By employing a spatial Fourier transform, the beam velocity function can be transformed from the Cartesian domain into the wavenumber domain. A good discussion of this topic and a development of the theory is presented by Keltie [13]. This section describes the spatial fourier transforms for both the semi-infinite/clamped beam and the infinite beam with a blocking mass.

The spatial Fourier transform is similar to the time based Fourier transform. The difference is that while the time based Fourier transform maps time based functions into the frequency spectrum, the spatial Fourier transform maps spatially

based functions into the wavenumber domain. As the fourier transform shows those frequencies present in a time signal, the spatial fourier transform shows those wavelengths present in a space function (since $k = 2\pi/\lambda$). This is important from a structural acoustics stand point because only those structural wavenumber components less than the wavenumber in the acoustic medium ($|k| < k_o$) are responsible for acoustic radiation [11].

Since in the case of the clamped beam the function is defined only for $x > 0$ and in the case of the beam with a blocking mass the function is split into regions of $x > 0$ and $x < 0$, the integral to be performed is only semi-infinite. This was accomplished by using the definition in Eq. 1.36 .

However, when considering subsonic waves, the Dirac delta functions contribute nothing to the supersonic wavenumber components [13]. This is because the Dirac delta function, as applied to these equations, is only defined for $k = \pm k_b$ where it approaches infinity. Since the structural wavenumber in all of these experiments is subsonic, no contribution is made to the supersonic wavenumber region by the delta functions. Because we are most interested in the supersonic region of the wavenumber spectrum since a plot approaching infinity is not practical, these terms are discarded in the presentation of the spatial fourier transform of the velocity distributions discussed below.

3.2.1 Semi-infinite/Clamped Beam

By applying Eqs. 1.31 & 1.36 to Eq. 3.1 the following equation for the velocity spatial fourier transform of the semi-infinite/clamped beam can be obtained.

$$\begin{aligned} V(k) &= A\left[\frac{i}{k_b+k}\right]+B\left[\frac{e^{ik\alpha}-e^{-k_b\alpha}}{k_b+ik}+\frac{ie^{k_b\alpha}}{k+ik_b}-\frac{e^{ik\alpha}-e^{k_b\alpha}}{ik-k_b}\right] \\ &\quad +C\left[\frac{e^{ik\alpha}-e^{ik_b\alpha}}{i(k-k_b)}+\frac{ie^{-ik_b\alpha}}{k+k_b}-\frac{e^{ik\alpha}-e^{-ik_b\alpha}}{i(k+k_b)}\right] \\ &\quad +D\left[\frac{i}{ik_b+k}\right]+E\left[\frac{i}{k-k_b}\right] \end{aligned} \tag{3.30}$$

3.2.2 Infinite Beam with Blocking Mass

Similarly, by applying Eqs. 1.31 & 1.36 to Eqs. 3.11 & 3.12 the following equation for the velocity spatial fourier transform of the infinite beam with a blocking mass can be obtained.

$$\begin{aligned} V(k) &= A\left[\frac{i}{k_b+k}\right]+B\left[\frac{i}{ik_b+k}\right]+C\left[\frac{i}{k-k_b}\right]+D\left[\frac{i}{ik_b+k}\right]-E\left[\frac{i}{k+k_b}\right] \\ &\quad +F\left[\frac{e^{-ik\alpha}-e^{k_b\alpha}}{-k_b-ik}-\frac{ie^{-k_b\alpha}}{k+ik_b}+\frac{e^{-ik\alpha}-e^{-k_b\alpha}}{ik-k_b}\right] \\ &\quad +G\left[\frac{e^{-ik\alpha}-e^{-ik_b\alpha}}{i(k_b-k)}-\frac{ie^{ik_b\alpha}}{k+k_b}+\frac{e^{-ik\alpha}-e^{ik_b\alpha}}{i(k+k_b)}\right] \end{aligned} \tag{3.31}$$

These equations were used to calculate the spatial Fourier transform of the velocity distribution obtained by decomposing the unknown, complex amplitudes of the displacement equation. The results of these calculations are presented in Ch. 4.

Chapter 4

Experimental Results

In this chapter the results form both the semi-infinite/clamped beam and infinite beam blocking mass experiments are presented. Several experimental variables are discussed and compared as follows:

- **Actuator location:** The effect of various actuator locations were compared.
- **Number of actuators:** The effects of employing one and two control actuators were compared.
- **Actuator type:** The differences in point force shaker control and line moment piezoelectric actuator control were compared.
- **Error microphone location:** The effects of various microphone locations were compared.
- **Number of error microphones:** A comparison of the number of error microphones used was made.
- **Frequency:** The system behavior was compared for various frequencies.

- **Blocking mass size comparison:** The effect of different sized blocking masses was discussed for the infinite beam experimental case.

For each experimental case presented there are four corresponding plots. Two plots from the perpendicular and axial microphone arrays before and after control are presented together in one figure. The second figure for each experimental case contains a plot of the beam displacement before and after control, calculated from the decomposed complex amplitudes discussed in Ch. 3. This is presented in the same figure with the velocity wavenumber spectrum calculated from the decomposed displacement equation using the spatial fourier transform (Eq. 1.31) before and after control. The wavenumber spectrum of the beam velocity (as opposed to the wavenumber spectrum of the displacement) is shown for comparison with theoretical results produced by Guigou [16]. This differs from the wavenumber spectrum of the displacement by a factor of $-i\omega$ since the time dependent part of the displacement is assumed to be harmonic. Each of the wavenumber spectrum plots have two vertical lines which define the region of supersonic wavenumber components. The wavenumber spectrum amplitudes are presented in dB referenced to 1.

In the discussion for each experimental case presented several common points are discussed which require some clarification. First the attenuation at the error microphone(s) is stated. This value is the difference (in dB re $20\mu Pa$) between the error microphone sound pressure level measured before control and after control. Following this a statement is made which quantifies the global acoustic attenuation (or the attenuation throughout the acoustic field). The global acoustic attenuation is a dB value which represents the average attenuation achieved throughout the acoustic field. This value is a qualitative estimate of the mean attenuation throughout

the acoustic field. It was obtained by visual inspection of the data and estimated based on this observation. If the average attenuation in the perpendicular and axial arrays was significantly different, the estimate of the average attenuation in each array is stated independently. These estimates of the average global attenuation are provided solely as a means of comparing one experimental case to another.

The location of the error microphone(s) are also provided with the discussion of each experimental case. These locations are given in terms of the microphones angular location in a particular array (perpendicular or axial) as identified in Figs. 2.11 and 2.12 and in Table 2.3.

Following the discussion of the acoustic field a description of the decomposed displacement and wavenumber spectrum is given. Here a description of the standing wave amplitude is provided. This describes the general change in the amplitude of the standing wave present in the beam displacement away from the effects of the flexural near-field. Along with this a general description of the behavior in the supersonic region of the wavenumber spectrum is given.

In addition to the many experimental cases presented in this chapter, a few theoretical cases developed by Guigou [16] are presented. These are discussed in order to demonstrate that the trends of the experimental cases agree with those predicted by theory.

4.1 Semi-infinite Clamped Beam

This section presents experimental results from the semi-infinite/clamped beam experiments described in Ch. 2 and shown schematically in Fig. 2.1 and photographically in Fig. 2.3. The actuators are referred to by number (#1 and #2) the locations of which are shown in Figs. 2.14 and 2.16.

4.1.1 Actuator Location Comparison

Figure 4.1 shows the acoustic field for the semi-infinite/clamped beam driven at 510Hz, controlled by point force shaker #1, and with an error microphone located at 51.4° on the axial array. The corresponding displacement and wavenumber spectrum are shown in Fig. 4.2. In this experimental case, an acoustic attenuation at the error microphone of $36dB$ was achieved. On a global scale the acoustic levels were attenuated by roughly $8dB$.

Fig 4.2 shows an increase in the standing wave amplitude of the beam as well as a decrease in the supersonic wavenumber region while under control. This behavior (increasing standing wave amplitude with decreasing supersonic wavenumber components) is consistent with the other experimental cases of the semi-infinite/clamped beam with point force control discussed in this thesis. The decrease in supersonic wavenumber components implies that, while attenuating the acoustic levels in the near-field (more precisely not in the far-field as previously discussed), the far-field acoustic levels are attenuated as well (see Eq. 1.18).

This behavior (decreasing supersonic wavenumber components while attenuating the

(a)

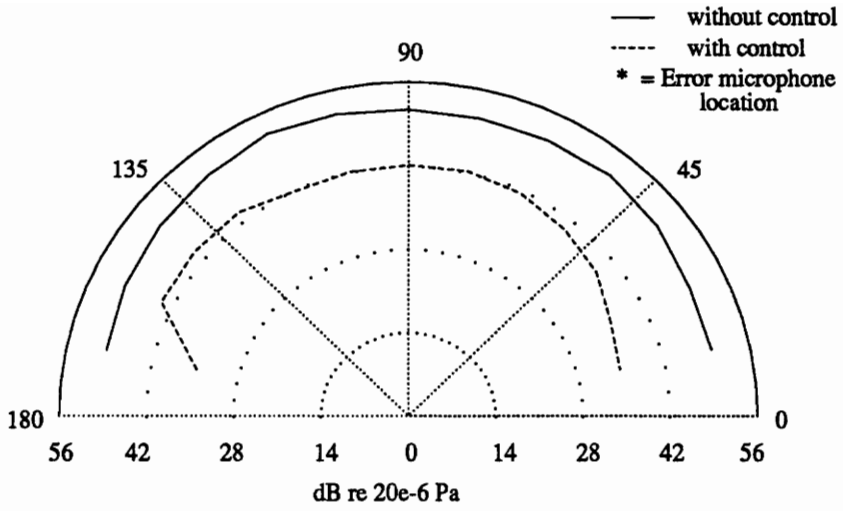

(b)

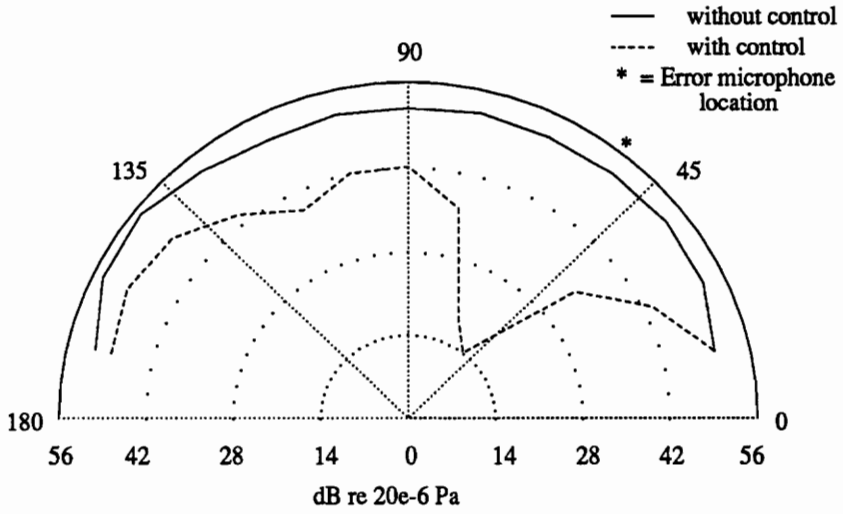

Figure 4.1: Semi-infinite/clamped beam acoustic field, 510Hz, shaker controller #1, error microphone 51.4° axial. (*a*) perpendicular microphone array data, (*b*) axial microphone array data.

(a)

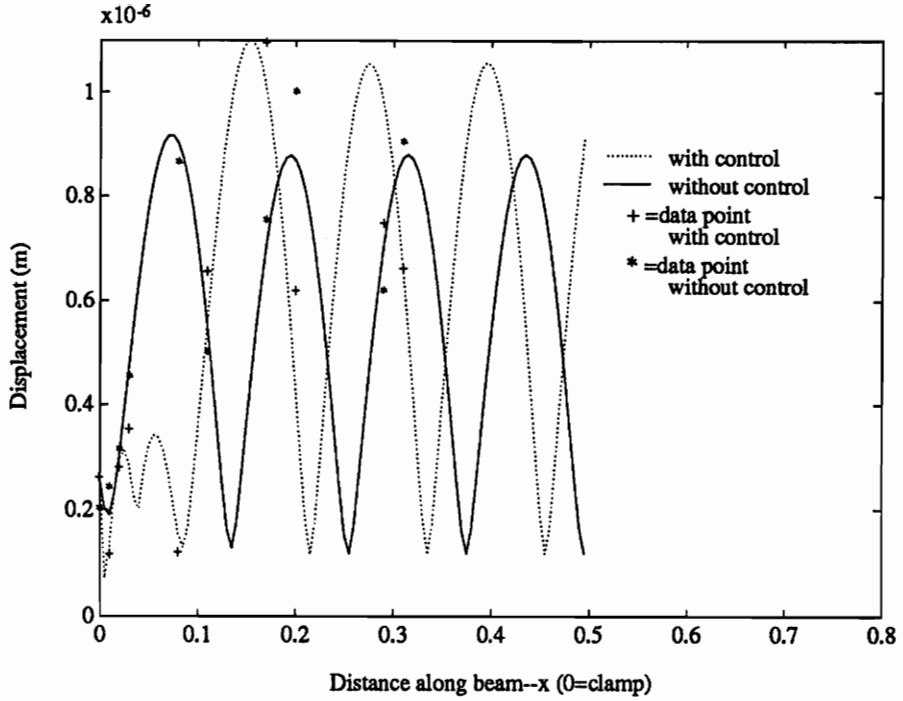

(b)

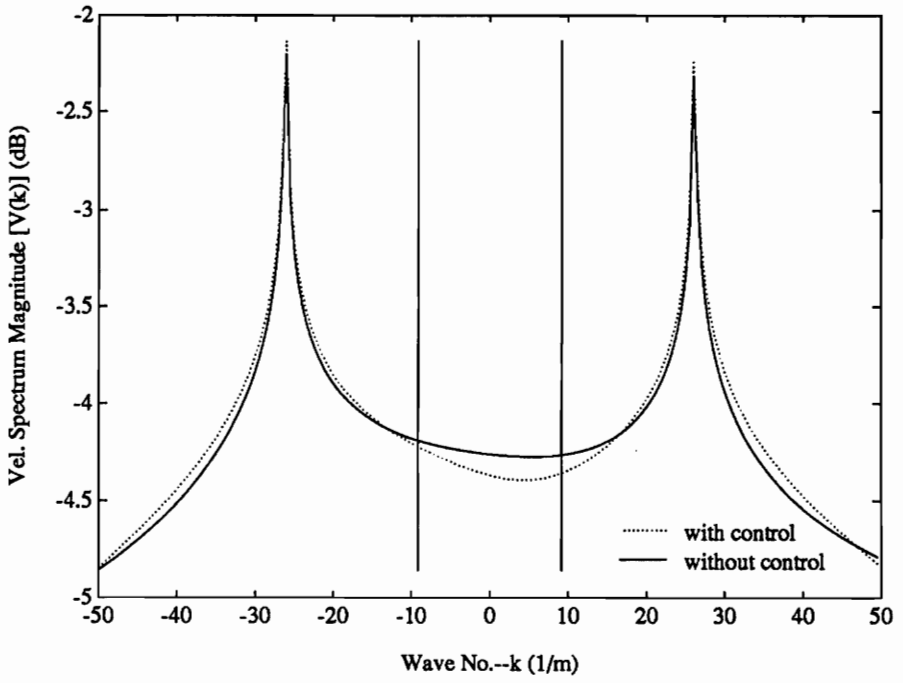

Figure 4.2: Semi-infinite/clamped beam, 510Hz, shaker controller #1, error microphone 51.4° axial. (*a*) decomposed displacement, (*b*) corresponding velocity wavenumber spectrum.

acoustic "near-field") is supported by theoretical results calculated by Guigou [16]. To produce these results the optimal control of the "near-field" acoustic radiation (using Eq. 1.24) at the error microphone (using the same geometry as was employed on the experimental rig) was calculated. From this the acoustic near-field (shown in Fig. 4.3), the beam displacement and the wavenumber spectrum (both shown in Fig. 4.4) were calculated (from Eqs. 1.24, 1.10 and 1.31 respectively). Then, using the prescribed displacement and wavenumber spectrum functions the acoustic far-field (shown in Fig. 4.5) was constructed from Eq. 1.18.

In general, the experimental results agree well with the results predicted by theory. In comparing the experimental acoustic field in Fig. 4.1 with the corresponding theoretical results in Fig. 4.3 the conclusion is drawn that the experiment behaved much like the theory predicted. The overall shape of the acoustic field is the same although the theory predicted better attenuation than was achieved by the experiment. This may be due to the noise floor associated with the error microphones employed in the array (about $8dB$). While the theory allowed the acoustic levels to be attenuated to zero, the experiment was limited by the noise floor.

Even with this limitation the general shape of the experimental acoustic field agreed very well with that predicted by theory. Both experiment and theory showed a constant attenuation throughout the perpendicular array and a large attenuation at the error microphone in the axial array.

Comparing the theoretical displacement and wavenumber spectrum with that obtained by experiment also shows similar behavior. While the supersonic regions of both the theoretical and experimental wavenumber spectra decrease, the standing wave amplitude in the experimental displacement increased under control while the

(a)

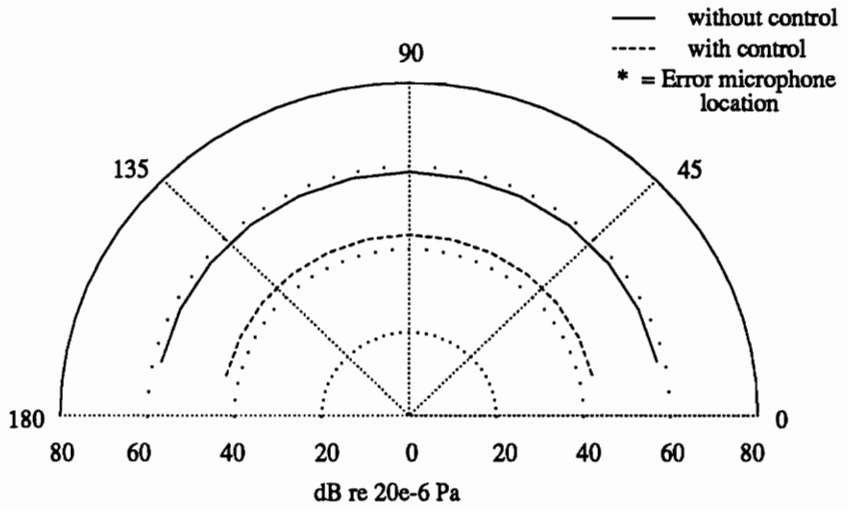

(b)

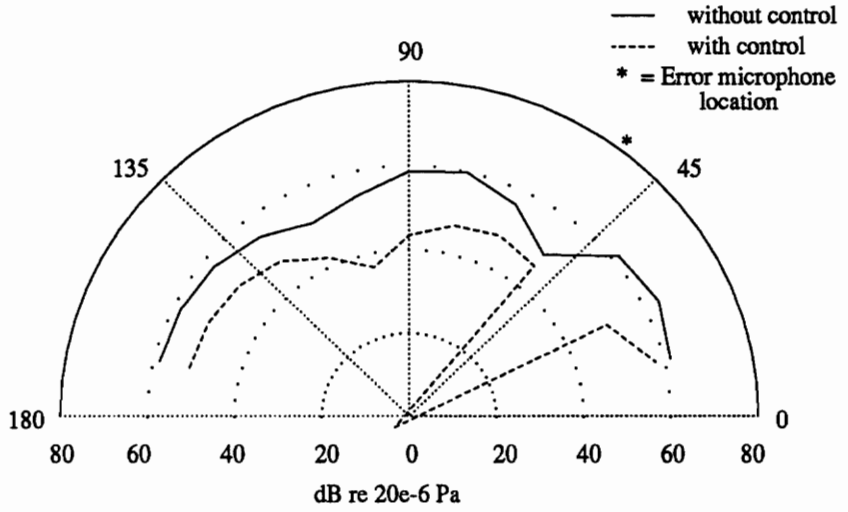

Figure 4.3: Semi-infinite/clamped beam theoretical acoustic "near-field", 510Hz, shaker controller #1, error microphone 51.4° axial. (*a*) perpendicular microphone array data, (*b*) axial microphone array data.

(a)

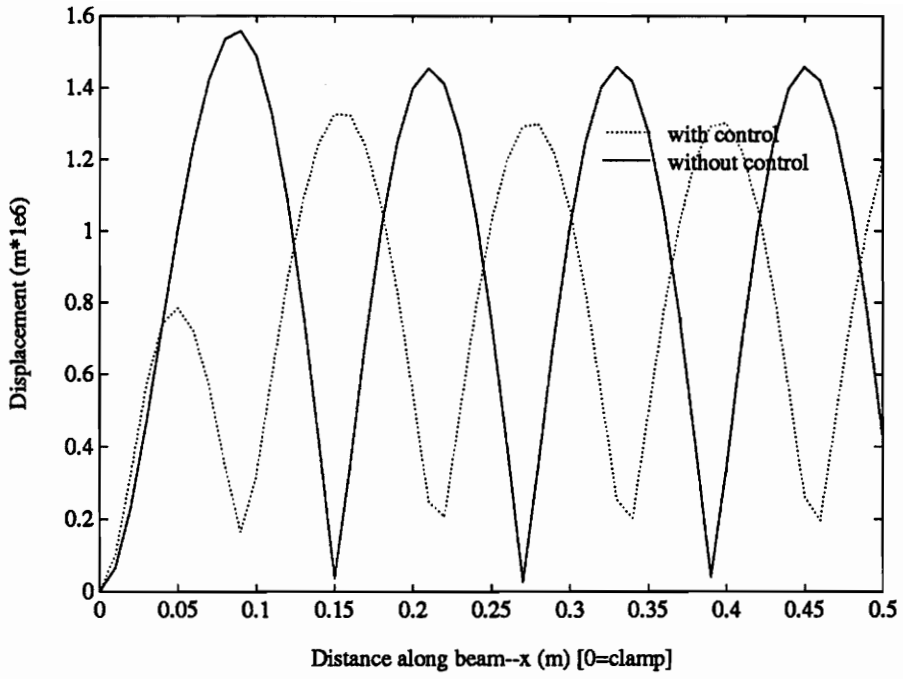

(b)

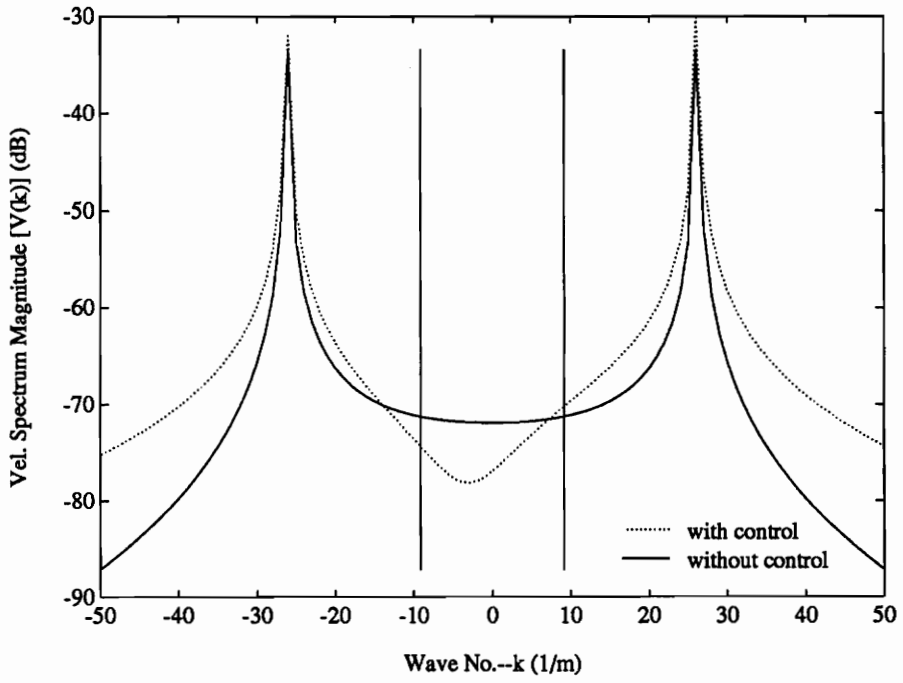

Figure 4.4: Semi-infinite/clamped beam theoretical data, 510Hz, shaker controller #1, error microphone 51.4° axial. (*a*) decomposed displacement, (*b*) corresponding velocity wavenumber spectrum.

(a)

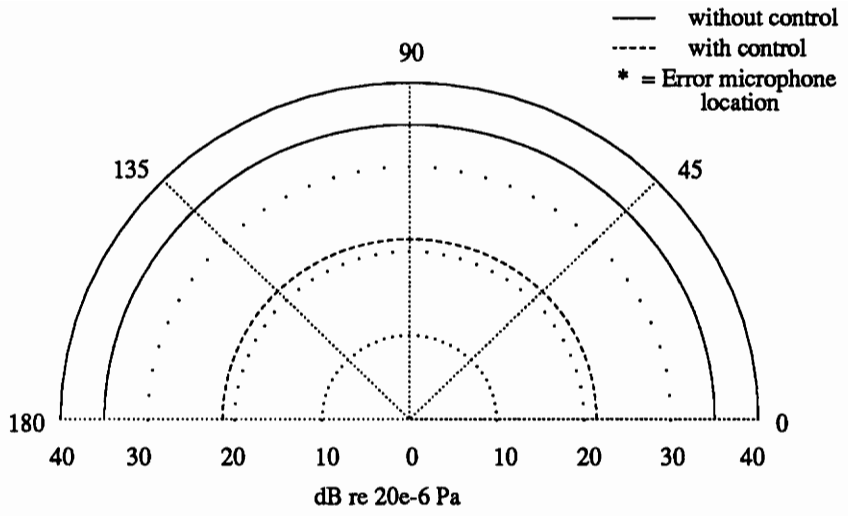

(b)

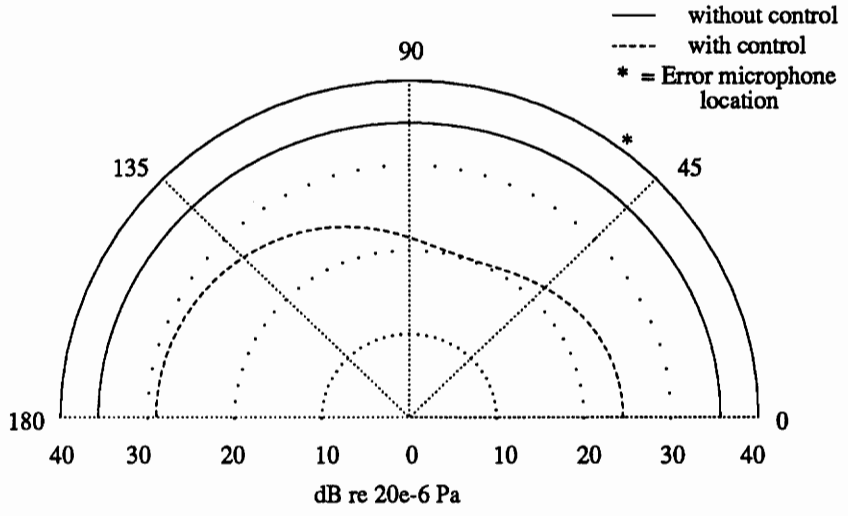

Figure 4.5: Semi-infinite/clamped beam theoretical acoustic far-field, 510Hz, shaker controller #1, error microphone 51.4° axial. (*a*) perpendicular microphone array data, (*b*) axial microphone array data.

opposite was predicted by theory. This was probably due to the imperfect nature of the clamped discontinuity used in the experiment compared to the perfect clamped discontinuity assumed in the theory and the error in the decomposition algorithm (discussed in App. A).

One further item to note in the comparison of the experiment and theory is the higher acoustic and vibrational levels predicted by theory. The theory assumed an input force of 1 Newton. During the experiments an attempt was made to keep the input force as close to 1 Newton as possible. Since no force transducer was available, the input force to the system was estimated from the voltage applied to the input shaker and a conversion factor supplied by the manufacturer. The author estimates that the actual input force to the system was less than the predicted input force due to estimation error and any inefficiencies in transmitting the force from the shaker to the beam. Therefore, it was expected that the acoustic and vibrational levels predicted by theory would be greater than those obtained by experiment. In addition, the losses associated with air slumping back and forth across the baffle (discussed in Ch. 2) would yield a lower acoustic level than predicted by theory (which assumed a perfect baffle).

Figures 4.6 and 4.7 show similar results for the experimental case driven at 510Hz, controlled by shaker #2, and with an error microphone located at 51.4° axially while Figs. 4.8 and 4.9 show a experimental case driven at the same frequency, but controlled by shakers #1 and #2 simultaneously with error microphones located at 51.4° and 128.6° axially.

For the experimental case where shaker #2 is used for control an attenuation of $47dB$ was achieved at the error microphone. This good performance at the error

(a)

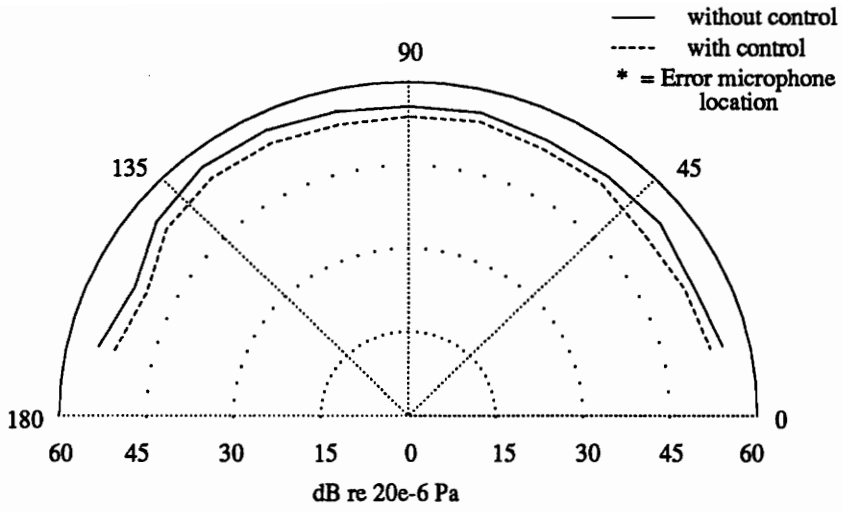

(b)

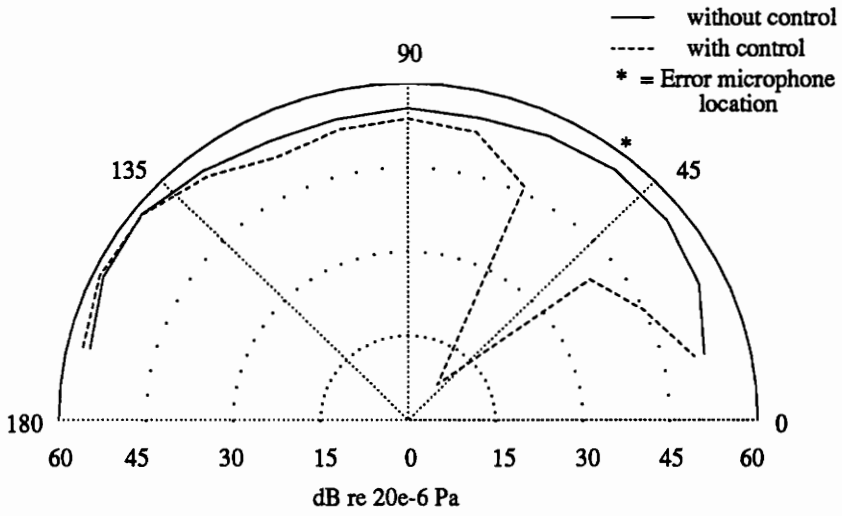

Figure 4.6: Semi-infinite/clamped beam acoustic field, 510Hz, shaker controller #2, error microphone 51.4° axial. (*a*) perpendicular microphone array data, (*b*) axial microphone array data.

(a)

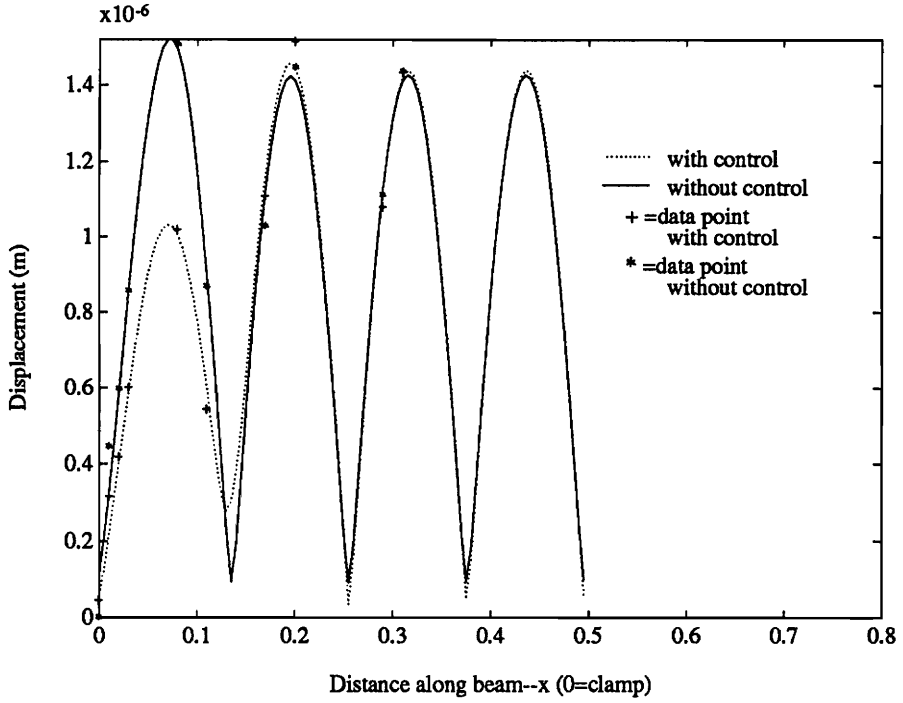

(b)

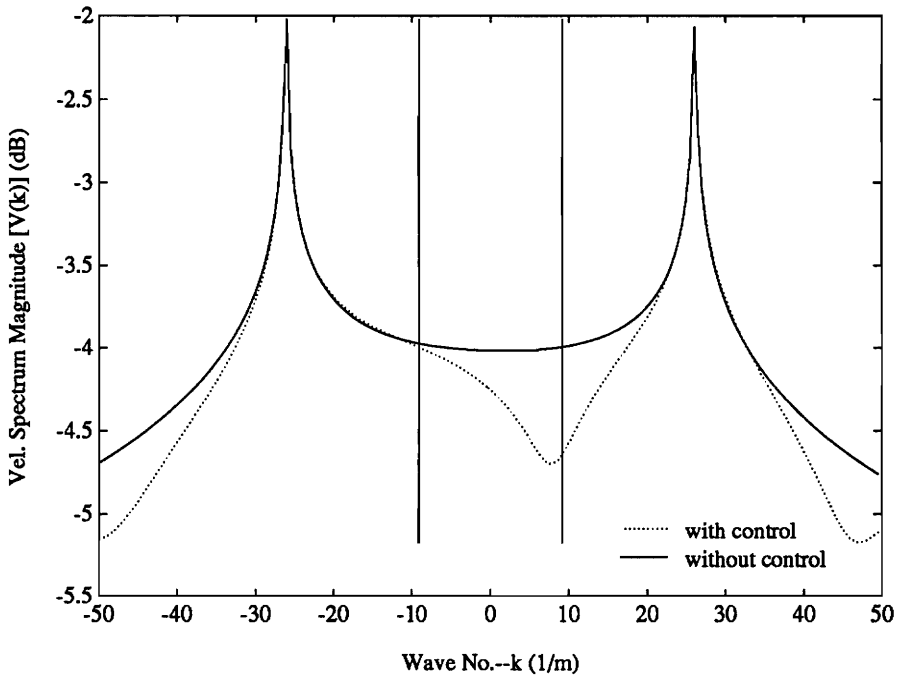

Figure 4.7: Semi-infinite/clamped beam, 510Hz, shaker controller #2, error microphone 51.4° axial. (*a*) decomposed displacement, (*b*) corresponding velocity wavenumber spectrum.

(a)

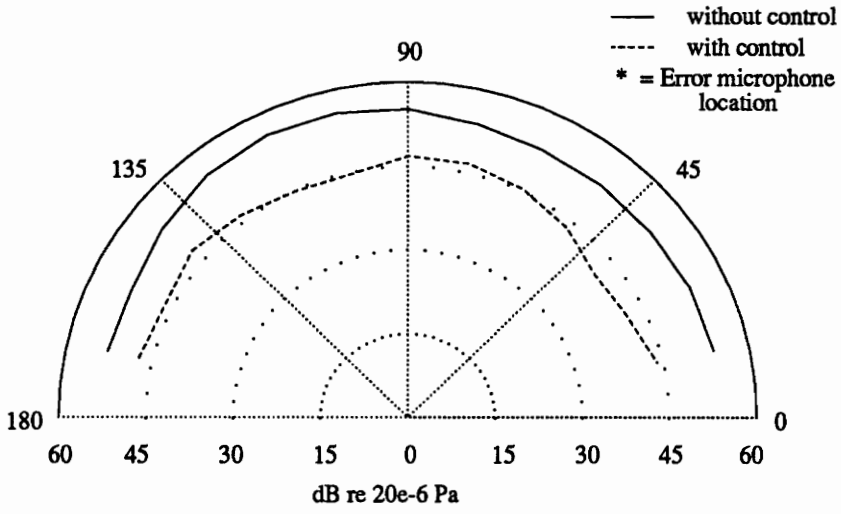

(b)

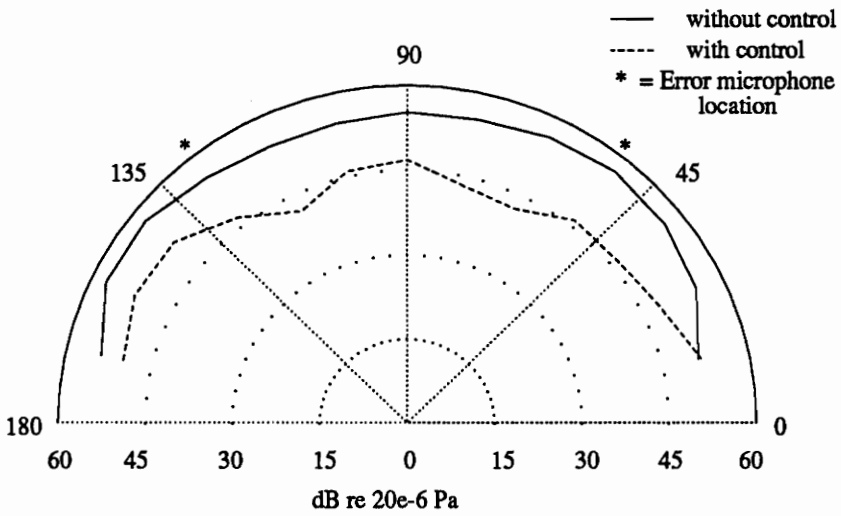

Figure 4.8: Semi-infinite/clamped beam acoustic field, 510Hz, shaker controllers #1 and #2, error microphones 51.4° and 128.6° axial. (*a*) perpendicular microphone array data, (*b*) axial microphone array data.

(a)

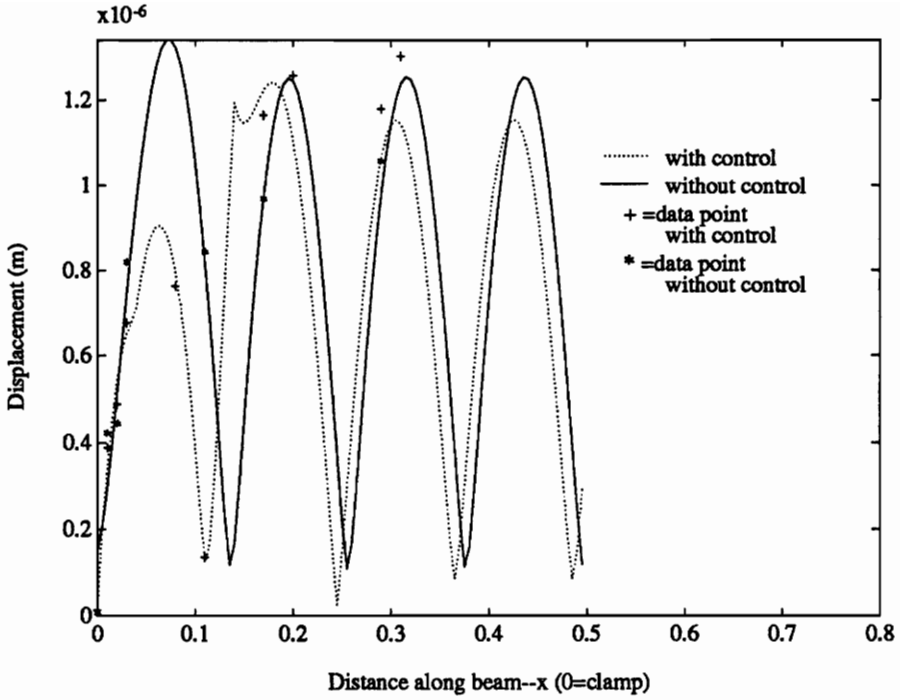

(b)

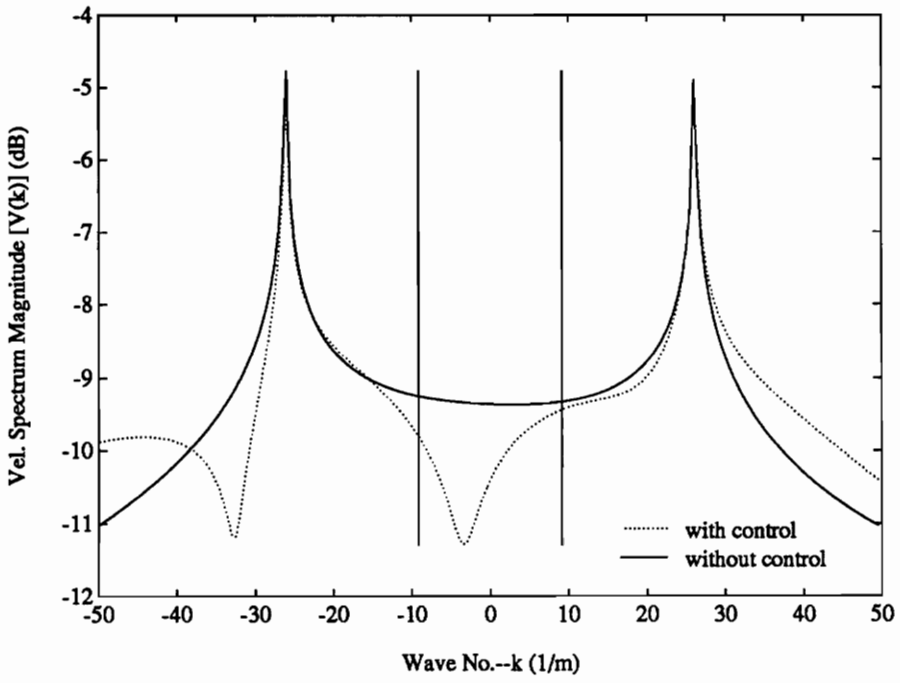

Figure 4.9: Semi-infinite/clamped beam, 510Hz, shaker controllers #1 and #2, error microphones 51.4° and 128.6° axial. (*a*) decomposed displacement, (*b*) corresponding velocity wavenumber spectrum.

microphone seems to be at the expense of global attenuation which was on the order of $3dB$. This was due to the fact that the controller has devoted all of its control authority to controlling a single point in the acoustic field. The fact that there was any global attenuation at all was just a benefit of the behavior of the system (since the controller did nothing to directly affect the global acoustic field, but only the acoustic level at the error microphone).

In the experimental case shown in Figs. 4.8 and 4.9 where both control shakers #1 and #2 were used simultaneously the attenuation at the error microphones was only $10dB$, however the global attenuation was much better (about $10dB$). This is due to the fact that the controller must optimize the control at both microphones which distributes the control over a broader range of the acoustic field, thus, attenuating over a larger area. In addition, one would expect the controller to operate more effectively with more control actuators since it has more degrees of freedom to achieve control. Extrapolating from this statement would imply that the more actuators (and error sensors) that are employed, the better the global attenuation would be.

In all of the previously discussed experimental cases the supersonic region of the wavenumber spectrum decreased under control. This implies that the far-field acoustic radiation was attenuated along with the "near-field" levels. In addition, the vibrational amplitude increased in the two experimental cases employing one control shaker while it decreased when two control actuators were used. This is due to the way in which the control actuator(s) affect the vibrational response of the beam. In the experimental cases employing one control actuator the waves present in the beam response were changed such that the standing wave amplitude increased due to

an increase in the reflected wave amplitude. At the same time the interaction of the flexural traveling wave and flexural near-field wave contributions to the supersonic region of the wavenumber spectrum were changed such that they decreased.

Comparing the effects of control on the acoustic fields shown in Fig. 4.1, 4.6 and 4.8 yield some interesting results. When one control shaker was employed, the best attenuation was achieved by shaker #1. This was due to the fact that shaker #1 was much closer to the clamped discontinuity (see Fig. 2.14) than shaker #2. This placed shaker #1 in a region more strongly influenced by the flexural near-field which allowed shaker #1 to affect the flexural near-field more directly. This, in turn, resulted in shaker #1 being more able to change the interaction of the supersonic components of the traveling wave and the near-field wave. Shaker #2, on the other hand, did not have as much control authority over the flexural near-field which made it less able to affect such a change. This topic is discussed more thoroughly in the frequency comparison section.

Finally, it was demonstrated that the best global attenuation was achieved when two control actuators were used. This was due to the more distributed nature of the error sensors (as discussed earlier).

4.1.2 Error Microphone Location Comparison

Figures 4.10 and 4.11 show the results for the experimental case of the semi-infinite/clamped beam driven at 690Hz, controlled by shaker #2, and with an error microphone located at 51.4° axially. This experimental case showed excellent attenuation at the error microphone ($42dB$) with poor global attenuation. In fact,

(a)

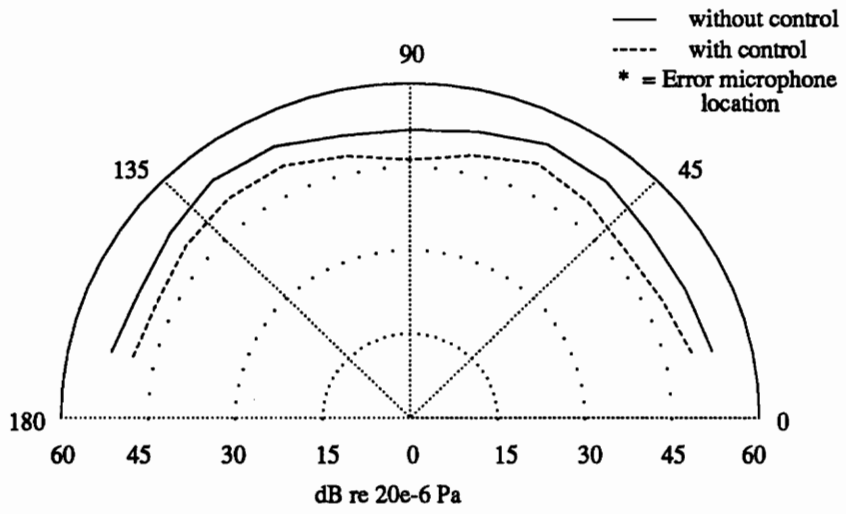

(b)

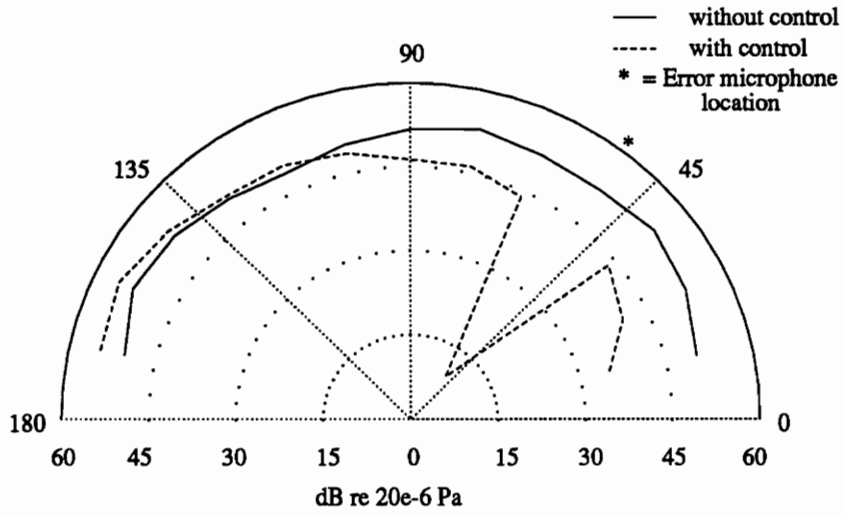

Figure 4.10: Semi-infinite/clamped beam acoustic field, 690Hz, shaker controller #2, error microphone 51.4° axial. (*a*) perpendicular microphone array data, (*b*) axial microphone array data.

(a)

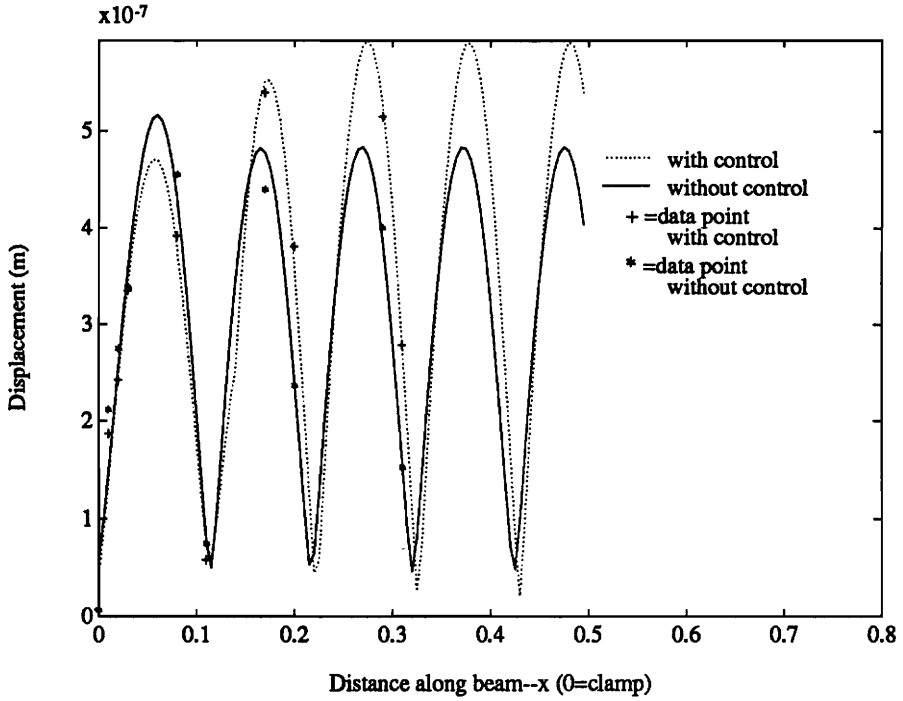

(b)

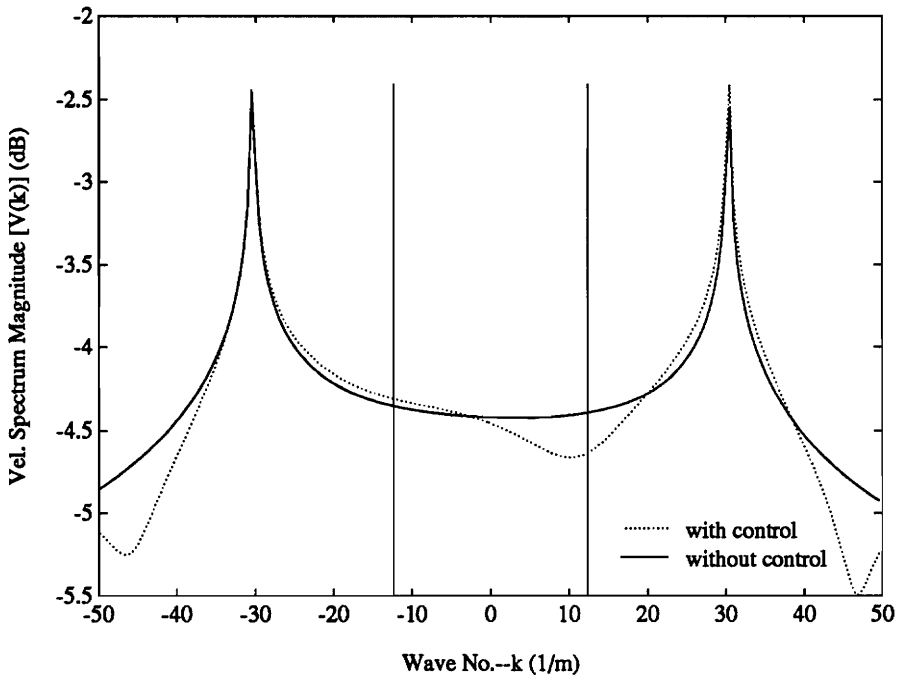

Figure 4.11: Semi-infinite/clamped beam, 690Hz, shaker controller #2, error microphone 51.4° axial. (*a*) decomposed displacement, (*b*) corresponding velocity wavenumber spectrum.

some of the acoustic field showed increases in the acoustic levels. This behavior was reflected in the wavenumber spectrum where parts of the supersonic wavenumber region increased while other parts decreased. This is because the optimal control achieved by the controller caused the sum of the various wave contributions to the supersonic wavenumber region to increase under control.

In Figs. 4.12 and 4.13 the results for the semi-infinite/clamped beam driven at 690Hz, controlled by shaker #2, and with an error microphone at 51.4° perpendicularly are shown. In this experimental case an attenuation of $35dB$ was achieved at the error microphone. Global attenuation was very good in the perpendicular array (on the order of $20dB$) while the axial array showed poor global attenuation performance (on the order of $3dB$). Like previously discussed experimental cases, the standing wave amplitude increased while the supersonic wavenumber region of the wavenumber spectrum decreased under control.

The results from the experimental case of the semi-infinite/clamped beam driven at 690Hz, controlled by shaker #2, and with an error microphone located at 90° are shown in Figs. 4.14 and 4.15. Here an attenuation of $37dB$ at the error microphone was achieved while the global attenuation in the perpendicular array was about $13dB$ and about $3dB$ in the axial array. Once again, the standing wave amplitudes increased while the supersonic wavenumber components decreased under control.

Next, in Figs. 4.16 and 4.17, the results for the experimental case of the semi-infinite/clamped beam driven at 690Hz, controlled by shaker #2, and with error microphones located at 51.4° and 128.6° axially are presented. In this experimental case only a $3dB$ attenuation at the error microphones was achieved while the perpendicular global attenuation was a consistent $10dB$ and the axial global atten-

(a)

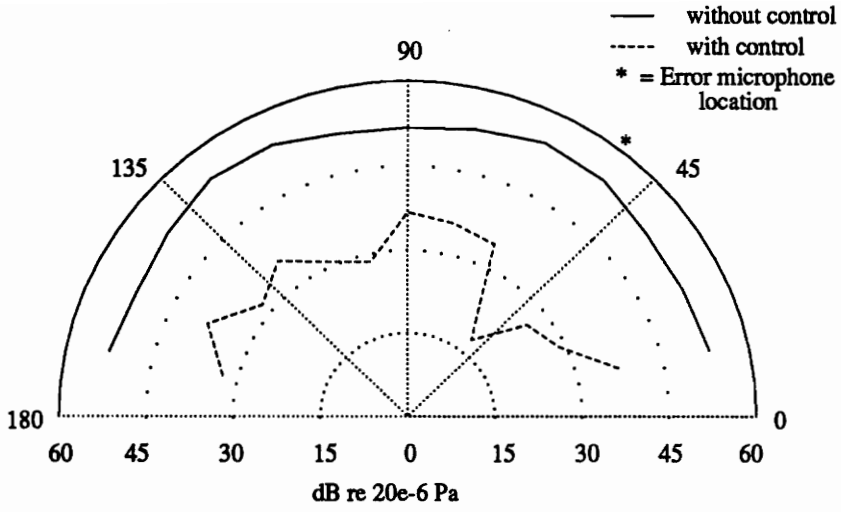

(b)

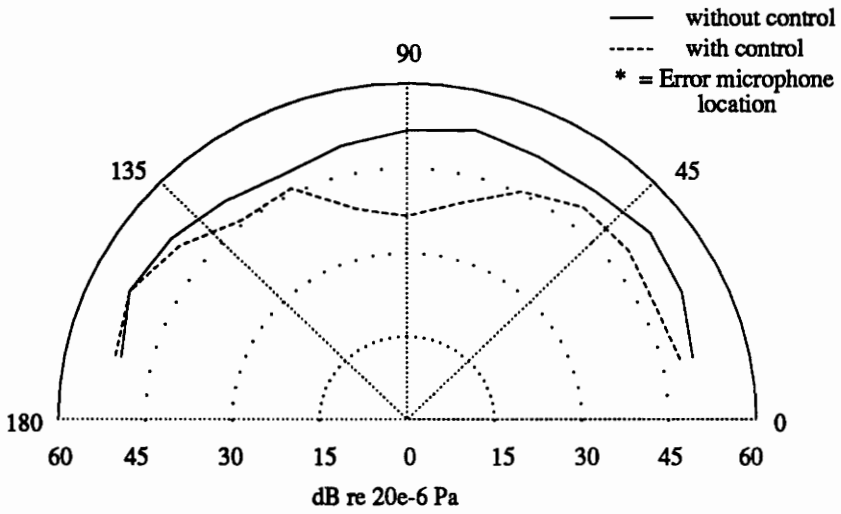

Figure 4.12: Semi-infinite/clamped beam acoustic field, 690Hz, shaker controller #2, error microphone 51.4° perpendicular. (a) perpendicular microphone array data, (b) axial microphone array data.

(a)

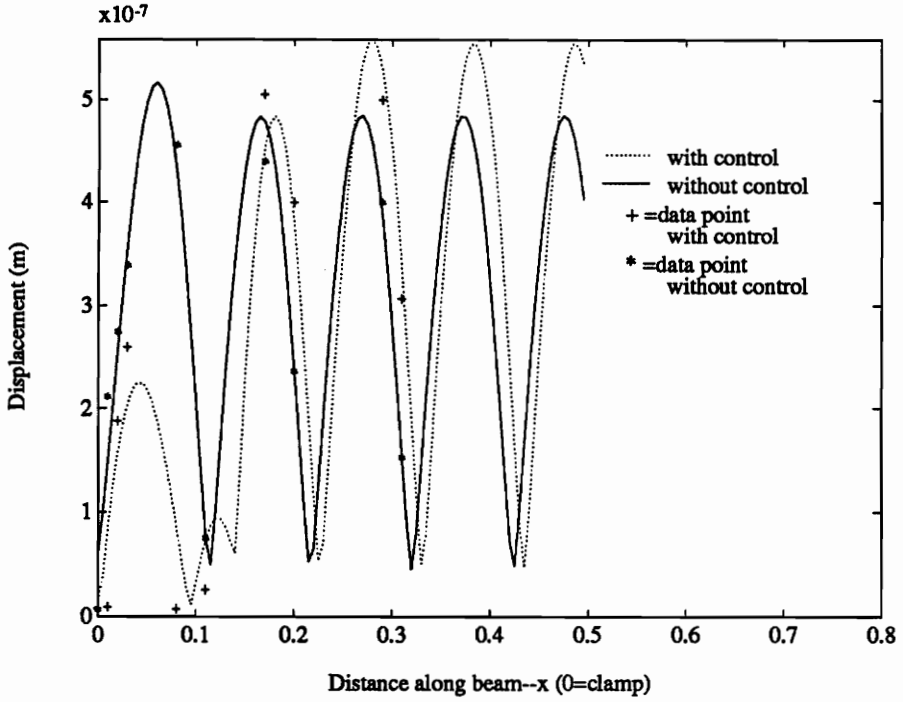

(b)

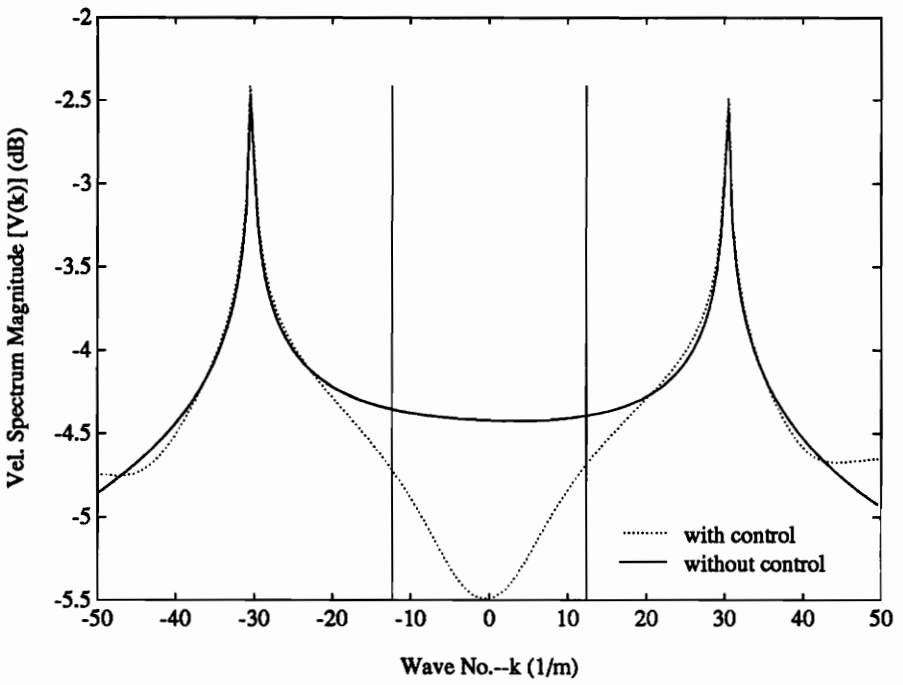

Figure 4.13: Semi-infinite/clamped beam, 690Hz, shaker controller #2, error microphone 51.4° perpendicular. (*a*) decomposed displacement, (*b*) corresponding velocity wavenumber spectrum.

(a)

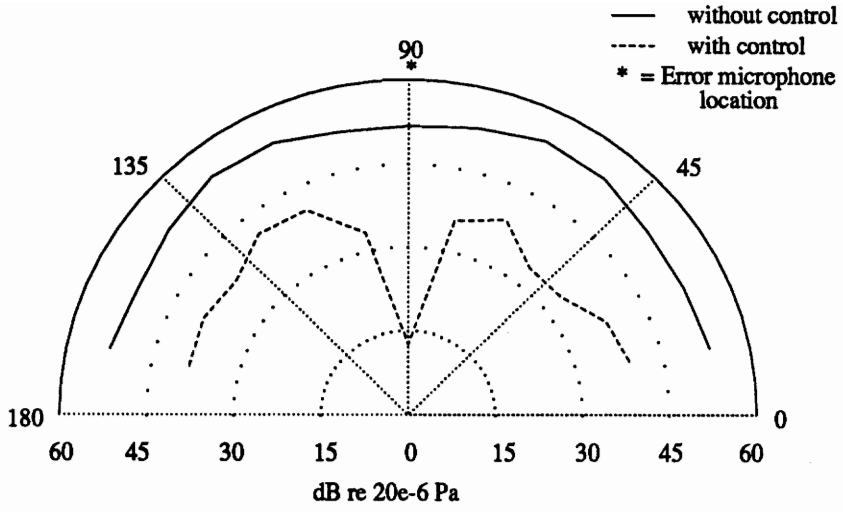

(b)

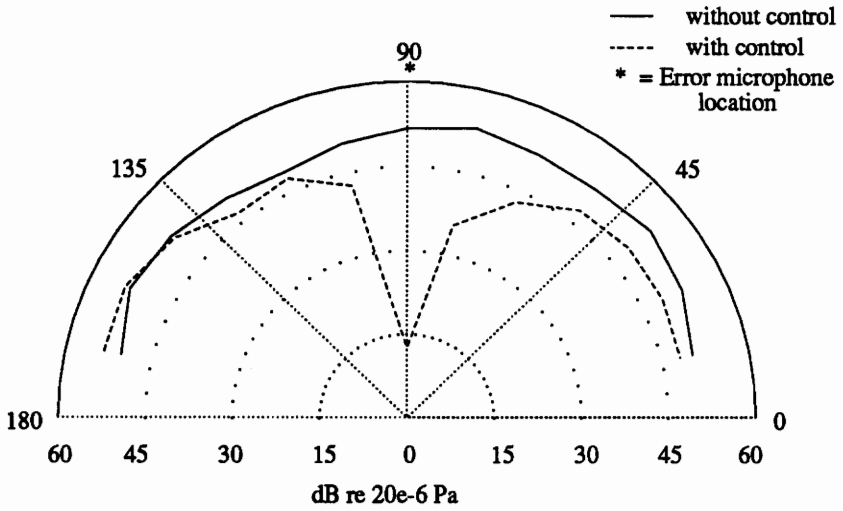

Figure 4.14: Semi-infinite/clamped beam acoustic field, 690Hz, shaker controller #2, error microphone 90°. (*a*) perpendicular microphone array data, (*b*) axial microphone array data.

(a)

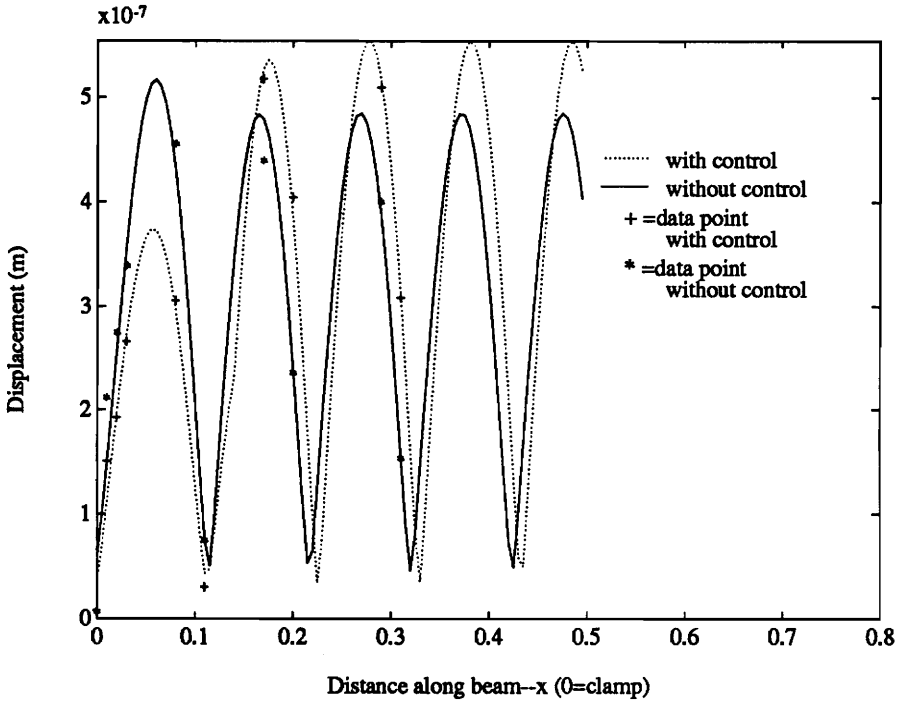

(b)

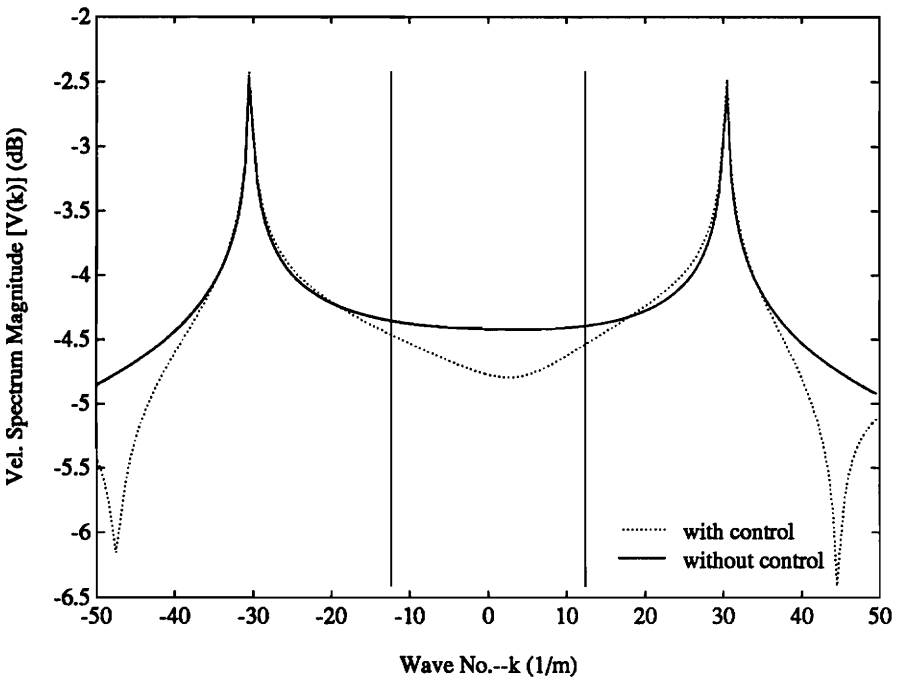

Figure 4.15: Semi-infinite/clamped beam, 690Hz, shaker controller #2, error microphone 90° . (*a*) decomposed displacement, (*b*) corresponding wavenumber velocity spectrum.

(a)

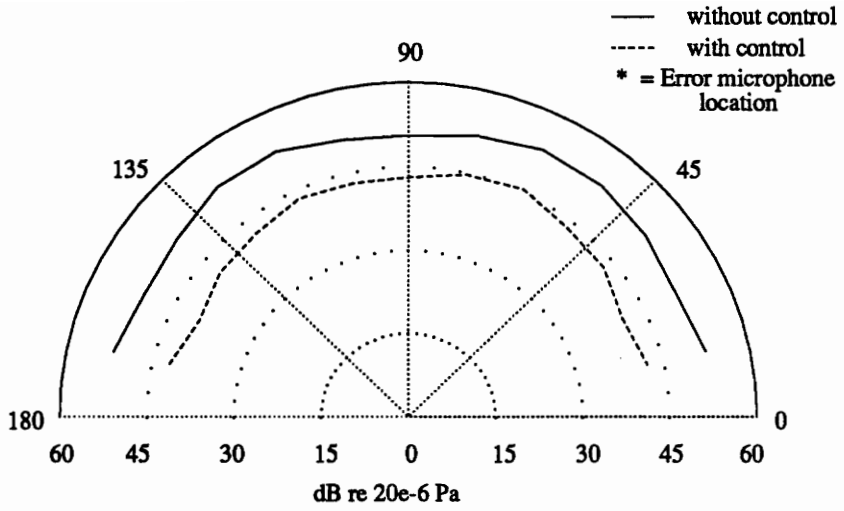

(b)

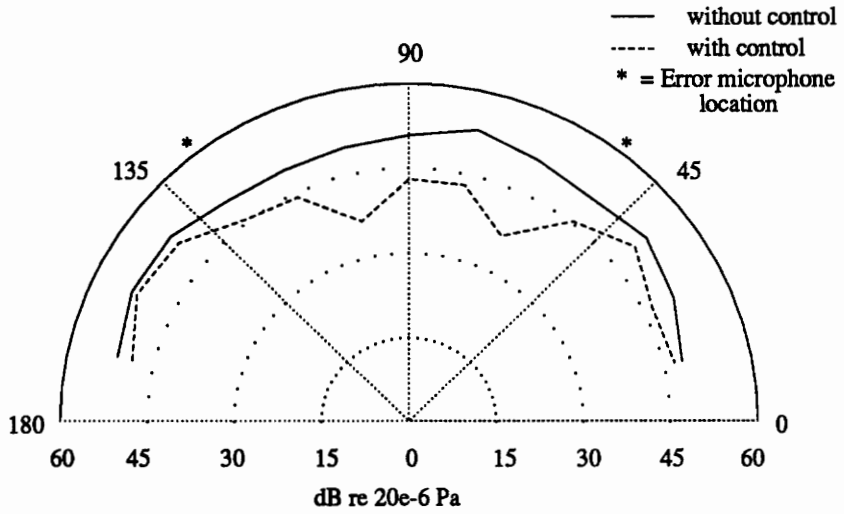

Figure 4.16: Semi-infinite/clamped beam acoustic field, 690Hz, shaker controller #2, error microphones 51.4° and 128.6° axial. (*a*) perpendicular microphone array data, (*b*) axial microphone array data.

(a)

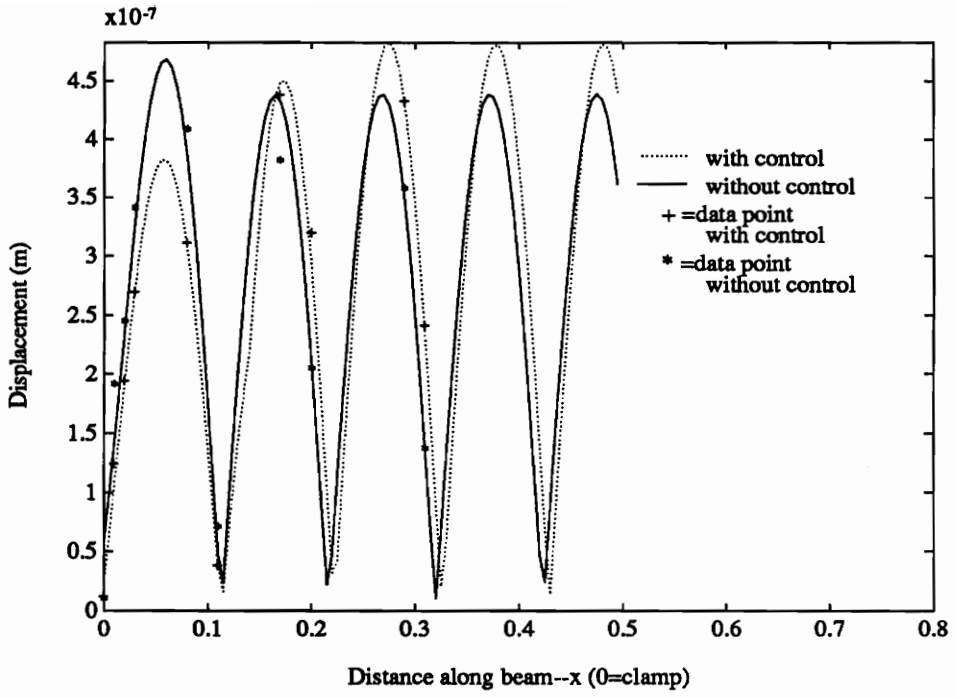

(b)

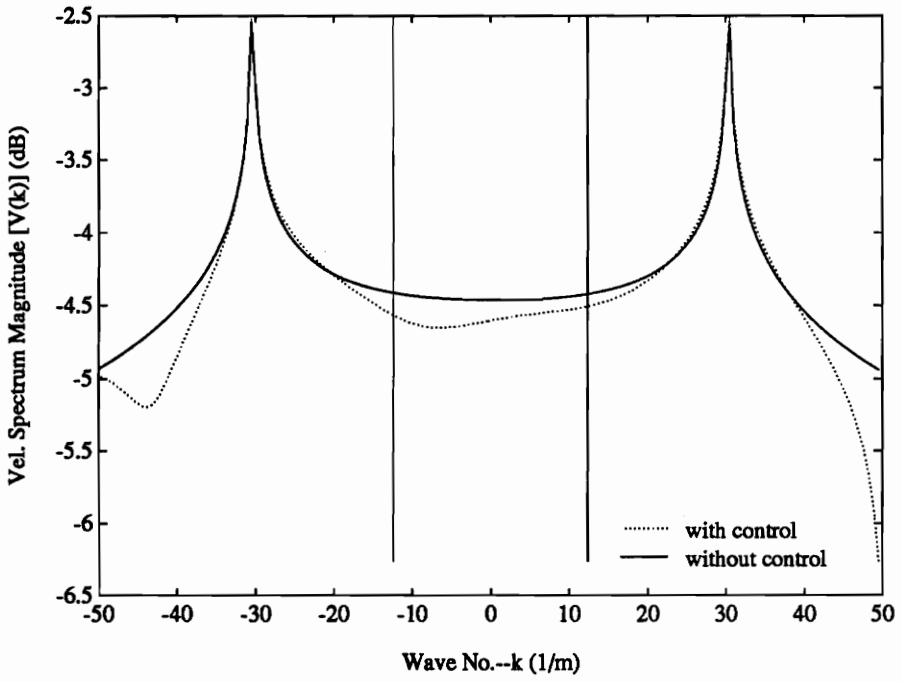

Figure 4.17: Semi-infinite/clamped beam, 690Hz, shaker controller #2, error microphones 51.4° and 128.6° axial. (*a*) decomposed displacement, (*b*) corresponding velocity wavenumber spectrum.

uation was roughly $3dB$. Again, an increase in the standing wave amplitudes with a decrease in the supersonic wavenumber components was seen under control.

The final experimental case presented for the error microphone location comparison is shown in Figs. 4.18 and 4.19. This is the experimental case of the semi-infinite/clamped beam driven at 690Hz, controlled by shaker #2, with error microphones located at 51.4° and 128.6° perpendicularly. In this experimental case an attenuation at both error microphones of $22dB$ was achieved. The global attenuation performance was good in the perpendicular plane (about $20dB$) while the axial global attenuation was not as good (about $3dB$). As in all previous experimental cases, the standing wave amplitudes increased while the supersonic wavenumber region decreased under control.

From these experimental cases presented (driven at 690Hz, and controlled by shaker #2) some interesting conclusions can be drawn. The best local attenuation was achieved with one error microphone and the best global attenuation was achieved using two error microphones. This is due to the fact that, with two error microphones, the control is distributed over a larger area of the acoustic field. An extension of this fact would imply that the more error microphones employed, the better the global attenuation would be and the worse the local attenuation would be.

Regardless of the number of error microphones used the best global attenuation was achieved with the error microphones in the perpendicular array and the best local attenuation was achieved with the error microphones in the axial array. This is because the acoustic field perpendicular to the axis of the beam was governed by the lateral beam vibrational response which, in these experiments, was constant. This

(a)

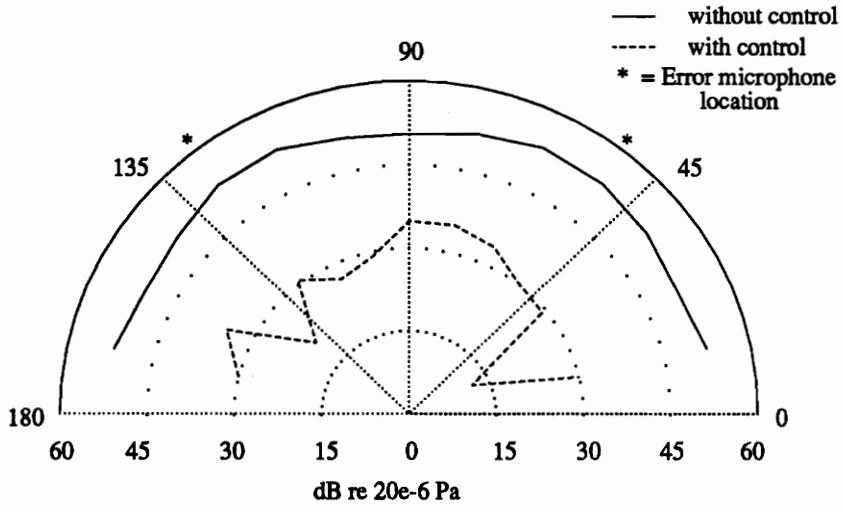

(b)

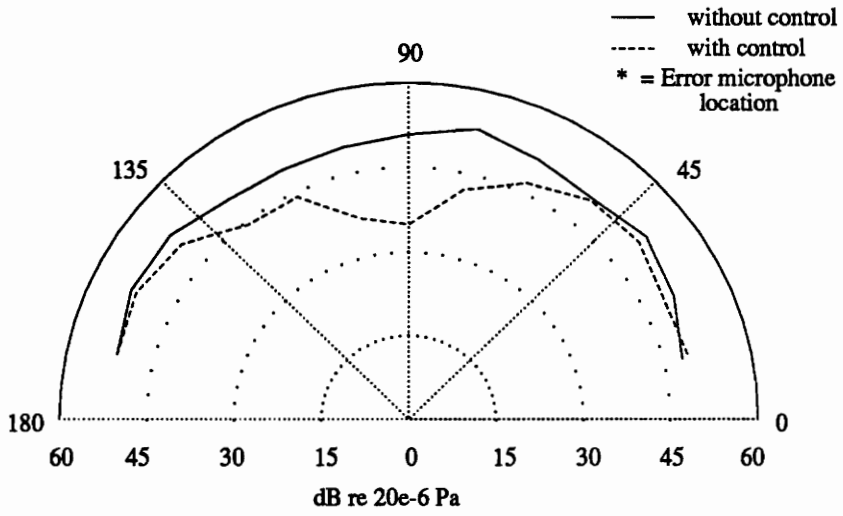

Figure 4.18: Semi-infinite/clamped beam acoustic field, 690Hz, shaker controller #2, error microphones 51.4° and 128.6° perpendicular. (*a*) perpendicular microphone array data, (*b*) axial microphone array data.

(a)

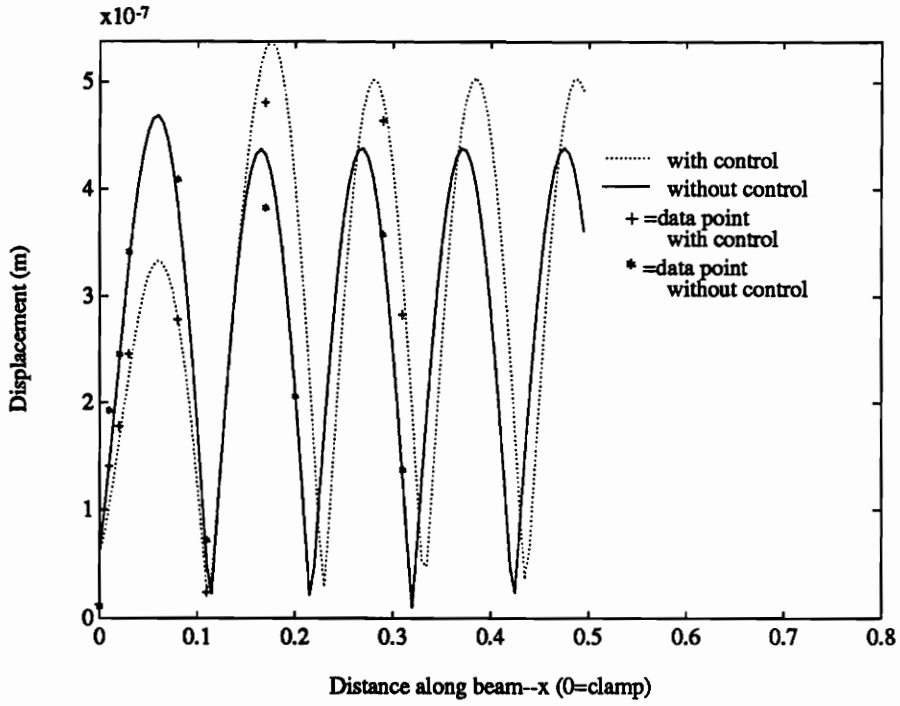

(b)

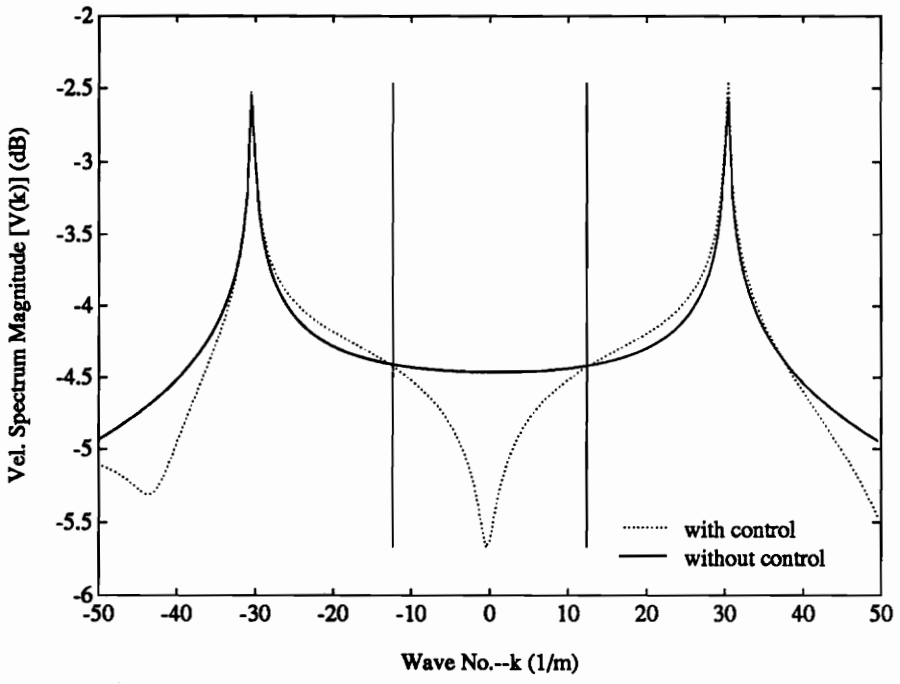

Figure 4.19: Semi-infinite/clamped beam, 690Hz, shaker controller #2, error microphones 51.4° and 128.6° perpendicular. (*a*) decomposed displacement, (*b*) corresponding velocity wavenumber spectrum.

results in the perpendicular acoustic field being more homogeneous (of nearly the same magnitude and phase) throughout which, in turn, resulted in a much greater controllability.

For example, if we consider a simple case of an acoustic field with the same magnitude and phase throughout, with one point in this field acting as the error source to be controlled, and with a control source that was similarly homogeneous, the entire acoustic field would experience the same attenuation as the point acting as the error source. This would be due to the fact that the controller would produce a signal out of phase with the error source and cancel it entirely, and hence, be out of phase with and cancel the entire acoustic field. On the other hand, if one half of the acoustic field were out of phase with the other half, only that half of the acoustic field which contained the error source would experience the same attenuation as the error location. The other half of the field would experience some attenuation less than that of the error location depending on the relative phasing of the control source and that portion of the acoustic field (this region could even see an increase in levels depending on the phasing). This example could be expanded to consider a very complex acoustical response with varying magnitude and phase throughout the field. The result of this would be that only those portions of the acoustical field that were of similar magnitude and phase to that part containing the error sensor would experience similar attenuations.

The perpendicular acoustic response of these experiments would compare with the more simple homogeneous situation in the previous example due to the relatively simple nature of the lateral beam response (which governs the perpendicular acoustic response). On the other hand, the axial acoustic response, being governed by the

axial beam vibration (a combination of traveling and near-field waves), is much more complex and would compare with the non-homogeneous situation in the previous example. Hence, an error sensor in the perpendicular array would result in improved attenuation over an error sensor in the axial array.

4.1.3 Frequency Comparison

In this section the performance of the active noise control at various frequencies is compared. An experimental case of the semi-infinite/clamped beam driven at 320Hz is presented and compared with experimental cases for 510Hz and 690Hz which have already been presented. Additionally, another experimental case driven at 690Hz is presented under the control of shaker #1.

In Figs. 4.20 and 4.21 the results for the experimental case driven at 320Hz, controlled by shaker #2, and with an error microphone located at 51.4° axially are shown. Here we see an attenuation of $23dB$ at the error microphone while the global attenuation is on the order of $8dB$. In this experimental case, however, the standing wave amplitude decreases along with the supersonic wavenumber components.

For the comparison of performance at various frequencies, first consider the experimental cases shown in Figs. 4.6, 4.7, 4.10, 4.11, 4.20 and 4.21. Each of these experimental cases was controlled by shaker #2 and with an error microphone located at 51.4° axially. For the two higher frequency experimental cases the attenuation at the error microphone was excellent while their global reduction is poor. On the other hand, the 320Hz experimental case showed a relatively poor attenuation at the error microphone with a superior global reduction.

(a)

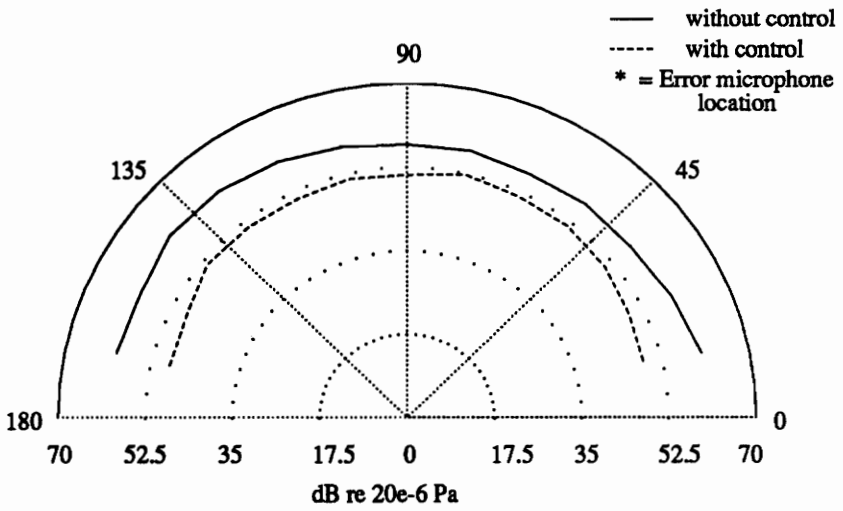

(b)

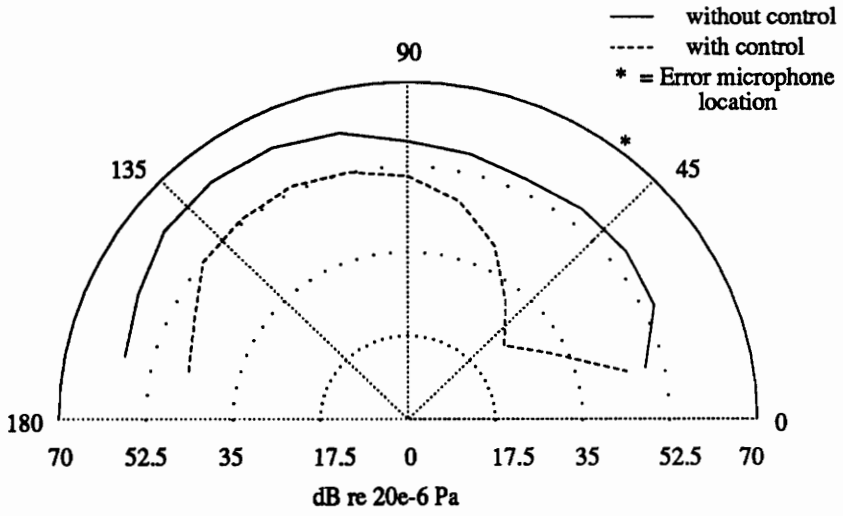

Figure 4.20: Semi-infinite/clamped beam acoustic field, 320Hz, shaker controller #2, error microphone 51.4° axial. (*a*) perpendicular microphone array data, (*b*) axial microphone array data.

(a)

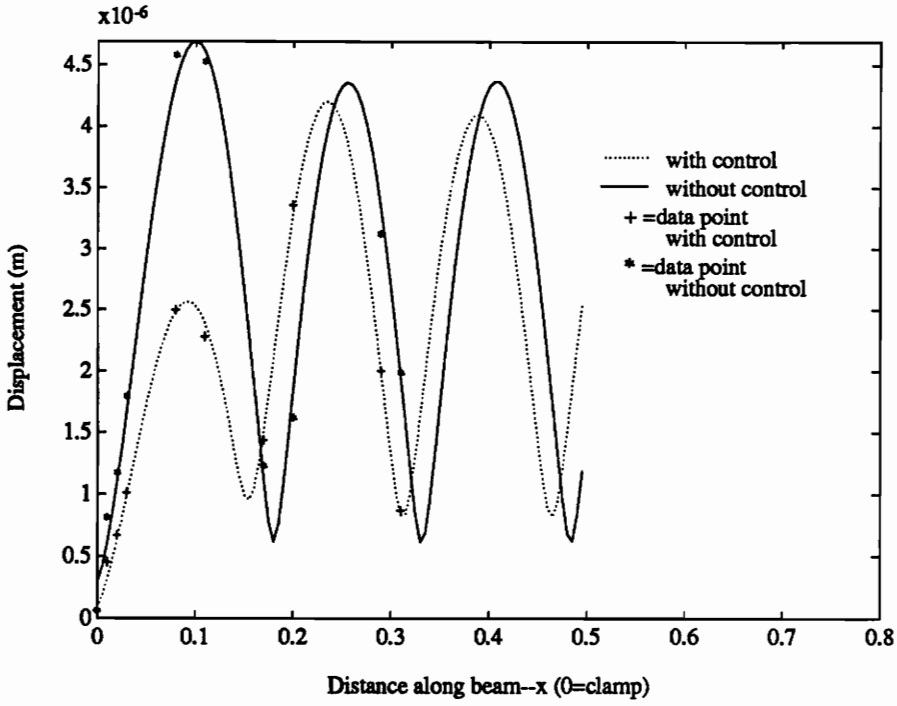

(b)

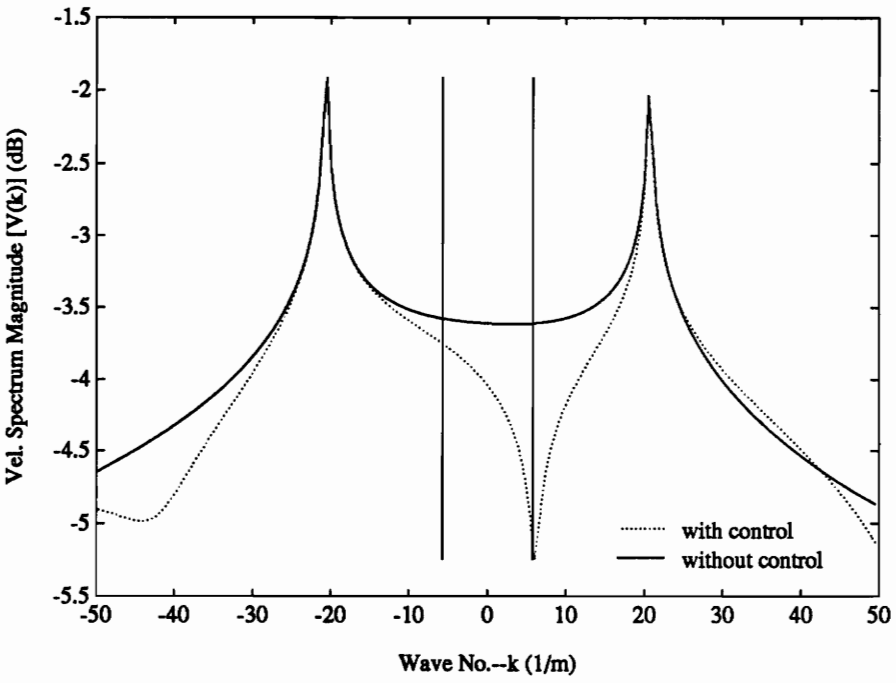

Figure 4.21: Semi-infinite/clamped beam, 320Hz, shaker controller #2, error microphone 51.4° axial. (*a*) decomposed displacement, (*b*) corresponding velocity wavenumber spectrum.

This behavior may be due to the fact that, in the two higher frequency experimental cases, control shaker #2 (located at $x = 13.9cm$) was outside of the displacement region affected by the reflected flexural near-field. At 690Hz the near-field effects had decreased to 1.5% of their maximum value at the location of shaker #2. Similarly, the flexural near-field has decreased to 2.7% for 510Hz and 10% for 320Hz. Therefore, the control actuator was in a region of very small flexural near-field influence for the higher two frequencies.

Figures 1.11 and 1.12 show the relative contributions of near-field and traveling waves to the wavenumber spectrum. The conclusion drawn from Fig. 1.12 is that the flexural near-field wave is a major contributor to the supersonic wavenumber spectrum, and hence, the far-field acoustic radiation. Therefore, if the reflected near-field wave is not controlled effectively, the controllability of the far-field radiation will be directly affected.

To further illustrate this point consider the experimental case driven at 510Hz, controlled by shaker #1, with an error microphone located at 51.4° axially shown in Figs. 4.1 and 4.2. In this experimental case the control shaker was much closer to the clamped discontinuity ($x = 3.8cm$) and the global acoustic attenuation was much improved over the similar experimental case controlled by shaker #2 shown in Figs. 4.6 and 4.7. This supports the conclusion that, for effective global control, the control actuator must be in the region with significant contribution by the reflected near-field wave.

4.1.4 Piezoelectric Actuator Control

In this section the relative effectiveness of the point force shaker and the line moment piezoelectric actuator is compared. Experimental cases employing one and two piezoelectric actuators along with an example at each of the three frequencies are discussed and compared with previously presented experimental cases. Finally, a theoretical case (as calculated by Guigou [16]) are presented and compared to the experimental results.

Figures 4.22 and 4.23 show the results for the experimental case driven at 510Hz, controlled by piezoelectric actuator #1, and with an error microphone located at 51.4° in the axial array. In this experimental case an attenuation at the error microphone of $39dB$ was achieved while the global reduction of the acoustic field was on the order of $10dB$. The standing wave levels in this experimental case decreased slightly while the supersonic region of the wavenumber spectrum decreased.

Comparing the experimental case shown in Figs. 4.22 and 4.23 to the similar experimental case controlled by shaker #1 (shown in Figs. 4.1 and 4.2) demonstrates that the piezoelectric actuator was superior to the shaker in controlling the acoustic field. This superior performance was demonstrated in both the acoustic attenuation at the error microphone and on a global scale. This was due to the fact that the piezoelectric actuator was distributed over a finite length of the beam where the shaker operates at a point. In addition, the piezoelectric was, in effect, two dependent actuators as discussed in Sec. 1.3.2. This is because the piezoelectric actuator exerts two equal magnitude and opposite direction line moments at either end of the piezoelectric patch pair.

(a)

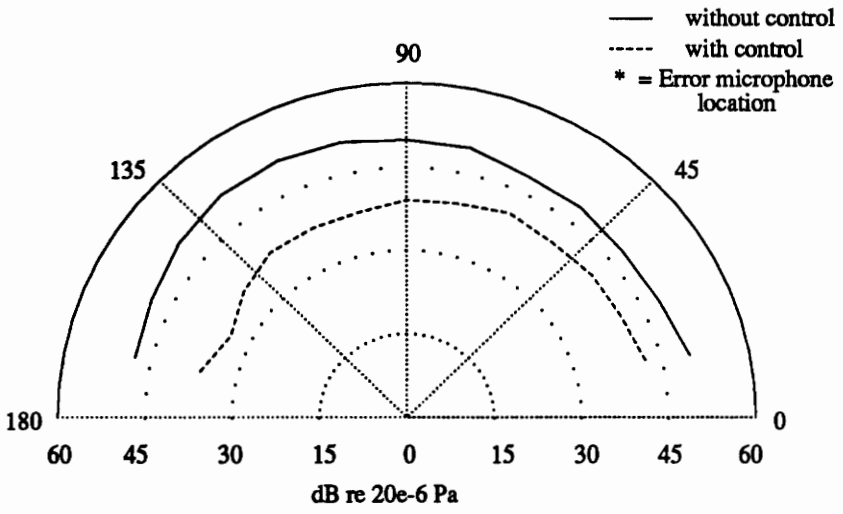

(b)

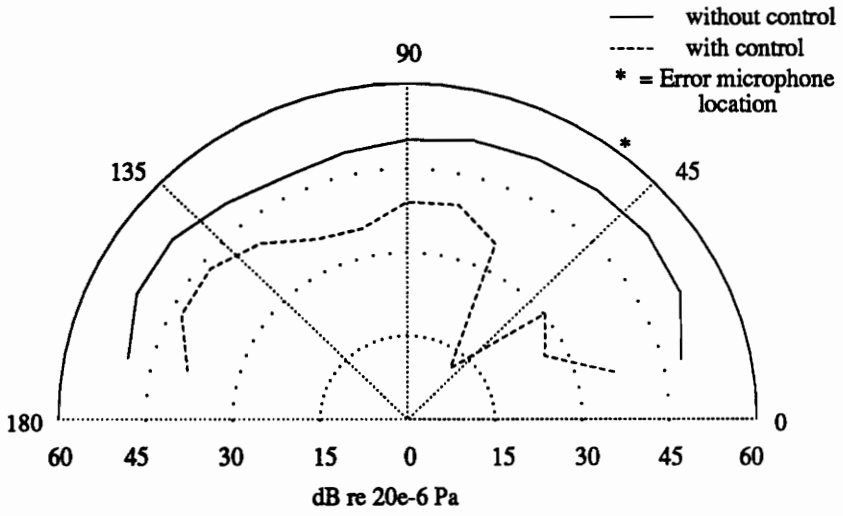

Figure 4.22: Semi-infinite/clamped beam acoustic field, 510Hz, piezoelectric controller #1, error microphone 51.4° axial. (*a*) perpendicular microphone array data, (*b*) axial microphone array data.

(a)

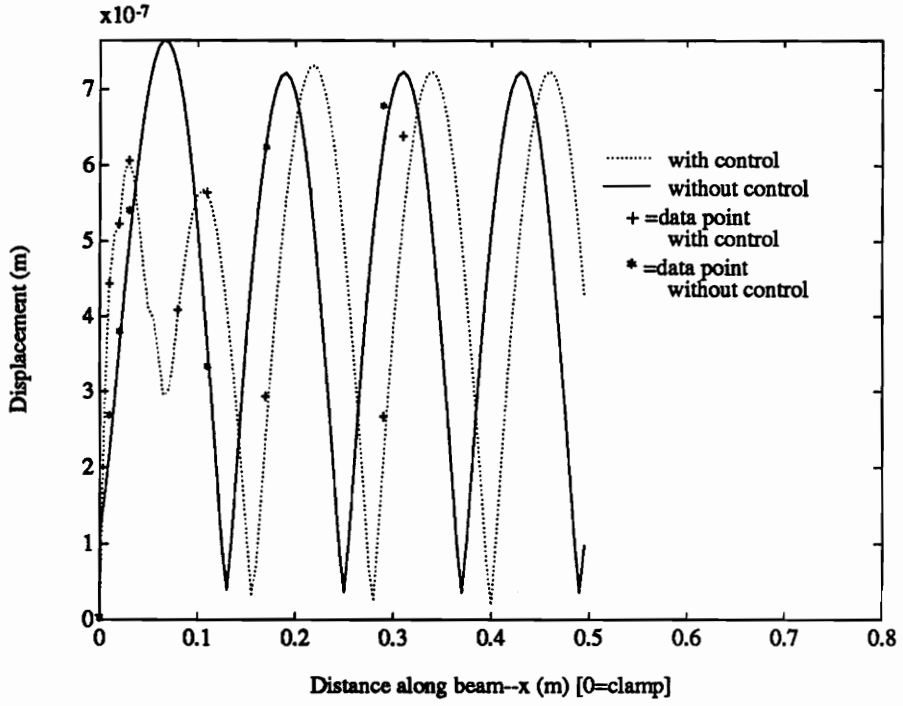

(b)

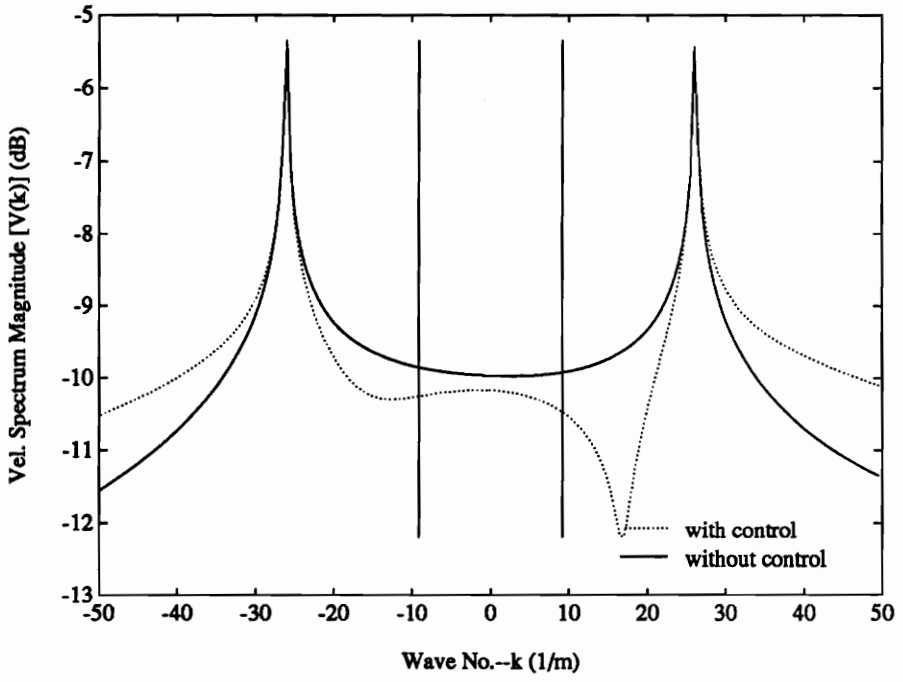

Figure 4.23: Semi-infinite/clamped beam, 510Hz, piezoelectric controller #1, error microphone 51.4° axial. (*a*) decomposed displacement, (*b*) corresponding wavenumber velocity spectrum.

The next experimental case, shown in Figs. 4.24 and 4.25, is a semi-infinite/clamped beam driven at 510Hz, controlled by piezoelectric actuator #2, and with an error microphone located at 51.4° axially. $46dB$ of attenuation was achieved at the error microphone while the acoustic field was globally reduced by roughly $15dB$. In this experimental case the standing wave amplitudes increased while the supersonic region of the wavenumber spectrum decreased.

Comparison of this experimental case with the similar experimental case controlled by shaker #1 (shown in Figs. 4.6 and 4.7) shows a similar reduction at the error microphone. However, the global attenuation under piezoelectric control was far superior to that achieved under shaker control. This, again, was due to the dual, dependant actuator nature of the piezoelectric actuator as previously described.

For further comparison, Figs. 4.26 and 4.27 show the experimental case driven at 320Hz, controlled by piezoelectric actuator #2, and with an error microphone located at 51.4° axially. In this experimental case, $24dB$ of attenuation was achieved at the error microphone while the global attenuation was on the order of $12dB$. Once again, the standing wave amplitudes decreased along with the supersonic wavenumber components.

Comparing this experimental case to the similar experimental case employing a point force shaker (shown in Figs. 4.20 and 4.21) demonstrates that the piezoelectric controlled experimental case showed improved global attenuation while the error microphone attenuation was about the same. This behavior, again, may be due to the distributed nature of the piezoelectric actuator.

For further comparison, consider the experimental case driven at 320Hz, with an

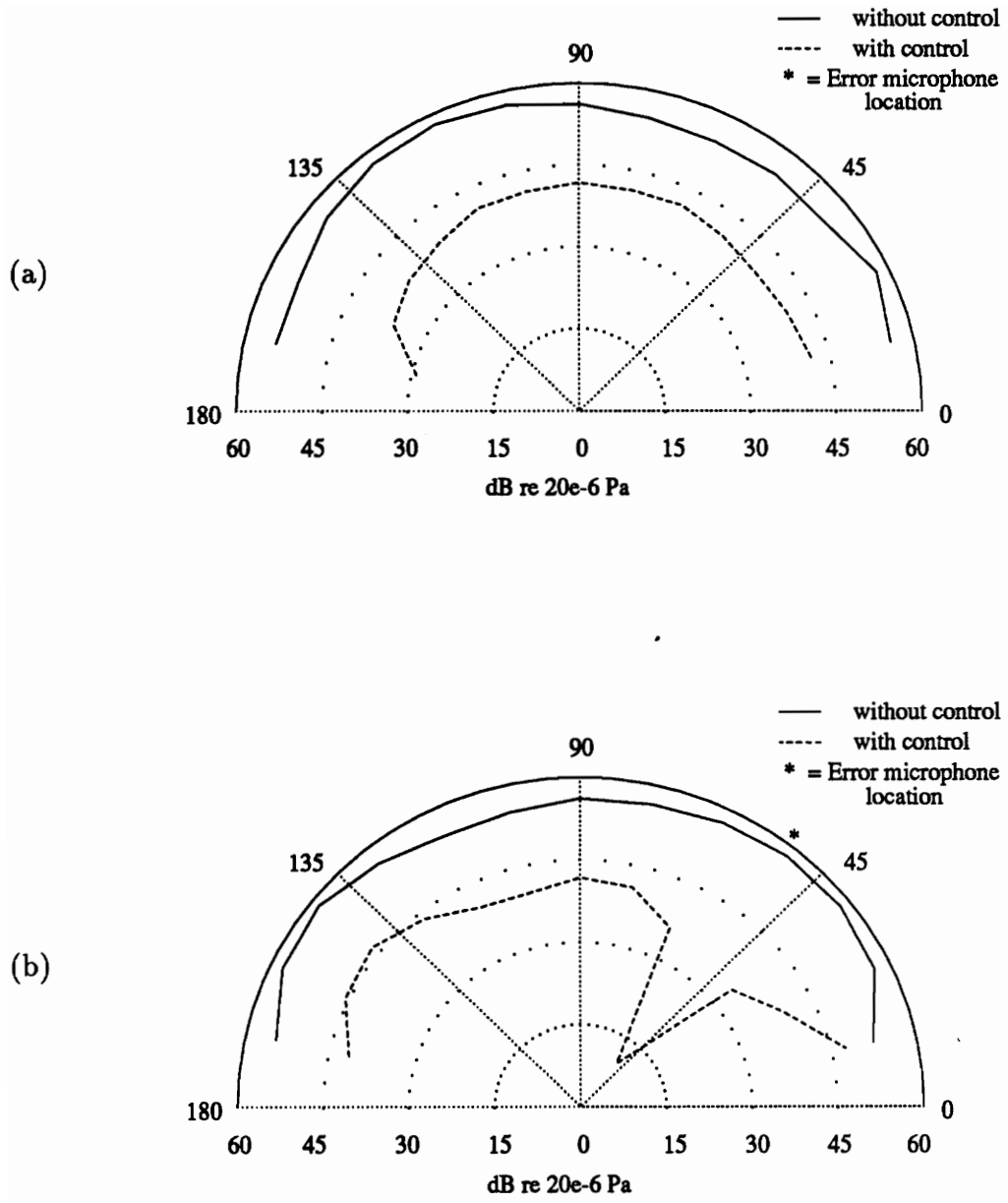

Figure 4.24: Semi-infinite/clamped beam acoustic field, 510Hz, piezoelectric controller #1, error microphone 51.4° axial. (*a*) perpendicular microphone array data, (*b*) axial microphone array data.

(a)

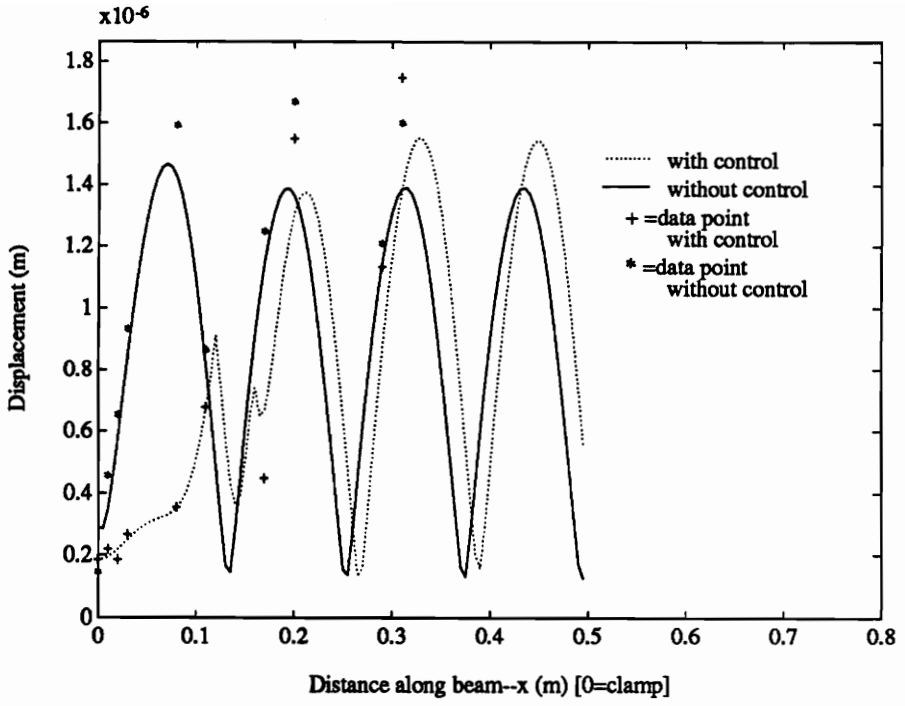

(b)

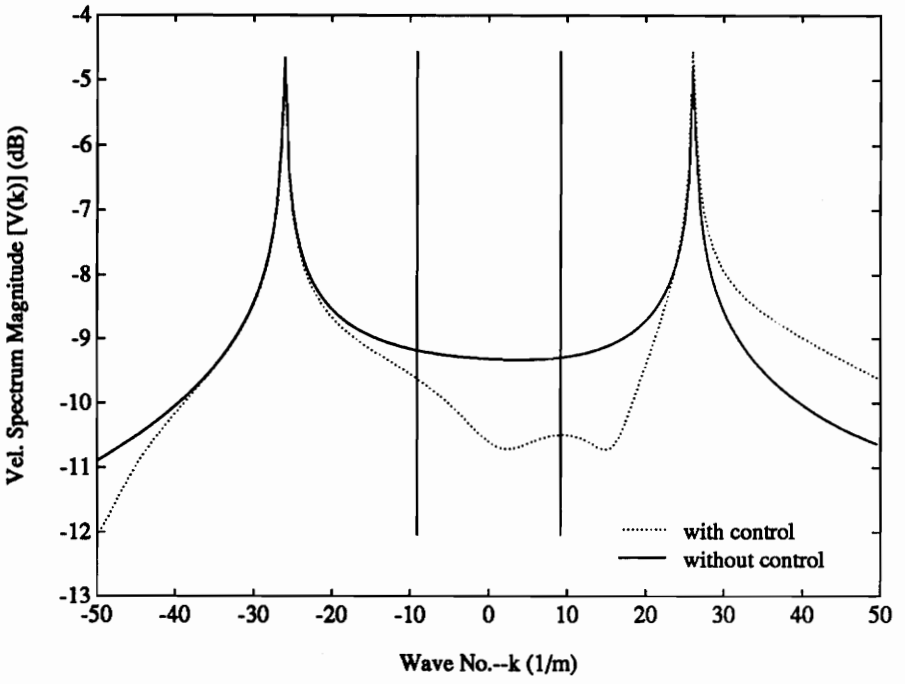

Figure 4.25: Semi-infinite/clamped beam, 510Hz, piezoelectric controller #2, error microphone 51.4° axial. (*a*) decomposed displacement, (*b*) corresponding velocity wavenumber spectrum.

(a)

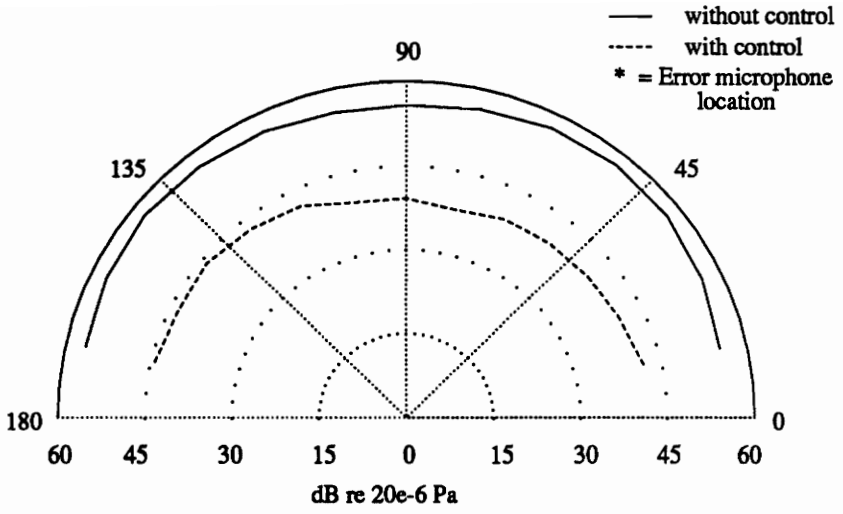

(b)

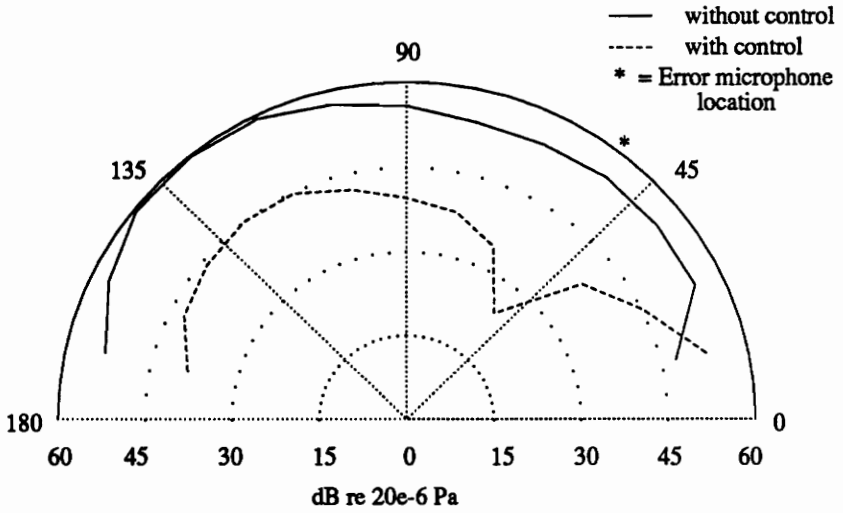

Figure 4.26: Semi-infinite/clamped beam acoustic field, 320Hz, piezoelectric controller #2, error microphone at 51.4° axial. (*a*) perpendicular microphone array data, (*b*) axial microphone array data.

(a)

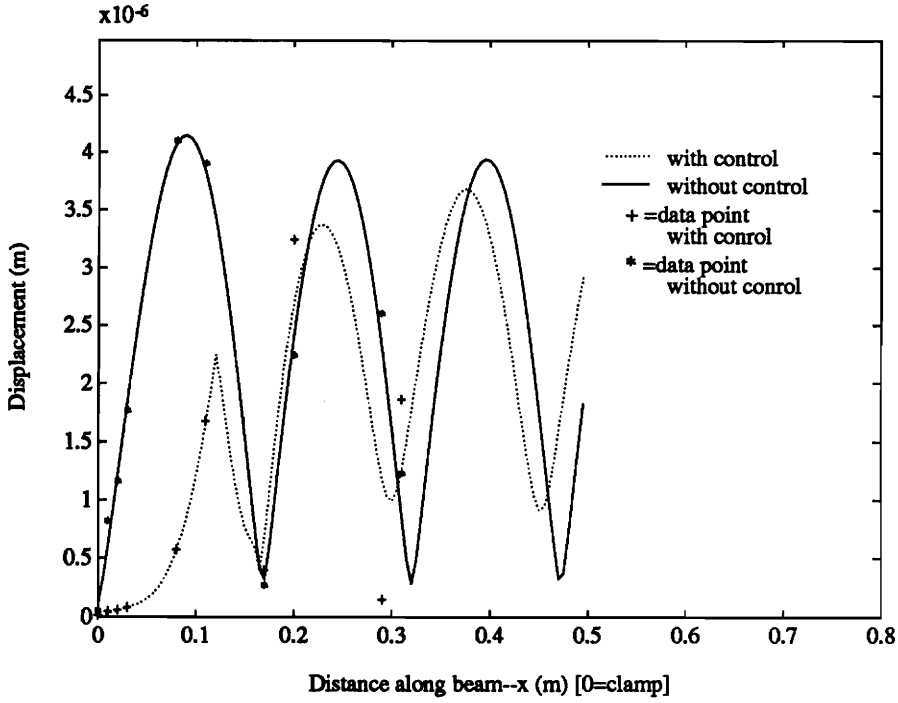

(b)

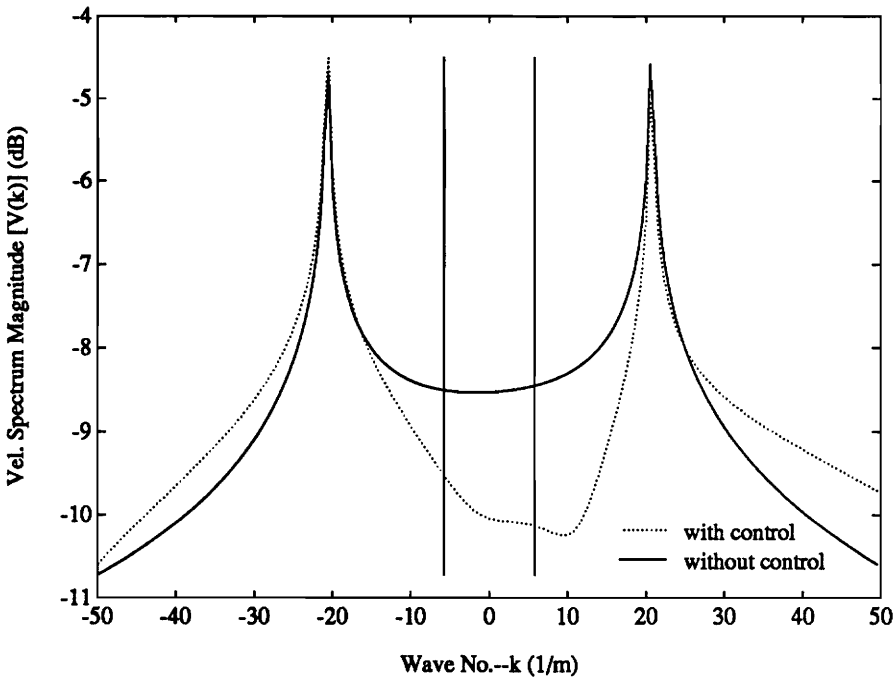

Figure 4.27: Semi-infinite/clamped beam, 320Hz, piezoelectric controller #2, error microphone at 51.4° axial. (*a*) decomposed displacement, (*b*) corresponding velocity wavenumber spectrum.

error microphone located at 51.4° axially (similar to the two experimental cases compared previously) but, controlled by piezoelectric actuator #1 (located much closer to the discontinuity). The results for this experimental case are shown in Figs. 4.28 and 4.29. In this experimental case an improvement in local attenuation was achieved ($36dB$) over the similar experimental cases previously compared while the global attenuation was about the same as for the experimental case controlled by piezoelectric #2 ($14dB$).

In order to demonstrate the effectiveness of the piezoelectric actuator at various frequencies, consider the experimental case shown in Figs. 4.30 and 4.31. In this experimental case, driven at 690Hz and controlled by piezoelectric #1, two error microphones were used located at 51.4° and 128.6° axially. In this experimental case the local attenuation was $20dB$ at the 51.4° microphone and $28dB$ at the 128.6° microphone. The global attenuation was on the order of $20dB$. This demonstrates an improved performance in global attenuation over the other piezoelectric controlled experimental cases and improvement (both globally and locally) over a similar shaker controlled experimental case shown in Figs. 4.16 and 4.17. This implies that the piezoelectric actuator had better performance at higher frequencies. This, in fact, was evident during experimentation. To obtain similar acoustic levels with the piezoelectric actuators a higher input voltage was required at lower frequencies.

For a comparison of these results consider the theoretical case presented in Fig. 4.32, 4.33 and 4.34. These theoretical results were calculated based on Eqs. 1.24, 1.17, 1.31 and 1.18 using the same geometry as in the experiments. The acoustic "near-field" was calculated at a radius of $0.86m$ which was the same radius as the experimental microphone array. The acoustic far-field was calculated at a radius of

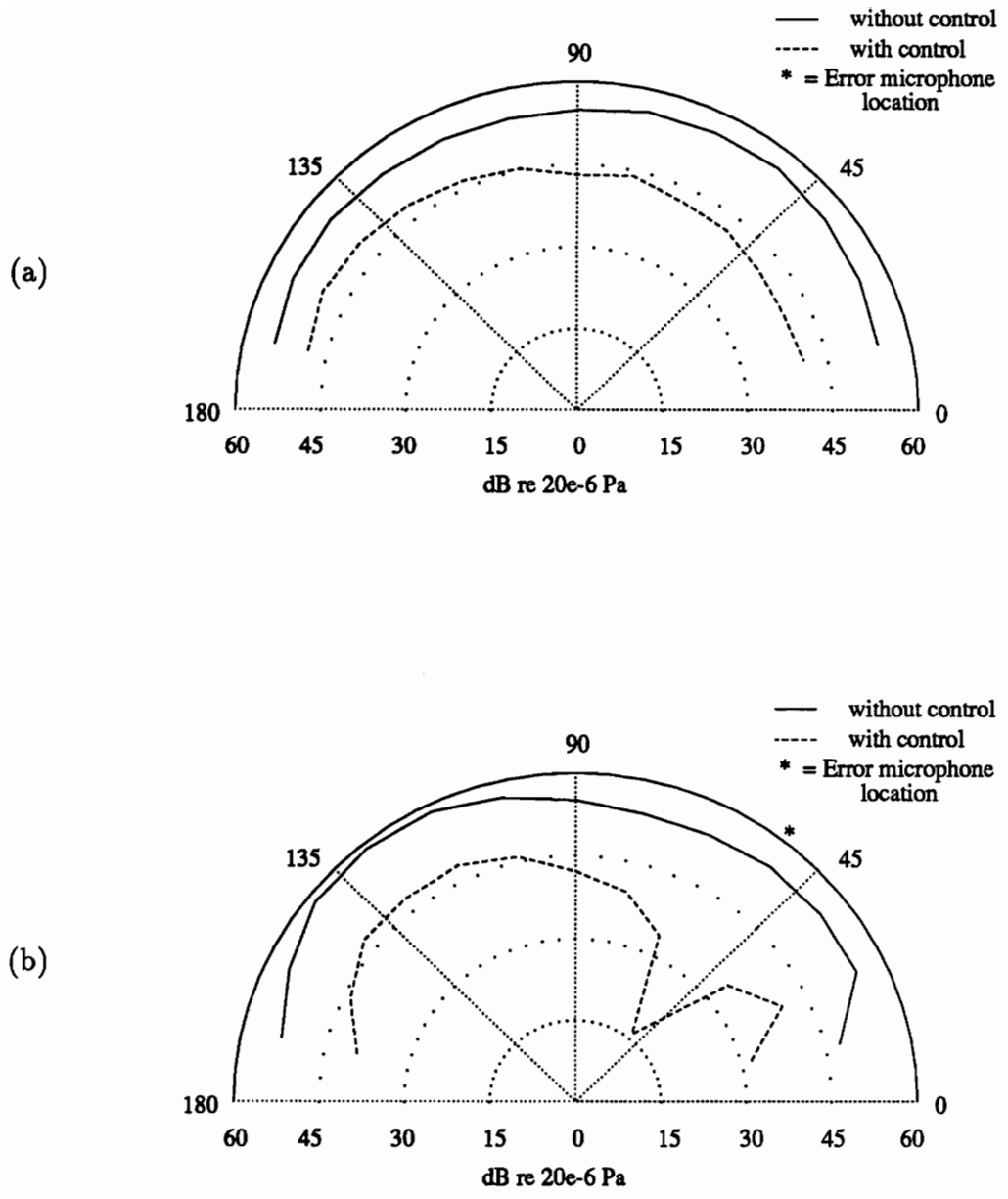

Figure 4.28: Semi-infinite/clamped beam acoustic field, 320Hz, piezoelectric controller #1, error microphone at 51.4° axial. (*a*) perpendicular microphone array data, (*b*) axial microphone array data.

(a)

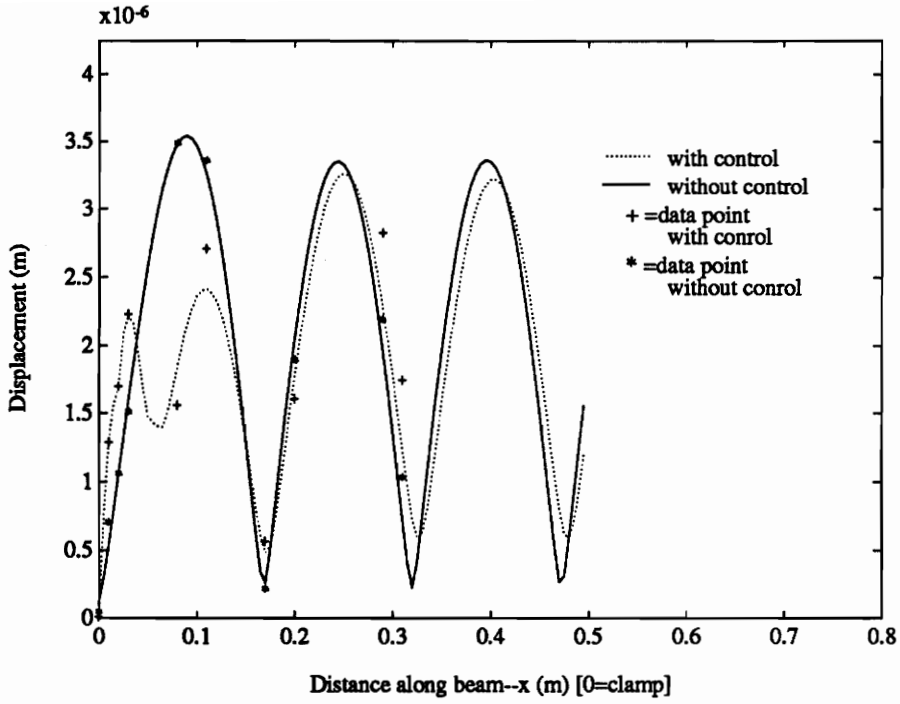

(b)

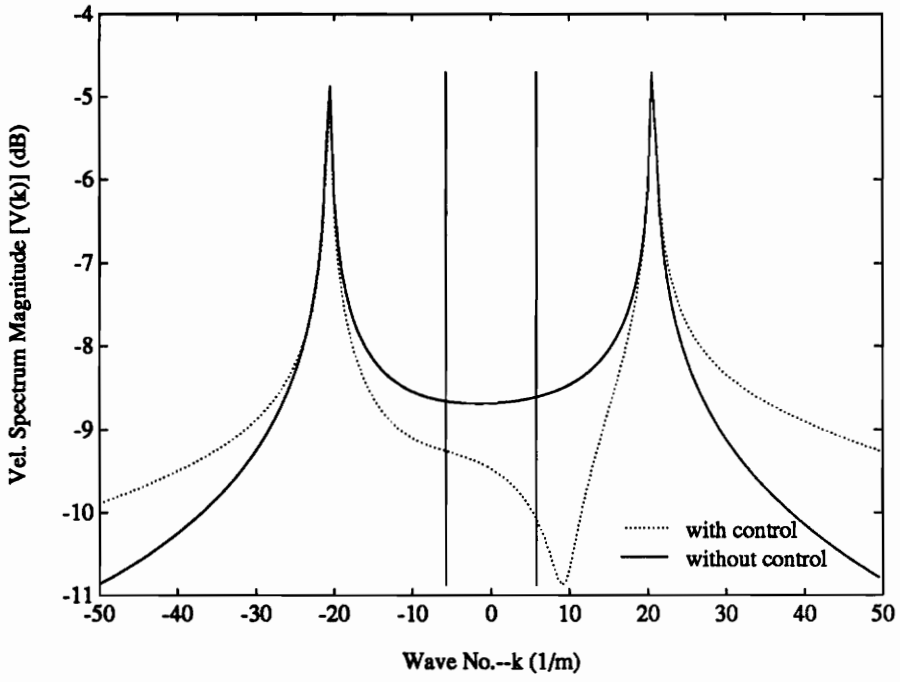

Figure 4.29: Semi-infinite/clamped beam, 320Hz, piezoelectric controller #1, error microphone at 51.4° axial. (*a*) decomposed displacement, (*b*) corresponding velocity wavenumber spectrum.

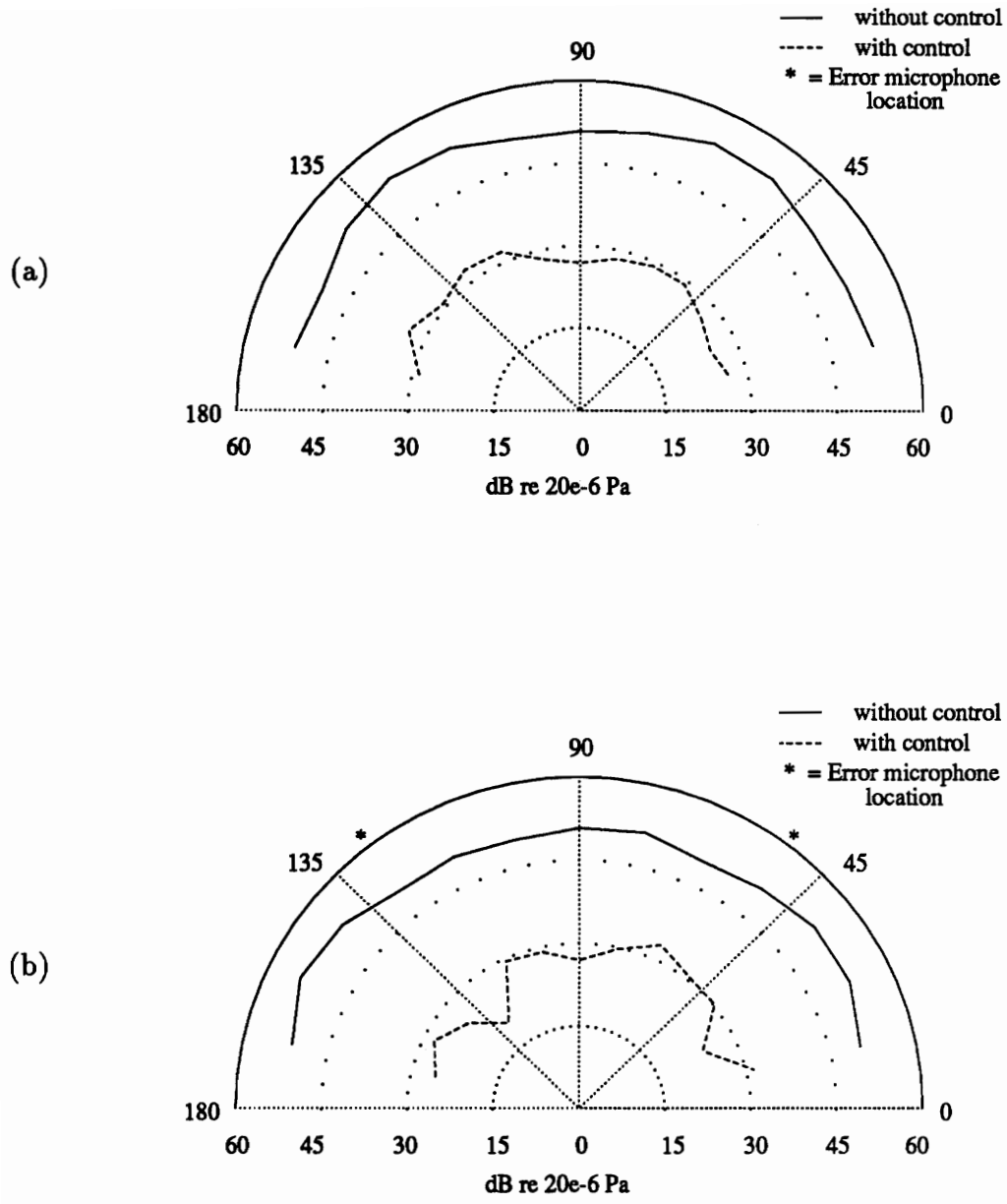

Figure 4.30: Semi-infinite/clamped beam acoustic field, 690Hz, piezoelectric controller #1, error microphones at 51.4° and 128.6° axial. (*a*) perpendicular microphone array data, (*b*) axial microphone array data.

(a)

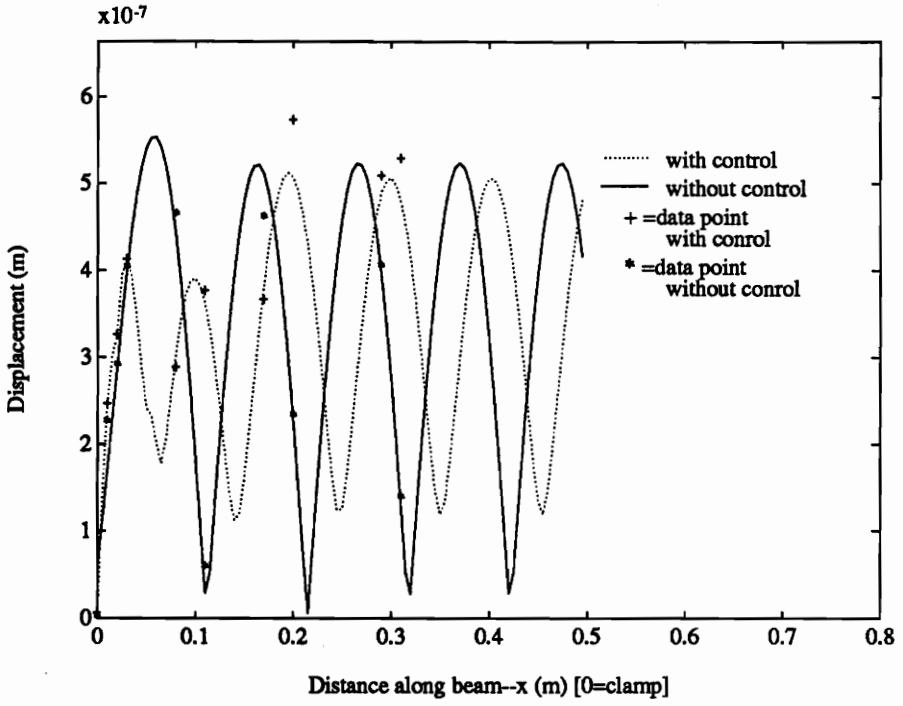

(b)

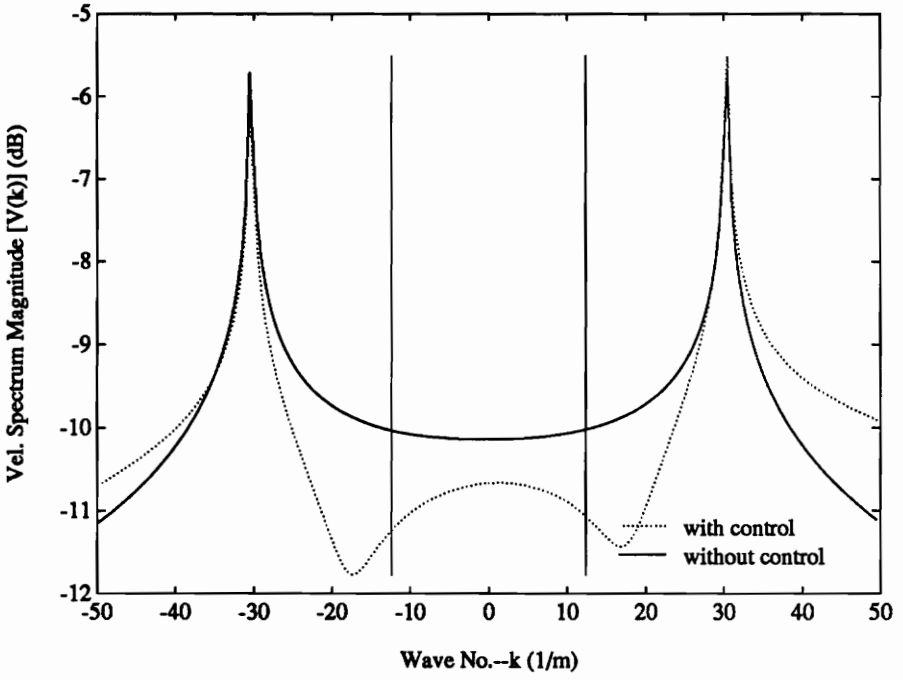

Figure 4.31: Semi-infinite/clamped beam, 690Hz, piezoelectric controller #1, error microphones at 51.4° and 128.6° axial. (*a*) decomposed displacement, (*b*) corresponding velocity wavenumber spectrum.

(a)

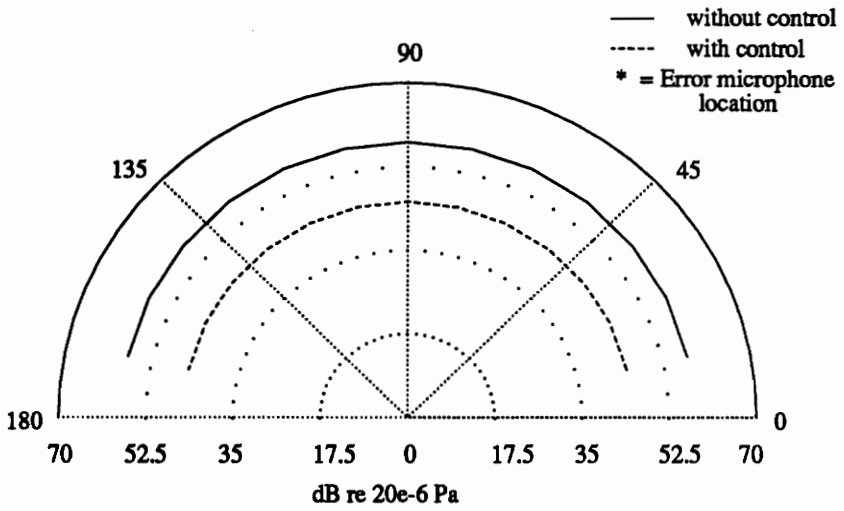

(b)

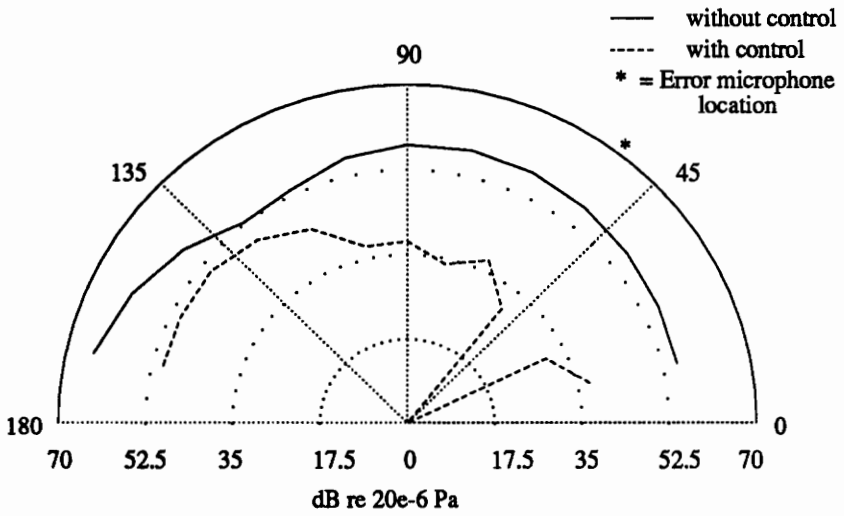

Figure 4.32: Semi-infinite/clamped beam theoretical acoustic "near-field", 320Hz, piezoelectric controller #1, error microphone 51.4° . (*a*) perpendicular microphone array data, (*b*) axial microphone array data.

(a)

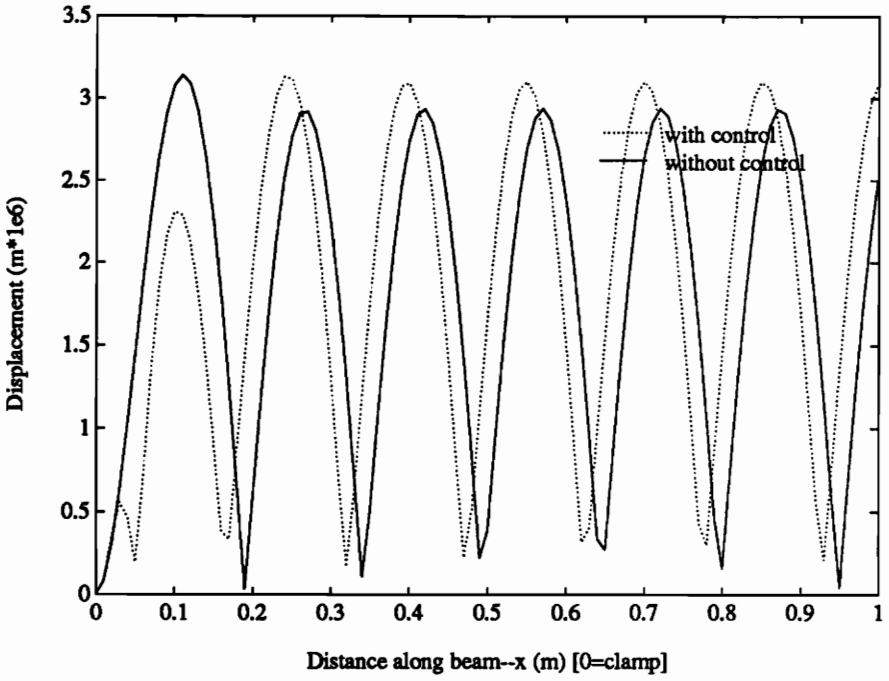

(b)

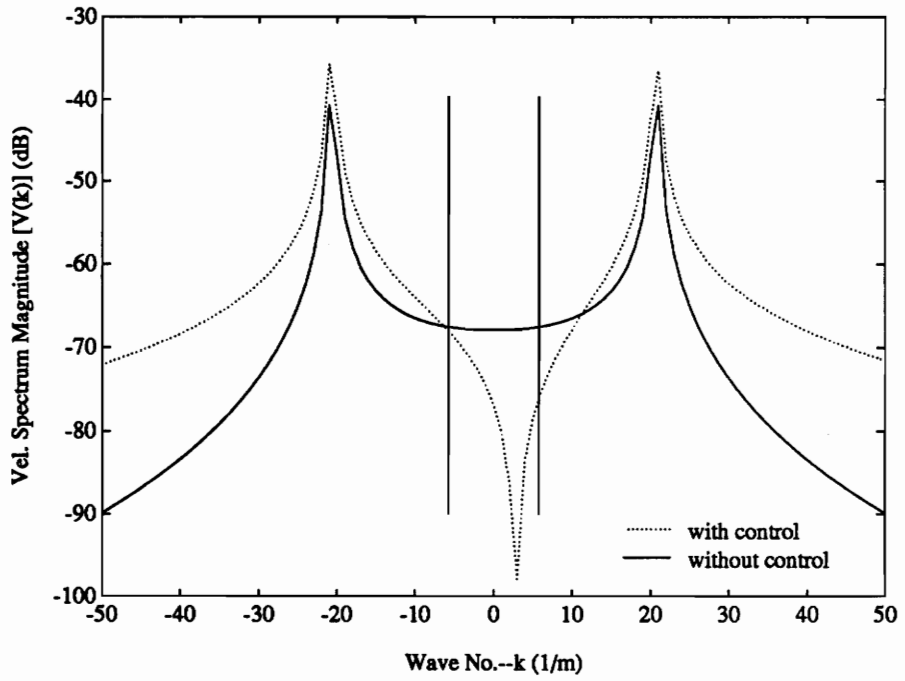

Figure 4.33: Semi-infinite/clamped beam theoretical data, 320Hz, piezoelectric controller #1, error microphone 51.4°. (*a*) decomposed displacement, (*b*) corresponding velocity wavenumber spectrum.

(a)

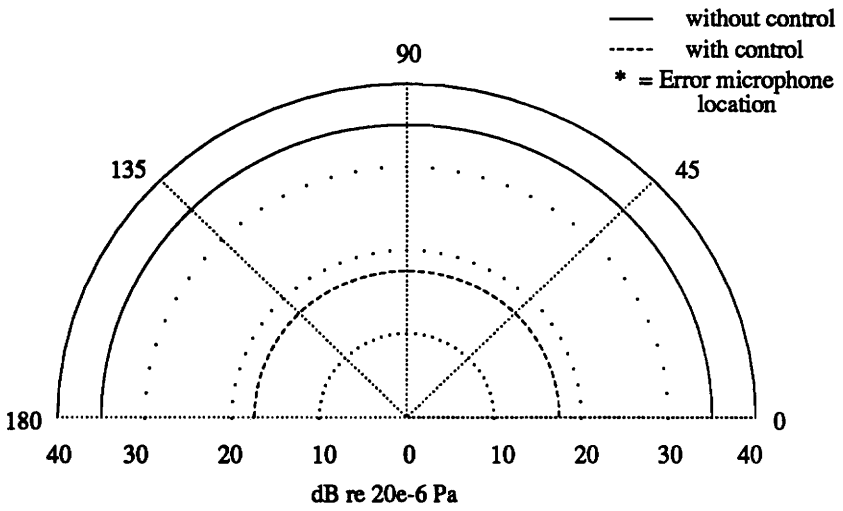

(b)

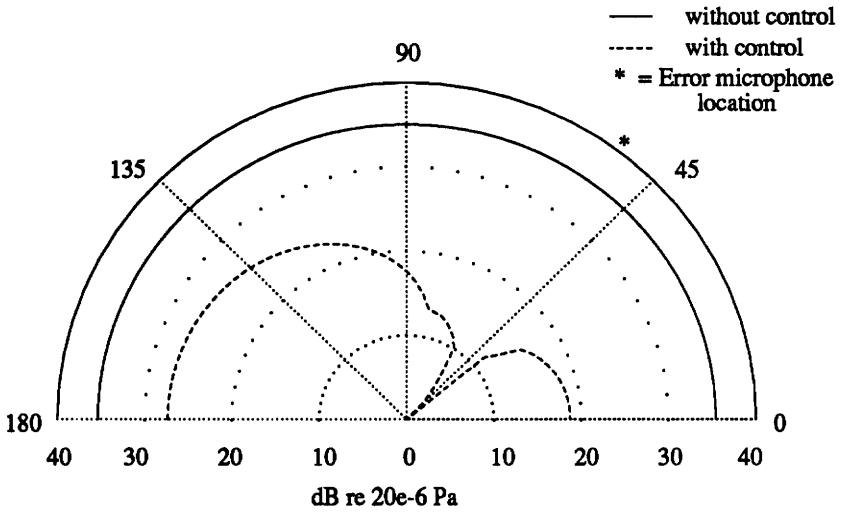

Figure 4.34: Semi-infinite/clamped beam theoretical acoustic far-field, 320Hz, piezoelectric controller #1, error microphone 51.4° . (*a*) perpendicular microphone array data, (*b*) axial microphone array data.

$10m$.

Comparing the acoustic "near-field" as predicted by theory shown in Fig. 4.32 with a similar experimental case shown in Fig. 4.28 we see that each case shows a large attenuation at the error microphone with global attenuation of the acoustic field. Comparing the wavenumber spectrum from the theoretical case shown in Fig. 4.33 with that shown in Fig. 4.28 a similar decrease in the supersonic wavenumber region was obtained. This implies that the far-field acoustic levels were attenuated as predicted by theory shown in Fig. 4.34.

4.1.5 Summary of the Semi-infinite/Clamped Beam Experimental Results

The following is a summary of the conclusions drawn from the results of the semi-infinite/clamped beam experiments.

- **Actuator Location and Number of Actuators**

    1. Global attenuation was better when the actuator was closer to the discontinuity. This was due to a better control authority over the flexural near-field waves when the control actuator was close to the discontinuity.
    2. When two actuators were used the local and global attenuation was better. This was because the controller had more degrees of freedom to control the error signal.

- **Error Microphone Location and Number**

1. Local attenuations were best when one error microphone was used. Global attenuations were best when two error microphones were used. This was because the controller had had to compromise between the minimizations of the two error signals.

2. For either one or two error microphones, the best global attenuations were obtained from the perpendicular array. This was due to the more simple pattern of the perpendicular acoustic field.

- **Frequency**

1. For the best global control the control actuator was within the region of the displacement that was significantly affected by the reflected flexural near-field wave as mentioned above.

2. Similar behavior was noted in the acoustic attenuation at all frequencies.

- **Actuator Type**

1. Overall, the piezoelectric actuators were superior to the point force shakers. This was supported by Guigou's theory [16] presented previously and was due to the distributed nature of the piezoelectric actuator.

- **Mechanisms of Control**

1. The mechanism by which attenuation of the acoustic far-field was achieved while controlling the acoustic "near-field" was demonstrated as a decrease in the supersonic wavenumber components under control.

4.2 Infinite Beam with a Blocking Mass

In this section the results from the infinite beam with a blocking mass experiments are presented. Experimental cases are presented which compare the actuator location and number, the error microphone location and number, the operation frequency, the actuator type and the blocking mass size. In addition, an experimental case is discussed which displays some problems associated with the second anechoic termination and the corresponding solution to the problem.

These experiments were described in Ch. 2 and are shown schematically in Fig. 2.2 and photographically in Fig. 2.4. The actuators considered in these experiments are referred to by their numbers as labeled in Figs. 2.15 and 2.17.

4.2.1 Problems with Anechoic Termination #2

In the first attempts at experiments on the infinite beam with a blocking mass some problems were encountered with anechoic termination #2 which was located inside the anechoic chamber. This termination, although it had good power reflection characteristics (see Fig. 2.7) did not absorb all of the incident flexural energy. The energy which was not absorbed was reflected in the form of traveling and near-field flexural waves. This scattering of the incident traveling wave produced supersonic wavenumber components which, in turn, made the region of the interface between the beam and termination an acoustic noise source. This source of acoustic radiation interfered with the experiments conducted on the infinite beam with a blocking mass. It is likely that termination #1 displayed similar behavior, however, since it was located outside of the anechoic chamber, the noise it produced did not interfere

with the experiments.

An experimental case driven at 320Hz, controlled by shaker #2 and with an error microphone located at 51.4° axially is shown in Figs. 4.35 and 4.36. This is an example of the worst behavior seen in these experiments. Notice that, although there was good attenuation at the error microphone, the acoustic field, on a global scale, increased dramatically. Also notice that the maximum increase occurs in the portion of the axial array that was closest to the anechoic termination (90° $\rightarrow$ 180°). This led the author to investigate the effect of the termination on the acoustic field and to a solution to the problem.

If the power reflection ratio for the termination located inside the anechoic termination (see Fig. 2.7) is considered, it is noted that this termination had its worst power reflection behavior at 320Hz (compared to 510Hz and 690Hz). It was evident in the experiments that the problem of the anechoic termination inside the anechoic chamber creating noise was worse at 320Hz, however, problems were also noted at the other frequencies.

In order to correct the problem, a $20cm$ layer of fiberglass insulation (similar to that lining the anechoic chamber walls) was placed over the area where the beam entered the termination. This layer of insulation served to absorb some of the sound produced in this region. Intensity measurements (shown in App. A) were taken at several points along the length of the beam $20cm$ above it in order to quantify the source strength of termination #2 and the effect of the insulation placed over it. The results from these measurements are shown in App. A.

It is shown in the intensity plots in App. A that the layer of insulation over the

(a)

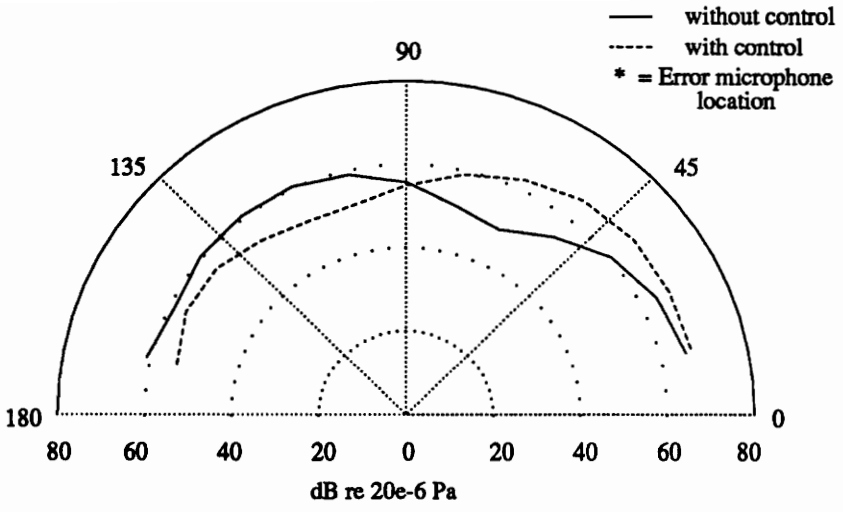

(b)

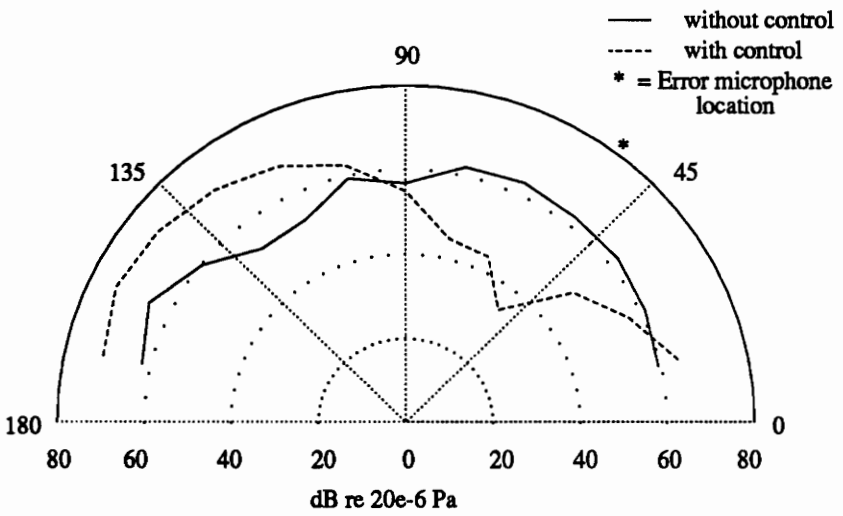

Figure 4.35: Infinite beam with blocking mass #1 acoustic field, 320Hz shaker controller #1, error microphone 51.4° axial. (*a*) perpendicular microphone array data, (*b*) axial microphone array data.

(a)

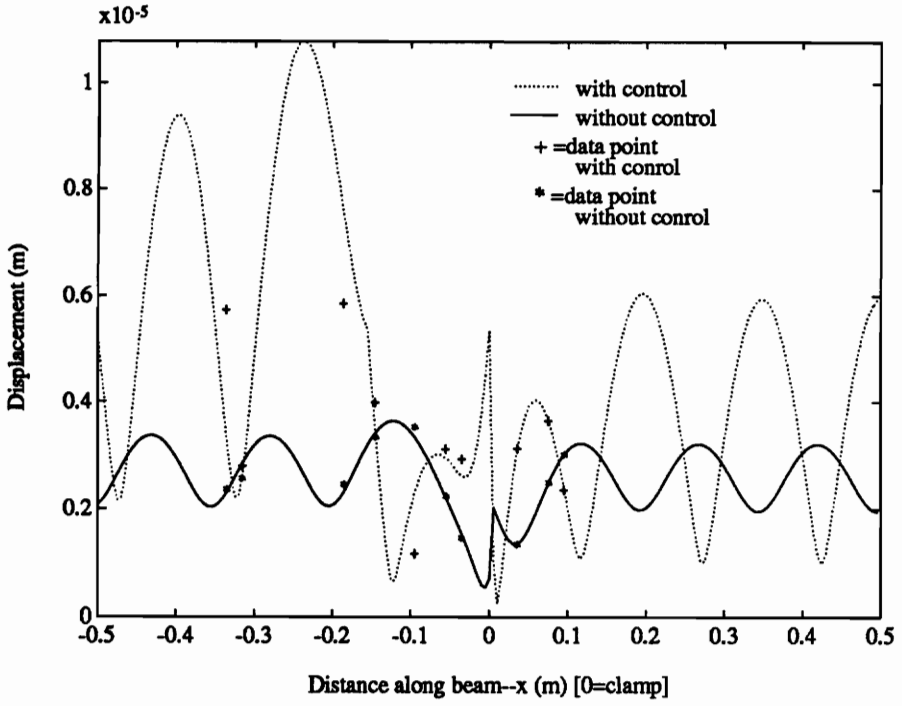

(b)

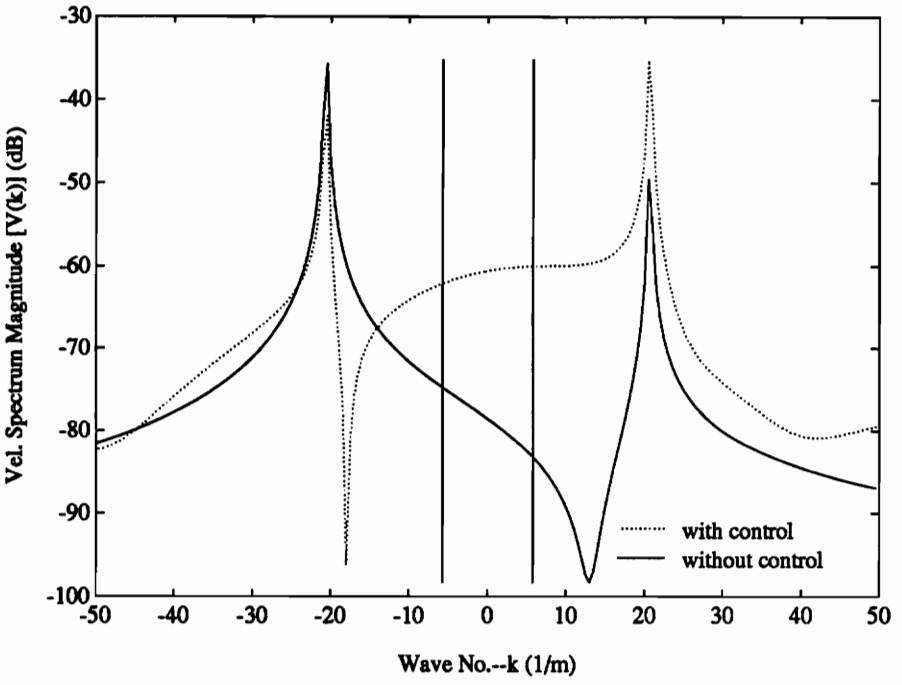

Figure 4.36: Infinite beam with blocking mass #1, 320Hz shaker controller #2, error microphone 51.4° axial. (*a*) decomposed displacement, (*b*) corresponding velocity wavenumber spectrum.

area of the termination/beam interface solved the problem. This was also evident in experiments performed later.

One other method of further reducing the source strength of termination #2 was to reduce the amplitude of the incident wave. This was accomplished by employing a larger blocking mass discontinuity. A larger discontinuity reflected more of the traveling waves incident on it while decreasing the amplitude of the wave transmitted through it (which was the wave incident on termination #2). Results from these experiments are presented in this chapter.

4.2.2 Actuator Location Comparison

Figure 4.37 shows the results of the acoustic field for the infinite beam with blocking mass #1, driven at 320Hz, controlled by shaker #1, and with error microphones located at 51.4° and 128.6° in the perpendicular array. The corresponding displacement and wavenumber spectrum are depicted in Fig. 4.38. In this experimental case an attenuation at the error microphones of $23dB$ was achieved while the global attenuation was on the order of $20dB$ in the perpendicular array and on the order of $5dB$ in the axial array.

The decomposed displacement for this experimental case (shown in Fig. 4.38) showed an increase in the standing wave amplitude in the region of $x > 0$ and a decrease in the standing wave amplitude in the region of $x < 0$. Notice that the supersonic region of the wavenumber spectrum showed an increase under control. This implies that the far-field acoustic levels were increasing while the "near-field" levels were decreasing under control.

(a)

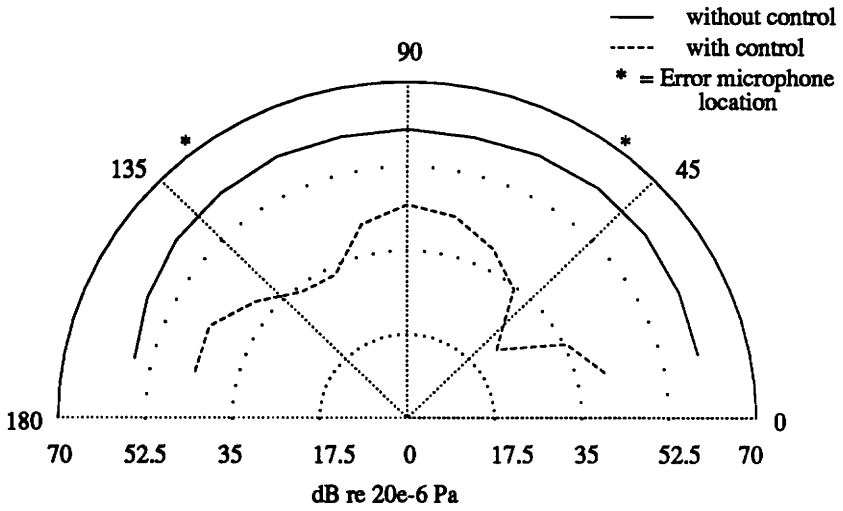

(b)

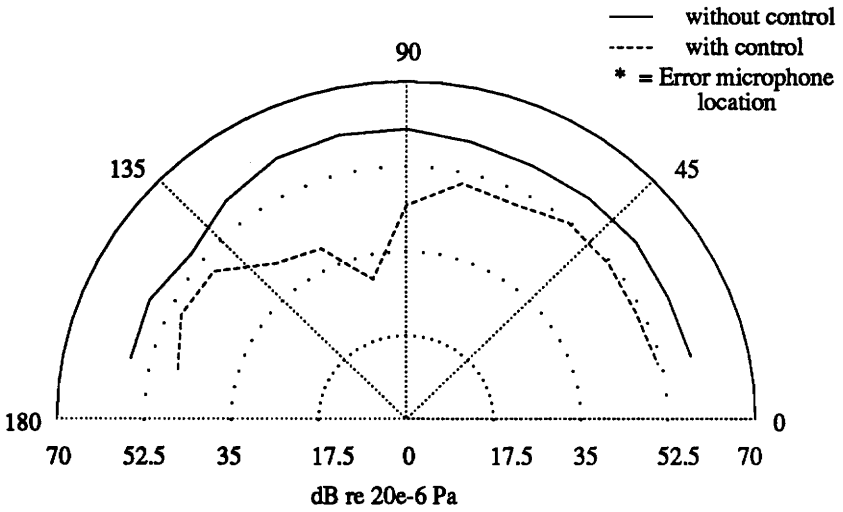

Figure 4.37: Infinite beam with blocking mass #1 acoustic field, 320Hz shaker controller #1, error microphones 51.4° and 128.6° perpendicular. (*a*) perpendicular microphone array data, (*b*) axial microphone array data.

(a)

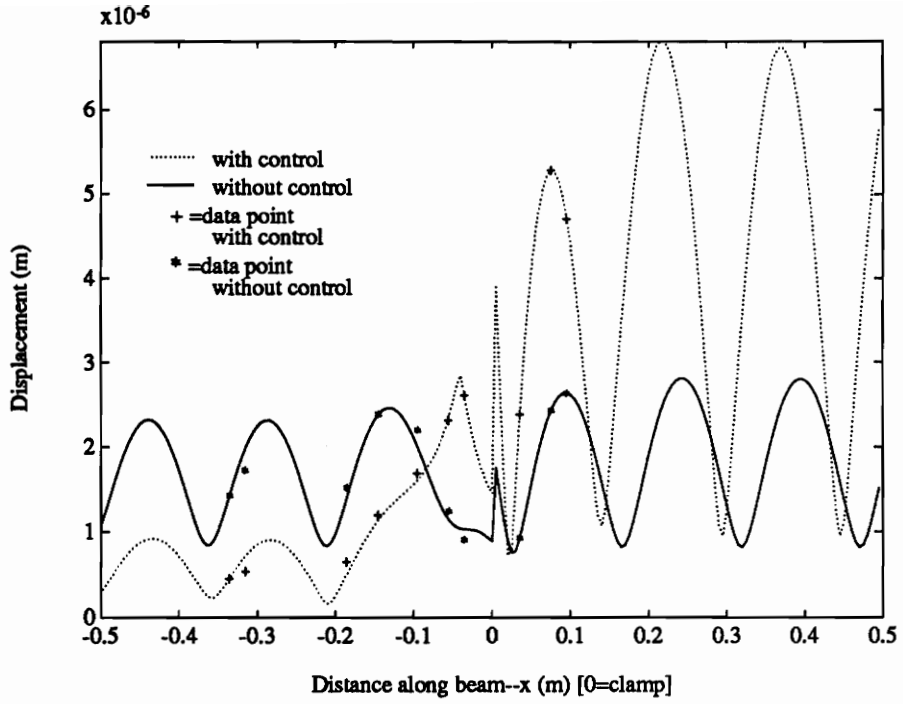

(b)

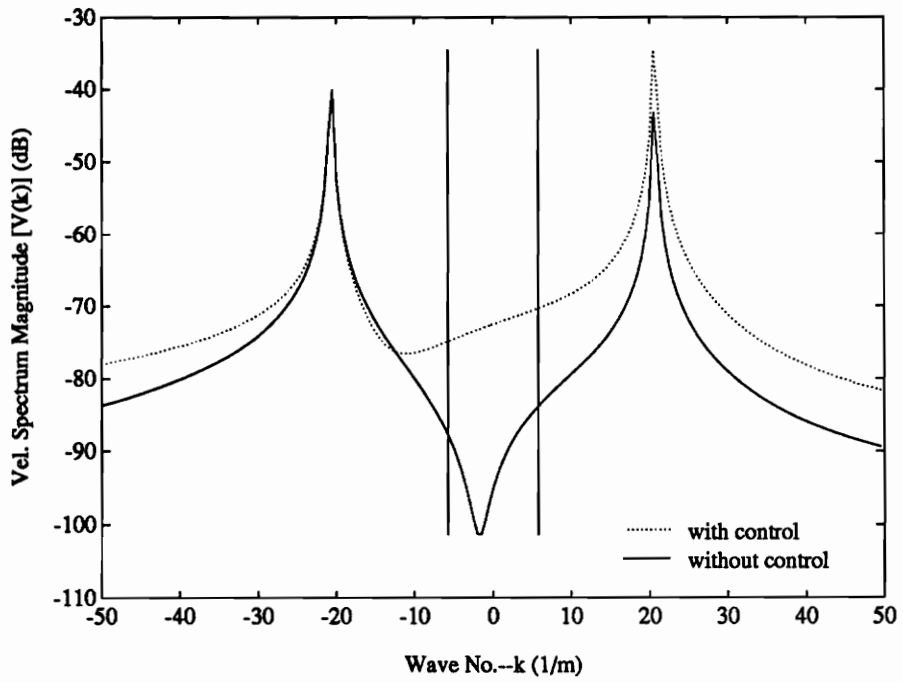

Figure 4.38: Infinite beam with blocking mass #1, 320Hz shaker controller #1, error microphones 51.4° and 128.6° perpendicular. (*a*) decomposed displacement, (*b*) corresponding velocity wavenumber spectrum.

This behavior in the supersonic region (as shown in Fig. 4.36) was consistent with the theoretical, optimal control situation for the infinite beam with a blocking mass. These results were calculated by Guigou [16] assuming the same geometry as was used in the experiments (including beam dimensions, blocking mass size, microphone array, etc.) and assuming an infinite baffle. The results of these calculations are presented in Figs. 4.39, 4.40 and 4.41. These figures show the acoustic "near-field" at a radius of $0.76m$ (computed from Eq. 1.24), the acoustic far-field at a radius of $10m$ (calculated from Eq. 1.18) and the corresponding displacement and wavenumber spectrum (calculated from Eqs. 1.14 and 1.31) respectively.

These results were constructed by applying optimal control to the "near-field" pressure at a location in the acoustic field corresponding to the error microphone location. A point force control actuator was assumed which was located at $x = -0.032m$. The acoustic "near-field" was then calculated (Fig. 4.39) along with the corresponding displacement and wavenumber spectrum (Fig. 4.41). Then, based on this displacement and wavenumber spectrum, the far-field acoustic field was calculated (Fig. 4.40).

It is shown in these results that, under these conditions, when the acoustic "near-field" was attenuated the supersonic wavenumber spectrum components increased along with the acoustic far-field. This, in fact, holds true for all experimental cases where the control was applied to the "near-field" on the infinite beam with a blocking mass. Since the equation describing the acoustic radiation in the "near-field" (Eq. 1.24) does not have a closed form solution, any interpretations from it which would explain this phenomenon would be difficult to obtain. An analogous situation (considered in Ch. 1) would be two point sources located close together with a

(a)

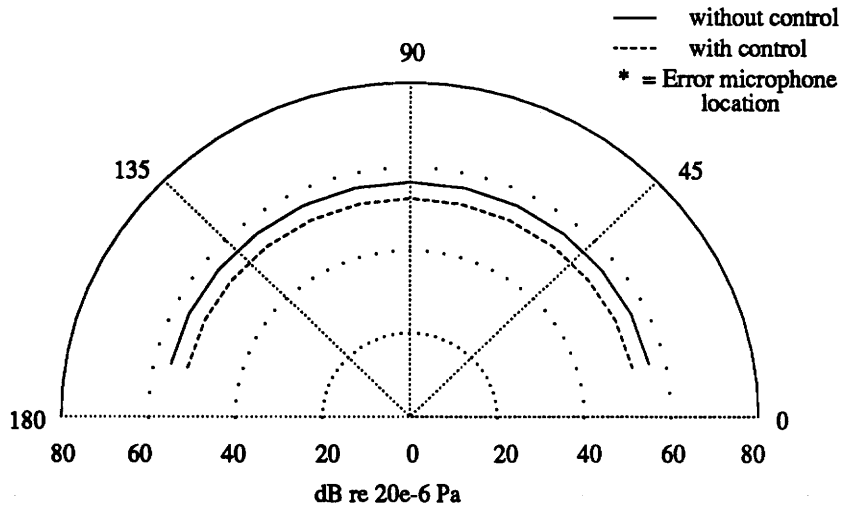

(b)

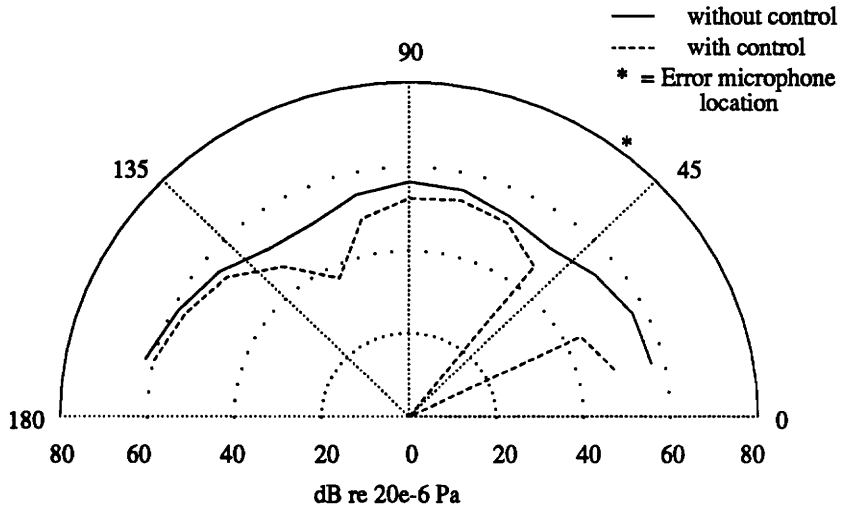

Figure 4.39: Infinite beam with blocking mass #1 theoretical acoustic "near-field", 320Hz, shaker controller #1, error microphone 51.4° axial. (*a*) perpendicular microphone array data, (*b*) axial microphone array data.

(a)

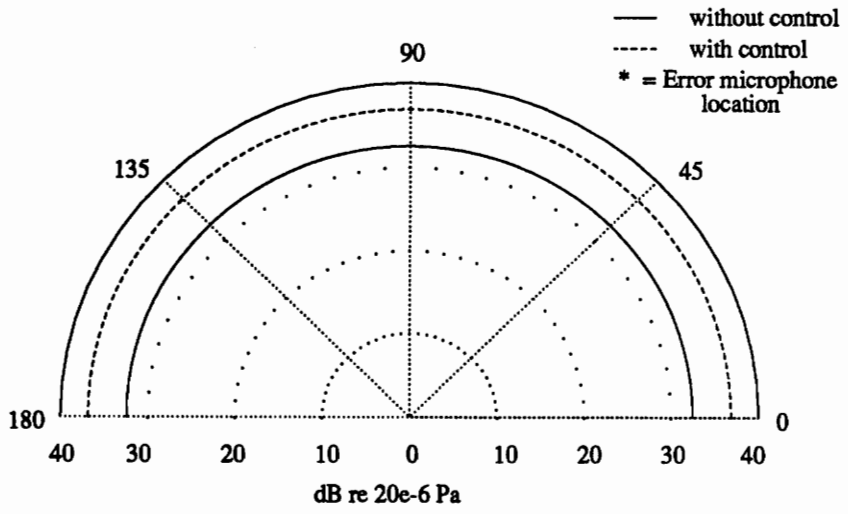

(b)

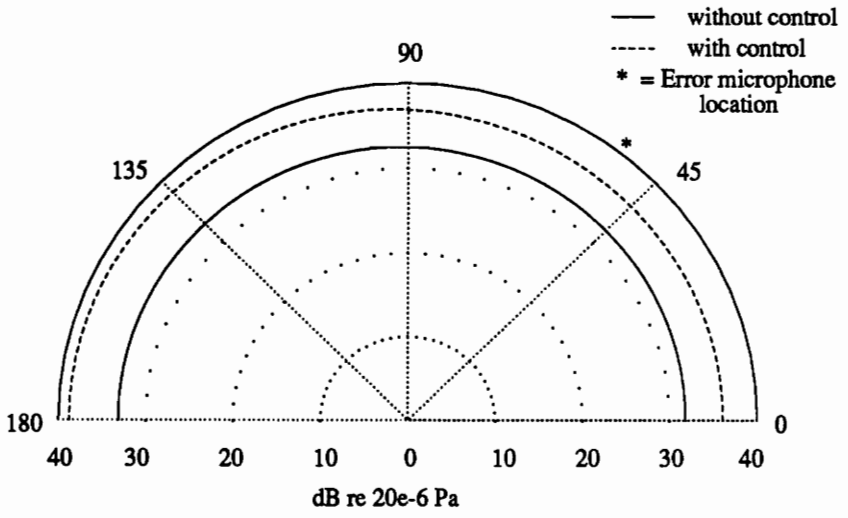

Figure 4.40: Infinite beam with blocking mass #1 theoretical acoustic far-field, 320Hz, shaker controller #1, error microphone 51.4° axial. (*a*) perpendicular microphone array data, (*b*) axial microphone array data.

(a)

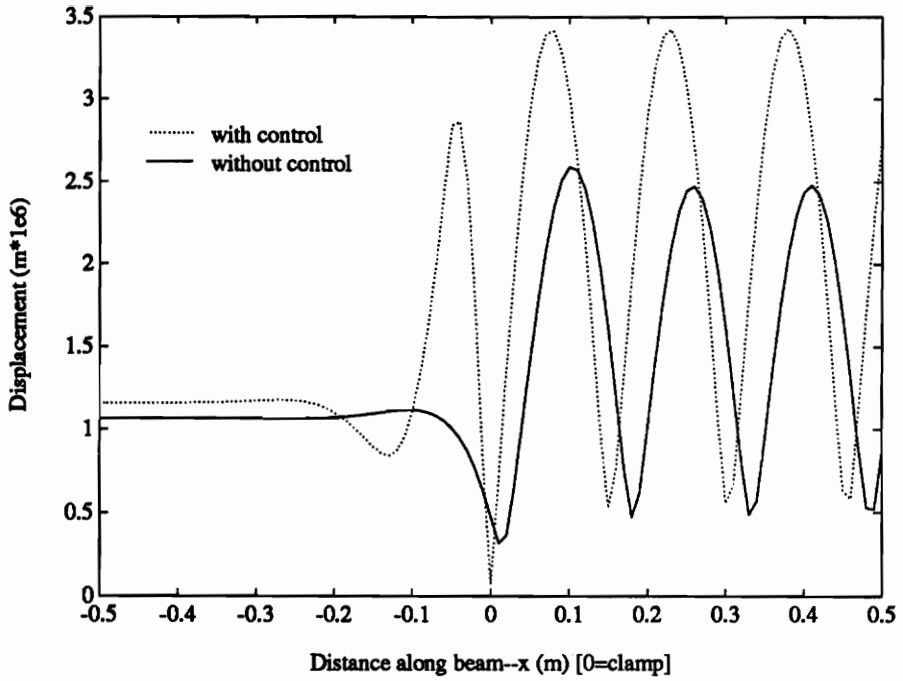

(b)

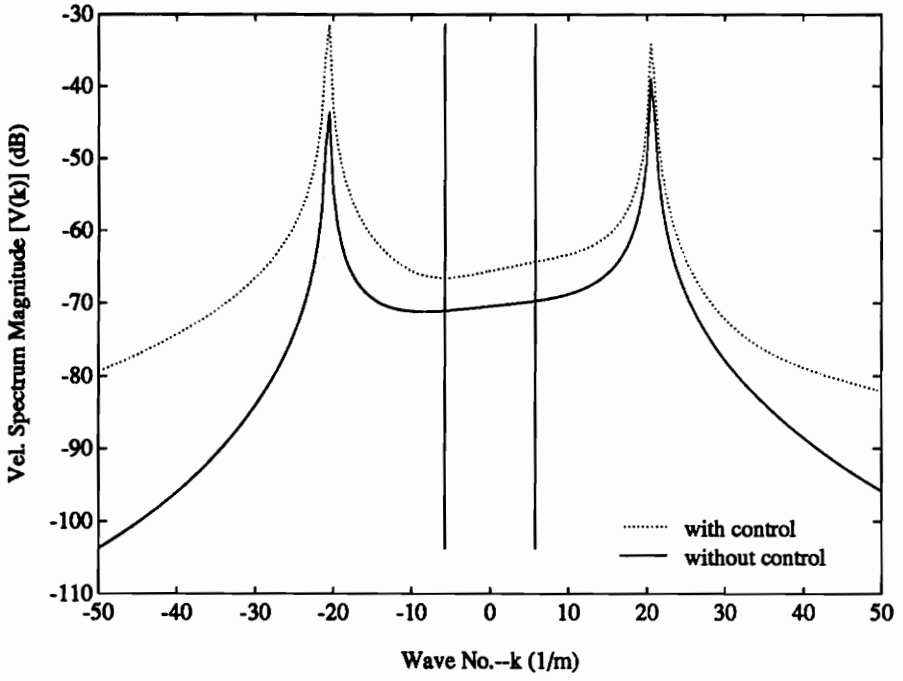

Figure 4.41: Infinite beam with blocking mass #1 theoretical data, 320Hz, shaker controller #1, error microphone 51.4° axial. (*a*) decomposed displacement, (*b*) corresponding velocity wavenumber spectrum.

variable phase between them. It was shown, in an earlier discussion in Ch. 1, that a situation could arise where the "near-field" acoustic levels were attenuated while the far-field levels increased (see Fig. 1.7).

Another possible explanation of decreasing "near-field" acoustic levels with increasing far-field levels is the two sided nature of the infinite beam with a blocking mass. The vibrational response had two flexural wave sets (both traveling and near-field), one on either side of the blocking mass. If one control actuator was employed it could only directly affect the flexural waves on the same side of the blocking mass. Hence, any change in the flexural waves on the other side of the blocking mass was a consequence of the changes in the traveling wave incident on the blocking mass on the side of the blocking mass with the controller. The incident and reflected flexural waves on the same side as the control actuator experienced some change in their amplitude and phase which resulted in the minimization of the acoustic level at the error microphone. The change in the transmitted flexural waves on the side of the blocking mass opposite the control actuator was a result of the changes in the incident and reflected waves and, hence, were indirectly affected by the control actuator. This could result in an increase in the supersonic wavenumber contribution by the waves on the transmitted side of the blocking mass which would explain the increase in the far-field radiation while the "near-field" levels decrease. This would also explain why the clamped beam (which did not have the two sided response that the beam with a blocking mass had) did not exhibit this behavior.

The previous explanation is only conjecture and would be very difficult to prove. An extensive set of theoretical cases which numerically evaluated Eq. 1.24 would be required with the intent of examining this behavior.

An attempt was made to control the acoustic radiation in the far-field. To do this a new microphone array with a $1.8m$ radius was constructed. Although, at 690Hz, the far-field would be at a radius of roughly $5m$ (which corresponds to 10 wavelengths) the attempt was still made in the hopes of displaying far-field behavior. Due to restrictions in the size of the anechoic chamber, the axial array could only cover part of the hemisphere. The results of this experiment are shown in Figs. 4.42 and 4.43. This experimental case was performed at 690Hz with a control shaker located at $x = 0$ and with an error microphone located at 51.4° axially. Although global attenuation was achieved the supersonic region of the wavenumber spectrum increased. This implies that the error microphone located at a radius of $1.8m$ was still in the "near-field". If the error microphone had been in the far-field, the supersonic region of the wavenumber spectrum would have decreased with a decreasing acoustic field.

The next experimental case considered for the actuator location comparison is shown in Figs. 4.44 and 4.45. This experimental case is the same as shown in Figs. 4.37 and 4.38 (driven at 320Hz, error microphones at 51.4° and 128.6°) except that shaker controller #2 was employed. In this experimental case an attenuation of $20dB$ was achieved at the 51.4° error microphone while $23dB$ of attenuation was achieved at the 128.6° error microphone. The global attenuation in the perpendicular array was about $20dB$ while only about $8dB$ was achieved in the axial array. The standing wave amplitude increases under control along with the supersonic wavenumber spectrum region.

Comparison of the previously discussed experimental case employing control shaker #1 (shown in Figs. 4.37 and 4.38) shows similar local attenuation when either con-

(a)

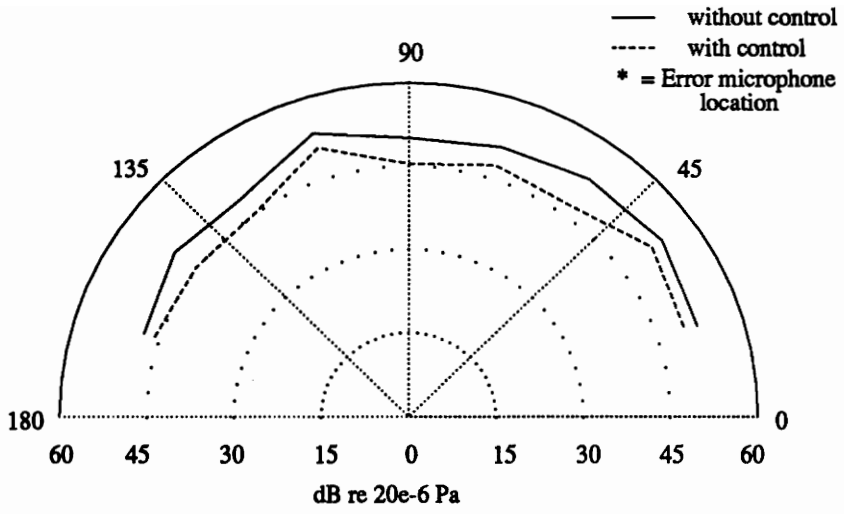

(b)

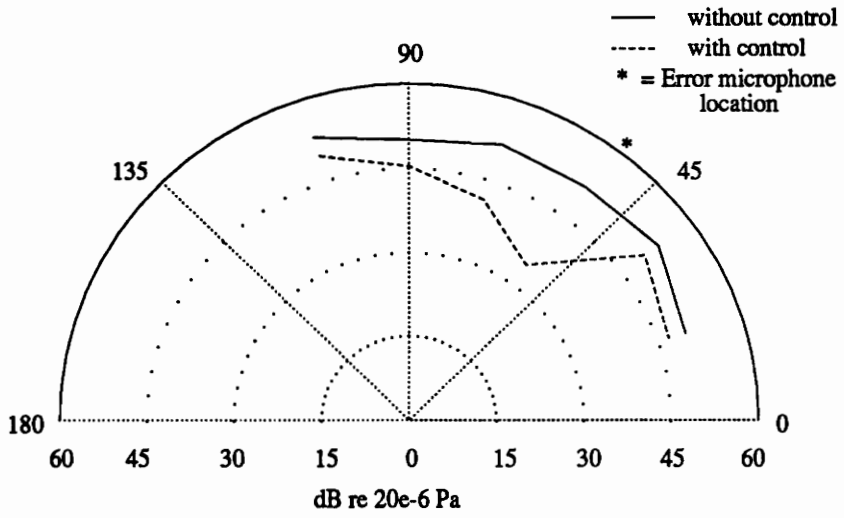

Figure 4.42: Infinite beam with blocking mass #2 acoustic field, 690Hz, shaker controller at $x = 0$, error microphone 51.4° axial at a radius of $1.8m$. (a) perpendicular microphone array data, (b) axial microphone array data.

(a)

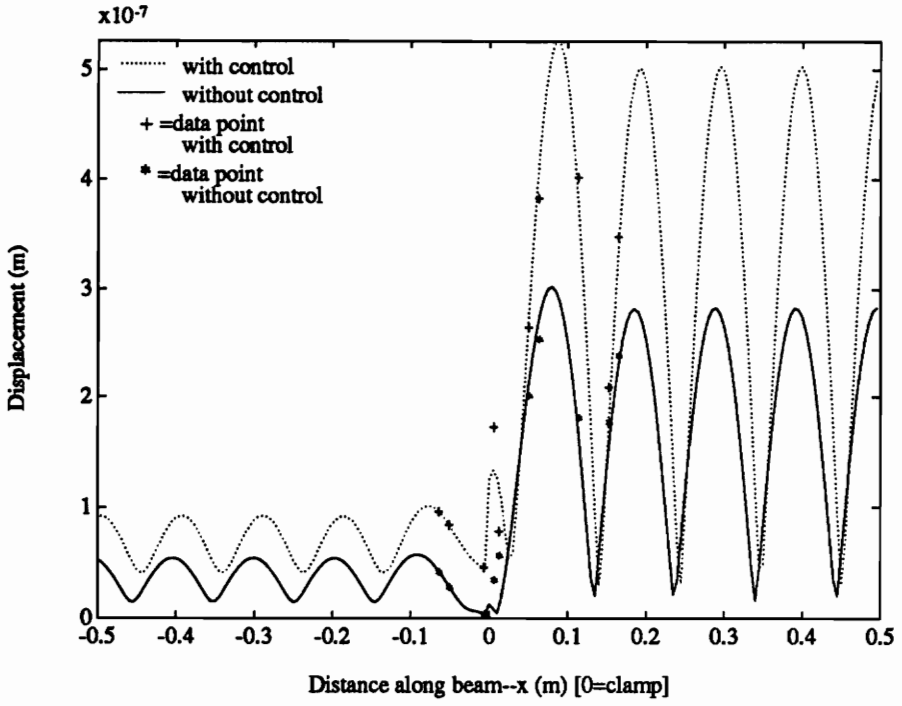

(b)

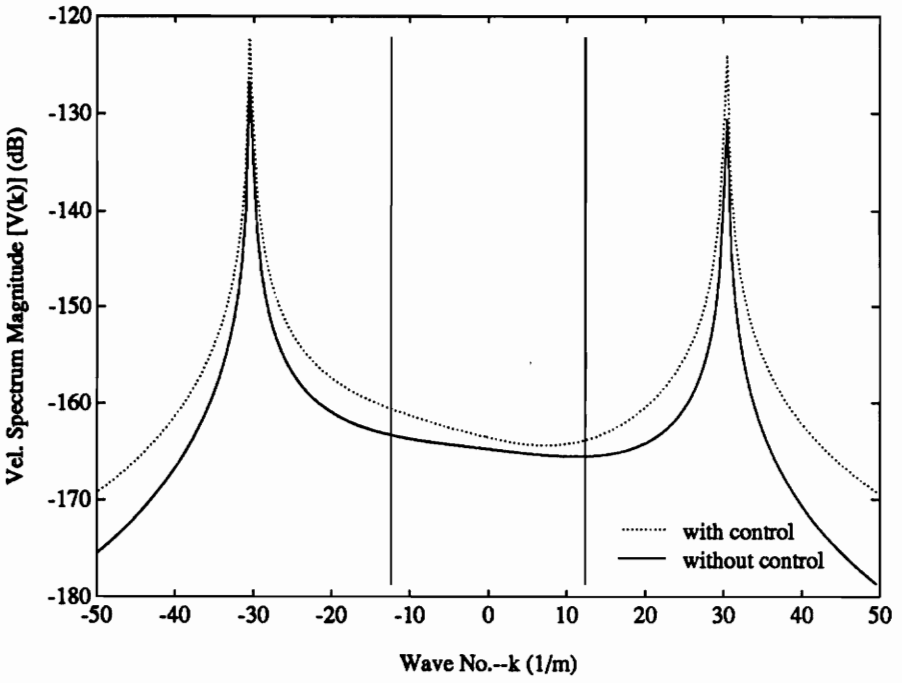

Figure 4.43: Infinite beam with blocking mass #2 data, 690Hz, shaker controller #1, error microphone 51.4° axial at a radius of $1.8m$. (a) decomposed displacement, (b) corresponding velocity wavenumber spectrum.

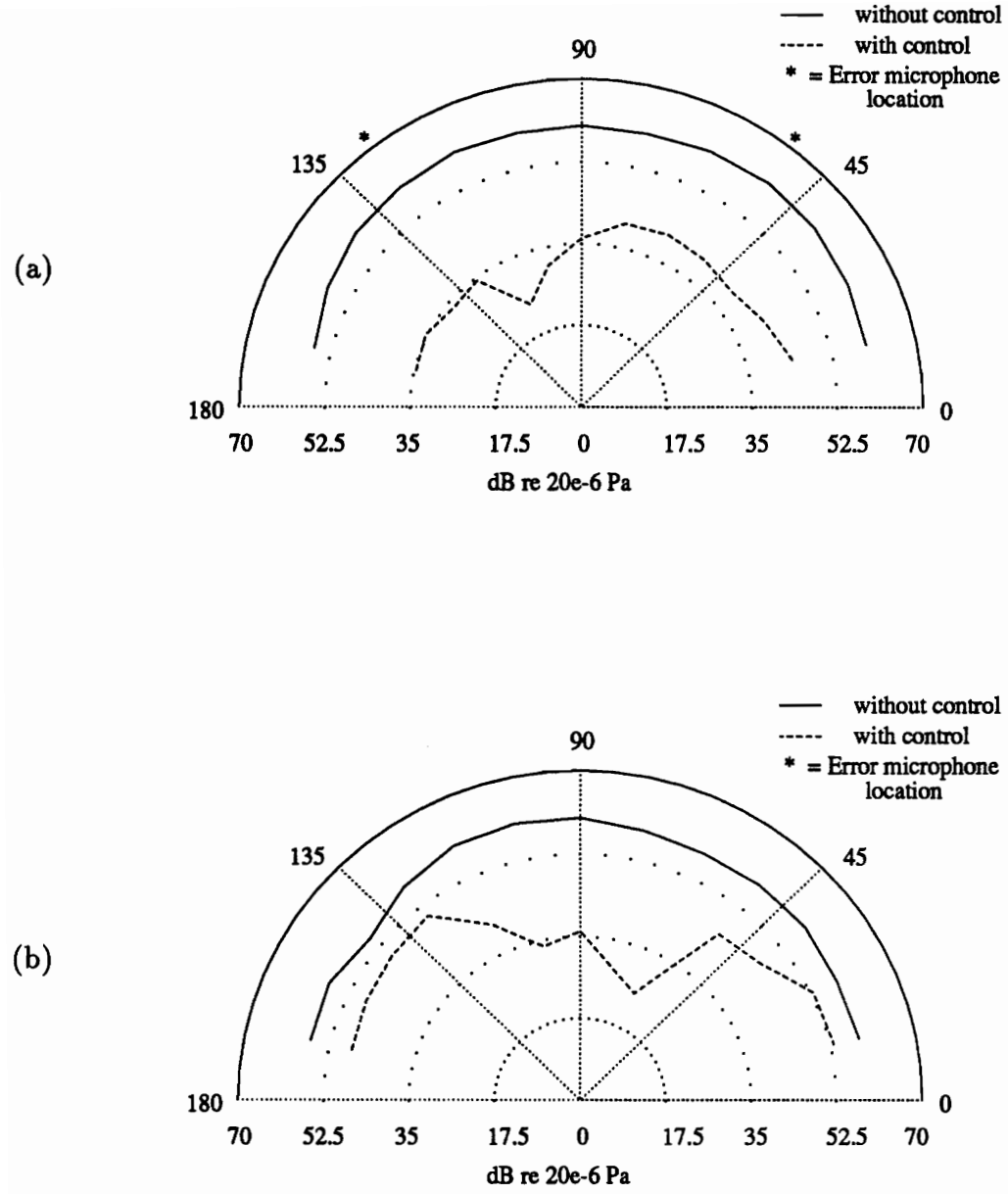

Figure 4.44: Infinite beam with blocking mass #1 acoustic field, 320Hz shaker controller #2, error microphones 51.4° and 128.6° perpendicular. (*a*) perpendicular microphone array data, (*b*) axial microphone array data.

(a)

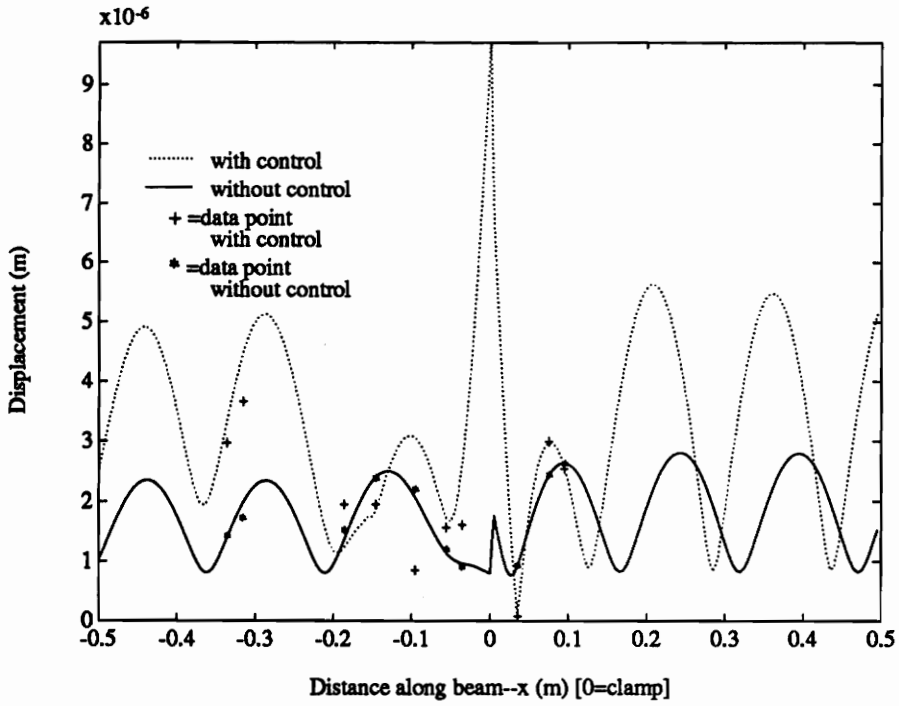

(b)

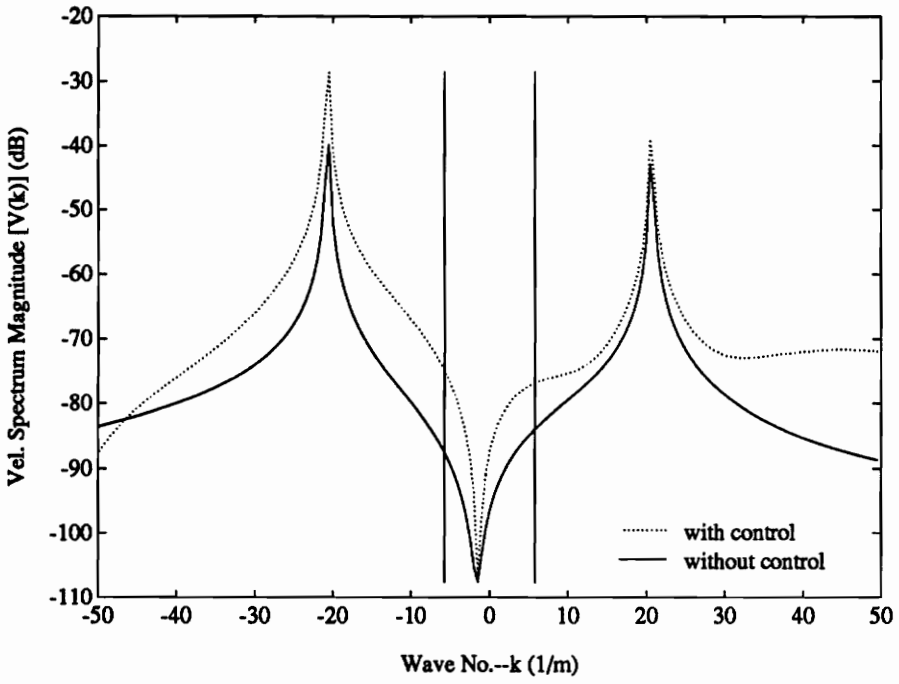

Figure 4.45: Infinite beam with blocking mass #1 data, 320Hz shaker controller #2, error microphones 51.4° and 128.6° perpendicular. (*a*) decomposed displacement, (*b*) corresponding velocity wavenumber spectrum.

troller was used and superior global attenuation when controller #2 was used. Since controller #2 was on the same side of the discontinuity as the input shaker, this implies that, by directly controlling the incident and reflected flexural waves, the global attenuation was improved. Since the incident and reflected waves were of greater amplitude they had a greater effect on the acoustic field than did the transmitted waves, thus, controlling the incident and reflected waves exhibited greater control on the acoustic field.

Finally, Figs. 4.46 and 4.47 show the experimental case where both shaker controllers #1 and #2 were used simultaneously. This experimental case was also driven at 320Hz and with error microphones located at 51.4° and 128.6° perpendicularly. In this experimental case an attenuation of $34dB$ was achieved at both error microphones while the global attenuation was on the order of $25dB$ in the perpendicular plane and about $10dB$ in the axial plane.

Comparing this experimental case to those using one control actuator (shown in Figs. 4.37, 4.38, 4.44, 4.45) shows that using two control actuators yielded improved attenuation both locally and globally. This was evident in the experiments on the semi-infinite/clamped beam as well. It was due to the fact that the controller had more degrees of freedom with which to affect the vibrational response of the beam and, hence, the acoustic field (as previously discussed).

4.2.3 Error Microphone Location Comparison

The first experimental case presented in the discussion of error microphone location is shown in Figs. 4.48 and 4.49. This experimental case was driven at 690Hz,

(a)

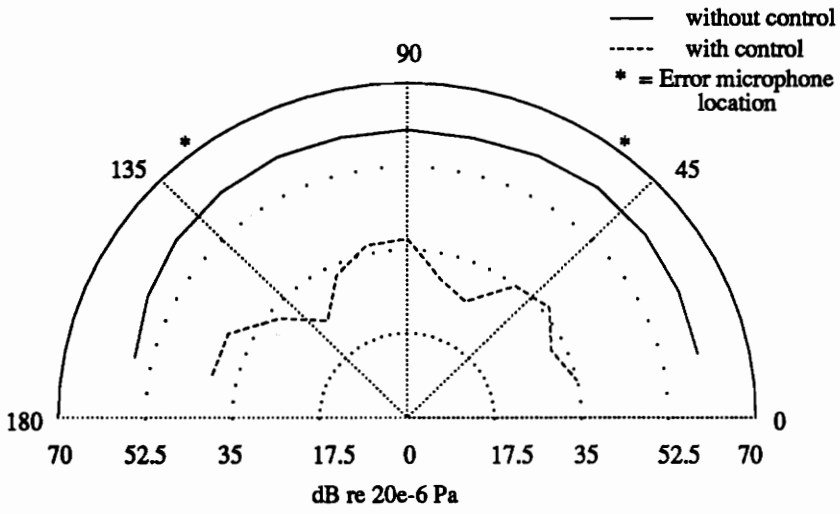

(b)

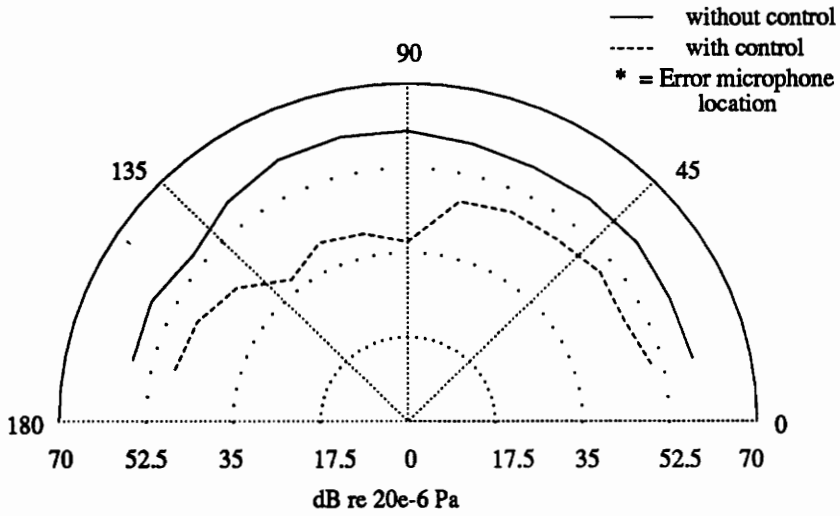

Figure 4.46: Infinite beam with blocking mass #1 acoustic field, 320Hz shaker controllers #1 and #2, error microphones 51.4° and 128.6° perpendicular. (*a*) perpendicular microphone array data, (*b*) axial microphone array data.

(a)

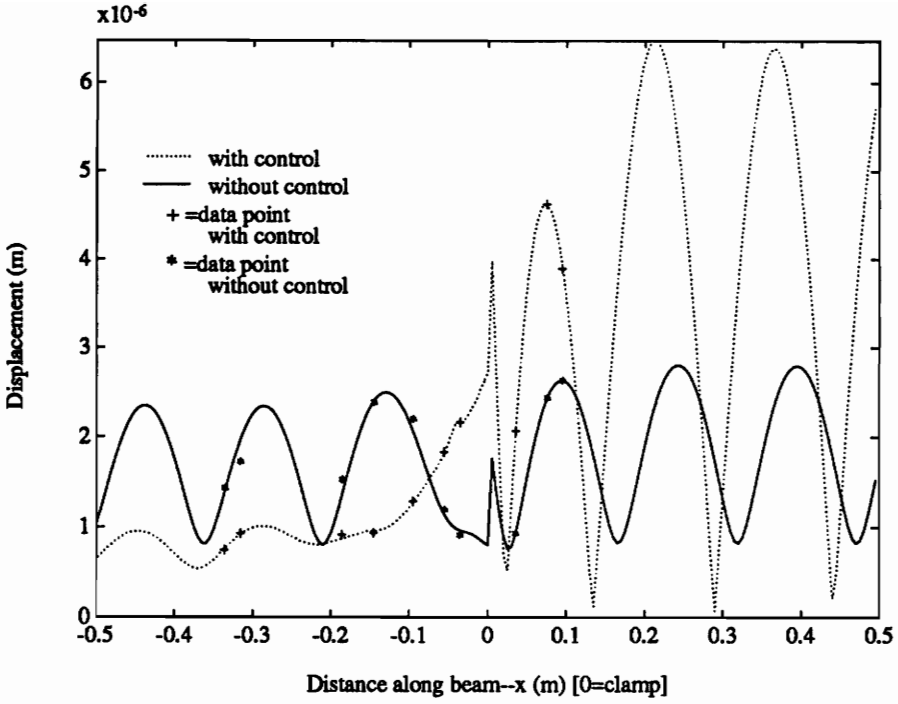

(b)

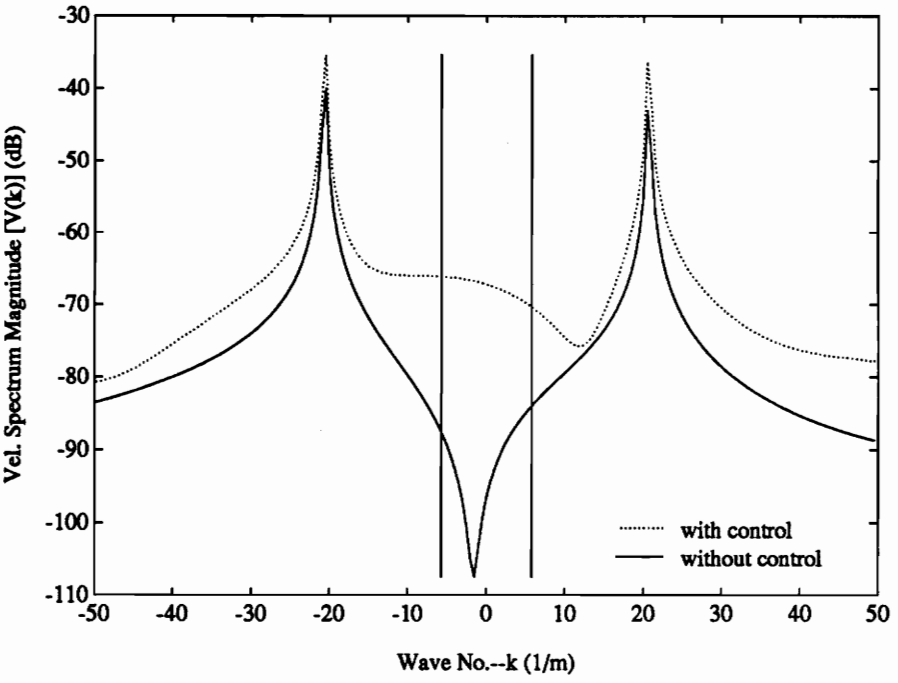

Figure 4.47: Infinite beam with blocking mass #1 data, 320Hz shaker controllers #1 and #2 , error microphones 51.4° and 128.6° perpendicular. (*a*) decomposed displacement, (*b*) corresponding velocity wavenumber spectrum.

(a)

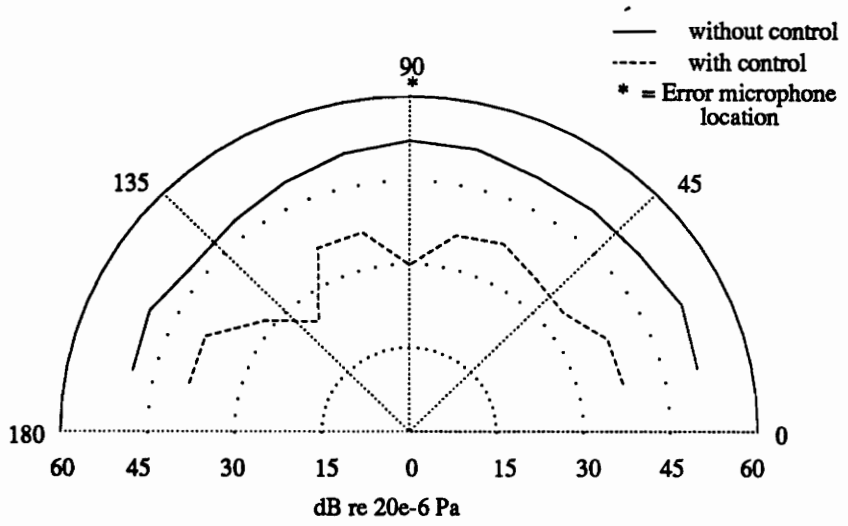

(b)

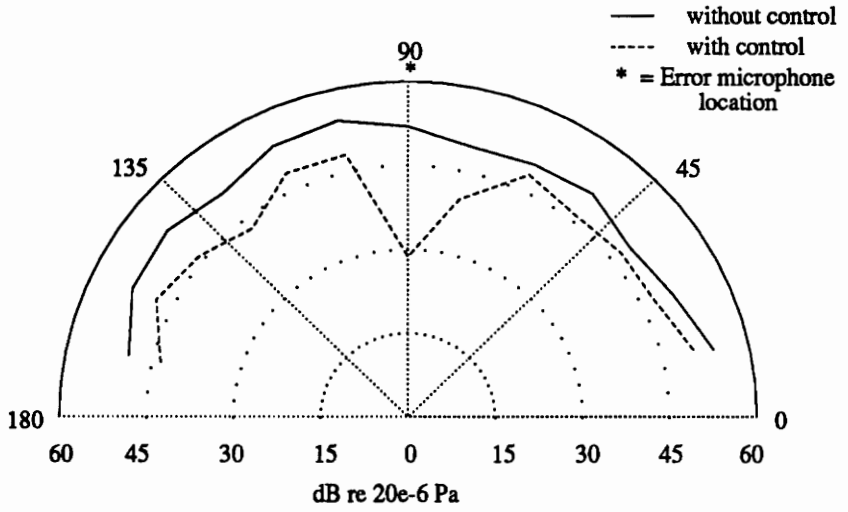

Figure 4.48: Infinite beam with blocking mass #1 acoustic field, 690Hz shaker controller #1 , error microphone 90°. (*a*) perpendicular microphone array data, (*b*) axial microphone array data.

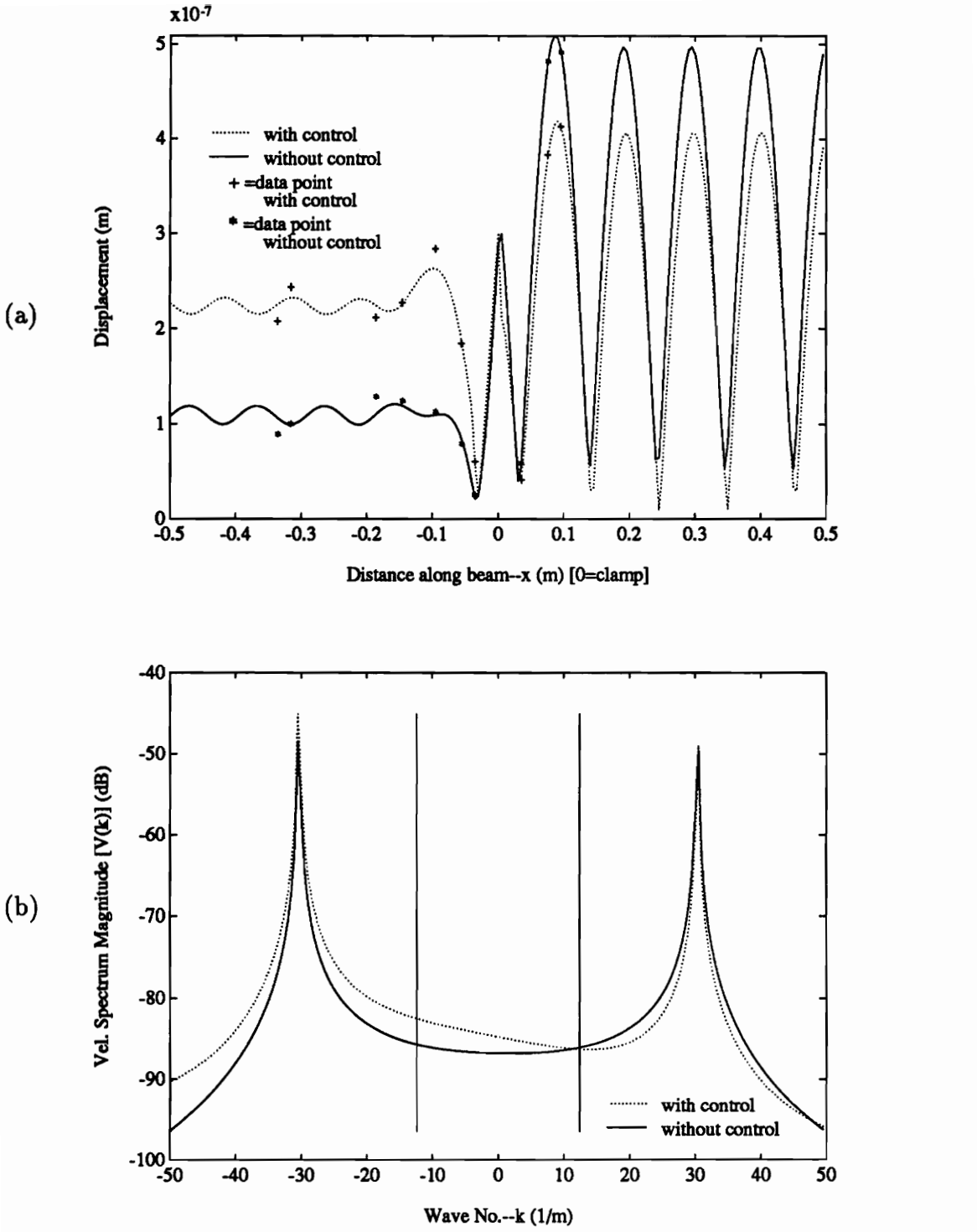

Figure 4.49: Infinite beam with blocking mass #1 data, 690Hz shaker controller #1, error microphone 90°. (*a*) decomposed displacement, (*b*) corresponding velocity wavenumber spectrum.

controlled by shaker #1 and had an error microphone located at 90°. An attenuation at the error microphone of $23dB$ was achieved while the global attenuation was on the order of $15dB$ in the perpendicular array and $5dB$ in the axial array. In the decomposed displacement the amplitude in the region of $x > 0$ decreased while it increased in the region of $x < 0$.

Notice in Fig. 4.49 in the region of $x < 0$ how the standing wave varies slightly about a constant magnitude displacement. This implies that the reflected wave from the termination is weak (almost non-existent) which shows good behavior by the anechoic termination. If there were no reflection from the termination this region of the displacement would be flat implying a pure traveling wave in one direction (as seen in the theoretical model shown in Fig. 4.41). This good behavior is due to the operating frequency of 690Hz which corresponds to a very good performance frequency for the anechoic termination (see Fig. 2.7). This behavior is shared by all of the experimental cases presented in this section that operated at 510Hz and 690Hz (except those with a controller in the region $x < 0$). Those experimental cases at 320Hz do not behave as well due to the relatively poor performance of the termination at this frequency.

Next, in Figs. 4.50 and 4.51, the experimental case driven at 690 Hz, controlled by shaker #1 and with an error microphone located at 128.6° in the perpendicular array is presented. In this experimental case an attenuation of $19dB$ was obtained at the error microphone while the global attenuation in the perpendicular array was about $12dB$ and only $8dB$ in the axial array. As before, the standing wave amplitude in the region of $x > 0$ decreased while it increased in the of $x < 0$. The supersonic region of the wavenumber spectrum increased under control which implies that the

(a)

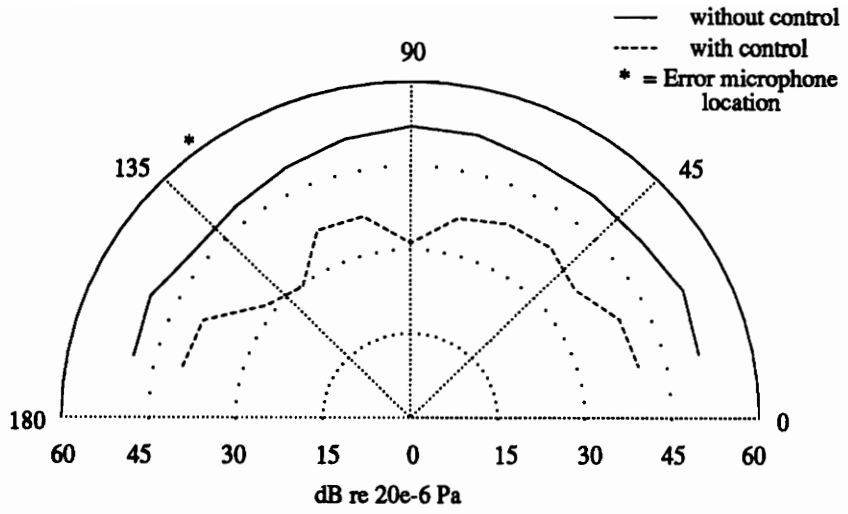

(b)

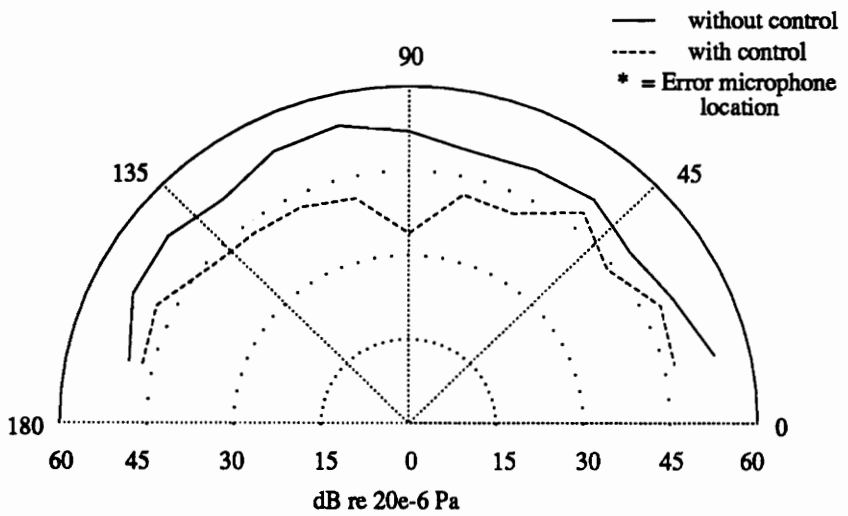

Figure 4.50: Infinite beam with blocking mass #1 acoustic field, 690Hz shaker controller #1, error microphone 128.6° perpendicular. (*a*) perpendicular microphone array data, (*b*) axial microphone array data.

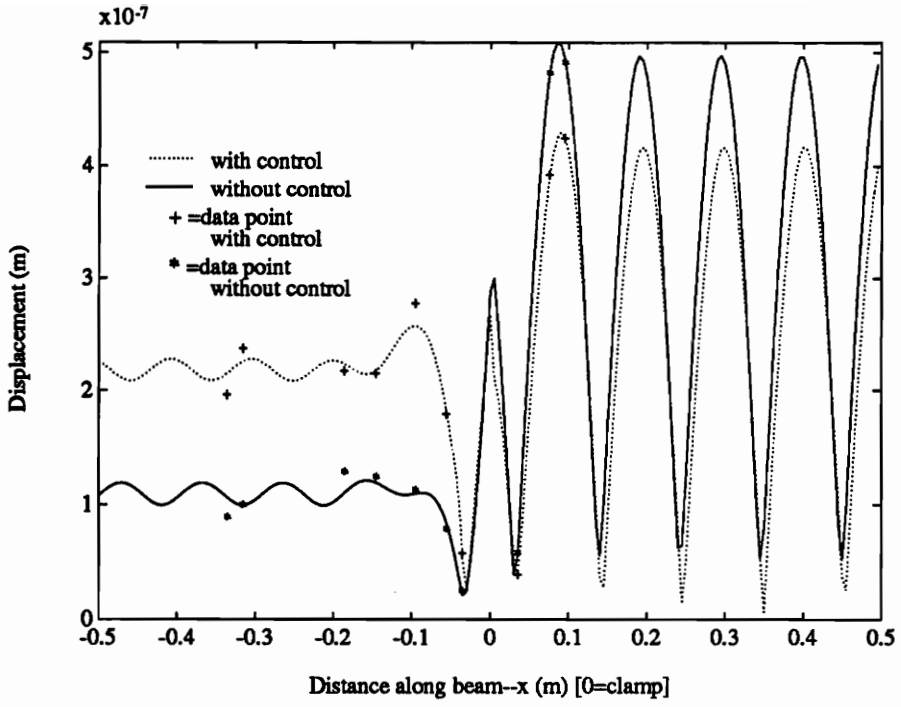

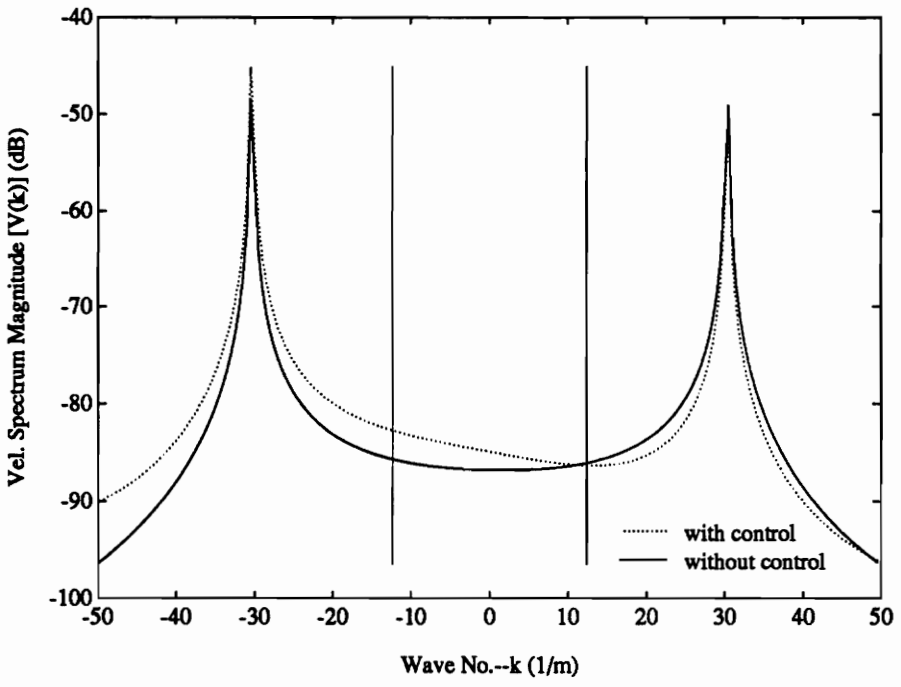

Figure 4.51: Infinite beam with blocking mass #1 data, 690Hz shaker controller #1, error microphone 128.6° perpendicular. (*a*) decomposed displacement, (*b*) corresponding velocity wavenumber spectrum.

far-field radiation increased under control.

Figures 4.52 and 4.53 show a similar experimental case (driven at 690Hz and controlled by shaker #1) but with an error microphone located at 128.6° axially. In this experimental case the attenuation at the error microphone was $24dB$ while the global attenuation in the perpendicular array was about $5dB$ and almost $0dB$ in the axial array. Once again, the displacement amplitude increased for $x < 0$ and decreased for $x > 0$ while the supersonic region of the wavenumber spectrum increased.

Comparison of this experimental case to the previous two experimental cases with one error microphone shows that for the 128.6° axially located error microphone a superior attenuation was achieved at the error microphone but, the global attenuation was not as good as the experimental case with a 90° error microphone or the 128.6° perpendicular error microphone.

Notice in Fig. 4.53 the "spike" in the displacement amplitude near $x = 0$. This type of behavior in the decomposition was seen in several experimental cases for the infinite beam. It is unlikely that this accurately depicts the displacement of the beam in this region, but, more likely, is evident of an inaccurate model of the beam displacement. These inaccuracies are a result of the assumption that the blocking mass was of infinitesimal width.

Recall that in the assumed equation of motion for the infinite beam (Eqs. 3.11 and 3.12) it was assumed that the blocking mass was of infinitesimal width and, therefore, was not considered in the model. In order for the assumption of an infinitesimal width blocking mass to be valid, the structural wavelength must be much greater

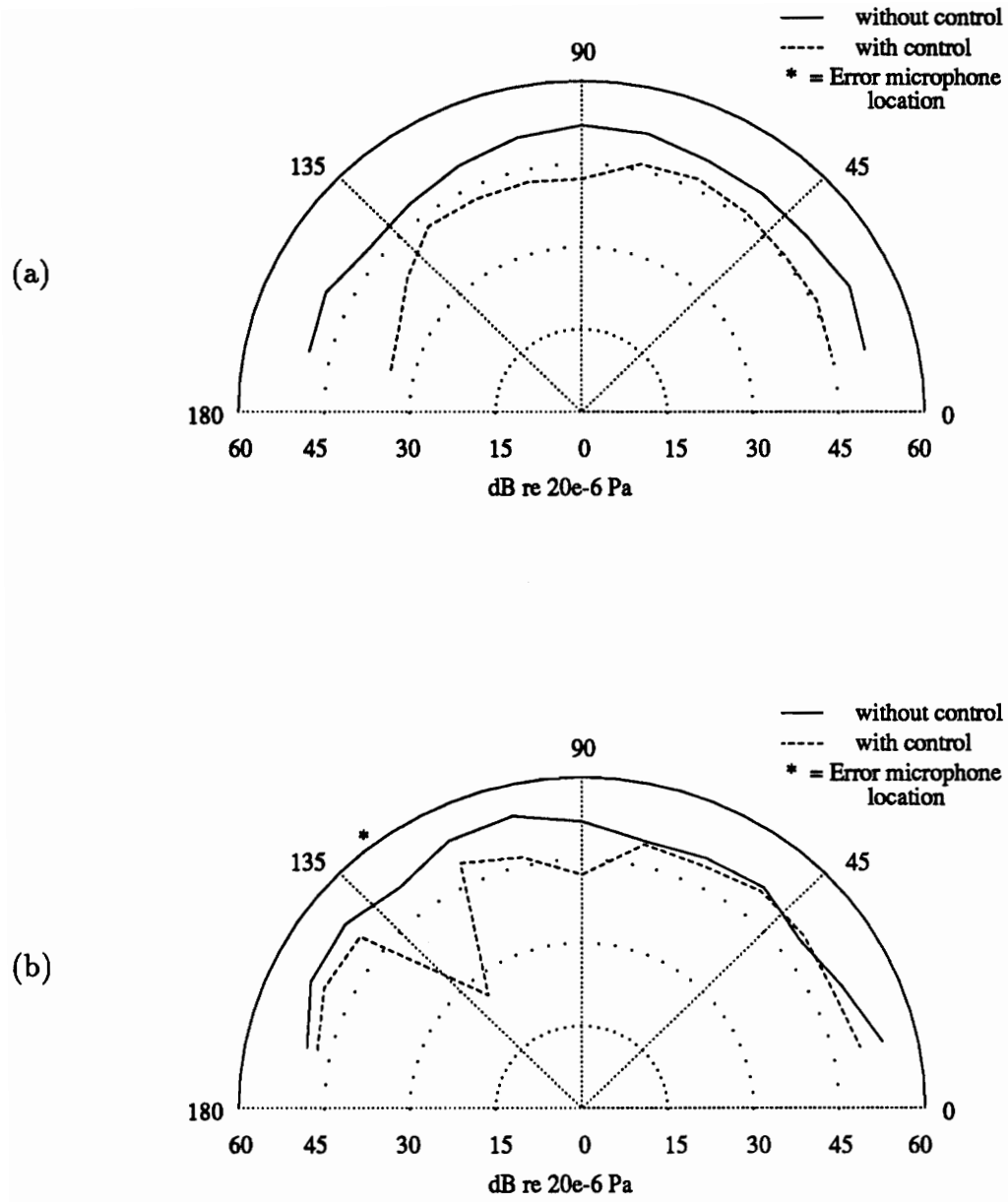

Figure 4.52: Infinite beam with blocking mass #1 acoustic field, 690Hz shaker controller #1, error microphone 128.6° axial. (*a*) perpendicular microphone array data, (*b*) axial microphone array data.

(a)

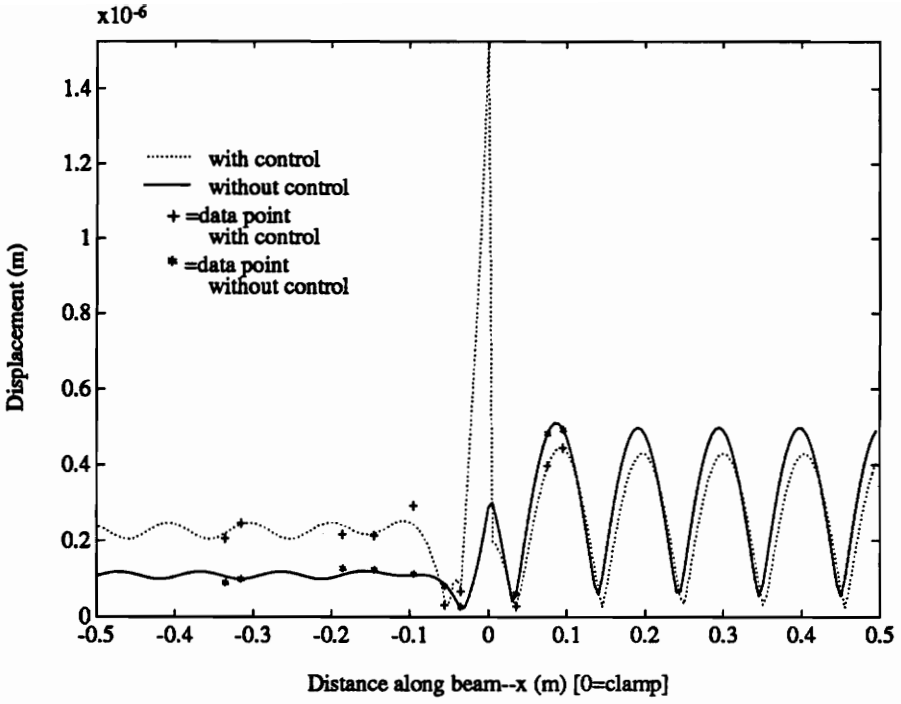

(b)

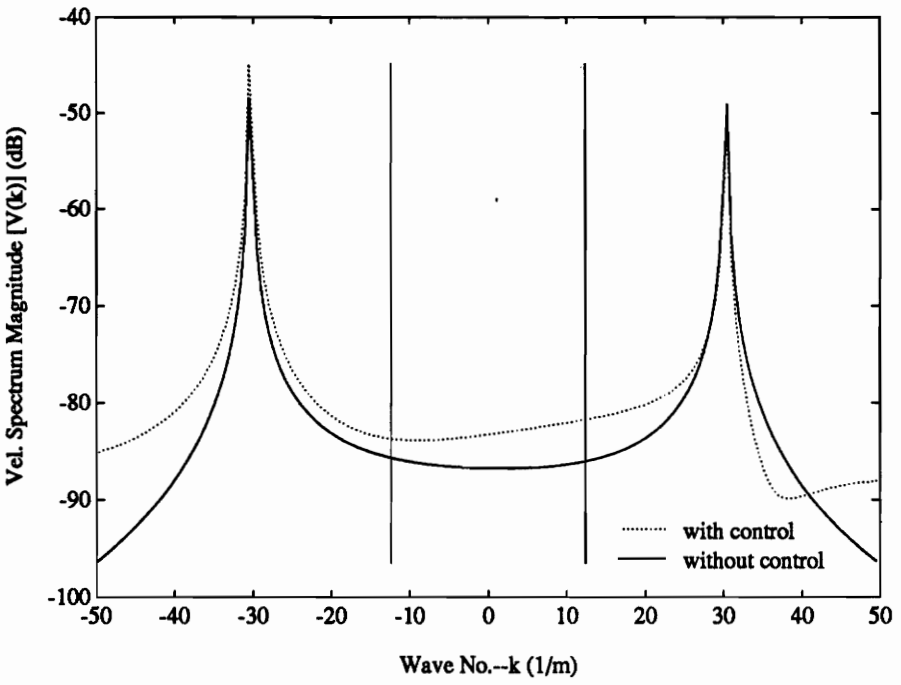

Figure 4.53: Infinite beam with blocking mass #1 data, 690Hz shaker controller #1, error microphone 128.6° axial. (*a*) decomposed displacement, (*b*) corresponding velocity wavenumber spectrum.

than the length of the blocking mass. For these experiments, the shortest structural wavelength was $20.7cm$ (corresponding to 690Hz) while blocking mass #1 had a width of $5.08cm$. This means that the wavelength is four times as long as the blocking mass. For blocking mass #2 ($2.54cm$ wide) this ratio is about eight. It may be noted that, for the experimental cases presented using blocking mass #2 these "spikes" in the displacement do not appear while they appear for a few of the experimental cases using blocking mass #1. Although the experimental cases that show such behavior may have inaccurate displacement and wavenumber spectrum results, the data still follows the trends depicted in other experimental cases and in the theoretical model, and is therefore included in these discussions.

In addition, modeling the blocking mass as having finite width would require several more unknowns to be introduced into the assumed equation of motion (at least two and possibly more for accurate modeling of displacement and rotation of the mass). This would require some accelerometers to be devoted to sensing the displacement of the blocking mass taking them away from the decomposition of the beam displacement and, in most control experimental cases, creating an under determined system of equations (since only ten accelerometers were available for these experiments).

The next experimental case to consider is similar to the previous three (driven at 690Hz and controlled with shaker #1) but with two error microphones located at 51.4° and 128.6° axially. This experimental case is shown in Figs. 4.54 and 4.55. In this experimental case an attenuation at both error microphones of $22dB$ was achieved while the global attenuation in the perpendicular array was about $4dB$ and about $10dB$ in the axial array. Just as in previous similar experimental cases, the displacement amplitude for $x > 0$ decreased and increased for $x < 0$ while the

(a)

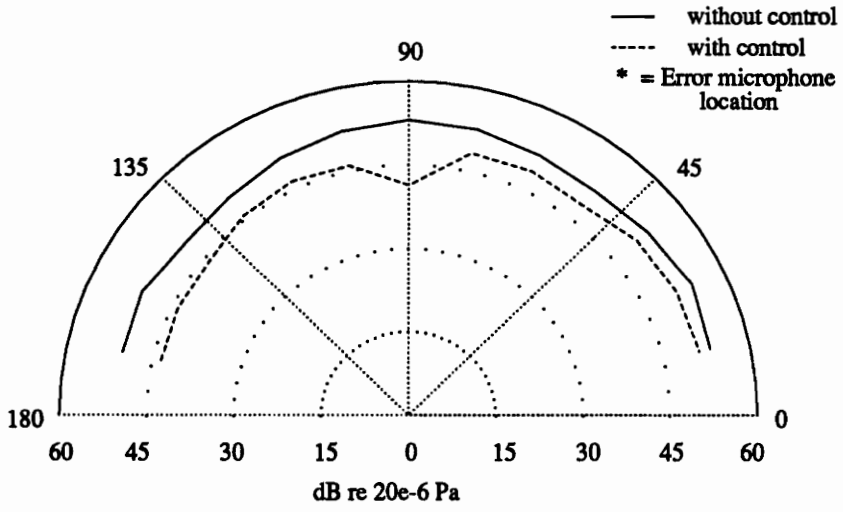

(b)

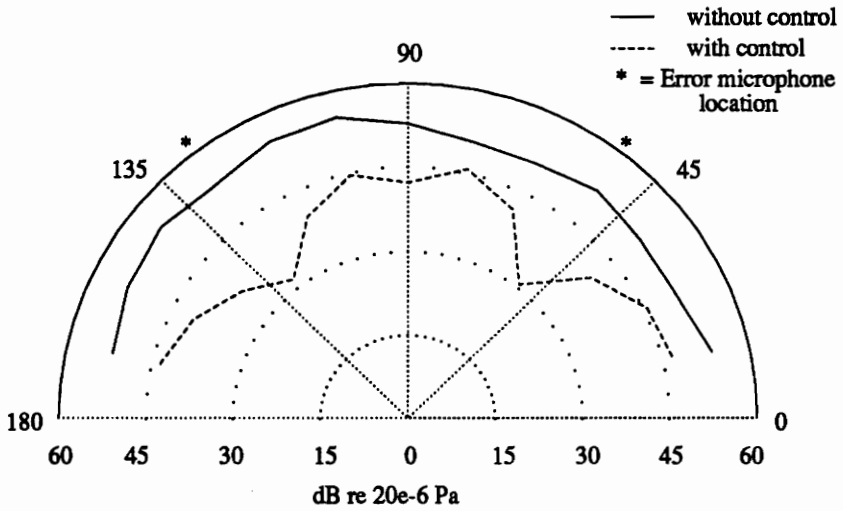

Figure 4.54: Infinite beam with blocking mass #1 acoustic field, 690Hz shaker controller #1, error microphone 51.4° and 128.6° axial. (*a*) perpendicular microphone array data, (*b*) axial array data.

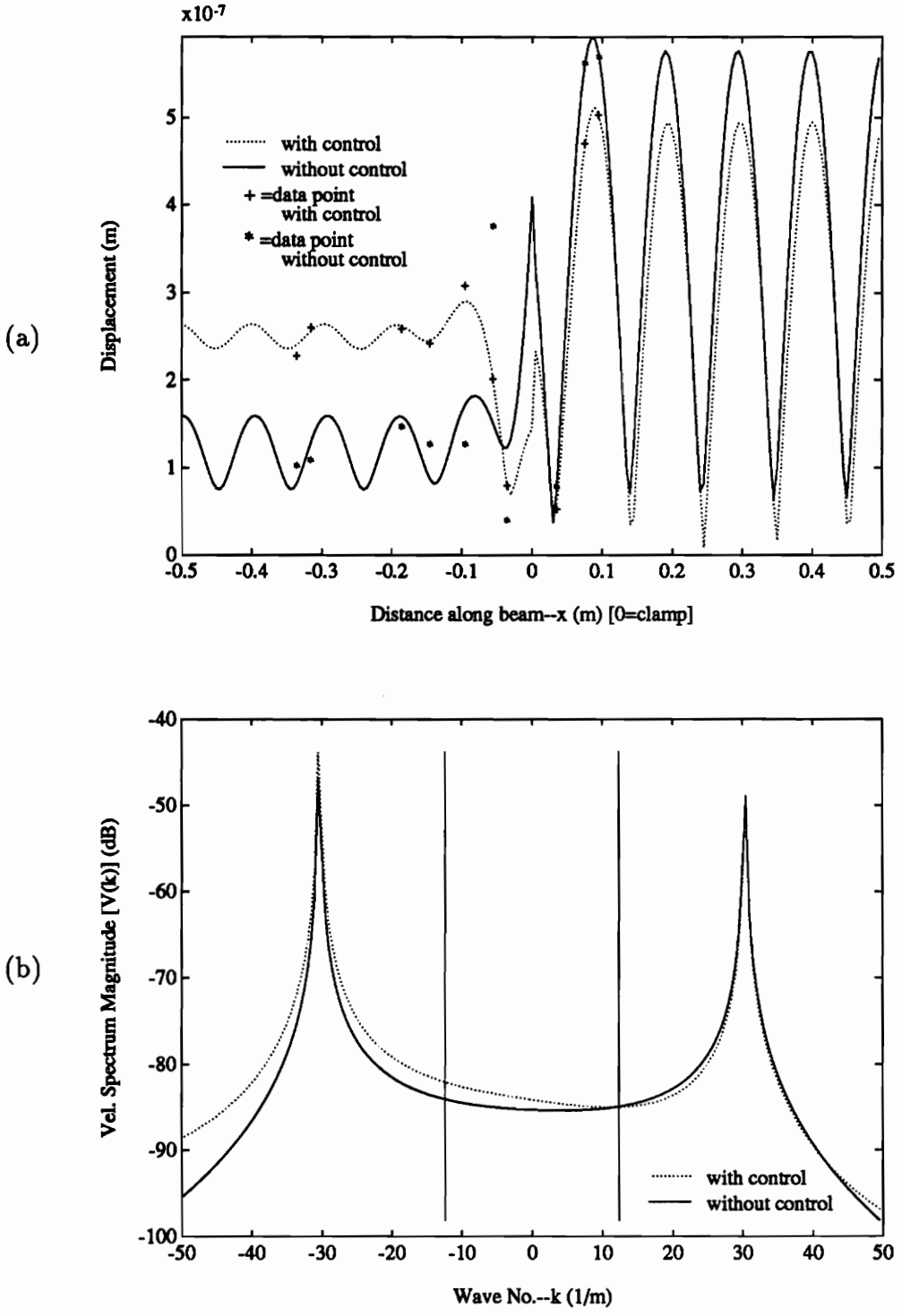

Figure 4.55: Infinite beam with blocking mass #1 data, 690Hz shaker controller #1, error microphone 51.4° and 128.6° axial. (*a*) decomposed displacement, (*b*) corresponding velocity wavenumber spectrum.

supersonic region of the wavenumber spectrum increased.

The last experimental case for the comparison of error microphone location is shown in Figs. 4.56 and 4.57. It is similar to the previous experimental cases (driven at 690Hz and controlled by shaker #1) except that the error microphones were located at 51.4° and 128.6° in the perpendicular array. In this experimental case an attenuation of $23dB$ was achieved at each error microphone. The global reduction of the acoustic levels was about $12dB$ in the perpendicular array and about $5dB$ in the axial array. Again, the displacement increased for $x < 0$ and decreased for $x > 0$ while the wavenumber spectrum increased in the supersonic region.

Comparison of the two experimental cases with two error microphones shows very similar results. Both experimental cases achieved about the same attenuation at the error microphones and the experimental case with the error microphones in the perpendicular array showed better global attenuation.

Comparing all of the experimental cases presented for error microphone location comparison shows that the best attenuation at a point was achieved when one error microphone was used. However, for global reduction of the acoustic field, two error microphones showed better performance. These two conclusions make sense when it is considered that, with two error microphones, the controller is trying to get the optimal reduction at both points and, therefore, must compromise between the two. With just one error microphone the controller can devote all of its ability to attenuation of the single signal.

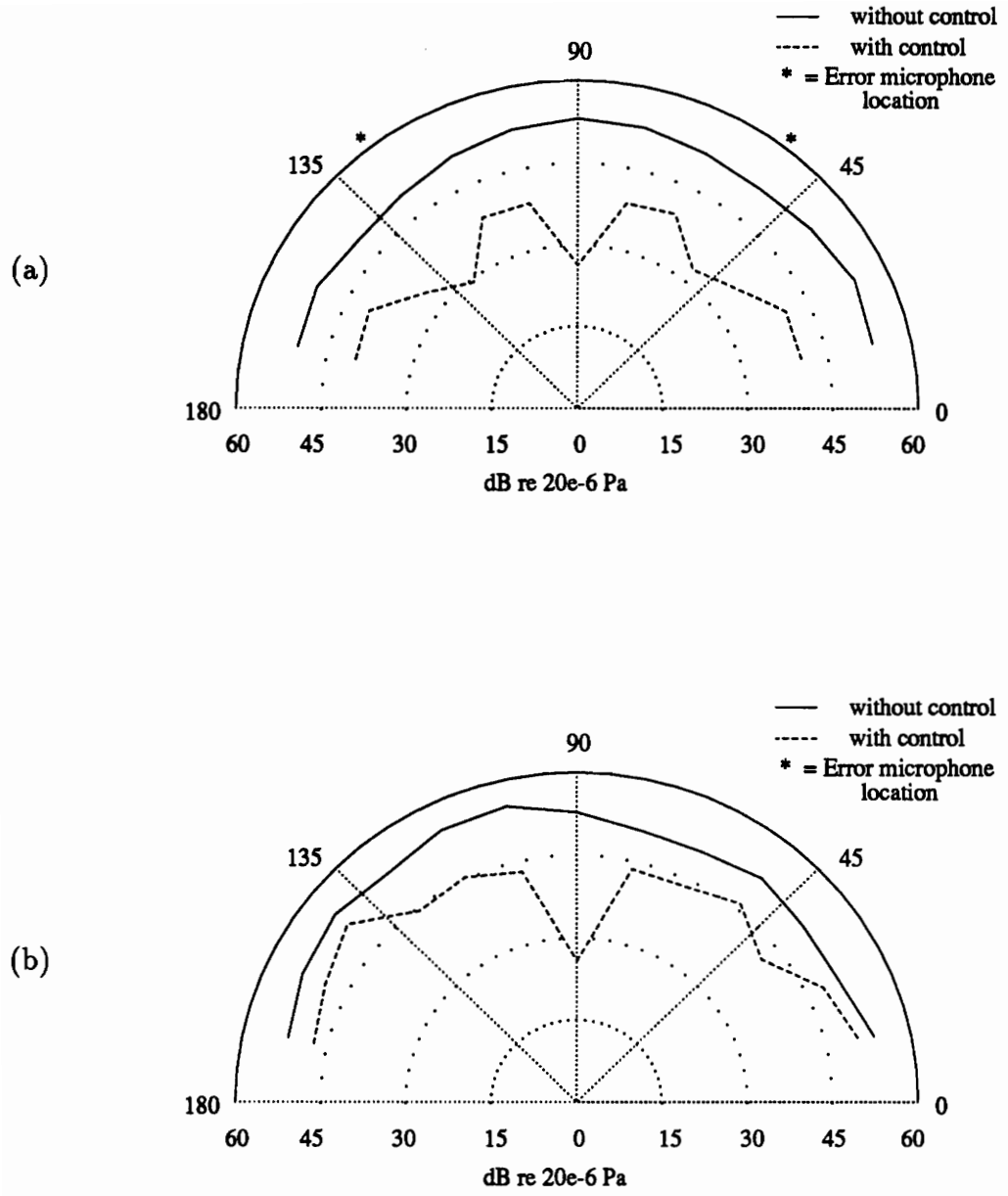

Figure 4.56: Infinite beam with blocking mass #1 acoustic field, 690Hz shaker controller #1, error microphone 51.4° and 128.6° perpendicular. (*a*) perpendicular microphone array data, (*b*) axial microphone array data.

(a)

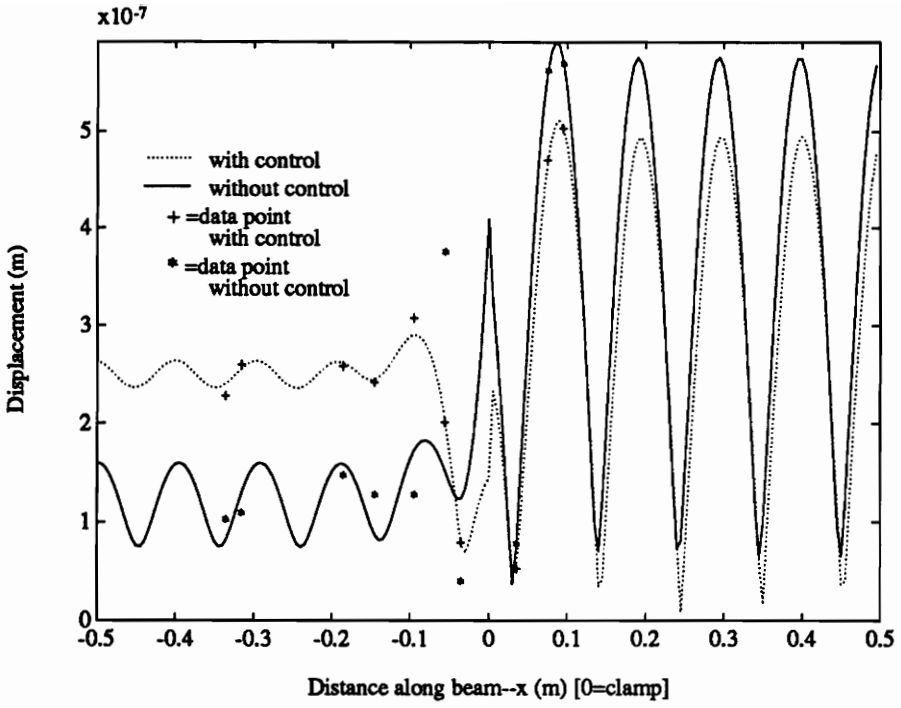

(b)

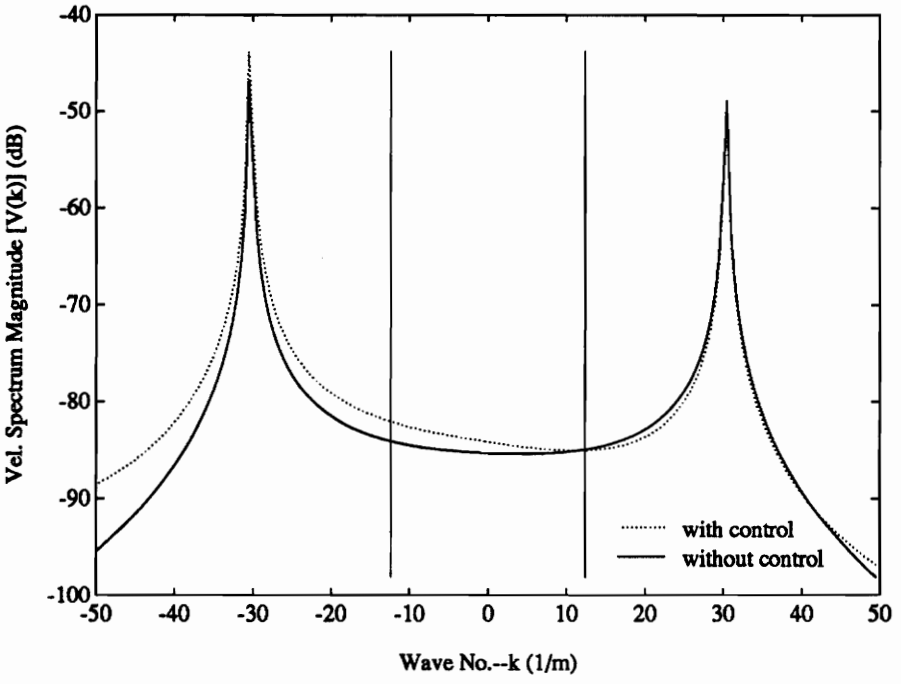

Figure 4.57: Infinite beam with blocking mass #1 data, 690Hz shaker controller #1, error microphone 51.4° and 128.6° perpendicular. (a) decomposed displacement, (b) corresponding velocity wavenumber spectrum.

4.2.4 Frequency Comparison

In order to compare experimental results at all of the frequencies the experimental results of the infinite beam with a blocking mass driven at 510Hz, controlled by shaker #1 and with error microphones located at 51.4° and 128.6° in the perpendicular array are presented in Figs. 4.58 and 4.59. Here, an attenuation at the 51.4° error microphone of $17dB$ and $32dB$ at the 128.6° error microphone was achieved. Both the displacement amplitude and supersonic region of the wavenumber spectrum increased under control.

Similar experimental cases to this one are shown in Figs. 4.37, 4.38, 4.56 and 4.57 where the first two figures refer to the experimental case driven at 320Hz and the latter two at 690Hz. Comparing these three experimental cases shows that the global and local reductions were very similar at all frequencies. This implies that the performance of the shaker controller was the same at all frequencies.

4.2.5 Blocking Mass Discontinuity Size Comparison

Consider the experimental case of the beam with blocking mass driven at 510Hz, controlled by shaker #1, with an error microphone located at 128.6°, and with blocking mass #2 as a discontinuity (shown in Figs. 4.60 and 4.61). Notice that the attenuation at the error microphone of $43dB$ is far superior to any of the previous experimental cases which employed shaker controllers. However, the global reduction of the acoustic field is not as good. It is also important to notice the relatively small transmitted traveling wave magnitude (in the displacement region of $x < 0$). This is caused by the larger mass of blocking mass #2 which reflects more

(a)

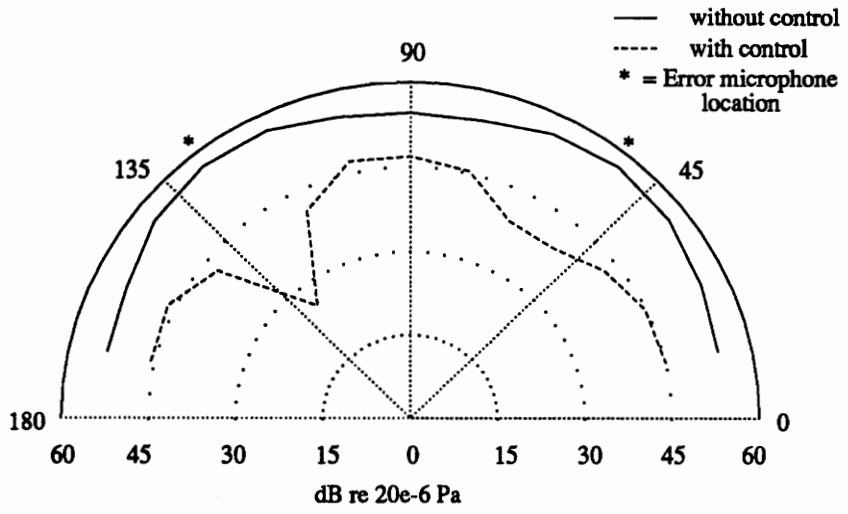

(b)

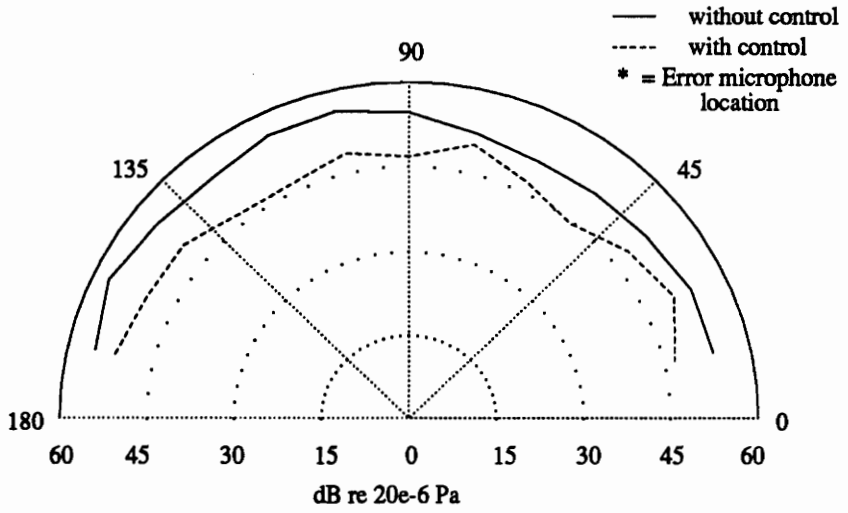

Figure 4.58: Infinite beam with blocking mass #1 acoustic field, 510Hz shaker controller #1, error microphone 51.4° and 128.6° perpendicular. (*a*) perpendicular microphone array data, (*b*) axial microphone array data.

(a)

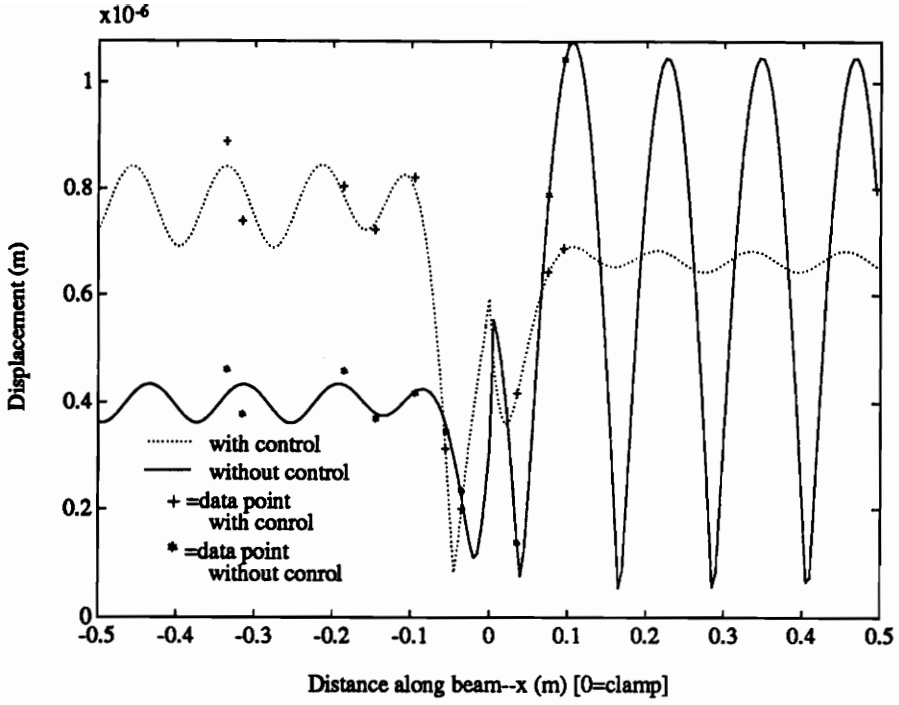

(b)

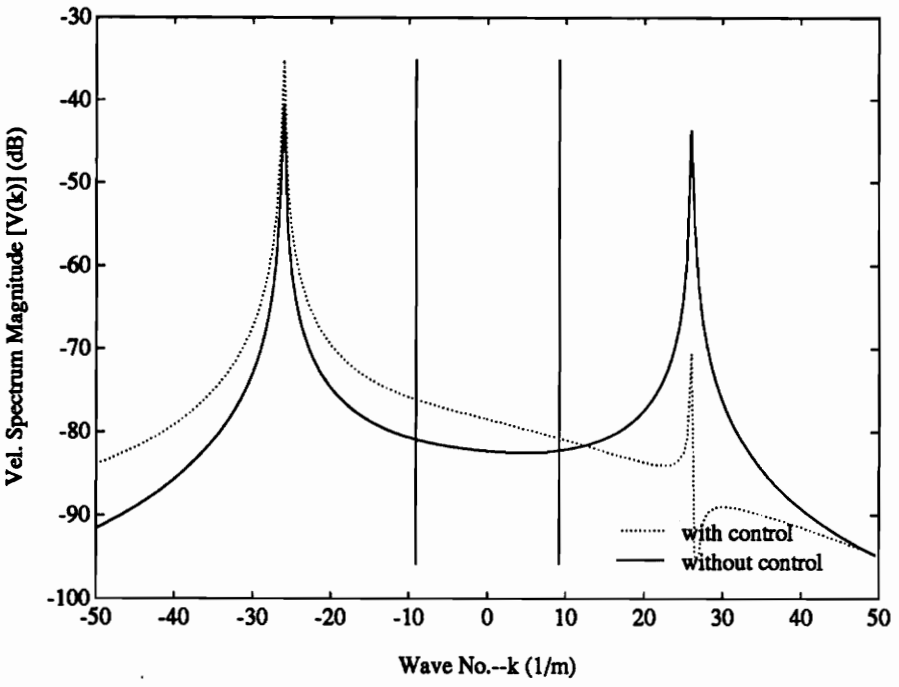

Figure 4.59: Infinite beam with blocking mass #1 data, 510Hz shaker controller #1, error microphone 51.4° and 128.6° perpendicular. (a) decomposed displacement, (b) corresponding velocity wavenumber spectrum.

(a)

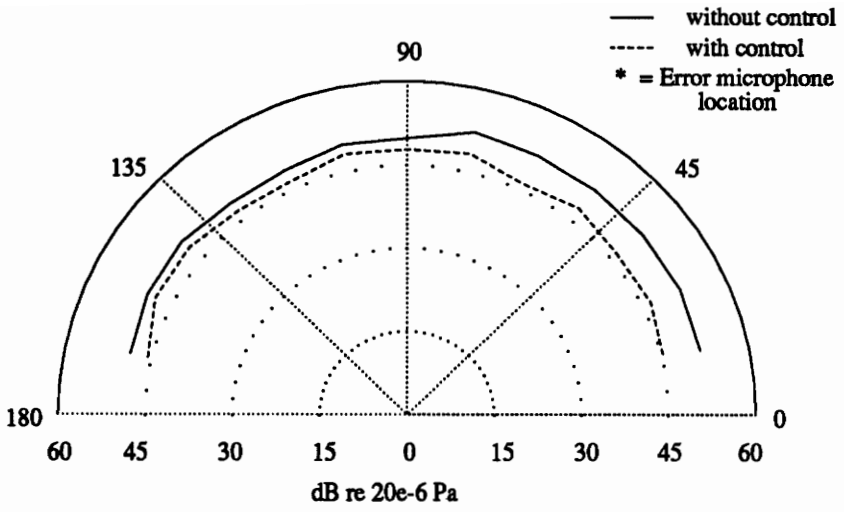

(b)

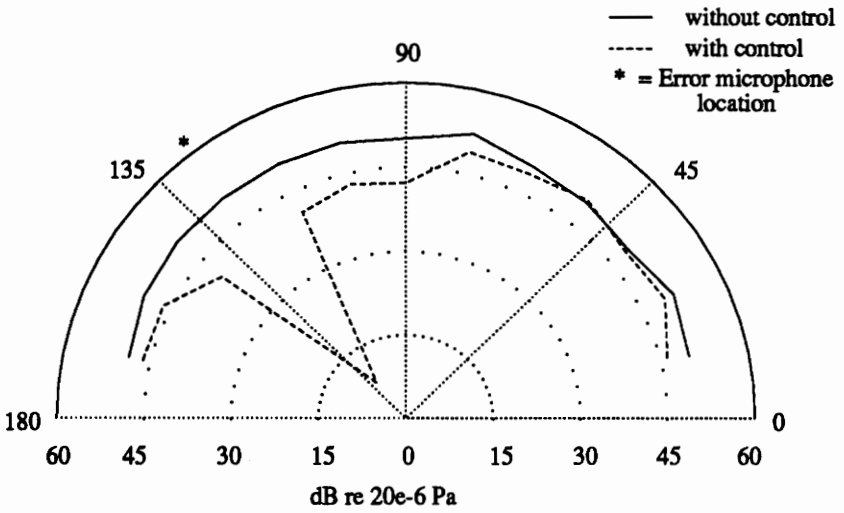

Figure 4.60: Infinite beam with blocking mass #2 acoustic field, 510Hz shaker controller #1, error microphone 128.6° axial. (*a*) perpendicular microphone array data, (*b*) axial microphone array data.

(a)

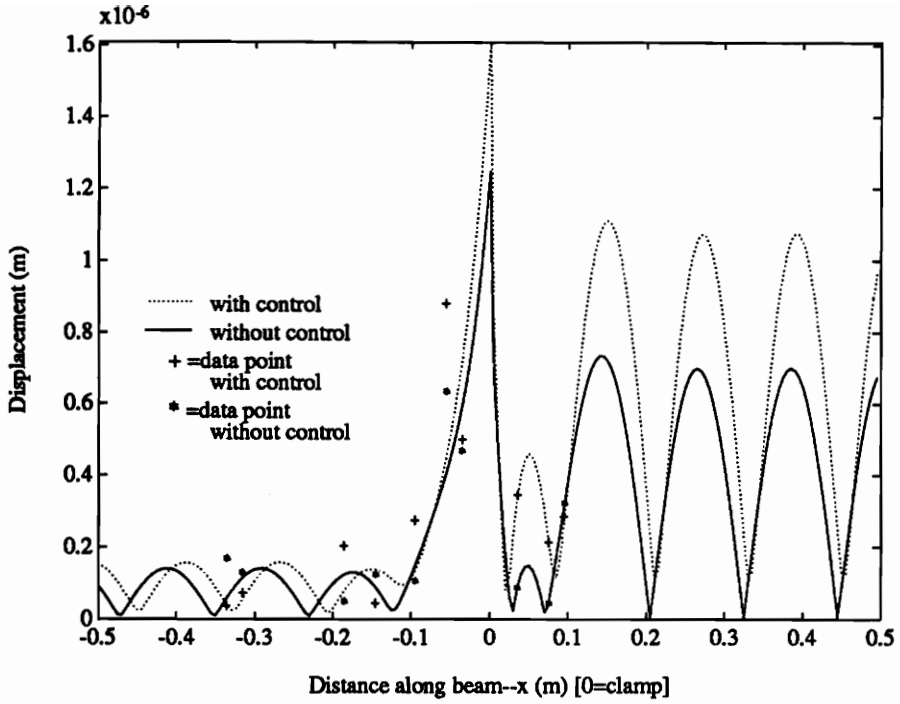

(b)

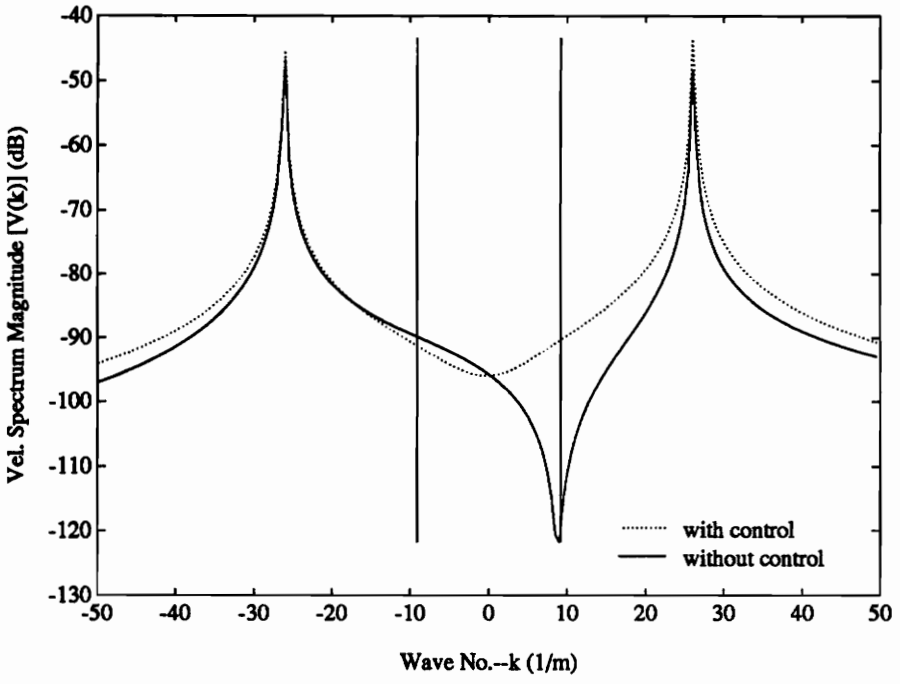

Figure 4.61: Infinite beam with blocking mass #2 data, 510Hz shaker controller #1, error microphone 128.6° axial. (*a*) decomposed displacement, (*b*) corresponding velocity wavenumber spectrum.

of the incident energy and allows less to be transmitted. (In the extreme hypothetical case of a blocking mass with infinite mass no energy would be transmitted and all of it would be reflected.)

This improved attenuation at the error microphone when blocking mass #2 is employed may be due to the decreased amplitude of the transmitted wave. This decreased the amount of acoustic radiation from the interface region of the beam and termination #2 (which was inside the anechoic chamber) by decreasing the magnitude of scattered waves and, hence , the supersonic wavenumber components associated with them. Therefore, the acoustic radiation associated with the termination had less effect on the experimental results.

4.2.6 Piezoelectric Actuator Comparison

An experimental case similar to that shown in Figs. 4.60 and 4.61 (driven at 510Hz, with an error microphone located at 128.6° axially and with blocking mass #2) is shown in Figs. 4.62 and 4.63. The only difference is that this experimental case was controlled by piezoelectric actuator #3. A reduction of $41dB$ was obtained at the error microphone while the global reduction was on the order of $8dB$. This piezoelectric controlled experimental case showed an increase in standing wave amplitudes while part of the supersonic region of the wavenumber spectrum increased while the rest decreased. However, since the magnitude of the change in the wavenumber spectrum is relatively small, this may be due to experimental error.

Comparison of this experimental case (in Figs. 4.62 and 4.63) with the similar experimental case controlled by point force shakers (shown in Figs. 4.60 and 4.61) showed

(a)

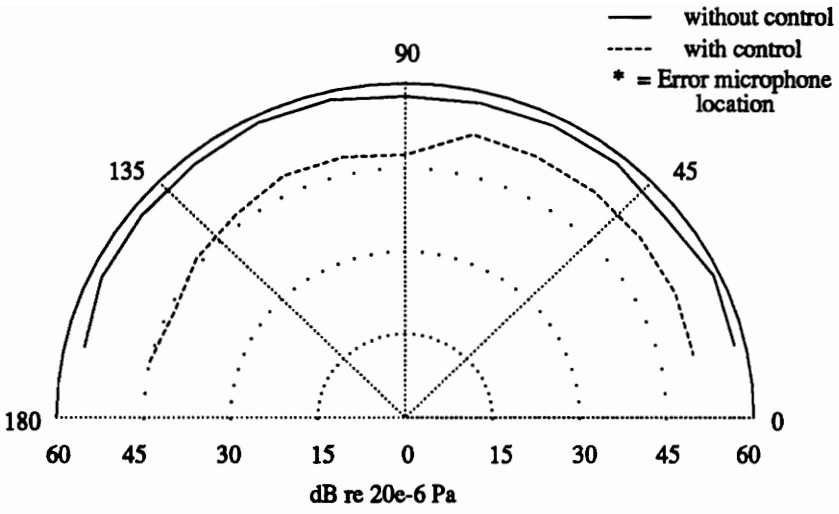

(b)

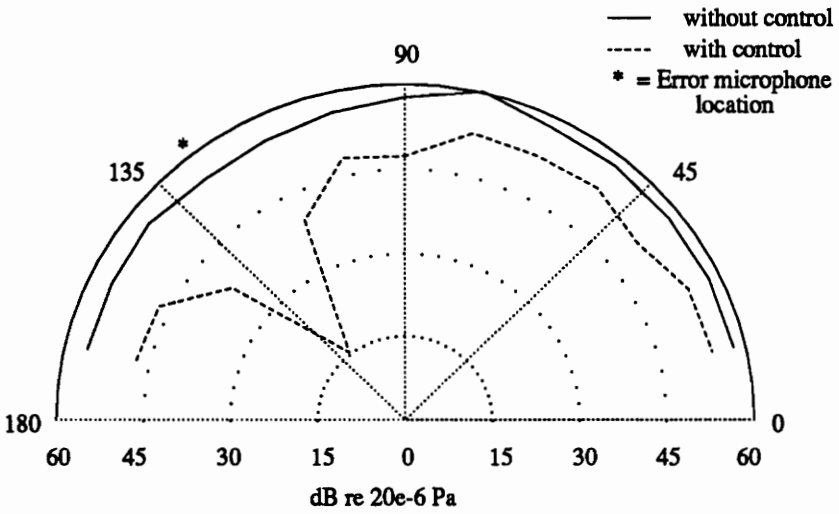

Figure 4.62: Infinite beam with blocking mass #2 acoustic field, 510Hz piezoelectric controller #3 , error microphone 128.6° axial. (*a*) perpendicular microphone array data, (*b*) axial microphone array data.

(a)

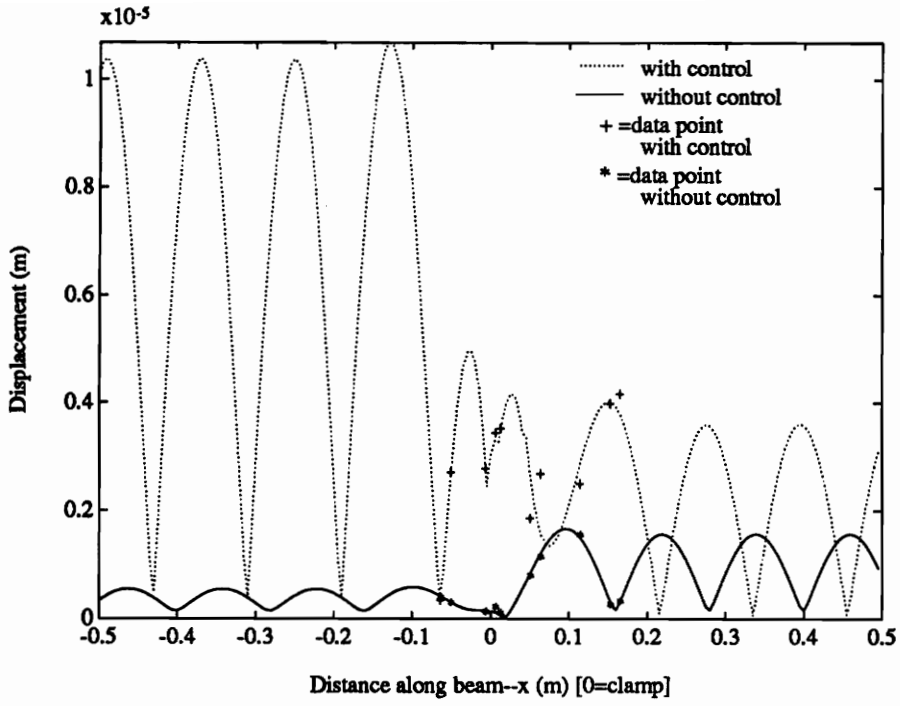

(b)

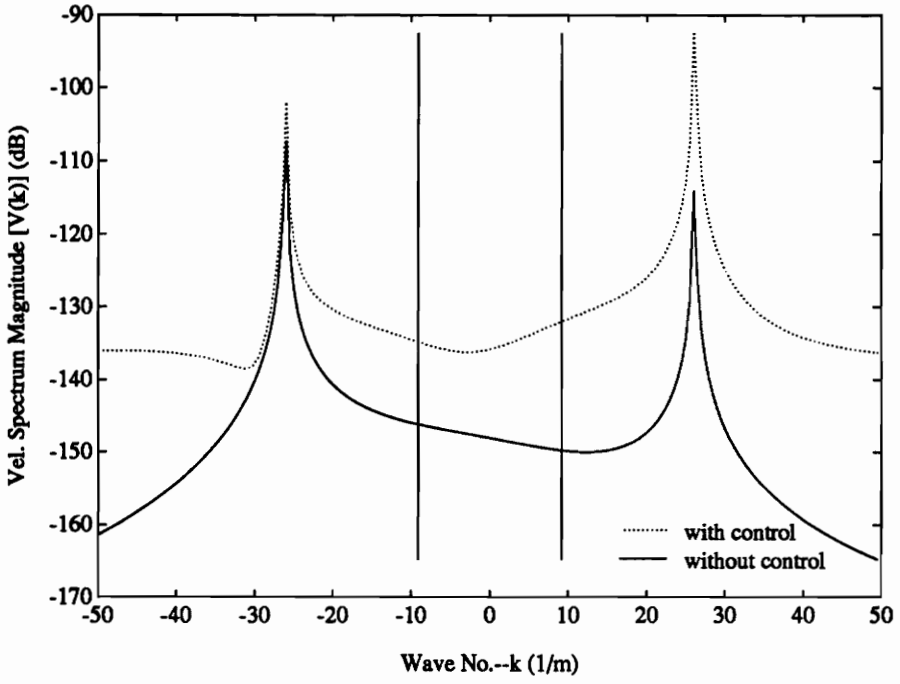

Figure 4.63: Infinite beam with blocking mass #2 data, 510Hz piezoelectric controller #3 , error microphone 128.6° axial. (*a*) decomposed displacement, (*b*) corresponding velocity wavenumber spectrum.

that the piezoelectric actuator performed better than the point force shaker. This is due to the distributed nature of the piezoelectric actuator as described in the discussions on the semi-finite/clamped beam experiments.

The data displayed in Figs. 4.64, 4.65 and 4.66 are presented in order to compare the previous results with theoretical prediction. These plots show the acoustic "near-field" (calculated from Eq. 1.24), the far-field acoustic response (calculated from Eq. 1.18) and the corresponding displacement and wavenumber spectrum (calculated from Eqs. 1.18 and 1.31 respectively) for a theoretical case driven at 510Hz, controlled by piezoelectric actuator #3 and with blocking mass #2. The geometry of the experiment was used to produce the theoretical results.

Comparing this with the similar experimental case shown in Figs. 4.62 and 4.63 we see that the experimental acoustic field results match very closely with those predicted by theory. The displacement results do not match very well, however, probably due to the theoretical assumption that the blocking mass was of infinitesimal width. This caused errors in the decomposition of the experimental complex wave amplitudes as discussed earlier. However, both the theory and the experiment showed an increase in the supersonic wavenumber components which resulted in an increase in the acoustic far-field levels as shown in Fig. 4.65.

4.2.7 Combined Shaker and Piezoelectric Actuator Control

The last experimental case presented in the infinite beam with a blocking mass section is shown in Figs. 4.67 and 4.68. This experimental case was driven at 510Hz and had error microphones located at 51.4° and 128.6° axially but, was controlled by

(a)

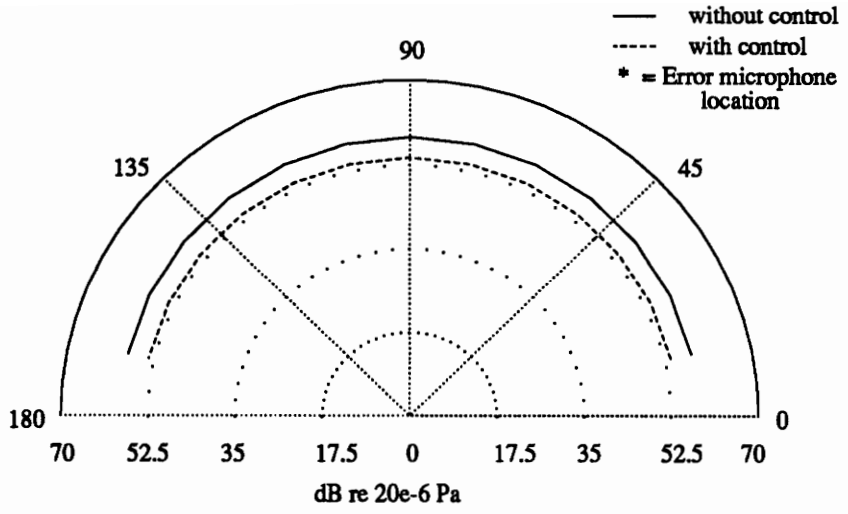

(b)

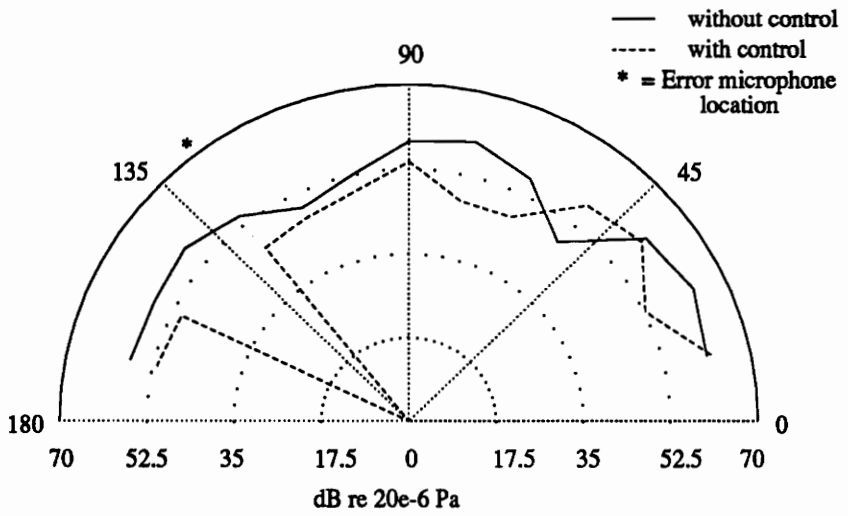

Figure 4.64: Infinite beam with blocking mass #2 theoretical acoustic near-field, 510Hz, piezoelectric controller #3, error microphone 128.6° axially. (*a*) perpendicular array data, (*b*) axial microphone array data.

(a)

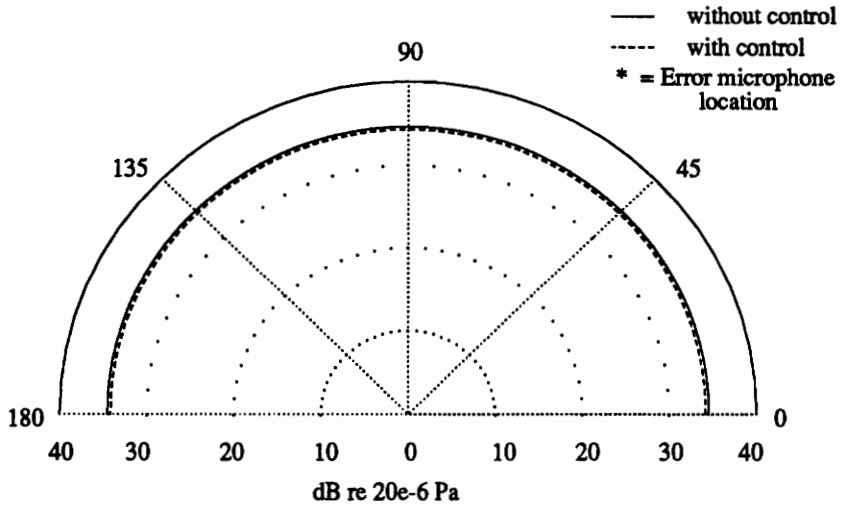

(b)

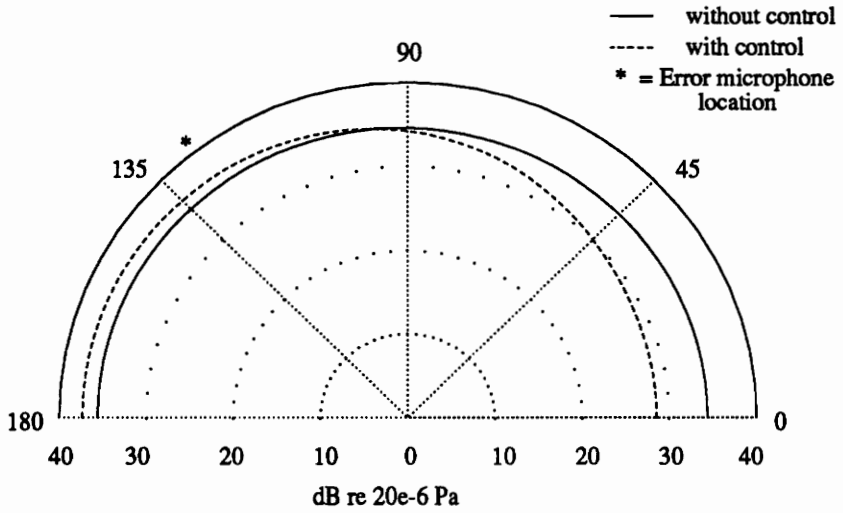

Figure 4.65: Infinite with blocking mass #2 theoretical acoustic far-field, 510Hz,piezoelectric controller #3, error microphone 128.6° axially. (*a*) perpendicular microphone array data, (*b*) axial microphone array data.

(a)

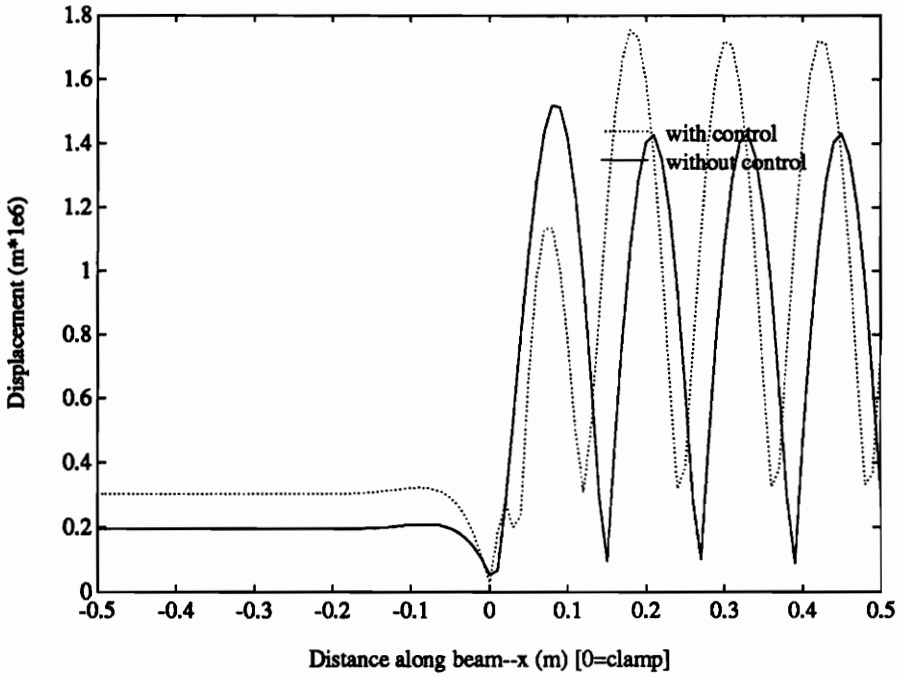

(b)

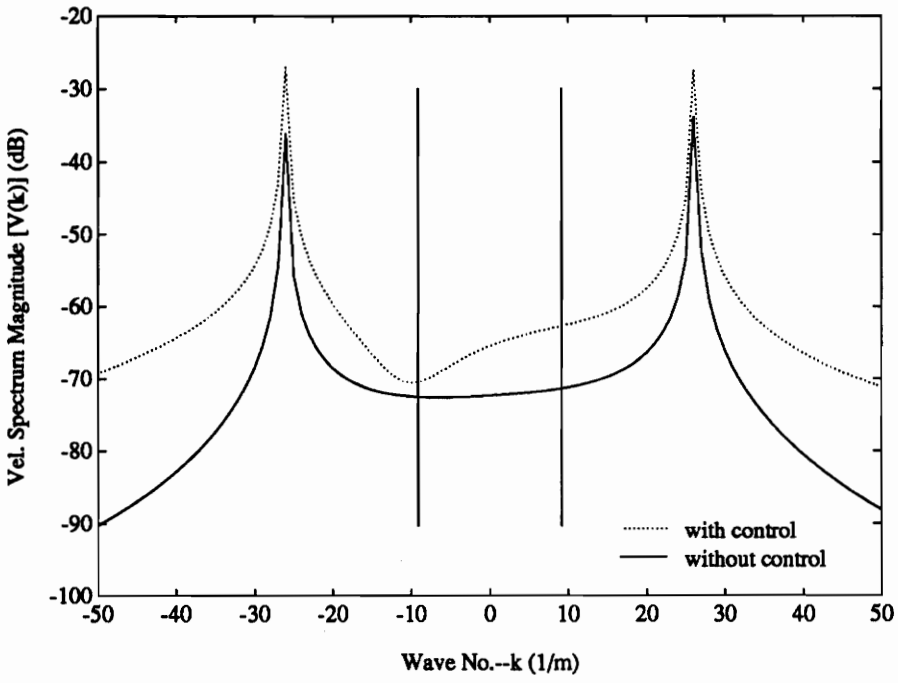

Figure 4.66: Infinite beam with blocking mass #2 theoretical data, 510Hz, piezoelectric controller #3, error microphone 128.6° . (*a*) decomposed displacement, (*b*) corresponding velocity wavenumber spectrum.

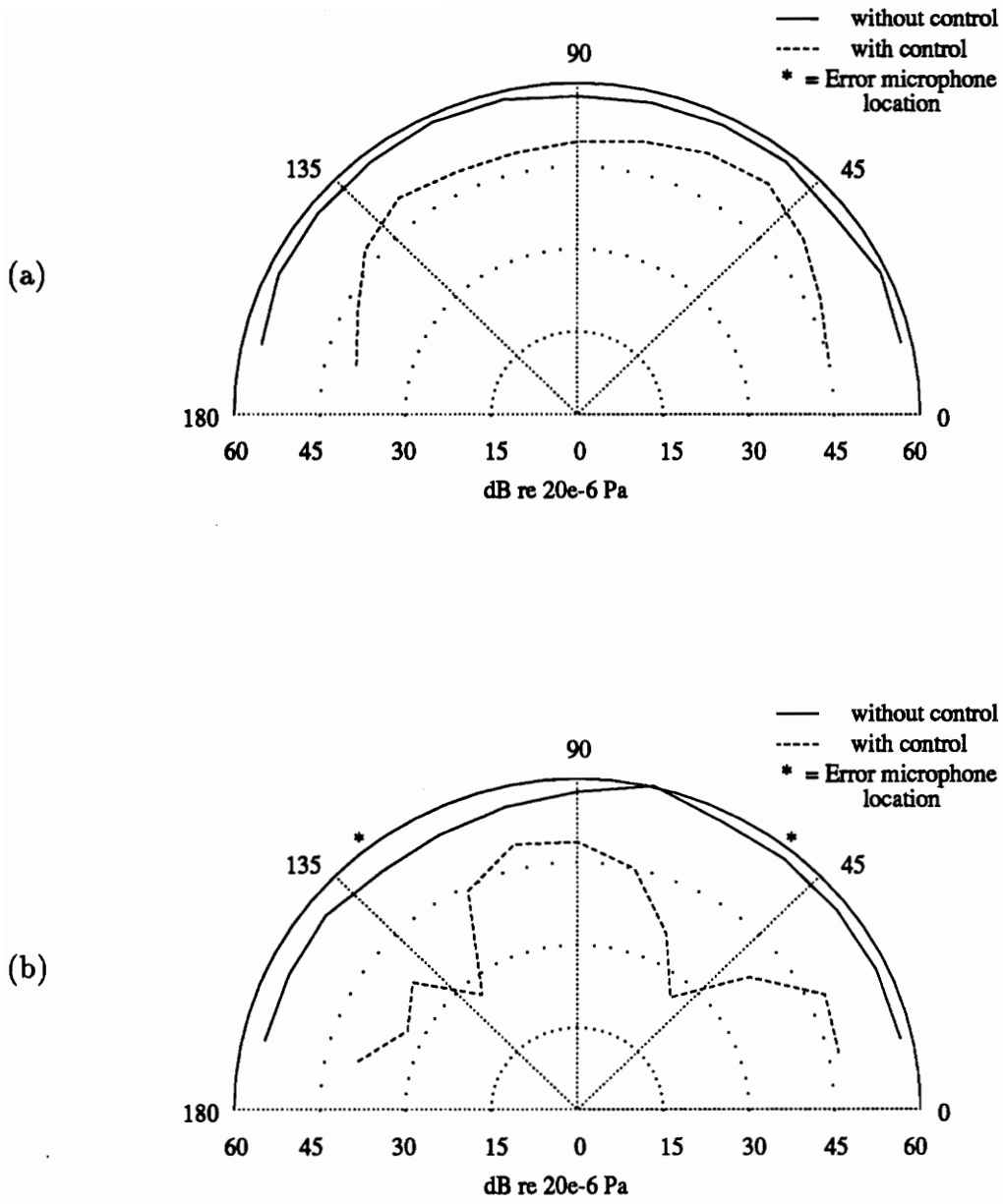

Figure 4.67: Infinite beam with blocking mass #2 acoustic field, 510Hz piezoelectric controller #3 and shaker controller at $x = 0$, error microphone 51.4° and 128.6° axial. (a) perpendicular microphone array data, (b) axial microphone array data.

(a)

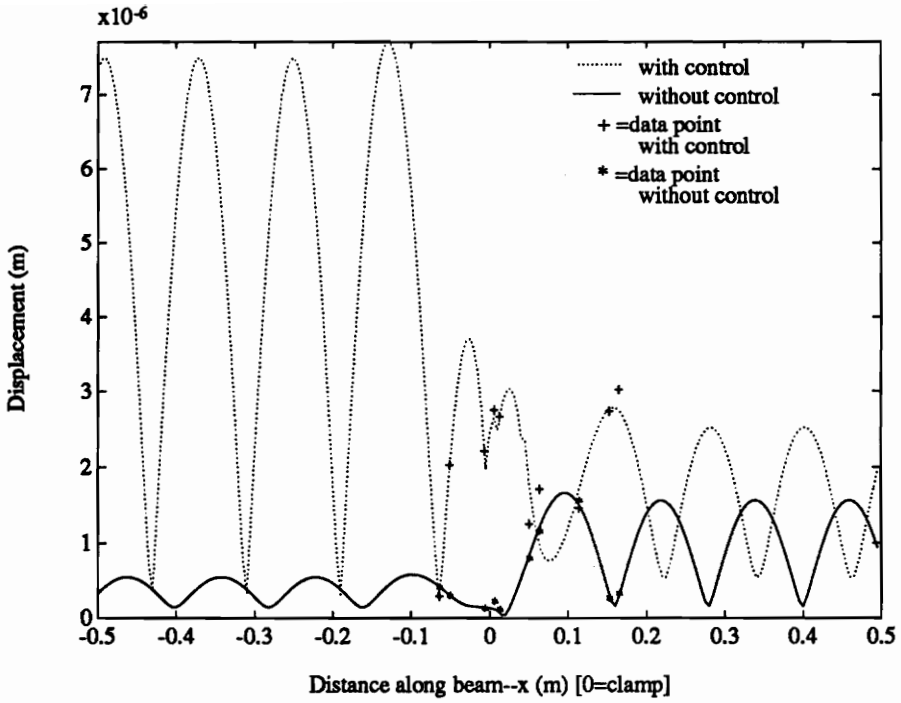

(b)

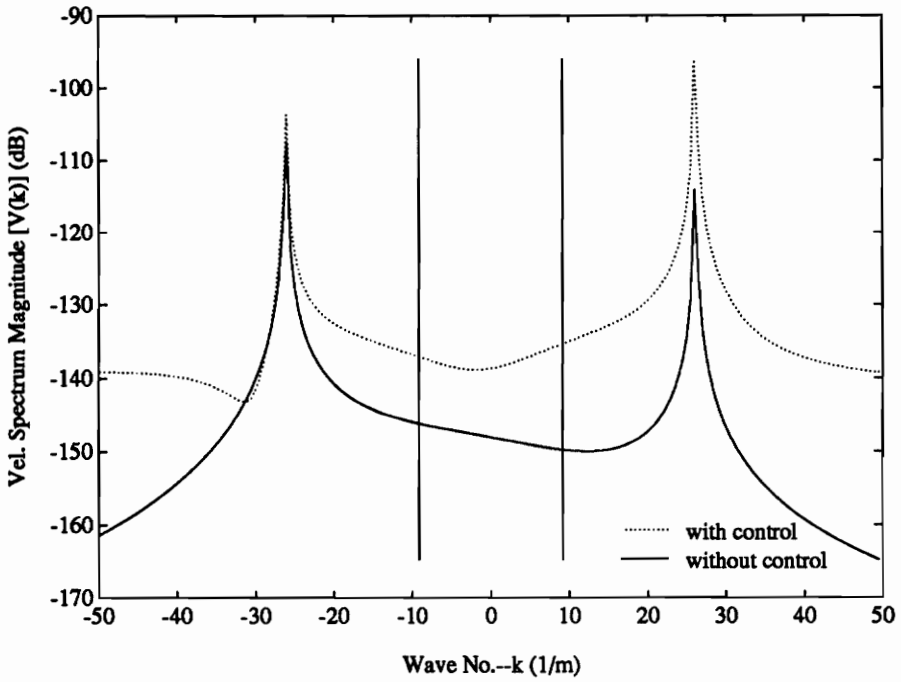

Figure 4.68: Infinite beam with blocking mass #2 data, 510Hz piezoelectric controller #3 and shaker controller at $x = 0$, error microphone 51.4° and 128.6° axial. (a) decomposed displacement, (b) corresponding velocity wavenumber spectrum.

a shaker located at $x = 0$ (attached directly to the blocking mass discontinuity) and piezoelectric actuator #3 simultaneously. An attenuation at each error microphone of $29dB$ was achieved while the global reduction in both arrays was on the order of $10dB$. This control was the best overall performance for any of the experimental cases presented for the infinite beam with a blocking mass.

This may be due to the fact that this actuator combination does the best job of counteracting the influence of the discontinuity. Since the discontinuity can be modeled as producing a reaction force and moment on the beam (discussed in Ch. 1), the combination of the point force applied directly to the blocking mass (at $x = 0$) and the line moments from the piezoelectric actuator are best able to counteract the reaction force and moment of the blocking mass. If this combination of actuators were able to completely counteract the reaction force and moment of the blocking mass discontinuity it would make the beam appear continuous with no discontinuity. Hence, no wave scattering would occur and no supersonic wavenumber components would be produced. This would result in no acoustic radiation since an infinite beam, excited by subsonic flexural waves, would not produce acoustic radiation (as discussed in Ch. 1 and in [11] and [12]).

4.2.8 Comparison with Semi-infinite/Clamped Beam Experiments

Overall the reduction of the acoustic field was better in the semi-infinite/clamped beam experiments than the reductions achieved in the infinite beam with a blocking mass experiments. When the global attenuations achieved in each experiment are compared it is evident that the attenuations obtained in the semi-infinite/clamped

beam experiments were far better than those in the infinite beam with a blocking mass experiments. However, when the local attenuations achieved in each experiment are compared, the results of the semi-infinite/clamped beam experiments are only slightly better.

The reason that the control was less successful on the beam with a blocking mass was most likely due to the more complex nature of the vibrational response of the beam with a blocking mass. As discussed previously, since there were more scattered waves contributing to the supersonic wavenumber spectrum with the blocking mass discontinuity, the control actuator(s) had a more difficult task trying to control these scattered waves. Consider the clamped beam experiments where only three waves (incident traveling, reflected traveling and reflected near-field) contributed to the supersonic wavenumber spectrum. On the other hand, in the beam with a blocking mass experiments, there were five waves which contributed to the supersonic wavenumber spectrum (incident traveling, reflected traveling, reflected near-field, transmitted traveling and transmitted near-field). The two additional waves in the beam with a blocking mass experiments made the task of controlling the acoustic field more difficult.

It should also be noted that, for the clamped beam experimental cases, the supersonic wavenumber components always decreased under control while the infinite beam with a blocking mass experimental cases always showed increases in the supersonic wavenumber region. Thus, the far-field was always controlled in the semi-infinite/clamped beam experiments but not in the beam with a blocking mass experiments.

This behavior ties in with the previous explanation about the improved acoustic

attenuations in the clamped beam experiments. The more intricate vibrational response of the beam with a blocking mass made controlling the acoustic field more difficult.

An additional explanation was given in Ch. 1 in the form of a a much simpler analogous situation. The equations for the "near-field" and far-field acoustic radiation due to two, proximal point sources were presented. From these it was shown that, when the "near-field" radiation was controlled by varying the phase between the point sources, a situation could arise where the far-field radiation levels increased. It is obvious that this case is far more simple than the situation involving a beam and discontinuity, but it does serve to show the mechanism by which such a condition could arise. Since the equation describing the acoustic radiation from a beam in the "near-field" has no closed form solution, we must result to such a simple case in order to interpret the behavior.

Chapter 5

Conclusions and Recommendations

5.1 Conclusions

In these experiments the active control of acoustic radiation from discontinuities on beams was studied. Two experiments were constructed: a beam with a clamped discontinuity and an beam with a blocking mass. One end of the clamped beam was placed in an anechoic termination which absorbed incident flexural waves and prevented any reflections. Both ends of the beam with a blocking mass were placed in anechoic terminations. These terminations made the beam appear infinite to incident traveling waves. This allowed the acoustic radiation due to wave scattering discontinuity to be isolated from any other acoustic sources.

A hemispherical microphone array was situated above the discontinuity in order to sample the acoustic radiation due to the wave scattering at the discontinuity. In addition, an array of accelerometers was attached to the beam in order to sample the vibrational response. From the data collected from the accelerometers the

complex amplitudes of the assumed displacement equation were decomposed. The spatial Fourier transform of the displacement equation permitted the supersonic wavenumber components present in the beam vibrational response to be studied. This supplied some insight into the mechanism by which control of the acoustic field was achieved.

The control of these experiments was performed by a DSP board resident on a PC which employed the filtered-x version of the LMS algorithm. This algorithm employed a gradient decent method to minimize the least square of the error signal (supplied by a microphone in the acoustic field) by converging to the set of optimal weighting coefficients for a variable coefficient FIR filter.

In each experiment many cases were performed which involved the variation of the following parameters:

- Control actuator location
- Number of control actuators
- Error microphone location
- Number of error microphones
- Frequency
- Control actuator type
- Discontinuity type

Several experimental cases were presented which demonstrated the effects of varying these parameters and a few results from theoretical studies were presented to show

that the experiments were following the trends predicted by theory. The results that were presented were representative of the behavior shown by all of the experiments performed (not all results obtained were presented in this thesis) and served as a comparison base to draw conclusions from concerning the above parameters.

Several conclusions were drawn from these experiments as follows:

1. Active control of acoustic radiation due to wave scattering from discontinuities in infinite beams is possible.

2. Large attenuations (as high as $50dB$) were achieved at error microphones located at various positions throughout the acoustic "near-field" (or, more precisely, not in the far-field).

3. While controlling the acoustic radiation at a single error microphone the acoustic radiation on a global scale was also attenuated. That is, attenuation at a point was not at the expense of increasing levels elsewhere in the acoustic field.

4. In the case of the semi-infinite/clamped beam, while controlling the acoustic radiation in the "near-field", the far-field radiation was attenuated as well. This was a result of the way which the control actuator changed the interaction of the contributions to the supersonic wavenumber region. These were changed such that the supersonic wavenumber region decreased under control.

5. In the case of the infinite beam with a blocking mass, while controlling the acoustic radiation in the "near-field", the far-field levels increased. This was shown to be caused by an increase in the supersonic wavenumber components

present in the beam response caused by the way which the control actuator affected these contributions. In other words, the contribution to the supersonic wavenumber spectrum by the control actuator interacted with those supersonic wavenumber contributions present before control such that the supersonic wavenumber region increased. The most likely reason for this behavior was the more complex system of flexural waves in the beam with a blocking mass response which the control actuators were less able to affect.

6. For the best attenuation at a point one error microphone yielded the best results. For a more global attenuation two error microphones gave the best results. If more error microphones were introduced into the system, the global attenuation would improve at the expense of local attenuations.

7. For the best control of local or global radiation two control actuators showed better performance than one. If more control actuators were employed it would result in further improved attenuations.

8. It was demonstrated that, if the control actuator was located closer to the discontinuity, it was better able to control the acoustic field. This was due to the fact that, closer to the discontinuity, the flexural near-field (which was a major contributor to the supersonic wavenumber region and, hence, the acoustic radiation) had more influence on the beam vibrational response. Therefore, the control actuator that was closer to the discontinuity was better able to affect the flexural near-field and the acoustic radiation.

9. Piezoelectric actuators achieved better control than point force shakers, particularly at higher frequencies. This was due to the dual, dependent nature of the piezoelectric actuator. Since the piezoelectric actuators exerted two line

moments at either end of the patch pair, their control authority was more distributed than a shaker acting at one point on the beam.

5.2 Recommendations

There are several things that could be done to further investigate active control of acoustic radiation due to wave scattering from discontinuities on beams and to improve the results obtained in these studies. Some of them entail improvements on the experimental rigs and others are suggestions for studies that were beyond the scope of these experiments.

1. To improve the experiments on the infinite beam with a blocking mass, an experiment could be set up which ran the beam completely through the anechoic chamber thus, placing both anechoic terminations outside of the chamber. This would prevent any sound emanating from the terminations, due to wave scattering at the interface with the beam, from interfering with the experiments.

2. It would be interesting to do some experiments that allow control and sensing in the acoustic far-field. This would allow for further confirmation of theoretical models and better understanding of the mechanism of control (since the equation for the acoustic near-field has no closed form solution but the far-field equation does). This would require either a larger anechoic chamber or a faster controller which would allow experiments to be performed at higher frequencies.

3. To improve on the global far-field attenuation a sensor could be developed which spatially filtered out subsonic wavenumber components. This sensor could then be used as the error sensor in the control loop. Since it would sense only supersonic wavenumber components they could be controlled independently which would directly control the far-field radiation [22].

4. An obvious way to improve the global attenuations achieved in these experiments would be to increase the number of error sensors and control actuators employed. As the speed of digital equipment increases the digital controllers will be able to employ more channels of control.

5. In order to improve the decomposition of the complex amplitudes for the displacement equations more data points must be used. One way to accomplish this would be to increase the number of accelerometers in the array. A better, and probably more accurate method, would be to employ a laser doppler vibrometer. This would greatly increase the accuracy of the decomposed complex wave amplitudes and improve the results.

6. With improved complex amplitude decomposition data an in-depth study of the interaction of flexural waves and the contributions they make to the supersonic wavenumber region could be conducted. By investigating not only the magnitude of supersonic contributions, but also the relative phasing of each, a greater understanding of the interactions occurring would be permitted. This would allow a more precise explanation of the way in which a control actuator affects the beam response and the supersonic wavenumber region.

Bibliography

[1] Widrow, et. al. "Adaptive Noise Cancelling: Principles and Applications," *Proceedings of the IEEE*,Vol. 63, No. 12, pp. 1692–1716, December 1975.

[2] Gonidou, Luc–Olivier, "Active Control of Flexural Power Flow in Elastic Thin Beams," Master of Science Thesis, Department of Mechanical Engineering, Virginia Polytechnic Institute and State University, February, 1988.

[3] C. R. Fuller, R. J. Silcox, V. L. Metcalf and D. E. Brown, "Experiments on Structural Control of Sound Transmitted through an Elastic Plate," *Proceedings of the 1989 American Control Conference*, Vol. 3(of 3), pp. 2079–2084, 1989.

[4] R. L. Clark and C. R. Fuller, "Experiments on Active control of Structurally Radiated Sound using Multiple Piezoceramic Actuators," accepted for publication in the *Journal of the Acoustical Society of America*, 1990, (also presented at the 120th ASA Meeting, Nov. 1990).

[5] C. R. Fuller, G. P. Gibbs and R. J. Silcox, "Simultaneous Active Control of Flexural and Extensional Waves in Beams," *Journal of Intelligent Material Systems and Structures*, Vol. 1, No. 2, pp. 235–247, April 1990.

[6] R. L. Clark and C. R. Fuller, "Control of Sound Radiation with Adaptive Structures," presented at the First Joint U. S. Japan Conference on Adaptive Structures, Nov. 13–15, 1990, Maui, Hawaii.

[7] S. J. Elliot, I. M. Stothers and P. A. Nelson, "A Multiple Error LMS Algorithm and its Application to the Active Control of Sound and Vibration," *IEEE transactions on acoustics, speech, and signal processing*, Vol. ASSP–35, No. 10, pp. 1423–1434, October 1987.

[8] B. R. Mace, "Active Control of Flexural Vibrations", *Journal of Sound and Vibration*, 114(2), pp. 253–270, 1987.

[9] J. Scheuren, "Non-Reflecting Termination for Bending Waves in Beams by Active Means", *Proceedings of Internoise 88*, pp. 1065–1068, 1988.

[10] D. W. Miller, S. R. Hall and A. H. von Flotow, "Optimal Control of Power Flow at Structural Junctions", *Proceedings of the American Controls Conference*, Pittsburg, 1989.

[11] F. Fahy, *Sound and Structural Vibration*, Academic Press, Orlando, Florida, 1987.

[12] M. C. Junger and D. Feit, *Sound, Structures, and Their Interaction*, The MIT Press, Cambridge, MA, 1972.

[13] R. F. Keltie, "Sound Radiation From Simple Structural Discontinuities," to be published in *The Journal of the Acoustical Society of America*, 1991.

[14] R. F. Keltie, "A Note on the Acoustic Radiation from Point-Forced Elastic Beams," *Journal of Sound and Vibration*, 1984, Vol. 92, No. 2, pp 253–260.

[15] B. R. Mace, "Wave Reflection and Transmission in Beams", *Journal of Sound and Vibration*, 97(2), pp. 237–246, 1984.

[16] C. Guigou, unpublished dissertation entitled "Active Control of Sound Radiation from Discontinuities in Thin Elastic Beams", VPI & SU, 1991.

[17] L. Meirovitch, *Analytical Methods in Vibrations*, Macmillan Publishing Co., New York, New York, 1967.

[18] "Piezoelectric Motor/Actuator Kit Manual," Piezo Systems, 186 Massachusetts Avenue, Cambridge, MA 02139.

[19] E. F. Crawley and E. H. Anderson, "Detailed Models of Piezoceramic Actuation of Beams," AIAA Paper 89–1388–CP, 1989.

[20] B. Widrow and S. D. Stearns, *Adaptive Signal Processing*, Prentice-Hall, NJ, 1985.

[21] N. Draper and H. Smith, *Applied Regression Analysis, Second Edition*, John Wiley & Sons, 1966.

[22] C. R. Fuller and R. A. Burdisso, "A Wavenumber Domain Approach to the Active Control of Structure-Borne Sound," accepted for publication in the *Journal of Sound and Vibration*, 1990.

[23] G. P. Gibbs and C. R. Fuller, "Excitation of Thin Beams by Asymmetric Piezoelectric Actuators," presented at the *121st Acoustical Society of America Conference*, April, 1991, Baltimore, Maryland.

[24] R. H. Lyon, "Sound Radiation from a Beam Attached to a Plate", *Journal of the Acoustical Society of America*, Vol. 34, No. 9, pp. 1265–1268, 1962.

Appendix A

Experimental Error Analysis

Several aspects of these experiments contributed error to the results. This appendix discusses several of these sources and attempts to quantify some of them.

A.1 Error in the Displacement Decomposition Method

One possible source of error in these experiments was the displacement decomposition method. Since the decomposition depended on experimental measurement of accelerometer data, the opportunity arose for error to enter the data.

For this reason the author will attempt to quantify the effect of experimental error on (and the robustness of) the decomposition algorithm . Error in accelerometer location, and in the magnitude and phase of data taken from the accelerometers could lead to errors in the decomposed complex amplitudes of the displacement equation, and therefore, the spatial Fourier transform .

For this reason, a computer code was written to operate in Matlab (listed in Appendix B) for the purpose of addressing these questions. To accomplish this an equation of motion for the beam was assumed along with the appropriate set of complex amplitudes as follows:

$$z(x) = Ae^{ik_b x} + Be^{-k_b|x-\alpha|} + Ce^{ik_b|x-\alpha|} + De^{-k_b x} + Ee^{-ik_b x} \qquad \text{(A.1)}$$

where the complex amplitudes represent the following waves:

$A \cong$ Incident traveling wave

$B \cong$ Controller near-field

$C \cong$ Controller traveling wave

$D \cong$ Reflected near-field

$E \cong$ Reflected traveling wave

This assumed equation was treated as the exact displacement of the beam. Using this equation, the displacement of the beam was calculated at several points. These points were used as accelerometer data points and fed into the decomposition algorithm. Running the decomposition algorithm with these data points produced the exact coefficients that were used to calculate the data points (as expected).

Next, the data points were multiplied by a random number which would simulate random error in the measurement magnitude. This random number had a mean of unity and a variance of 0.1. This had the effect of adjusting the magnitude such that a random error with a variance of 10% was produced in the data. Then,

using these randomly adjusted data points, the coefficients were calculated using the decomposition algorithm. Table A.1 lists a comparison of the exact complex amplitudes and those calculated with adjusted data points.

Next, a random phase error was introduced into the accelerometer data points. This was done by multiplying the original data points by $e^{i\phi}$, where ϕ was a random angle with a mean of zero and a variance of about 6°. This had the effect of shifting the phase of each data point by some random phase. The results of this are given in Table A.2.

The final error source investigated with the decomposition algorithm was a random error in the accelerometer location. To simulate this each accelerometer location used in the decomposition method was first adjusted by some random number of mean zero and variance of $.001m$. This had the effect of randomly adjusting the accelerometer locations by an amount with a variance of $1mm$. The results of this are shown in Table A.3.

In each of these cases ten data points were used (just as ten accelerometer data points were used in the actual experiments). In the case of the beam response without control, three unknown amplitudes had to be calculated. With control, the number of unknown amplitudes was five. Therefore, the system of equations solved by the decomposition routine consisted of ten equations and three unknowns, and ten equations and five unknowns respectively.

As is shown in the three error cases presented, the error in the decomposed coefficients is equal to or less than the error which was introduced. This implies that the least square regression method does, in fact, reduce the amount of resultant error.

Without Control						
Wave	Correct Data		Adjusted Data		Error	
Coefficient	Mag.($\times 10^7$)	Phase	Mag.($\times 10^7$)	Phase	Mag.(%)	Phase
A	2.8284	135°	2.8832	135°	1.9	0.0°
D	3.0414	−80.5°	3.3605	−81.5°	10.5	1.0°
E	1.2806	−51.3°	1.3305	−51.2°	3.9	0.1°
With Control						
Wave	Correct Data		Adjusted Data		Error	
Coefficient	Mag.($\times 10^7$)	Phase	Mag.($\times 10^7$)	Phase	Mag.(%)	Phase
A	2.8284	135°	2.7746	136°	1.9	1.0°
B	2.0000	89.7°	2.0522	89.3°	2.6	0.4°
C	2.0396	−11.3°	1.9713	−11.5°	3.3	0.2°
D	3.0414	−80.5°	3.3577	−92.2°	10.4	11.7°
E	1.2806	−51.3°	1.2966	−51.2°	1.2	0.1°

Table A.1: Decomposition method error due to adjusted accelerometer data magnitude. A=incident traveling wave, B=controller near-field wave, C=controller traveling wave, D=reflected near-field wave, E=reflected traveling wave.

Without Control						
Wave	Correct Data		Adjusted Data		Error	
Coefficient	Mag.($\times 10^7$)	Phase	Mag.($\times 10^7$)	Phase	Mag.(%)	Phase
A	2.8284	135°	2.8229	135°	.19	0.0°
D	3.0414	−80.5°	2.6401	−138°	13.2	57.5°
E	1.2806	−51.3°	1.2371	−53.1°	3.4	1.8°
With Control						
Wave	Correct Data		Adjusted Data		Error	
Coefficient	Mag.($\times 10^7$)	Phase	Mag.($\times 10^7$)	Phase	Mag.(%)	Phase
A	2.8284	135°	2.8241	135°	.15	0.0°
B	2.0000	89.7°	1.9650	90.4°	1.8	0.7°
C	2.0396	−11.3°	2.0347	−12.8°	0.24	1.5°
D	3.0414	−80.5°	3.3075	−72.1°	8.7	8.4°
E	1.2806	−51.3°	1.2601	−51.5°	1.6	0.2°

Table A.2: Decomposition method error due to adjusted accelerometer data phase. A=incident traveling wave, B=controller near-field wave, C=controller traveling wave, D=reflected near-field wave, E=reflected traveling wave.

Without Control						
Wave	Correct Data		Adjusted Data		Error	
Coefficient	Mag.($\times 10^7$)	Phase	Mag.($\times 10^7$)	Phase	Mag.(%)	Phase
A	2.8284	135°	2.8341	135°	.20	0.0°
D	3.0414	−80.5°	2.9486	−70°	3.1	10.5°
E	1.2806	−51.3°	1.2943	−51.5°	1.1	0.2°
With Control						
Wave	Correct Data		Adjusted Data		Error	
Coefficient	Mag.($\times 10^7$)	Phase	Mag.($\times 10^7$)	Phase	Mag.(%)	Phase
A	2.8284	135°	2.8788	135°	1.8	0.0°
B	2.0000	89.7°	1.9133	92.7°	4.3	3.0°
C	2.0396	−11.3°	2.0942	−11.8°	2.7	0.5°
D	3.0414	−80.5°	2.2650	−63.2°	25.5	17.3°
E	1.2806	−51.3°	1.3053	−51.5°	1.9	0.2°

Table A.3: Decomposition method error due to adjusted accelerometer location. A=incident traveling wave, B=controller near-field wave, C=controller traveling wave, D=reflected near-field wave, E=reflected traveling wave.

By minimizing the square of the error associated with each data point, the total resultant error in the decomposed coefficients is less than it would be in an exactly determined system.

It should be noted that, although the error in the traveling wave coefficients is less than the introduced error in all of the cases, the error in the near-field waves is on the same order as the introduced error. This is due to the fact that the traveling waves are present at all points along the beam while the near-field waves are present only in certain areas (such as near the discontinuity and application point of control). This means that, for the decomposition of the traveling waves, all of the accelerometer data points contribute to the traveling waves while only some of the data points contribute to the near-field waves decomposition. With all ten data points contributing to the decomposition of the traveling waves, the error in their coefficients is greatly reduced. The near-field waves have, at best, three or four data points which contribute to their decomposition .

This larger error is important to these experiments since the flexural near-fields contribute significantly to the supersonic region of the wavenumber spectrum and, hence, are a significant cause of the acoustic radiation. This is also the reason that the experimental wavenumber spectra did not match well with those predicted by theory. However, the calculations of the near-field amplitudes was accurate enough to follow the general trends predicted by theory.

A similar study was done with the decomposition algorithm for the infinite beam with a blocking mass. Waves of similar amplitude were assumed in the unadjusted equation and the same amount of random error was introduced into the data points. The results obtained from this were the same as those obtained in

the semi-infinite/clamped beam study. Therefore, the infinite beam study is not presented here and the presented study for the semi-infinite/clamped beam stands as representative.

It should be considered that the errors introduced in these studies are quite probably higher than the actual experimental errors incurred. The accuracy of the accelerometers used in these experiments is better than the 10% magnitude and 6° phase error introduced in this study. In addition, the error in location of the accelerometers would not have a standard deviation of $1mm$ since measurements errors of this magnitude could have easily been detected and corrected. Therefore, although there would obviously be some experimental error in the data presented in this thesis, it would be less than the error obtained in this study.

A.2 The Anechoic Termination as a Noise Source

As was pointed out in Ch. 4, it was discovered that the anechoic termination that was inside the anechoic chamber for the infinite beam with a blocking mass experiment was a source of acoustic radiation and interfered with the experiment. This was due to the termination reflecting small amounts of the incident flexural waves, thus producing supersonic wavenumber components which caused acoustic energy to propagate away from the termination and beam interface.

To solve this problem a layer of $20cm$ thick fiberglass insulation was placed over the beam/termination interface area. This served to absorb some of the sound produced in this region.

In order to demonstrate the effectiveness of this control technique intensity measurements were taken at several locations along the beam at a height of $20cm$ above the beam with and without the insulation. This was accomplished with a Bruel & Kjaer intensity probe and a Bruel & Kjaer signal analyzer. The intensity probe was held directly over the beam with the axis of the intensity probe pointing directly at the beam below. This orientation sample the sound generated at the point directly below the intensity probe without contributions from other points along the beam (due to the directionality of the intensity probe). Therefore, one would expect, in a perfectly infinite beam with a blocking mass discontinuity, to see the acoustic intensity peak directly over the blocking mass and drop off as the measurement point moved away from the discontinuity. One would also expect to see standing waves in the acoustic pattern due to the standing waves present in the beam response and the near-field proximity of the intensity probe.

The results from these measurements are shown in Figs. A.1, A.2 and A.3. It is shown in these figures that the area of the beam and termination interface (located at $x = -0.9m$) is a source of acoustic radiation which is attenuated when the insulation is in place (corresponding to the legend "with control"). The termination is a particularly strong radiator at 320Hz (only $5dB$ less than the strength of the blocking mass source). However, when the insulating layer was placed on the beam the source strength dropped considerably.

The author estimates that the difference in the source strength of the termination (without control insulation) in the microphone array relative to the source strength of the blocking mass was about $5dB$ at 320Hz and about $15dB$ at 510Hz and 690Hz. However, the affect of the termination as an acoustic source would vary greatly in

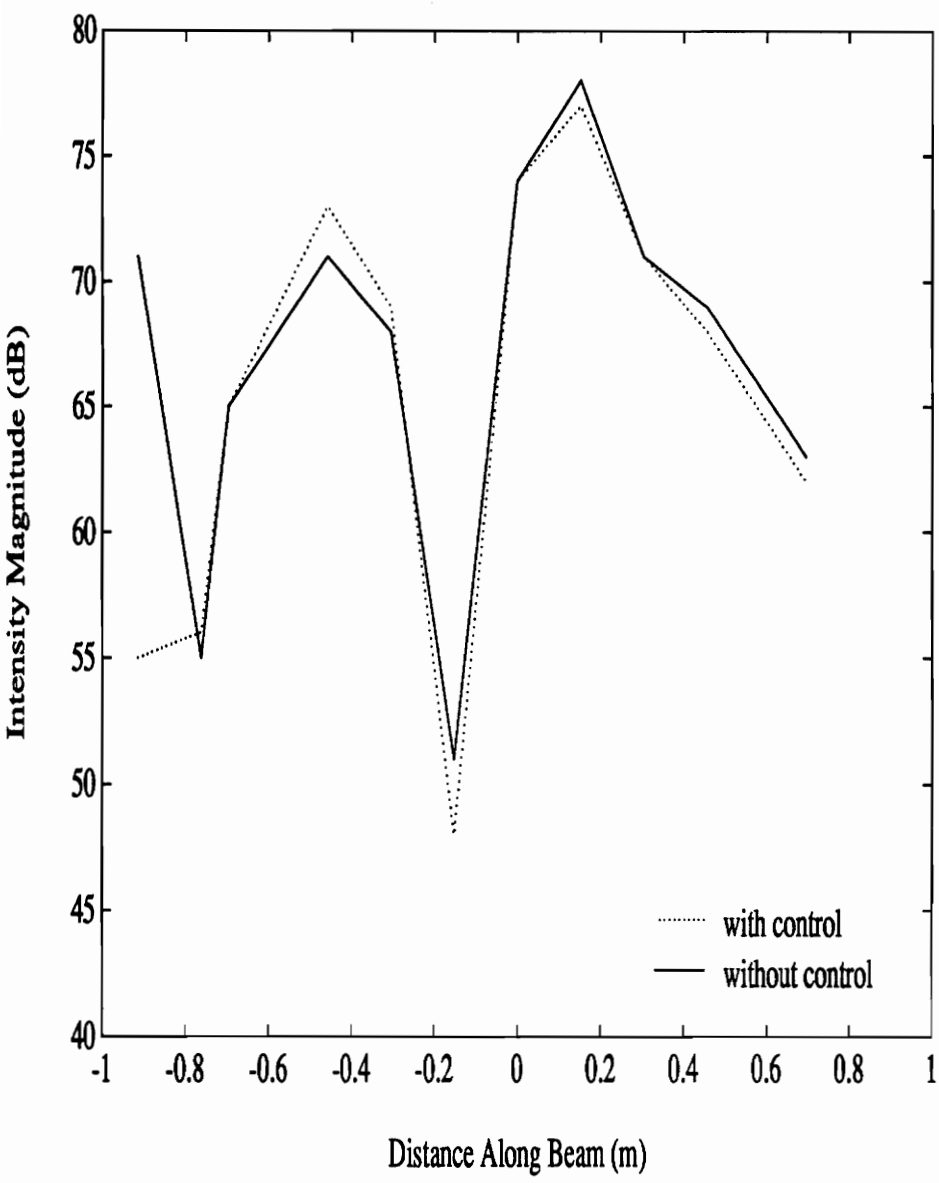

Figure A.1: Intensity measurements for the infinite beam with a blocking mass at 320Hz. Blocking mass located at $x = 0$, termination located at $x = -0.9m$.

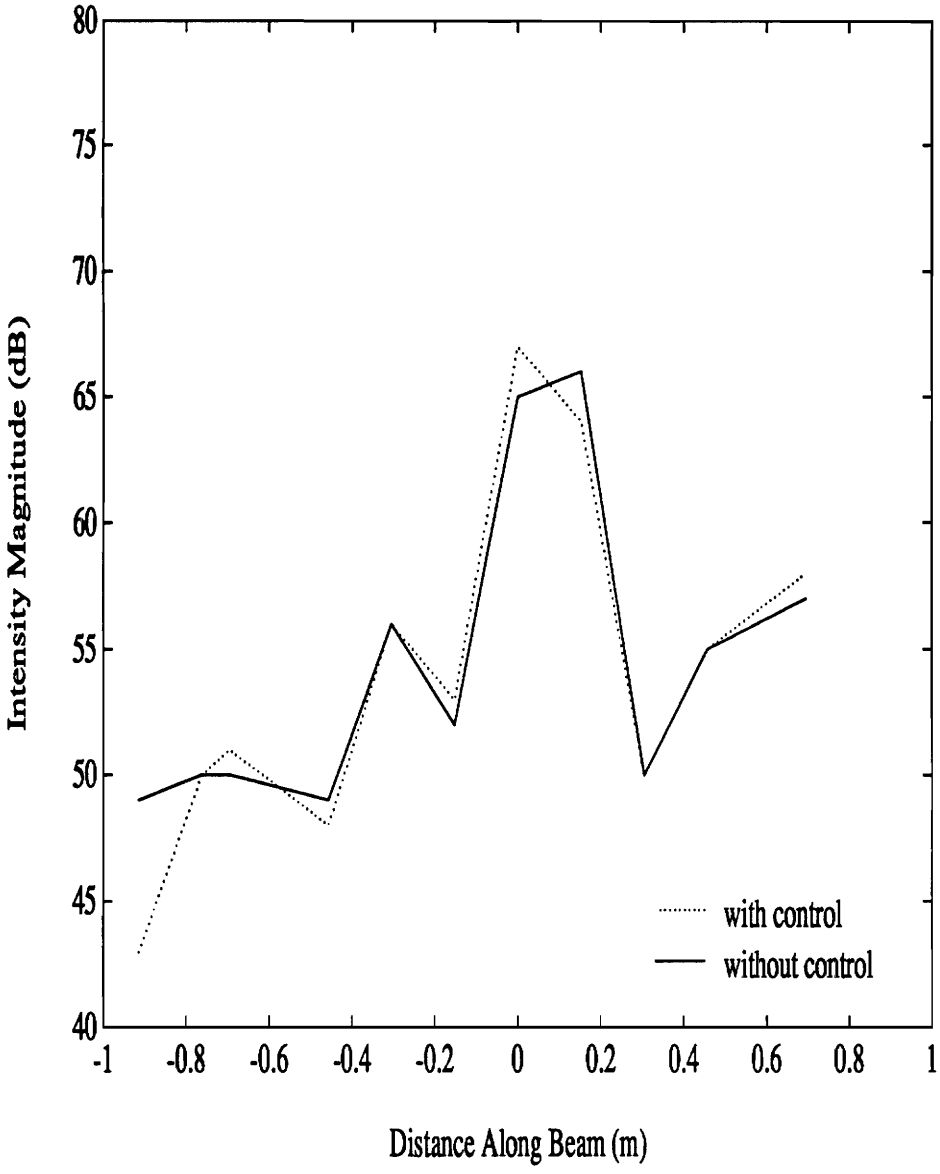

Figure A.2: Intensity measurements for the infinite beam with a blocking mass at 510Hz. Blocking mass located at $x = 0$, termination located at $x = -0.9m$.

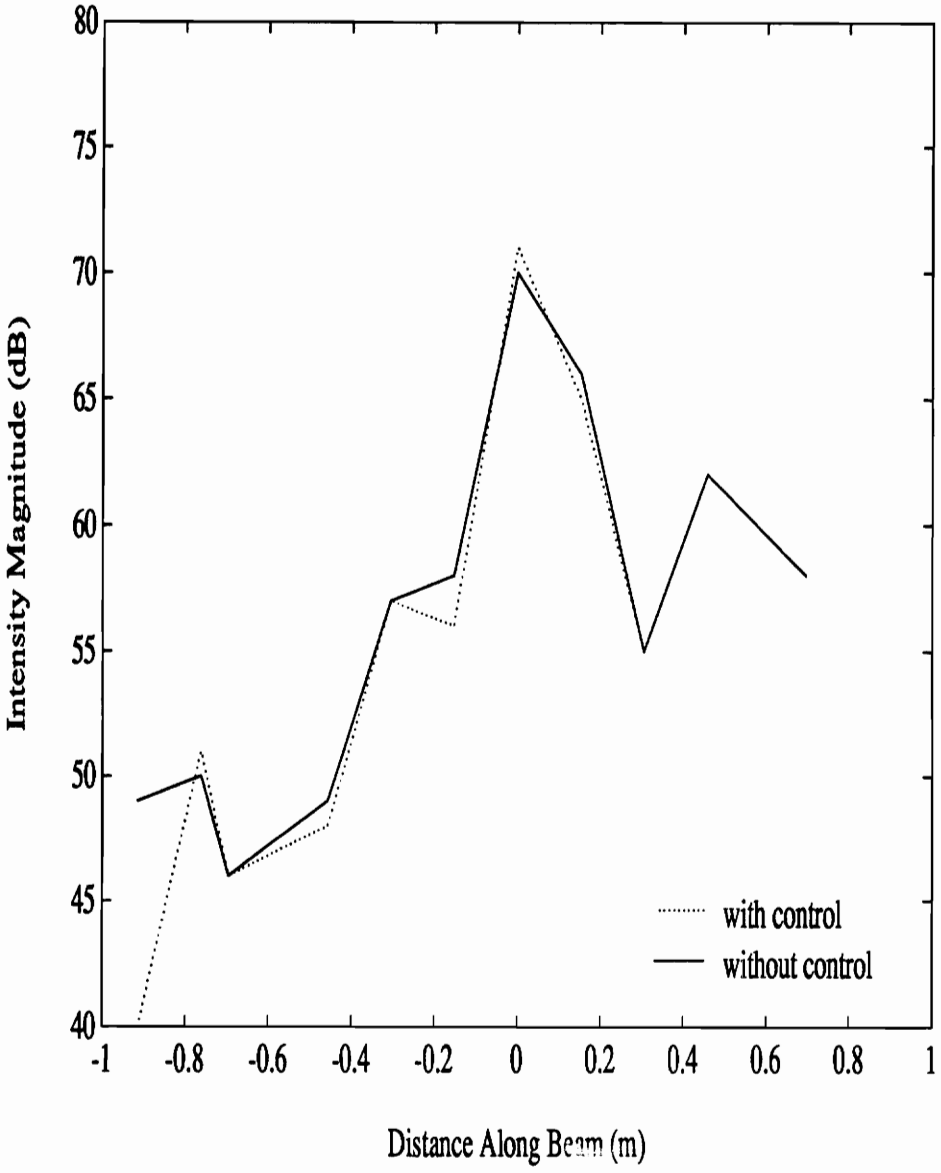

Figure A.3: Intensity measurements for the infinite beam with a blocking mass at 690Hz. Blocking mass located at $x = 0$, termination located at $x = -0.9m$.

the axial microphone array. This is because some of the microphones in the array were much closer to the termination than others. This enhanced effect was evident in the experiments performed before the attenuating insulation was put in place (see Fig. 4.35). The effects of the termination as an acoustic source were reduced to about a $25dB$ difference with the insulation in place. This was deemed an acceptable level and the experiments began to perform much better after this solution was found.

Another adjustment in the experimental rig that helped reduce the effects of the anechoic termination as an acoustical source was increasing the size of the blocking mass. This had the effect of reducing the magnitude incident on the termination by reducing the magnitude of the traveling wave transmitted through the blocking mass. Since the traveling wave incident on the termination was smaller, the scattered waves due to the termination were smaller. This served to reduce the supersonic wavenumber components produced at the termination/beam interface which reduced the acoustic radiation form the region.

Appendix B

Computer Programs

B.1 Semi-infinite/Clamped Beam Accelerometer Decomposition Program

In this section the program (written to operate in Matlab) used to decompose complex amplitudes for the displacement equation of the semi-infinite/clamped beam is listed. The particular case listed is for a single, point force controller. However, this can be easily altered to accommodate more control forces or moments.

```
%%%%%%%%%%%%%%%%%%%%%%%%%%%%%%%%%%%%%%%%%%%%%%%%%%%%%%%%%%%%%%%%%%%%%%%%%%%%
% This program decomposes the accelerometer data from the file
% acc.dat into the unknown coefficients of the assumed equation of
% motion for  the semi-infinite/clamped beam with one point force
% controller and stores the plot of the decomposed function under
% the given file name.
%%%%%%%%%%%%%%%%%%%%%%%%%%%%%%%%%%%%%%%%%%%%%%%%%%%%%%%%%%%%%%%%%%%%%%%%%%%%
%kw=structural wave number
%Magb=Accelerometer magnitude before control
%Maga=Acc. magnitude after control
%Accb=Transfer function before control
%Accam=Transfer function after control
%cal=Calibration transfer functions for the accelerometers
%disb & disa=before and after control displacements from acc. data
%%%%%%%%%%%%%%%%%%%%%%%%%%%%%%%%%%%%%%%%%%%%%%%%%%%%%%%%%%%%%%%%%%%%%%%%%%%%
```

```
  j=sqrt(-1);
  cal=[1+.0616*j;.943+.0349*j;1.32+.160*j;.921+.114*j;1.17+.095*j
       ;1.15+.131*j;1.14+.158*j;1.22+.0687*j;1.26+.120*j;1];
  g=input('File name: ','s');
  f=['meta c:\kdf\thesis\plots\' g];

 for i=1:10;
      disb(i)=Magb*Accb(i)/(w^2*cal(i));
      disa(i)=Maga*Acca(i)/(w^2*cal(i));

      ae(i)=exp(j*kw*x(i));
      be(i)=exp(-kw*abs(x(i)-a));
      ce(i)=exp(j*kw*abs(x(i)-a));
      de(i)=exp(-kw*x(i));
      ee(i)=exp(-j*kw*x(i));
 end

Yb=disb.';
Ya=disa.';

Xa=[ae;be;ce;de;ee].';
Xb=[ae;de;ee].';

Ub=inv(Xb.'*Xb)*Xb.'*Yb          %Coefficients before control
Ua=inv(Xa.'*Xa)*Xa.'*Ya          %Coefficients after control

%%%%%%%%%%%%%%%%%%%%%%%%%%%%%%%%%%%%%%%%%%%%%%%%%%%%%%%%%%%%
%Calculate and plot the function for displacement
%     xxb=displacement before control
%     xxa=displacement after control
%%%%%%%%%%%%%%%%%%%%%%%%%%%%%%%%%%%%%%%%%%%%%%%%%%%%%%%%%%%%

for i=1:100
   xx(i)=i/200-.005;
   xxb(i)=Ub(1)*exp(j*kw*xx(i))+Ub(2)*exp(-kw*xx(i))
         +Ub(3)*exp(-j*kw*xx(i));
   xxa(i)=Ua(1)*exp(j*kw*xx(i))+Ua(2)*exp(-kw*abs(xx(i)-a))
          +Ua(3)*exp(j*kw*abs(xx(i)-a))+Ua(4)*exp(-kw*xx(i))
          +Ua(5)*exp(-j*kw*xx(i));
end

xz=[.65 .7];
yz=[.77 .77];

axis([0 .8 0 abs(max([max(xxa) max(xxb)]))]);
plot(xx,abs(xxb),xx,abs(xxa),':',x,abs(disb),'*',x,abs(disa),'+')
title('Beam Motion Decomposition')
xlabel('Distance along beam--x (m) [0=clamp]')
ylabel('Displacement (m)')
polyline(xz,yz,':','sc')
```

```
text(.72,.75,'with control','sc')
polyline(xz,yz-.04,'-','sc')
text(.72,.71,'without control','sc')
text(.675,.67,'+ =data point','sc')
text(.72,.64,'with conrol','sc')
text(.675,.6,'* =data point','sc')
text(.72,.57,'without conrol','sc')
eval(f)
axis;

%%%%%%%%%%%%%%%%%%%%%%%%%%%%%%%%%%%%%%%%%%%%%%%%%%%%%%%%%%%%%%%%%%%%%%%
% This section calculates and plots the spatial fourier transform
%%%%%%%%%%%%%%%%%%%%%%%%%%%%%%%%%%%%%%%%%%%%%%%%%%%%%%%%%%%%%%%%%%%%%%%

for i=1:200
   k(i)=(i/2)-50.5;
   Abx=Ub(1)*j/(kw+k(i));
   Dbx=Ub(2)*j/(k(i)+j*kw);
   Ebx=Ub(3)*j/(k(i)-kw);

   Aax=Ua(1)*j/(kw+k(i));
   Bax=Ua(2)*((exp(j*k(i)*a)-exp(-kw*a))/(kw+j*k(i))
       +j*exp(kw*a)/(k(i)+j*kw)
       -(exp(j*k(i)*a)-exp(kw*a))/(j*k(i)-kw));
   Cax=Ua(3)*((exp(j*k(i)*a)-exp(j*kw*a))/(j*(k(i)-kw))
       +j*exp(-j*kw*a)/(kw+k(i))
       -(exp(j*k(i)*a)-exp(-j*kw*a))/(j*(kw+k(i))));
   Dax=Ua(4)*j/(k(i)+j*kw);
   Eax=Ua(5)*j/(k(i)-kw);

   Vkb(i)=j*w/sqrt(2*pi)*(Abx+Dbx+Ebx);
   Vka(i)=j*w/sqrt(2*pi)*(Aax+Bax+Cax+Dax+Eax);
   Va(i)=abs(Vka(i))^2;
   Vb(i)=abs(Vkb(i))^2;
end
ko=[1 1]*w/350;
zz=[max([max(Vkb) max(Vka)]) min([min(Vkb) min(Vka)])];
xz=[.67 .72];
yz=[.22 .22];

plot(-ko,20*log10(zz),'-',ko,20*log10(zz),'-',k,20*log10(abs(Vkb)),k,
      20*log10(abs(Vka)),':')
title('Velocity Fourier Transform')
xlabel('Wave No.--k (1/m)')
ylabel('Vel. Spectrum Magnitude [V(k)] (dB)')
polyline(xz,yz,':','sc')
text(.74,.2,'with control','sc')
polyline(xz,yz-.04,'-','sc')
text(.74,.16,'without control','sc')
meta
```

B.2 Infinite Beam with a Blocking Mass Decomposition Program

This is a list of the code used to decompose the complex wave amplitudes of the assumed equation of motion for the infinite beam with a blocking mass. This program was written to operate in Matlab. This version is for a single, point force control actuator but can easily be modified to accommodate more control forces or moments.

```
%%%%%%%%%%%%%%%%%%%%%%%%%%%%%%%%%%%%%%%%%%%%%%%%%%%%%%%%%%%%%%%%%%%%%%%%%%%%
% This program decomposes the accelerometer data from the file
% acc.dat into the unknown COEFFICIENTS of the assumed equation of
% motion for the infinite beam with a blocking mass and one point
% force controller and stores the plot of the DECOMPOSED function
% under the given file name.
%%%%%%%%%%%%%%%%%%%%%%%%%%%%%%%%%%%%%%%%%%%%%%%%%%%%%%%%%%%%%%%%%%%%%%%%%%%%
% kw=structural wave number
% Magb=Accelerometer magnitude before control
% Maga=Acc. magnitude after control
% Accb=Transfer function before control
% Accam=Transfer function after control
% cal=Calibration transfer functions for the accelerometers
% disb & disa=before and after control displacements from acc. data
% x=accelerometer coordinates
%%%%%%%%%%%%%%%%%%%%%%%%%%%%%%%%%%%%%%%%%%%%%%%%%%%%%%%%%%%%%%%%%%%%%%%%%%%%

  load acc.dat
  j=sqrt(-1);
  cal=[1+.0616*j;.943+.0349*j;1.32+.160*j;.921+.114*j;1.17+.095*j;
       1.15+.131*j;1.14+.158*j;1.22+.0687*j;1.26+.120*j;1];
x=[.00635 .0127 .0508 .0635 .1143 .1524 .1651 -.00635 -.0508 -.0635];

 for i=1:10;
      disb(i)=Magb*Accb(i)/(w^2*cal(i));
      disa(i)=Maga*Acca(i)/(w^2*cal(i));

      ae(i)=exp(j*kw*x(i));
      be(i)=exp(-kw*x(i));
      ce(i)=exp(-j*kw*x(i));
      de(i)=exp(-kw*abs(x(i)-a));
      ee(i)=exp(j*kw*abs(x(i)-a));
      fe(i)=exp(kw*x(i));
```

```
      ge(i)=exp(j*kw*x(i));
      he(i)=exp(-j*kw*x(i));
 end

Ypb=disb(1:7).';
Ypa=disa(1:7).';

Xpa=[ae(1:7).' be(1:7).' ce(1:7).' de(1:7).' ee(1:7).'];
Xpb=[ae(1:7).' be(1:7).' ce(1:7).'];

Upb=inv(Xpb.'*Xpb)*Xpb.'*Ypb        %Coefficients before control x>0
Upa=inv(Xpa.'*Xpa)*Xpa.'*Ypa        %Coefficients after control x>0

Ymb=disb(8:10).';
Yma=disa(8:10).';

Xma=[ge(8:10).' fe(8:10).' he(8:10).'];
Xmb=[ge(8:10).' fe(8:10).' he(8:10).'];

Umb=inv(Xmb.'*Xmb)*Xmb.'*Ymb        %Coefficients before control x<0
Uma=inv(Xma.'*Xma)*Xma.'*Yma        %Coefficients after control x<0

%%%%%%%%%%%%%%%%%%%%%%%%%%%%%%%%%%%%%%%%%%%%%%%%%%%%%%%%%%%
%Calculate and plot the function for displacement
%     xxb=displacement before control
%     xxa=displacement after control
%%%%%%%%%%%%%%%%%%%%%%%%%%%%%%%%%%%%%%%%%%%%%%%%%%%%%%%%%%%
for i=1:200
   xx(i)=i/200-.505;
 if xx(i)>=0
   xxb(i)=Upb(1)*exp(j*kw*xx(i))+Upb(2)*exp(-kw*xx(i))
          +Upb(3)*exp(-j*kw*xx(i));
   xxa(i)=Upa(1)*exp(j*kw*xx(i))+Upa(2)*exp(-kw*xx(i))
          +Upa(3)*exp(-j*kw*xx(i))+Upa(4)*exp(-kw*abs(xx(i)-a))
          +Upa(5)*exp(j*kw*abs(xx(i)-a));

 elseif xx(i)<0
   xxb(i)=Umb(1)*exp(j*kw*xx(i))+Umb(2)*exp(kw*xx(i))
          +Umb(3)*exp(-j*kw*xx(i));
   xxa(i)=Uma(1)*exp(j*kw*xx(i))+Uma(2)*exp(kw*xx(i))
          +Uma(3)*exp(-j*kw*xx(i));
 end
end

xz=[.12 .17];
yz=[.9 .9];

axis([-.50 .5 0 abs(max([max(xxa) max(xxb)]))]);
plot(xx,abs(xxb),xx,abs(xxa),':',x,abs(disb),'*',x,abs(disa),'+')
title('Beam Motion Decomposition')
```

```
xlabel('Distance along beam--x (m) [0=clamp]')
ylabel('Displacement (m)')
polyline(xz,yz,':','sc')
text(.19,.88,'with control','sc')
polyline(xz,yz-.04,'-','sc')
text(.19,.84,'without control','sc')
text(.145,.8,'+ =data point','sc')
text(.19,.77,'with conrol','sc')
text(.145,.73,'* =data point','sc')
text(.19,.7,'without conrol','sc')
axis;

%%%%%%%%%%%%%%%%%%%%%%%%%%%%%%%%%%%%%%%%%%%%%%%%%%%%%%%%%%%%%%%%%%%%%%%%%%%
% This section calculates and plots the spatial fourier transform
%%%%%%%%%%%%%%%%%%%%%%%%%%%%%%%%%%%%%%%%%%%%%%%%%%%%%%%%%%%%%%%%%%%%%%%%%%%

for p=1:200
   k(p)=(p/2)-50.5;
   Abx=Upb(1)*j/(k(p)+kw);
   Bbx=Upb(2)*j/(k(p)+j*kw);
   Cbx=Upb(3)*j/(k(p)-kw);
   Fbx=-Umb(2)*j/(k(p)-j*kw);
   Gbx=-Umb(1)*j/(k(p)+kw);
   Hbx=-Umb(3)*j/(k(p)-kw);

   Aax=Upa(1)*j/(k(p)+kw);
   Bax=Upa(2)*j/(k(p)+j*kw);
   Cax=Upa(3)*j/(k(p)-kw);
   Dax=Upa(4)*((exp(-j*k(p)*a)-exp(-kw*a))/(kw+j*k(p))
       +j*exp(kw*a)/(k(p)+j*kw)
       +(-exp(j*k(p)*a)+exp(kw*a))/(j*k(p)-kw));
   Eax=Upa(5)*((exp(j*k(p)*a)-exp(j*kw*a))/(j*(k(p)-kw))
       +j*exp(-j*kw*a)/(kw+k(p))
       +(-exp(-j*k(p)*a)+exp(-j*kw*a))/(j*(kw+k(p))));
   Fax=-Uma(2)*j/(k(p)+j*kw);
   Gax=-Uma(1)*j/(k(p)+kw);

   Vkb(p)=j*w/sqrt(2*pi)*(Abx+Bbx+Cbx+Fbx+Gbx+Hbx);
   Vka(p)=j*w/sqrt(2*pi)*(Aax+Bax+Cax+Dax+Eax+Fax+Gax);
   Va(p)=abs(Vka(p))^2;
   Vb(p)=abs(Vkb(p))^2;
end
ko=[1 1]*w/350;
zz=[max([max(Vkb) max(Vka)]) min([min(Vkb) min(Vka)])];
xz=[.67 .72];
yz=[.22 .22];

plot(k,20*log(Vkb),k,20*log(Vka),':')
title('Velocity Fourier Transform')
xlabel('Wave No.--k (1/m)')
```

```
      de(i)=exp(-kw*x(i));
      ee(i)=exp(-j*kw*x(i));
end

Yb=wb.';
Ya=wa.';

Xa=[ae.' be.' ce.' de.' ee.'];
Xb=[ae.' de.' ee.'];

Ub=inv(Xb.'*Xb)*Xb.'*Yb          %Coefficients before control
Ua=inv(Xa.'*Xa)*Xa.'*Ya          %Coefficients after control
stop
```

Vita

Kenneth Donald Frampton was born on January 18, 1966 in Woodbury, New Jersey. When he was very young his family moved to Marietta, Ohio which he considers his home town. In the fall of 1984 he went to Virginia Tech and received a bachelors degree in mechanical engineering in 1989. Upon completion of his undergraduate studies, he began work towards his masters degree in mechanical engineering which he received in the spring of 1991. He may currently be found soaring the ridges of the Blue Ridge mountains, coursing his greyhounds or working for Wyle Laboratories in Arlington, VA.